



Universidad de Granada

FACULTAD DE CIENCIAS
DEPARTAMENTO DE FÍSICA APLICADA

TESIS DOCTORAL

**VISCOELASTIC
MAGNETORHEOLOGICAL FLUIDS
(FLUIDOS MAGNETO-REOLÓGICOS
VISCOELÁSTICOS)**

Programa de Doctorado: Programa Oficial de
Doctorado en Física y Ciencias del Espacio

Juan Pablo Segovia Gutiérrez

Granada, Julio de 2013

**Supervisores: Juan de Vicente Álvarez Manzaneda, Roque
Hidalgo Álvarez y Antonio Manuel Puertas López**

Editor: Editorial de la Universidad de Granada
Autor: Juan Pablo Segovia Gutiérrez
D.L.: GR 507-2014
ISBN: 978-84-9028-814-6



Respeto de los Derechos de Autor

El doctorando Juan Pablo Segovia Gutiérrez y los directores de la tesis Roque Hidalgo Álvarez, Juan de Vicente Álvarez Manzaneda y Antonio Manuel Puertas López, garantizamos, al firmar esta tesis doctoral, que el trabajo ha sido realizado por el doctorando bajo la dirección de los directores de la tesis y hasta donde nuestro conocimiento alcanza, en la realización del trabajo, se han respetado los derechos de otros autores a ser citados, cuando se han utilizado sus resultados o publicaciones.

Granada, a 12 de Julio de 2013.

Director/es de la Tesis



Fdo.: Roque Hidalgo Álvarez

Doctorando



Fdo.: Juan Pablo Segovia Gutiérrez



Fdo.: Juan de Vicente Álvarez Manzaneda



Fdo.: Antonio Manuel Puertas López





AGRADECIMIENTOS

En primer lugar quiero agradecer a mis directores de Tesis, Juan de Vicente, Roque y Antonio el grandísimo apoyo que me han dado durante estos casi 5 años de doctorado que han sido, con momentos difíciles a veces, realmente maravillosos y productivos, tanto profesional como personalmente. También quiero agradecerles la gran confianza depositada en mí, y por supuesto, su inestimable paciencia. Por tanto, para mí ha sido un orgullo trabajar bajo su batuta y espero que en un futuro no muy lejano podamos volver a estar bajo el mismo techo.

En segundo lugar quiero agradecer todo el apoyo que he recibido por parte de mi familia, de mis padres y, muy especialmente, de mi novia Adriana, que ha sido el pilar de mi vida los últimos 3 años (espero que el resto de mi vida lo siga siendo) y que sin ella todo hubiera sido mucho más complicado. Te quiero, Adriana.

En tercer lugar, y con muchísimo cariño, dar las gracias a todos mis compañeros: a Efrén por su inestimable ayuda; a Miguel Peláez por su picardía; a Miguel Wulff por su inmejorable humor; a Amelia por su buen hacer; a Paola por su maravillosa forma de ver la vida; a Pablo por aguantarme durante años a su lado y escuchar de todo; a José Antonio por su inmensa simpatía y amistad; a Carmen y a Felipe por ser como son, porque son muy especiales; a Migue y Leo por ser la pareja más luchadora de la Sala; cómo no, a Azahara por guiarnos a todos en mil situaciones; a Miriam, por su grandeza de espíritu; a Diego por ser una gran persona con maravillosas convicciones; a Dani, porque aunque fugaz en la sala, anima la fiesta y a Álvaro, por aportar un toque de juventud a la sala.



Por supuesto, y no se me olvidaba, dar las gracias a Luisma, mi querido sevillano, que con mucho arte y salero nos alegró la vida a todos durante unos mesecillos.

Quiero dar las gracias también al grupo en general por formar un grandísimo equipo de buenas personas y buenos profesionales y, especialmente, a Fernando Vereda por estar ahí cuando le he necesitado.

Finalmente, a título póstumo, quiero recordar a Manu que, aunque lo conocí poco por desgracia, para mí fue alguien especial.

**Dedicado a mi familia
y a mi novia, Adriana**

◆

OUTLINE

I.	INTRODUCTION.....	9
II.	INTRODUCCIÓN.....	17
III.	BACKGROUND.....	25
	<i>a. Colloids.....</i>	25
	<i>b. Magnetic colloids.....</i>	27
	i. Ferrofluids.....	27
	ii. Magnetorheological (MR) fluids.....	28
	<i>c. MR fluids.....</i>	30
	i. Basics about Rheology.....	31
	ii. Boger fluids.....	40
	iii. Basics about Magnetism.....	44
	iv. Experimental rheological tests.....	52
	<i>d. Brownian Dynamic Simulations on MR fluids.....</i>	59
	<i>e. References.....</i>	77
IV.	PART I: EFFECT OF THE PARTICLE MORPHOLOGY.....	81
	<i>a. Dynamic rheology of sphere- and rod-based magnetorheological fluids.....</i>	81
	<i>b. Effect of the particle shape in magnetorheology.....</i>	121
	<i>c. On the effect of particle porosity and roughness in magnetorheology.....</i>	175
V.	PART II: YIELD STRESS AND THE EFFECT OF PARTICLE CONCENTRATION.....	209
	<i>a. Nonlinear viscoelasticity and two-step yielding in magnetorheology: A colloidal gel approach to understand the effect of particle concentration.....</i>	209



	<i>b. Average particle magnetization as an experimental scaling parameter for the yield stress of dilute magnetorheological fluids.....</i>	<i>251</i>
VI.	PART III: BROWNIAN DYNAMIC SIMULATIONS IN MR FLUIDS.....	273
	<i>a. Brownian dynamics simulations in magnetorheology and comparison with experiments.....</i>	<i>273</i>
VII.	STRONGLY VISCOELASTIC MR FLUIDS.....	305
VIII.	CONCLUSIONS.....	319
IX.	CONCLUSIONES.....	323
X.	APPENDIX A: SIMULATION CODES.....	327
XI.	BRIEF CV.....	391



INTRODUCTION

“Set of knowledge obtained through observation and reasoning, systematically structured and from which principles and general laws are deduced”. This sentence is the definition of Science which appears in the “Real Academia Española de la Lengua” dictionary. Through the History, the human curiosity about natural events has led to better understand our environment and this fact has allowed us to evolve and to achieve a very high level of knowledge, that has given and is giving the best and the worst of the human intelligence. Within this great knowledge that is Science, we find one of the most important disciplines, **Physics**. This scientific branch focuses on studying measurable properties of matter and energy and is able to address scenarios such vast as the Universe and its galaxies, and as small as the inside of an atomic core. Looking at that scale, we encounter the **microscopic range** where we can place **colloids**. The *leitmotiv* that occupies this dissertation is an attempt to contribute to understand what are the fundamental physical mechanisms of very versatile systems such as magnetic colloids and more specifically, **magnetorheological (MR) fluids**.

What is a MR fluid? The typical composition of these systems consists in a solid phase, usually formed by **ferromagnetic microparticles** (from 100 nm to 10 μm in diameter), dispersed in a **non-magnetizable medium** (mineral oils, aqueous solutions, gels, etc.). The solid phase commonly is constituted by **magnetite** or **iron** particles, which can have **different morphologies and sizes**. The main feature of these particles is their ability to be magnetically **polarized under the application of an external magnetic field**. The field-induced magnetic moment in each particle is aligned in the direction of the magnetic field and, as a first



approximation, they behave like **magnetic dipoles** which interact between them; and due to this fact, particles attract or repel each other as a function of their relative positions, i.e. when particles are in the perpendicular to the magnetic field plane they suffer a total repulsion, contrary to what happens when particles are aligned in the magnetic field direction, where the attracting force reaches a maximum. In that process, particles move through the bulk, relocating and forming **columnar aggregates in the direction of the magnetic field**. In a few **milliseconds**, structures are completely formed and the final result, which involves rigidity and columnar thickness, mainly and strongly depends on the **particle size, the particle morphology, the particle concentration, and the intensity of the external magnetic field**. By maintaining an active field, these structures remain over time, but if the magnetic field is turned off, because of the ferromagnetic nature of particles, they depolarize and particle aggregates dissolve, so it is a reversible effect.

One of the **main handicaps** which present MR fluid technology is **particle sedimentation**. As we mentioned above, the typical composition of particles is magnetite or iron and it is well known that these materials have a much higher density (5.2 and 7.8 g/cm³, respectively), specially in the case of iron, with respect to the solvent density (in the case of oils, $\rho \sim 1$ g/cm³). This fact makes it difficult to manufacture a stable commercial MR fluid and many efforts have been made in the past to prevent particle settling. Due to this fact, a new condition has to be introduced in the formulation of MR fluids: particles must have an appropriate size, which should be large enough so that the magnetic forces overcome thermal motion and small enough in order to prevent sedimentation.


How could we study the physical properties of MR fluids? These systems are well known because of their **magnetic field-tunable rheological properties**. In the absence of a magnetic field, these systems typically behave as Newtonian fluids. Nonetheless, under the application of a magnetic field, dispersed particles are polarized and consequently, as it was mentioned above, they form **columnar aggregates aligned in the direction of the magnetic field**, the so-called “**magnetorheological effect**” or “**MR effect**”, first described more than 60 years ago. Then, the most extended techniques to study MR fluids are placed in the field of Rheology and therefore, our experimental tests are mainly based on its methods. To better understand experimental results and their interpretation, it is convenient to go deeply into the comprehension of what is the mechanism behind the magnetorheological response and which parameters are determinant.

To carry out rheological tests, the MR fluid sample is confined between two parallel plates, where the upper plate is free to move and the lower one is fixed (in our case the plates are made of titanium), and they are separated by a certain gap distance (usually $300\ \mu\text{m}$). In this configuration, an electromagnet is used to apply the external magnetic field. Then, when a high enough magnetic field is applied perpendicular to the plates, particles form chain-like aggregates that, to a greater or lesser extent, **span throughout the gap and connect the plates**. At first glance, the number of **connecting aggregates** will vary as a function of the particle volume fraction and the value of the magnetic field strength. In line with the latter, one might be surmised that the magnetorheological effect may be dependent on the nature of these microstructures and the number of gap spanning aggregates. Hence, it is reasonable to argue that gap spanning columns offer a certain resistance to the



movement of the upper plate and this fact is directly related with the macroscopic response. Therefore, by means of rheological tests, we are able to build a bridge which connects microscopic behavior of the structure with measurable physical magnitudes of MR fluids.

Rheological tests, basically, consist in the study of the relationship between the stress and the deformation that suffers a sample. Throughout this work, four kinds of tests were mainly carried out. One of them was the magneto-sweep test, in which the sample is subjected to a constant amplitude oscillatory shear deformation, at a constant frequency, and then a progressive increase in the magnetic field is applied from very low fields to values in the order of 800 kA/m, where particles are magnetically saturated. In this test **viscoelastic moduli**, i.e. the storage and the loss modulus (G' and G'' , respectively), **corresponding to the ability of the system to storage or dissipate energy**, can be quantified as a function of the magnetic field strength. As discussed above, we could suggest that the more elastic or the more viscous character of the system is due to a stronger or a weaker microstructure. The next two rheological tests were the strain amplitude sweep and the frequency sweep. For both methods, the sample is **under a constant magnetic field** from the beginning to the end of the test. This allows us to observe the **transition from the elastic to viscous behavior** and therefore, from these results, we can extract information about how the microstructure works under different conditions. The fourth test consists in varying the shear rate (or deformation velocity at which the sample is subjected; shear rate-controlled tests) or the shear stress (shear stress-controlled tests), i.e. the sample is continuously deformed in both cases. Again, this test is executed under constant magnetic fields. Under these flow conditions, if the particle concentration and the magnetic field strength are high



enough, a **yielding process** can be observed, which consists in the appearance of a **shear stress threshold**, below which the sample does not flow. The phenomenon can be identified in the log-log representation of shear stress *versus* shear rate as the shear stress plateau at medium shear rate values. Concretely, this stress is the so-called **static yield stress** because it refers to the minimum stress value to reach the onset of the flow. Also in the same tests, the **dynamic yield stress** can be observed, which corresponds to the stress needed to continuously break the aggregates which reform in the presence of the magnetostatic forces once the stress exceeds the static yield stress. This yield stress can be easier observed in a lin-lin shear stress-shear rate representation.

Under a colloidal gel approach, we were capable to model the internal structure of a magnetized MR fluid from a fractal point of view. In addition, we checked some theoretical models reported in the MR literature which try to explain the dependence of the storage modulus and the yield stress on magnetic field, particle volume fraction and particle magnetization. Also we proposed an alternative theoretical model referring to the dependence of the storage modulus on particle anisotropy.

An important contribution to this dissertation is the computational section. As a way to complete experimental results and to reinforce the knowledge about the mechanisms behind the structural behavior, we carried out Brownian Dynamics Simulations. This tool allows us to understand **how the structuration process occurs and connection between structure and dynamics of the system**. On the one hand, this computational technique provides a complete vision about the structure, by parametrizing the most relevant structural aspects. On the other hand, we can obtain, from numerical calculations, very important physical



magnitudes such as **the viscosity, the shear stress** and **the viscoelastic moduli**. Also we can study the dynamics of particles inside the structure by means of **the mean square displacement** and **the stress correlation function**. Interestingly, results obtained from simulations and from experiments are satisfactorily compared, as there was a very good agreement that reinforces our assumptions.

Why to study MR fluids? There are many motivations to embark on this study, such as basic physics which is important itself due to the contribution to the knowledge, in general, and to understanding physical mechanisms in magnetic colloidal systems, in particular. On the other hand, from a commercial application point of view, MR fluids are very adequate because of their controllable properties. Some of these applications are, for example, shock absorbers, brakes, seismic vibration dampers and sound propagation, and biomedical applications among others.

The opening of this dissertation is the **Background** where the main objective is to give the reader a broader view of the fundamental physical mechanisms of MR fluids. Regarding the morphology of particles, in **Part I** we perform a systematic study about the influence of that feature (we take spherical, rod-like and plate-like particles with different surfaces) in the magnetorheological response under different conditions, and we also take into account the effect of particle composition in the rheological properties. In **Part II**, we try to better understand the yielding processes (static and dynamic yield stress) and the effect of particle concentration, varying the volume fraction from 0.5 to 50 vol%, and using the colloidal gel approach to understand the effect. As a way to complete the experimental studies, we developed computational methods based on **Brownian Dynamics Simulations** techniques to describe and



comprehend the formation of particle aggregates at microscopic level and to extrapolate simulation results to macroscopic measurements. The use of Brownian Dynamics will be justified in the corresponding part (**Part III**) and, as additional information, simulation codes are shown in **Appendix A**. The main conclusions of this work are written in **Part IV**. Finally, in the concluding section (**Conclusions**) the main important conclusions from this dissertation will be given.





INTRODUCCIÓN

“Conjunto de conocimiento obtenido a través de la observación y el razonamiento, sistemáticamente estructurado y del cual los principios y las leyes generales son deducidos”. Esta frase es la definición de Ciencia que aparece en el diccionario de la Real Academia Española de la Lengua. A través de la Historia, la curiosidad humana sobre los eventos naturales ha permitido un mejor entendimiento sobre nuestro entorno y este hecho nos ha permitido evolucionar y alcanzar un alto nivel de conocimiento, que ha dado y está dando lo mejor y lo peor de la inteligencia humana. Dentro del gran conocimiento que es la Ciencia, encontramos una de las más importantes disciplinas, la Física. Esta rama científica se centra en el estudio de las propiedades medibles de la materia y es capaz de abarcar escenarios tan inmensos como el Universo y sus galaxias así como tan pequeños como el núcleo atómico. Mirando a esta escala, encontramos el rango microscópico, donde podemos situar a los coloides. El *leitmotiv* que nos ocupa en esta disertación es un intento de contribuir al entendimiento en los mecanismos físicos fundamentales de sistemas tan versátiles como los son los coloides magnéticos y, más concretamente, los fluidos magneto-reológicos (fluidos MR).

¿Qué es un fluido MR? La composición típica de estos sistemas consiste en una fase sólida, normalmente formada por micropartículas ferromagnéticas (con diámetros entre 100 nm y 10 μm), dispersas en un medio no magnetizable (aceites minerales, soluciones acuosas, geles, etc.). La fase sólida comúnmente está constituida por partículas de magnetita o hierro, las cuales pueden tener diferentes morfologías y tamaños. La característica principal de estas partículas es su habilidad para ser polarizadas magnéticamente en presencia de un campo



magnético externo. El momento magnético inducido en cada partícula se alinea en la dirección del campo magnético y, como primera aproximación, las partículas se comportan como dipolos magnéticos que interactúan entre ellos; y debido a este hecho, las partículas se atraen o se repelen entre sí en función de su posición relativa, es decir, cuando las partículas están en un mismo plano perpendicular al campo magnético sufren una repulsión total, al contrario de lo que ocurre cuando las partículas se encuentran alineadas en la dirección del campo magnético, donde la fuerza de atracción es máxima. En este proceso, las partículas se mueven a través de la fase continua, recolocándose y formando agregados columnares en la dirección del campo magnético. En unos pocos milisegundos, las estructuras son completamente formadas, dependiendo el resultado final principalmente y fuertemente del tamaño de partícula, de su morfología, de la fracción de volumen y de la intensidad del campo magnético. Manteniendo el campo activo, estas estructuras se mantiene en el tiempo, pero si el campo magnético se desactiva, debido a la naturaleza ferromagnética de las partículas, se despolarizan y los agregados se disuelven, lo que implica reversibilidad.

Uno de los principales inconvenientes que presenta la tecnología que usa fluidos MR es la sedimentación de las partículas. Como se dijo antes, la composición típica de las partículas es de magnetita o hierro y es bien sabido que estos materiales tienen unas densidades más altas (5.2 y 7.8 g/cm³, respectivamente), especialmente el hierro, que la densidad del solvente (en el caso de aceites de silicona, $\rho \sim 1$ g/cm³). Este hecho hace difícil la fabricación de fluidos MR comerciales estables y, por tanto, muchos esfuerzos se han puesto en el pasado para prevenir la sedimentación. Por ello, una nueva condición se ha de introducir en la formulación de los fluidos MR: las partículas deben de tener un

tamaño apropiado que sea lo suficientemente grande como para que las fuerzas magnéticas superen a la agitación térmica y lo suficientemente pequeño como para prevenir la sedimentación.

¿Cómo se pueden estudiar las propiedades físicas de los fluidos MR? Estos sistemas son bien conocidos porque sus propiedades reológicas pueden ser controladas y modificadas. En ausencia de campo magnético, estos sistemas típicamente se comportan como fluidos Newtonianos. Sin embargo, bajo la aplicación de un campo magnético, las partículas dispersas se polarizan y, consecuentemente, como se dijo antes, forman agregados columnares en la dirección del campo magnético, lo que se conoce con el nombre de “efecto MR”, descrito por primera vez hace unos 60 años. Por ello, las técnicas más extendidas en el estudio de los fluidos MR se sitúan dentro del campo de la Reología y, por tanto, nuestros experimentos están principalmente basados en estos métodos. Para entender mejor los resultados experimentales y su alcanzar una interpretación razonada, es conveniente profundizar en la comprensión de los mecanismos que hay detrás de la respuesta magneto-reológica y cuáles son los parámetros determinantes.

Para llevar a cabo los ensayos reológicos, la muestra de fluido MR se confina entre dos platos paralelos, donde el plato superior es libre de rotar y el inferior se fija (en nuestro caso estos platos están fabricados de titanio), separados una cierta distancia (normalmente $300 \mu m$). En esta configuración, un electroimán es usado para aplicar el campo magnético externo. Entonces, cuando el campo magnético es lo suficientemente intenso y se aplica perpendicular a los platos, las partículas forman agregados en forma de cadenas, más o menos extendidos, que conectan ambos platos. A primera vista, el número de agregados que conectan los platos variará en función de la fracción de volumen de partículas y



del valor de la intensidad del campo magnético. En línea con lo último, uno podría intuir que el efecto MR pudiera depender de la naturaleza de las microestructuras y del número de agregados que conectan los platos. Por tanto, es razonable argumentar que las columnas que conectan los platos ofrecen una cierta resistencia al movimiento del plato superior y que este hecho está directamente relacionado con la respuesta macroscópica. Así, mediante los ensayos reológicos seríamos capaces de construir un puente que uniese el comportamiento microscópico de la estructura con las magnitudes físicas medibles de los fluidos MR.

Los ensayos reológicos, básicamente, consisten en el estudio de la relación entre el esfuerzo y la deformación que sufre la muestra. A través de este trabajo se llevaron a cabo, principalmente, cuatro tipos de ensayos. Uno de ellos fue el barrido de campo, en el cual la muestra es sometida a una deformación oscilatoria con una amplitud constante a una cierta frecuencia, y un progresivo incremento del campo magnético es aplicado desde valores muy bajos hasta valores del orden de 800 kA/m, donde las partículas están saturadas magnéticamente. En este ensayo, los módulos elástico y viscoso (G' y G'' , respectivamente), es decir, los módulos viscoelásticos, que corresponden con la habilidad del sistema de almacenar o disipar energía, pueden ser cuantificados en función del campo magnético. Como se discutió anteriormente, podríamos sugerir que el carácter más elástico o más viscoso del sistema se debe a estructuras más fuertes o más débiles.

Los dos siguientes ensayos reológicos fueron el barrido de amplitud de deformación y el barrido de frecuencia. Para ambos métodos, la muestra se encuentra bajo un campo magnético constante desde el comienzo hasta el final del test. Esto nos permite observar la transición desde el estado elástico al

viscoso y, por tanto, de estos resultados, podemos extraer información sobre cómo la micro-estructura funciona bajo diferentes condiciones.

El cuarto ensayo consiste en variar la velocidad de deformación a la cual se somete la muestra (la muestra es continuamente deformada) y, de nuevo, este ensayo se lleva a cabo bajo un campo magnético constante. En estas condiciones de flujo, si la concentración de partículas y la intensidad del campo magnético son suficientemente elevadas, se puede observar un nuevo fenómeno que consiste en la aparición de un esfuerzo de umbral de cizalla por debajo del cual la muestra no fluye. El fenómeno se puede identificar en una representación log-log del esfuerzo frente a la velocidad de deformación como un plateau del esfuerzo de cizalla a valores intermedios de la velocidad de deformación. Concretamente, este esfuerzo se conoce como esfuerzo umbral estático porque se refiere al mínimo valor del esfuerzo para iniciar el flujo. También, en el mismo ensayo se puede observar el esfuerzo umbral dinámico, que corresponde con el esfuerzo necesario para continuar rompiendo los agregados que se reestructuran en presencia de las fuerzas magnetostáticas, una vez se ha excedido el esfuerzo umbral estático. Este esfuerzo umbral puede ser observado fácilmente en una representación lin-lin del esfuerzo de cizalla frente a la velocidad de deformación.


Dentro del marco de geles coloidales, fuimos capaces de modelar la estructura interna de los fluidos MR magnetizados desde un punto de vista fractal. Además, testeamos algunos modelos teóricos que aparecen en la bibliografía de fluidos MR, que intentan explicar la dependencia del módulo elástico y del esfuerzo umbral con el campo magnético, la concentración de partículas y la magnetización de las mismas. También, propusimos un modelo teórico



alternativo que se refiere a la dependencia del módulo elástico con la anisotropía de las partículas.

Una importante contribución a esta disertación es la sección computacional. A modo de completar los resultados experimentales y de reforzar el conocimiento sobre los mecanismos detrás del comportamiento estructural, llevamos a cabo simulaciones en Dinámica Browniana. Esta herramienta nos permite entender cómo es el proceso de estructuración así como la conexión entre la estructura y la dinámica del sistema. Por un lado, la técnica computacional nos regala una visión completa de la estructura mediante la parametrización de los aspectos estructurales más relevantes. Por otro podemos obtener, mediante cálculo numérico, magnitudes físicas tan importantes como la viscosidad, el esfuerzo de cizalla y los módulos viscoelásticos. Además, podemos estudiar la dinámica de las partículas dentro de la estructura mediante el desplazamiento cuadrático medio y la función de correlación de esfuerzos. Es relevante hacer notar que los resultados obtenidos de las simulaciones fueron comparados de forma satisfactoria con los datos experimentales.

¿Por qué estudiar los fluidos MR? Hay muchas motivaciones para embarcarse en este estudio, tal como el entendimiento de la base física de los mismos, que es importante en la contribución al conocimiento, en general, además del entendimiento de los mecanismos físicos en sistemas coloidales magnéticos, en particular. Por otro lado, desde un punto de vista de las aplicaciones comerciales, los fluidos MR son muy adecuados por sus propiedades controlables. Algunas de estas aplicaciones son, por ejemplo, dispositivos de absorción de vibraciones, frenos, amortiguadores sísmicos y control en la propagación del sonido, además de aplicaciones en biomedicina, entre otras.



El comienzo de esta Tesis es un **Background**, donde el principal objetivo es dar al lector una amplia visión de los mecanismos físicos fundamentales de los fluidos MR. Fijándonos en la morfología de las partículas en **Part I** llevamos a cabo un estudio sistemático sobre la influencia de esta característica (tomamos partículas en forma de esfera, de varilla y de plato con diferentes superficies) en la respuesta magneto-reológica bajo diferentes condiciones, y también tenemos en cuenta el efecto de la composición de las partículas en las propiedades reológicas. En **Part II**, intentamos entender mejor el fenómeno del esfuerzo umbral y el efecto de la concentración de partículas sobre el mismo, variando la fracción de volumen del 0.5 al 50 vol% además del uso de una aproximación de geles coloidales para entender este efecto. A modo de completar los resultados experimentales, desarrollamos métodos computacionales basados en simulaciones en Dinámica Browniana para describir y comprender la formación de los agregados de partículas a nivel microscópico y extrapolar estos resultados de simulación a las medidas macroscópicas. El uso de la Dinámica Browniana será justificado en la parte correspondiente (**Part III**) y, como información adicional de las simulaciones, en **Appendix A** se exponen los principales códigos. Además, también estudiamos la influencia de solventes altamente viscoelásticos en la preparación de fluidos MR en **Strongly Viscoelastic MR Fluids**. Finalmente, las conclusiones principales de este trabajo se muestran en **Conclusions**.





BACKGROUND

Throughout this dissertation, many physical concepts and specific rheological magnitudes as well as certain experimental techniques are used and therefore, this section is an attempt to provide the reader the essential tools which make possible a comprehensive monitoring of the present work.

Colloids

By following a logical way, the first concept that must be introduced is “colloids”. In typical solutions (true solutions) formulated as the dissolution of one substance in another, the ultimate particles of the solute have a comparable size with solvent molecules and we normally assume that solute molecules are dispersed uniformly through the solvent. On the other hand, we find an important class of materials in which the particles that are dispersed in the solvent have a much larger size than solvent molecules. These systems are the so-called **colloidal dispersions**.

When one substance is insoluble in another, the first substance will usually be broken down into very small particles that can be distributed more or less uniformly through the other substance. The dispersed particles are usually called the **dispersed phase** and the other substance is called the **continuous phase**.

Referring to the size of disperse particles we find a lower limit which corresponds to 1 nm , below which, colloids would become indistinguishable from true solutions. On the contrary, the upper limit is usually established by the presence of thermal motion (known as Brownian motion in colloids), as is



taken at a diameter of $2\ \mu\text{m}$ but there is no clear distinction between the behavior of particles of $1\ \mu\text{m}$ and the somewhat larger particles often encountered in emulsions, in mineral separation processes, and in ceramic engineering¹.

The importance of studying colloidal systems and all of the related phenomena lies in its wide presence in nature, on the one hand, and in many important applications in different industrial and/or technological processes, on the other hand. It is sufficient to mention the implication of the related colloidal phenomena in several fields of interest, such as the manufacturing of colloids or surface active materials (detergents, paints, inks, food, etc.), the direct application in colloidal and surface phenomena (lubrication, adhesion, wetting, **control of rheological properties**, emulsions, etc.), the use in purification and the improvement in synthetic or natural materials (treatment of wastewater, refining processes, etc.) and physiological applications (respiration, enzymes, etc.).

Currently, there is a growing interest in obtaining new colloidal materials with different features and properties, depending on the specific application, where the research involved is based on the control of chemical surface properties of colloids, the manufacturing of particles with an adequate size or morphology, the properties of the constituent material, etc. For example, the functionalization of the colloidal surface allows copolymerization processes which result in the formation of high molecular weight organic polymers. Also, by means of growing metal oxide crystals, very monodisperse particles can be obtained and used in the experimental contrasting of theoretical models.

Within the described colloidal frame, we are going to focus on a specific kind of colloids, **for which we can control their properties by applying magnetic fields.**

The next section refers to **magnetic colloids.**

Magnetic colloids

Commonly, magnetic colloids are known as **magnetic fluids**, which can be controlled by the application of external magnetic fields of moderate strength (they are **smart materials**). This fact is a challenging subject for research interest in the fundamentals of fluid mechanics as well as for industrial applications. The use of these systems provides a wide range of applications and opens a fascinating field of new phenomena. The ability to control magnetic induced forces can be considered as other incentive to put our attention in magnetic fluids.

By focusing on the formulation and intrinsic characteristics of magnetic fluids, we can distinguish three main types: ferrofluids, inverse ferrofluids and **MR fluids.**

Ferrofluids

The basic composition of these systems consists in **nanoscale ferrimagnetic particles** suspended in a carrier fluid (usually organic solvents or water) and these nanoparticles are coated by some kind of surfactant to inhibit coagulation due to Van der Waals and magnetostatic interactions. Regarding the stability of the suspension, which is of crucial importance, the main aspect to address is the stability against particle settling, which can be induced by gravitational and magnetic forces. Therefore, due to this fact, it must be ensured that **thermal energy**, or implicit **Brownian motion**, is capable to dominate. From a theoretical



point of view, a good approximation in the definition of ferrofluids is to assume that these systems are composed by non-interacting spherical particles. When polydispersed ferrofluids are subjected to an external shearing and, at the same time are under the presence of an high enough magnetic field, the **magnetoviscous effect**⁴ is manifested.

Some highlighted applications of ferrofluids involve lubrication in mechanical devices, thermal applications, e.g. ferrofluid as cooling agent in loudspeakers² or medical applications, as for example their use as a contrast agents in x-ray examinations³.

As a direct consequence of the reduced particle size, particle magnetization that can be achieved is very limited and hence, the magnetic response is relatively weak, contrasting with the intense induced magnetic forces that develop in magnetic fluids with micrometric particles. Thus, at the same external magnetic field, e.g. 250 kA/m , a typical value of the magnetization in a usual ferrofluid is of the order of 30 kA/m , well below the value ($M \sim 400 \text{ kA/m}$) that reaches a magnetorheological fluid with similar particle concentration⁵.

Magnetorheological (MR) fluids

Unlike ferrofluids, the disperse phase of MR fluids is composed by **micrometric ferromagnetic particles** (from 100 nm to $10 \mu\text{m}$) suspended in a non-magnetizable continuous liquid phase (typically mineral oils, aqueous solutions, synthetic hydrocarbon, etc.) and, as commented above, it is expected that the magnetic response of MR fluids is much higher. These fluids are characterized by a reversible and very fast (of the order of milliseconds) transition from liquid to nearly solid state⁵ under the presence of external magnetic fields⁶. Thus, for

example, the apparent viscosity of MR fluids can change several orders of magnitude for applied magnetic flux densities of order of magnitude 1 T (Tesla). Not only the particle size but also the constituent material of particles is determinant in the MR effect and hence, the use of carbonyl iron particles (iron particles obtained from the thermal decomposition of iron pentacarbonyl) is widespread in the formulation of MR fluids because of their large saturation magnetization ($M_s \sim 1500 \text{ kA/m}$)⁵. As in the case of ferrofluids, the magnetorheological effect confers to MR fluids a claim for industrial applications. Shock absorbers, brakes, clutches, seismic vibration dampers, control valves and artificial joints⁷; also control of thermal energy transfer^{8,9}, biomedical applications¹⁰, precision polishing¹¹⁻¹³, sound propagation¹⁴, isothermal magnetic advection¹⁵, and chemical sensing applications¹⁶⁻¹⁸ among others, are suitable applications which involve the use of MR fluids.

One of main properties of ferrofluids was the stability versus particle settling. However, ferrofluids experience a lower magnetic response if compared with MR fluids. Now, the trend is reversed for magnetorheological fluids: the magnetic response is much more significant but, due to the larger particle size and the high particle density (typical density of iron is 7.8 g/cm^3), the density mismatch between the particles and the surrounding fluid induces sedimentation. Thus, inclusion of additives in the formulation of MR fluids to inhibit sedimentation and aggregation as well as to provide extra lubrication, is a usual practice in commercial and homemade MR fluids. These extra-components typically consist in thixotropic agents, polymers and surfactants.

When an external magnetic field is applied on the system, disperse particles are magnetized and, as a first approximation, behave like **magnetic dipoles**. Induced magnetic forces make particles attract one another and then, columnar



aggregates are formed in the field direction. As a direct consequence of the latter we find the MR effect, which plays a fundamental role in the origin of the remarkable changes that the MR fluid suffers, namely a very large increment in the shear viscosity, an enhance in the viscoelastic properties and eventually, the appearance of a yield stress.

One could demand from an application point of view that MR fluids have some basic features, i.e. a large saturation magnetization, a small coercivity or remnant magnetization, be active over a wide range of temperatures and be stable against settling, irreversible flocculation and chemical degradation/oxidation⁵. One of the main reasons to require these features is to get a **long lifetime** for devices based on MR fluids.

As a way to complete this subsection, just to mention other type of MR fluids based on micrometric nonmagnetic particles dispersed in a ferrofluid, the so-called **inverse ferrofluids**. The response under magnetic field strengths follows, basically, the same mechanism as in conventional MR fluid but gives a lower magnetic response because of the limited magnetic response of the ferrofluids. The main reason to use inverse ferrofluids lies in the fact of **the high monodispersity** and **tunable morphology** that available nonmagnetic particles have.

Henceforth, we are going to focus on the study of conventional magnetorheological fluids and their rheological properties.

MR fluids

Due to the fundamental role of Rheology in this dissertation, firstly we will address the basics of this physical discipline, where necessary rheological

magnitudes and concepts will be described as a way to better understand the following chapters.

Basics about Rheology

What is Rheology? This term was coined by E. C. Bingham in 1928 (the word comes from the Greek words “ρέω” and “λόγος”, pronounced rheos and logos, meaning “to flow” and “study”, respectively) and, as a wide definition, *consists in the study of the deformation and flow of matter*¹⁹. Conventional MR fluids with low particle concentrations behave as **Newtonian fluids under shear in the off-field state** and, when the magnetic field is activated, transit to a non-Newtonian regime where the fluid acquires **viscoelastic properties** and commonly exhibits a **shear-thinning behavior** (the viscosity decreases as the shear rate increases). Therefore, it is remarkable to know the fundamentals about the viscoelastic regime. In Figure 1, typical shear thinning curves are shown for a suspension of carbonyl iron particles in glucose syrup at a particle concentration of 5 vol%, for different constant magnetic fields

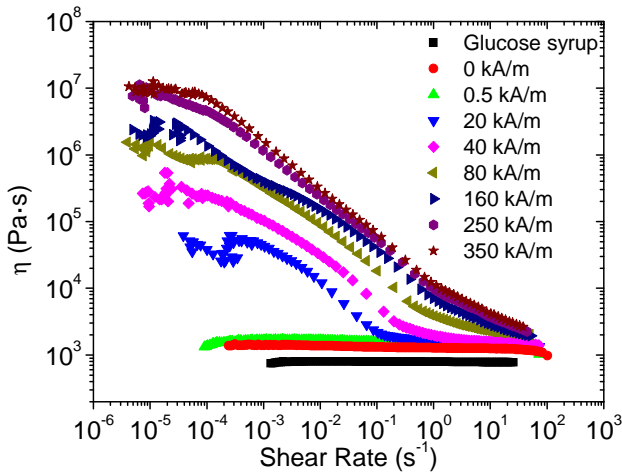


FIG. 1 Shear thinning behavior of a suspension of carbonyl iron particles in glucose syrup of high viscosity, at several external magnetic fields. Each point is an average over 30 s.

Newtonian fluids, also called **viscous fluids**, obey the **Newton's law** that indicates a proportional dependence of shear stress on the deformation velocity or shear strain:

$$\sigma = \mu \dot{\gamma} \quad (1)$$

where σ (in units of Pa) is the applied shear stress that is defined as the applied force per unit area, $\dot{\gamma} = v/d$ (in units of s^{-1}) is the velocity gradient (or the shear rate) and μ (in $Pa \cdot s$) is the dynamic shear viscosity. To better understand this equation, in Figure 2, a schematic representation of a fluid under constant shear is shown.

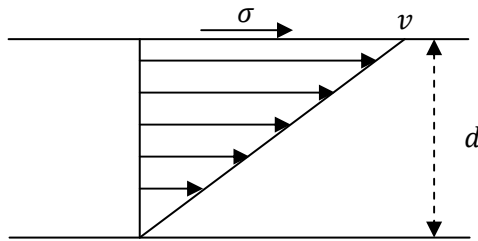


FIG. 2 Schematic representation of a fluid subjected to a constant shear flow, where v is the velocity of the upper plate; d is the gap distance between plates and σ is the applied shear stress. Black arrows within the triangle represent a lineal velocity profile along the vertical axis¹⁹.

Main properties of Newtonian fluids, which could be deduced from Equation (1), are its instantaneous response to shear and its lack of memory. Also, these fluids suffer a permanent and irreversible deformation. On the other hand, although elastic solids are not exactly the goal of this work, it is worth introducing an important concept, namely the elastic modulus, which appears in the Hooke's law: $\sigma = G \cdot \gamma$, where γ is the strain (or relative deformation at which the solid is subjected) and G is the elastic modulus. This idea involves some important implications, such as the existence of a system memory and the ability of these systems to recover their initial states. As an implicit consequence, the energy is stored, contrary to the energy dissipation process in viscous fluids. Later we will see that, under high enough magnetic fields, both the elastic and the viscous characters will take part at the same time in the rheological responses of MR fluids (viscoelastic behavior) and there will be a



competition between them, as a function of the magnetic field and the particle concentration.

Returning to Equation (1), we can classify, basically, the vast majority of fluid behaviors under a continuous shear, such as viscoelastic solids, ideal solids, Newtonian fluids, shear thinning fluids, shear thickening fluids and Bingham fluids. As a way to clarify this classification, a schematic representation for each system is shown in Figure 3, where the shear stress is plotted as a function of the shear rate.

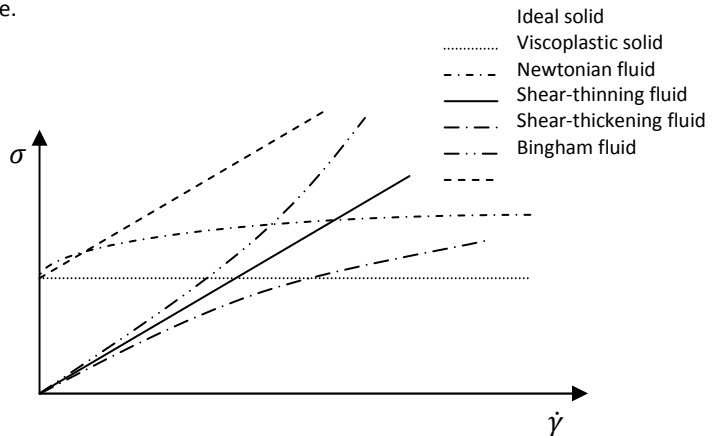


FIG. 3 Schematic representation of the shear stress versus shear rate for different fluids under a continuous shear.

In Figure 3, the curve corresponding to the Newtonian fluid is a linear function of the shear stress versus shear rate, indicating a constant slope and hence, a constant viscosity. This means that Newtonian fluids, under a continuous shear flow, manifest a constant viscosity and therefore, MR fluids have the same behavior in the absence of magnetic field. Putting now our attention in the shear-thinning fluid, we can observe that the slope decreases when the shear rate increases, meaning that the viscosity decreases. This behavior is common in

magnetized MR fluids in steady shear flow tests: at low shear rate values, MR fluids present a high apparent viscosity (depending on the magnetic fluid and the particle concentration) because the internal structure remains within the elastic region; when the shear rate increases, columnar aggregates begin to break and the structure becomes unstable, implying that the viscosity decreases; finally, at higher shear rate values the structure is completely dissolved and the fluid flows with a very low resistance and eventually the viscosity reaches a plateau value (see Figure 2). We will return to the origin of the viscosity in MR fluids later. Focusing on the curve which corresponds to the Bingham fluid, we observe that the line begins at a non-zero shear stress at zero shear rates, in accordance with the existence of a static yield stress. In this case, the governing equation is the Bingham Equation¹⁹ (in the stationary regime):

$$\sigma = \sigma_0 + \eta_p \dot{\gamma} \quad (2)$$

where σ_0 is the static yield stress and η_p is the plastic viscosity. We can define for conventional MR fluids two action regions: the first one, in the region of Newtonian fluids when they are in the off-field state; the second one, in the case of magnetized MR fluids, if the magnetic field or the particle concentration are adequate, they can be placed between Bingham and shear-thinning fluids, because they exhibit not only a yield stress but also a shear-thinning behavior.

Up to now we have seen what occurs when a fluid is subjected to a **continuous shear flow** and from that, we have extracted remarkable information about its behavior. However, fluids can be exposed to other kinds of standard rheological tests which provide complementary important information about the physics behind the fluid response. These rheological experiments are basically two:



frequency sweep and strain sweep tests. The first test consists in applying a constant oscillatory strain amplitude while frequency is increasing at a certain rate. On the other hand, a second test is carried out by maintaining a constant frequency while an increasing strain amplitude is applied. Schematically, in Figure 4 an oscillatory test is shown. The upper plate oscillates at the indicated frequency and amplitude. In the case of frequency tests, the strain has a sinusoidal dependence on the angular frequency:

$$\gamma(t) = \gamma_0 \cdot \sin \omega t, \quad \dot{\gamma}(t) = \gamma_0 \cdot \omega \cdot \cos \omega t \quad (3)$$

where γ_0 is the shear strain amplitude, ω is the angular frequency and t is the time. In the case of strain sweeps, the angular frequency is fixed and the strain amplitude increases with time. The dependence of the strain on the angular frequency implies a **sinusoidal dependence of the shear stress** with the following form, in the case the strain is small enough:

$$\sigma(t) = \sigma_0(\omega) \cdot \sin[\omega t + \delta(\omega)] \quad (4)$$

where δ refers the phase difference of the stress with respect to the strain. From Equations (3) and (4), we can see that the response of the system under time-dependent stimuli may depend on the timescale of measurements ($\sim 1/\omega$) and also we can suppose that different materials have different time-dependent responses. Before proceeding with the understanding of oscillatory tests, we are going to deepen in a fundamental concept that was mentioned above and which is much related with the behavior of fluids under time-dependent conditions: **viscoelasticity**.

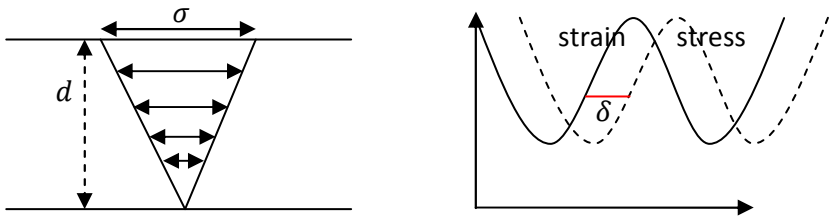


FIG. 4 Schematic representation of a typical oscillatory test. The upper plate oscillates under controlled frequencies and/or strains. In the graph to the right, the difference phase between the strain and the stress is shown.

Depending on the external stimulus to which the fluid is subjected, we can obtain different responses, that could be included within three time-dependent behaviors: elastic relaxation, viscous relaxation and viscoelastic relaxation. The latter is a mix between two others. As a way to clearly comprise these concepts, in Figure 5 typical relaxation curves and their mechanical interpretations are shown. Graph (a) represents a sudden step strain: a certain step deformation is applied and **maintained constant over time**. In Graph (c), the response of an **elastic system** is shown: the stress reaches a constant value and remains constant with time; **storage of energy**. The response of a completely viscous system is shown in Graph (b), where the stress **instantaneously relaxes**; energy is completely dissipated. Finally, in Graph (d), a viscoelastic response is shown: the **stress relaxation time is non-zero** and depends on the physical features of the system; **there is some memory in the system**. In the figure, G is the so-called **stress relaxation modulus** which, in general, has this expression:



$$G(t) = \frac{\sigma(t)}{\gamma_0} \quad (5)$$

in which γ_0 , in this case, is the step strain value. Then, by measuring the stress relaxation with time, the relaxation modulus can be determined. In the case of a viscous system, the **relaxation modulus is proportional to the Delta function** and is calculated by means of $G(t) = \eta\delta(t)$. In the case of elastic systems, the relaxation modulus acquires this shape: $G(t) = G$, where G refers to the elastic modulus which appears in Hooke's Law. The relaxation time can be estimated via this expression: $t_r = \frac{\eta}{G}$.

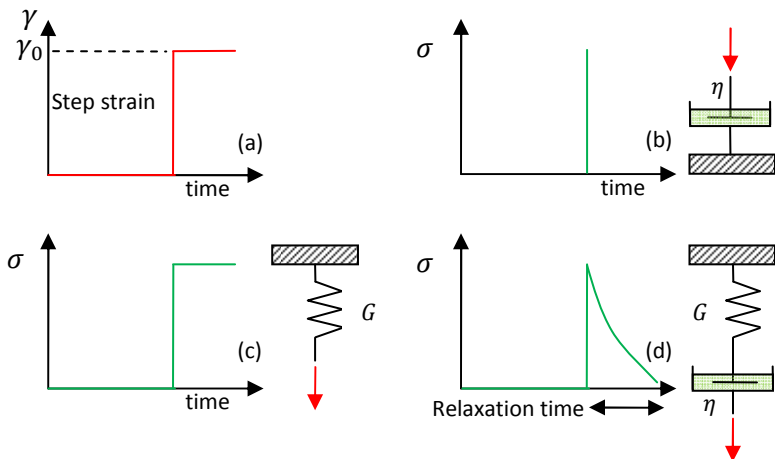


FIG. 5 Step strain deformation (a) and its response in an elastic (c), viscous (b) and viscoelastic (d) systems are shown. Next to each graph, the mechanical equivalent physical mechanism is illustrated, as a way to better understand the involved phenomenon.

As we have defined expressions for the behavior of an elastic solid and a viscous fluid, we can also interpret a viscoelastic behavior. Returning to Equation (4) and by taking into account the elastic and the viscous character of the system, we deduce the following expression:

$$\sigma(t) = \gamma_0 \cdot G' \cdot \sin \omega t + \gamma_0 \cdot G'' \cdot \cos \omega t \quad (6)$$

where γ_0 is again the strain amplitude in the oscillatory tests and both G' and G'' represent the viscoelastic behavior of the system. G' or the storage modulus gives essential information about the elasticity of the system and its capacity to storage energy. On the other hand, the loss modulus or G'' represents the ability of the system to dissipate energy, which concerns to viscous part. These two magnitudes are known as the viscoelastic moduli and they can be considered parts of the complex modulus $G^* = G' + iG''$, and are calculated through the following expressions:

$$G' = \frac{|G^*|}{\gamma_0} \cos \delta, G'' = \frac{|G^*|}{\gamma_0} \sin \delta \quad (7)$$

In this case, δ is the out of phase between the strain and the stress and its tangent represents the damping factor, $\tan \delta = \frac{G''}{G'}$ and gives a balance between the viscous and the elastic behavior. This magnitude is very useful to evaluate how the system dissipates or stores energy.

Most of the solvents used in this dissertation were Newtonian (viscous) fluids, so its properties are well explained by the Newton's Law of viscosity. However, also there is other solvent that we used to prepare MR fluids and that was not Newtonian, but highly viscoelastic (specifically a **Boger fluid**) and that needs a



special attention. In the next subsection, an overview of this kind of fluid is shown. As we mentioned above, one of the main problems in commercial MR fluids is the particle settling. For that purpose, Boger fluids provide a non-negligible solution to minimize sedimentation rate and therefore, this is an added motivation to study these fluids and their effects in magnetorheology.

Boger fluids

This kind of fluids are viscoelastic fluids because both their elastic and viscous moduli (viscoelastic moduli) are non-zero. The basic composition of these systems is a dilute polymer solution usually prepared in a high viscosity solvent. The main characteristic of Boger fluids is its constant viscosity when they are sheared. Due to the fact that viscosity is independent of the shear rate or nearly so, we can separate elastic effects from viscous effects in viscoelastic flows²⁰. The use of these fluids in our preparation of MR suspensions is justified because its high viscosity, which supposes an important improvement to prevent particle settling as mentioned above, and due to the intrinsic viscoelastic properties of Boger fluids, a new vision in the formulation of MR fluids is conferred.

The composition of Boger fluids greatly varies, resulting fluids with higher or lower viscosities depending on the purpose, and the viscoelastic properties will be more or less pronounced. In our case, we prepared a Boger fluid by dispersing polyacrylamide in doubly-distilled water and then, this was mixed with glucose syrup of very high viscosity. In order to prevent proliferation of microorganisms because of the presence of the glucose syrup, sodium azide (in a very low proportion) was added²¹. Because of the mechanical degradation of polymer chains, we took special care in the latter process. Apart from the fact

that the viscosity of this fluid is nearly constant under flow, other important properties are exhibited in rheological tests. That is the case of the **first normal stress difference**, N_1 and the **first normal stress coefficient**, Ψ_1 , which are defined as follows:

$$N_1 = \sigma_{11} - \sigma_{22}, \Psi_1 = \frac{N_1}{\dot{\gamma}^2} \quad (8)$$

where σ_{11} and σ_{22} are the first and the second diagonal components of the **shear stress tensor**, respectively. The stress tensor plays a key role in the present work, and must be defined in detail.

As an illustrative example of the functionality of the stress tensor, in Figure 6 a general form of the microscopic shear stresses in the case of a simple shear flow is shown. In the figure, different stress tensor components acting on a differential portion of fluid under shear are shown¹⁹.

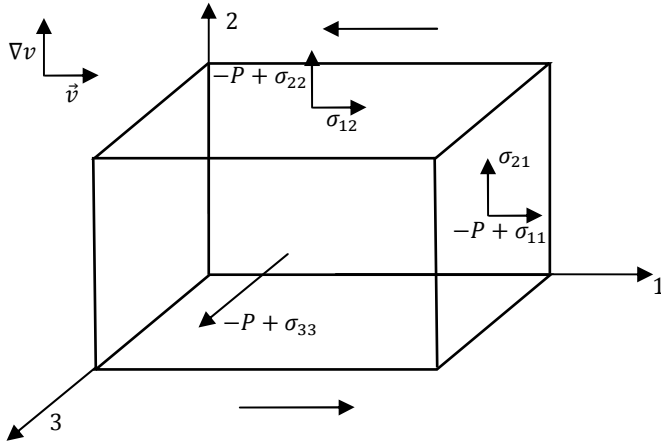


FIG. 6 Differential portion of fluid subjected to a simple shear flow, where each face is under a certain stress. ∇v is the velocity gradient along the vertical axis and \vec{v} is the velocity of the upper and the lower plates. P is the hydrostatic pressure and σ_{ij} is the ij th stress tensor component.

The mathematical structure of the stress tensor in its general form is:

$$\bar{\sigma} = \begin{pmatrix} -P + \sigma_{11}^E + \sigma_{11}^V & \sigma_{12} & \sigma_{13} \\ \sigma_{21} & -P + \sigma_{22}^E + \sigma_{22}^V & \sigma_{23} \\ \sigma_{31} & \sigma_{32} & -P + \sigma_{33}^E + \sigma_{33}^V \end{pmatrix} \quad (9)$$

Because of the symmetry, typically $\sigma_{ij} = \sigma_{ji}$. On the other hand, σ_{ii}^E and σ_{ii}^V are the diagonal stress tensor components and correspond to the elastic contribution and the viscous contribution, respectively. In a Newtonian fluid, both the first normal stress difference and the first normal stress coefficient are zero and hence, this fact can be used to distinguish between Newtonian and

Boger fluids. Directly related to the strong viscoelastic nature of Boger fluids, it takes place an important effect when the system is under moderate or high flow rates, the so-called **Weissenberg effect** (or rod climbing effect), that is a clear manifestation of the existence of the characteristic first normal stresses in viscoelastic fluids. This effect appears in simple shear experiments and, without going into further detail, can be explained, from a microscopic point of view, because of the coupling of two effects: a stretching of the elastic particles (polymer chains) under the action of local shear; once deformed, their tendency to align along the flow direction. These two effects are based in the “dumbbell model”, widely employed in rheology of polymers¹⁹. A schematic qualitative description is shown in the next figure (Figure 7).

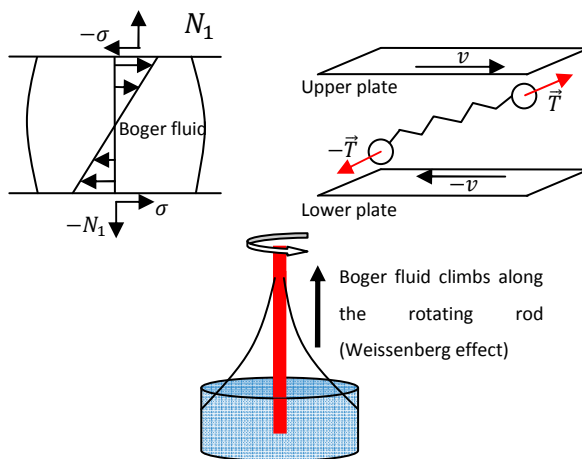


FIG. 7 Left: Weissenberg effect of a sheared sample of viscoelastic fluid between two parallel plates. In the right, microscopic representation of the dumbbell model which provides an explanation for the exhibited normal force, based on the stretching and aligning of the polymer chains along the flow.



After this basic introduction of Rheology, it is necessary to understand the magnetic mechanisms behind the MR effect and therefore, we are going to dedicate the following section to this end.

Basics about Magnetism

The magnitude of the MR response depends on the details of the particle magnetization²², which controls the magnetostatic force between particles. Estimating the force requires to know what is the the magnetic field intensity, \vec{H} , in the vicinity of the particle. This magnitude is related to the magnetic flux density, \vec{B} , as follows:

$$\vec{B} = \mu_0(\vec{H} + \vec{M}) \quad (10)$$

where $\mu_0 = 4\pi \cdot 10^{-7} \text{ N/A}^2$ is the magnetic permeability of the vacuum, and \vec{M} is the particle magnetization. In nature, most materials fall under one of the following three magnetic types:

-Diamagnetic materials: these materials have a negative magnetization, which implies that, for a given magnetic field intensity, \vec{H} , the magnetic flux density (\vec{B}) of this material is smaller in magnitude than the magnetic flux density of the vacuum or free space under the same magnetic field intensity.

-Paramagnetic materials: this kind of material has a small but positive magnitude of the magnetization, so \vec{B} would be slightly larger in magnitude than the corresponding to free space.

-Ferromagnetic materials: in this case, they have a very large (in magnitude) magnetization, so the magnetic flux density would be much larger than that of the vacuum.

In the formulation of MR fluids, the use of ferromagnetic materials is the most common, due to the large magnetic flux densities that can be generated. For ferromagnetic materials that do not exhibit permanent magnetization, the value of \vec{M} depends on the applied magnetic field. An important factor that evaluates the latter is the relative magnetic permeability, μ , which relates \vec{H} and \vec{M} through this expression:

$$\vec{M} = (\mu - 1)\vec{H} \quad (11)$$

where the magnetic permeability is not a constant and depends on the magnitude of \vec{H} : $\mu = \mu(|\vec{H}|)$. Therefore, by using this expression and the Equation (11) in (10), we deduce:

$$\vec{B} = \mu(|\vec{H}|)\vec{H} \quad (12)$$

In the range of low values **of the magnetic field intensity**, the magnetization is directly proportional to the magnetic field intensity, \vec{H} so, in that case, the **relative magnetic permeability is a constant**. When $|\vec{H}|$ increases, the material magnetization begins to saturate and, if the magnetic field intensity is high enough, it will be reached a field-independent value of \vec{M} , the saturation



magnetization \vec{M}_s . Because of this behavior under magnetic fields, $\mu(|\vec{H}|)$ can be represented by these three expressions:

-At low fields: $\mu(|\vec{H}|) = \mu^0 \mu_0$.

-At moderate fields: $\mu(|\vec{H}|) = \mu_0 \left(1 + \frac{|\vec{M}(|\vec{H}|)|}{|\vec{H}|} \right)$.

-In the region of saturation: $\mu(|\vec{H}|) = \mu_0 \left(1 + \frac{M_s}{|\vec{H}|} \right)$.

In the first equation, μ^0 refers to a constant of proportionality between $|\vec{H}|$ and $|\vec{B}|$ at low magnetic fields and $|\vec{M}(|\vec{H}|)|$ is the field-dependent magnitude of the magnetization at moderate fields. In Figure 8, a typical magnetization curve for a MR fluid prepared with carbonyl iron particles at 5 vol% dispersed in silicone oil is shown. We can observe that at low magnetic field intensities, there is a proportional relation between the magnetization and the magnetic field intensity. Then, the slope of the curve decreases up to reach a constant value at high magnetic field strengths, where the MR fluid is completely saturated. In light of this behavior, it is clear that when the system is very close to the saturation region, Equation (10) tends to $\vec{B} = \mu_0(\vec{H} + \vec{M}_s)$.

The relative magnetic permeability of ferromagnetic materials is expressed empirically by the Fröhlich-Kennely Equation²³:

$$\frac{\mu(|\vec{H}|)}{\mu_o} = 1 + \frac{(\mu^0 - 1) \frac{|\vec{M}_s|}{|\vec{H}|}}{(\mu^0 - 1) + \frac{|\vec{M}_s|}{|\vec{H}|}} \quad (13)$$

This equation was compared to experimental data²⁴ for $\mu^0 = 100$ and $\mu^0 |\vec{M}_s| = 2 T$ and it was found that equation fitted the data better at large magnetic field strengths than at lower values. In Figure 8, a conventional $M - H$ curve is shown.

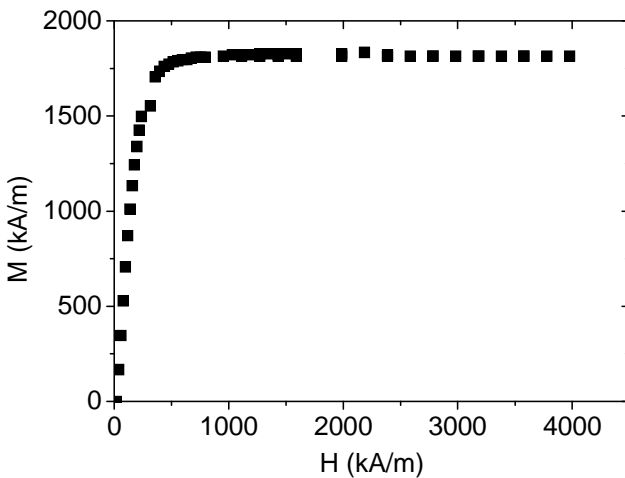


FIG. 8 Suspension magnetization of a MR fluid based on carbonyl iron particles at 5 vol% in silicone oil, as a function of the external magnetic field intensity.



The calculation of the **inter-particle magnetostatic force** is fundamental to understand the MR effect. To determine these forces we need to solve the appropriate **Maxwell equations**. The current density in the steady-state in the suspension, \vec{J}_f , is related to the applied magnetic field via $\nabla \times \vec{H} = \vec{J}_f$ but, because the current is zero in our case, then the magnetic field intensity of each phase in the suspension can be defined by using a magnetic potential, Φ_i :

$$\vec{H}_i = -\nabla\Phi_i, \quad \nabla \cdot \vec{B} = 0 \quad (14)$$

where the subscript i refers to the i th suspension phase. Now, using Equations (12) and (14) leads to a differential equation for the magnetic potential with this general form:

$$\nabla(\mu(\Phi)) \cdot \nabla\Phi + \mu(\Phi)\nabla^2\Phi = 0 \quad (15)$$

When the magnetic field tends to the lowest values, \vec{B} is directly proportional to the magnetic field intensity, \vec{H} and then, under these conditions, we lead to:

$$\nabla^2\Phi_i = 0 \quad (16)$$

The next step is to consider the boundary conditions:

-In the interface between the particle and the continuous medium we have that $\vec{B}_p \cdot \vec{n} = \vec{B}_c \cdot \vec{n}$ and $\Phi_p = \Phi_c$, where \vec{n} is the normal to the particle surface and the subscripts p and c refer to the particle and the continuous medium,

respectively. Due to the nature of the magnetostatic interactions, it is convenient to introduce two additional conditions:

$$\begin{aligned} \Phi_c &\rightarrow -\vec{H}_0 \cdot \vec{x} \text{ as } |\vec{x}| \rightarrow \infty \\ \Phi_p &\text{ is finite as } r \rightarrow 0 \end{aligned} \quad (17)$$

where r is the distance from the particle's center. Before proceeding with the analysis of the magnetic equations, it is convenient to show a schematic diagram illustrating the definitions of the spherical coordinates used in the magnetostatic force resolution (see Figure 9). In these coordinates, the magnetostatic potential in the medium is:

$$\Phi_c = -H_0 r \cos \theta \left[1 - \left(\frac{a}{r} \right)^3 \beta_M \right], \beta_M = \frac{\mu_p - \mu_c}{\mu_p + 2\mu_c} \quad (18)$$

where a is the particle radius, β_M is the magnetic contrast factor ($0 < \beta_M < 1$) and μ_c and μ_p are the magnetic permeability of the medium and the particles, respectively. In most of cases, the magnetic permeability of the medium is taken as the free space (μ_0).

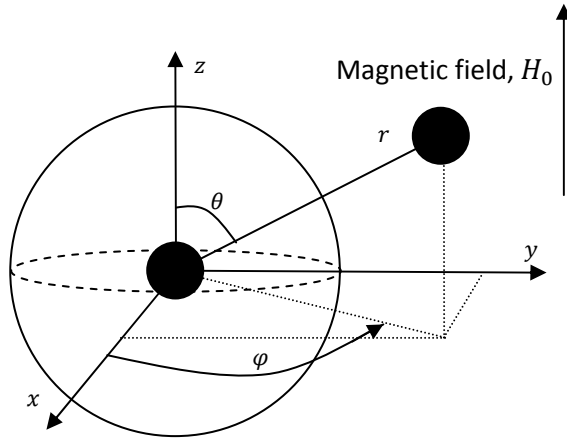


FIG. 9 Schematic representation of spherical coordinates which are involved in the representation of inter-particle magnetic forces.

The real magnetization of particles in a magnetized system containing millions of these units is really difficult to determine but as a way to get a first approximation in the resolution of equations, we suppose that particles, when they are magnetized, interact like magnetic dipoles whose magnetic moments are only induced by the external magnetic field (multibody effects are neglected). Therefore, we can define the potential in the surrounding medium due to one sphere as the potential generated by a magnetic dipole at the origin with a dipole moment:

$$\vec{m}^{eff} = 4\pi\beta_M\alpha^3H_o\hat{z} \quad (19)$$

Then, this dipolar magnetic moment induces a magnetic flux density:

$$\vec{B}^{dip} = \mu_0 \mu_c \vec{H}^{dip} = \mu_0 \mu_c \beta_M H_0 \left(\frac{a}{r}\right)^3 [2 \cos \theta \hat{r} + \sin \theta \hat{\theta}] \quad (20)$$

In the point-dipole limit, where the later assumption takes place, the force on the particle at the origin (particle 1) due to another particle (particle 2) at (r, θ) is

$$\vec{F}_{12}^M = \vec{m}_1^{eff} \cdot \nabla \vec{B}_2^{dip}(\vec{x}_1) \quad (21)$$

where \vec{m}_1^{eff} is the magnetic moment of particle 1 and $\vec{B}_2^{dip}(\vec{x}_1)$ is the magnetic flux density generated by the particle 2 at the center of particle 1. Introducing expressions for the magnetic moment and the magnetic flux density into equation (21), we obtain the magnetic force exerted on a sphere at the origin due to another particle in the position (r, θ) :

$$\vec{F}_{12}^M = 12\pi\mu_0\mu_c a^2 (H_0\beta_M) \left(\frac{a}{r}\right)^4 [(3 \cos^2 \theta - 1)\hat{r} + \sin \theta \hat{\theta}] \quad (22)$$

From the expression of the magnetostatic force it can be deduced the following: when particles are aligned in the direction of the magnetic field, particles attract each other and the magnitude of the force is a maximum. Contrary, if particles are in the same horizontal plane, they repel each other. Any other pair of particles which form an angle will suffer a rearrangement in the direction of the magnetic field due to other particles. As a result, this force causes the particle aggregation into columnar structures along the magnetic field direction.



It is clear that the magnetorheological effect is greatly determined by this microscopic interaction between particles and the parameters involved in its calculation. Therefore, it is not strange that these interactions are directly related with macroscopic magnitudes measured in rheological tests. The magnetization model predicts at low fields, for example, that the yield stress is directly proportional to the squared of the magnetic field intensity, $\sigma_y \propto H_0^2$. At high fields, in saturation, the model predicts that the yield stress does not depend on the magnetic field intensity but the squared saturation magnetization, $\sigma_y \propto M_s^2$. The case of intermediate fields is more complicated. The relationship between the yield stress and the magnetic field has this form: $\sigma_y \propto H_0^n$, where $0 < n < 2$ and then numerical calculations are necessary. Ginder *et al.* (1996) employed a finite element method to predict the behavior of model MR suspensions idealized as single-particle width chains²⁶. They used the Fröhlich-Kennely equation to estimate the dependence of the magnetic permeability on the magnetic field intensity. These results were in a good agreement with published MR data. They postulated that particles, at moderate fields, begin to saturate in their polar regions and, with this approach, they predicted that $\sigma_y \propto H_0^{3/2}$ and that the elasticity of the suspension (G') was proportional to the magnetic field intensity at intermediate fields.

Experimental rheological tests

Basically, we carried out four kinds of rheological tests to characterize MR fluids: magneto-sweeps, frequency and strain sweeps and steady shear flow tests.

Magneto sweep tests

In these experiments we studied the evolution of the viscoelastic moduli as a function of the magnetic field intensity. For this purpose, a MR sample was confined between two non-magnetizable parallel plates (made of titanium; diameter 20 mm) with a gap distance of 300 μm . Before the test, the sample was homogenized by manual stirring and sonication. To determine the viscoelastic moduli, the sample is sheared at constant strain amplitude (usually $\gamma_0 = 0.003\%$) and frequency ($f = 1 \text{ Hz}$) while the magnetic field strength increases. The experimental procedure was: (i) the sample is sheared at a constant shear rate $\dot{\gamma} = 200 \text{ s}^{-1}$ during 30 s; (ii) the sample is left to rest during one minute; (iii) the magnetic field is increased (logarithmically) from nearly zero magnetic field values to 885 kA/m, which corresponds to a current intensity in the electromagnet of 5 A. The field is applied in the normal direction of the flow. The evolution of G' and G'' in a conventional magneto sweep test is shown in Figure 10. At low magnetic fields, attraction between particles is too weak to induce the formation of aggregates and due to this fact, both the storage and the loss moduli are very low and measured with high deviations because we are in the resolution limit of the rheometer. This does not occur if the particle concentration is high. At a certain value of the magnetic field strength, in the region of intermediate magnetic field intensities, an increase is clearly observed for the viscoelastic moduli (there are some particle aggregates that span the gap), reaching maximum values at high magnetic fields (saturation region; thick particle columnar aggregates connect the upper and the lower plates). In this region we observed that the elastic character of the system clearly overcomes the dissipation behavior.

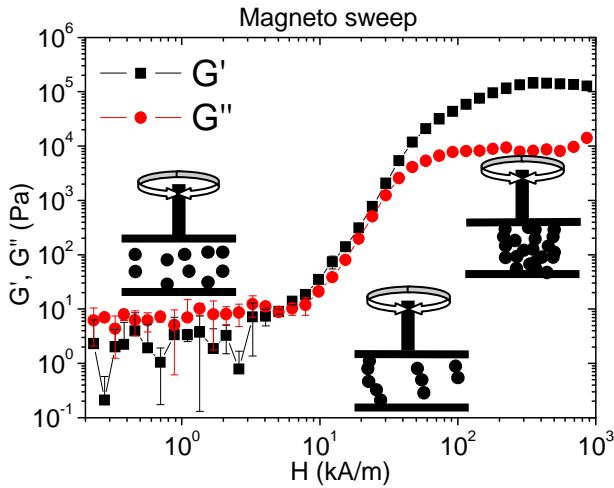


FIG. 10 Conventional magneto sweep test of a MR fluid based on carbonyl iron particles dispersed in silicone oil at 5 vol%.

Strain amplitude sweep tests

In this test we wanted to study the rheological response of MR fluids when they are subjected to a continuous increasing strain amplitude, at a fixed frequency of 1 Hz. The experimental protocol is basically the same that of magneto-sweep tests. Also in this case, the magnetic field is applied in the normal direction to the flow. Equilibration (under constant magnetic field) is important because the microscopic structures present before the test, determine the later rheological response: not only the length of **the linear viscoelastic region (LVR)**, where there is a linear relationship between the stress and the deformation) but also the initial plateau values of the viscoelastic moduli can be altered because of the initial conditions. In Figure 11, a strain amplitude sweep for a MR suspension

based on a mixture of glucose syrup and water, at a carbonyl iron particle concentration of 5 vol% is shown. At very low strains, we envisage a small plateau in the storage modulus which corresponds to LVR. While the sample structure is maintained, the viscoelastic moduli are constant; when the applied strain becomes too high, breakdown occurs and the moduli decrease and, at higher strain amplitude values, the structure is completely broken and then, the viscous behavior dominates. The length of the LVR is a measure of stability and, in the case of MR fluids, the length of this region decreases when the magnetic field increases, becoming extremely small at high magnetic fields (below 0.01 %). There are some criteria about the calculation of the length of the LVR. In our case the exit of the LVR is considered when $G' = 0.9G'_0$, where G'_0 is the low strain storage modulus plateau (critical strain, γ_c).

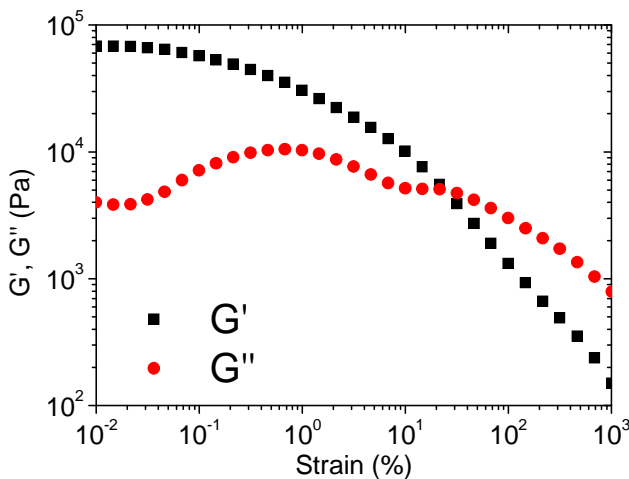


FIG. 11 Strain amplitude sweep test for a sample prepared by carbonyl iron particles at 5 vol%, dispersed in a mix of glucose syrup and water. This test was carried out under a magnetic field intensity of 259 kA/m. The angular frequency remains constant at 1 Hz.



Frequency (oscillatory) sweep tests

In this test, the sample is subjected to a constant strain amplitude (well within the LVR), only varying the oscillation frequency. Preconditions were the same as in the case of the strain sweep test. The rheological response of a conventional MR fluid under a standard frequency sweep test is shown in Figure 12.

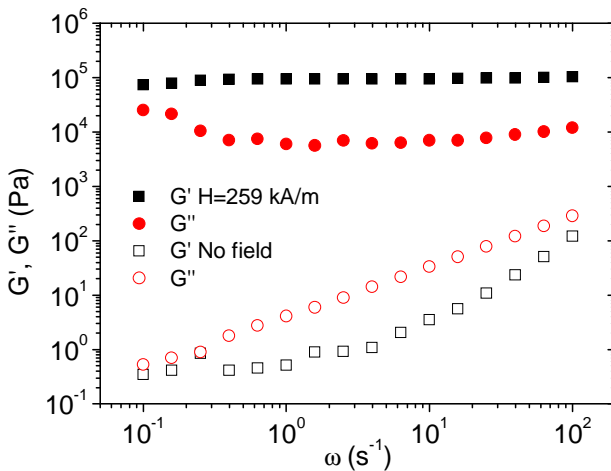


Fig. 12 Viscoelastic moduli as a function of the angular frequency. The sample was under a constant magnetic field intensity of 259 kA/m and subjected to a constant strain amplitude of 0.003% , well within the LVR. Also results from the same test and the same material **without magnetic field** are shown in order to observe the effect of the magnetic field on the system.

Results from frequency sweeps can be interpreted as follows. At strain amplitude values below γ_c , the storage modulus, G' (in the on-field state), is often nearly independent of angular frequency, as would be expected from a

structured or solid-like material. The more frequency dependent the elastic modulus is, the more liquid-like is the system. Also, as we observe in the figure, the effect of the magnetic field is totally determinant in the MR response: under no field conditions, the viscous behavior overrides the elastic response and viscoelastic moduli are not constant with frequency (fluid-like behavior).

Steady shear flow tests

These tests were usually carried out after the previous tests in order to facilitate interpretation of the results. Under this experimental approach we wanted to determine the shear viscosity. Again, preconditions in protocols are the same than in the previous tests and also the effect of the applied magnetic field is determinant. In the test, the shear rate is increased from nearly zero shear rate values to 1000 s^{-1} (shear rate-controlled tests). Also it is possible to carry out flow tests by varying the shear stress (in so-called shear stress-controlled test). As we said in previous sections, MR fluids in off-field state behave as Newtonian fluids and then, the shear stress is directly proportional to the shear rate via the viscosity. But the rheological response greatly changes in presence of magnetic fields. The initial particle structure induces high values of the apparent viscosity at low shear rate values and a later shear thinning behavior, falling the viscosity to values several orders of magnitude below the initial data points, at larger shear rates. Depending on the magnetic field and the particle concentration, this viscosity drop is more or less pronounced. In Figure 13 a conventional steady shear flow test is shown for a MR fluid based on glucose syrup with carbonyl iron particles at 5 vol%.

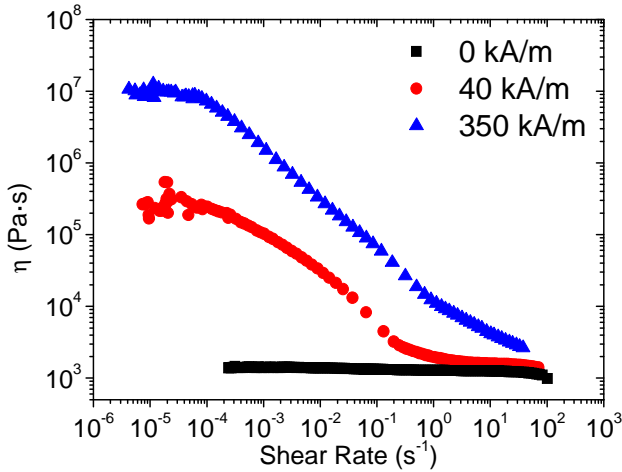


FIG. 13 Shear thinning behavior for a MR fluid based on glucose syrup and carbonyl iron particles at 5 vol%.

During these rheological tests, hydrodynamic and magnetic forces are confronted within the physical mechanisms behind rheological response, so it would be important to know about the influence of each force on the overall behavior. The **Mason number**, that establishes a balance between those two forces, and denoted as ***Mn***:

$$Mn = \frac{8\eta_c \dot{\gamma}}{\mu_0 \mu_{cr} \beta_M^2 H_0^2} \quad (23)$$

where η_c is the solvent viscosity and $\mu_{cr} = \frac{\mu_c}{\mu_0}$ is the relative magnetic permeability of the continuous medium (~ 1). Regarding expression (23), the Mason number is, basically, a dimensionless shear rate that can be defined as

the ratio of hydrodynamic drag (estimated as Stokes drag) and magnetostatic forces (estimated as the dipole force magnitude) acting on the particles⁵. Usually the Mason number is used to scale viscosity versus shear rate and gets a collapse of all the curves onto a master curve, indicating that the hydrodynamic and magnetic force dominate the physics.

Brownian Dynamics Simulations on MR fluids

During the last two decades, computational techniques have played a relevant and complementary role in the development of Science and its importance has been growing until our days, occupying an undeniable place in the scientific method and therefore, we have sufficient arguments to include these techniques in our work. There are many different computational methods to tackle physical problems as the present case, but we are going to focus on solving that by using **Brownian Dynamics Simulations**. As its name suggests, the core of this technique is the **Brownian or random motion** that will be introduced in the system dynamics. One can think that because of the large size of particles in MR fluids (of the order of one micron), Brownian motion does not have great influence in the global behavior but as it will be seen later, the introduction of this motion will perform a remarkable role in the dynamics. As it was mentioned above, Brownian motion consists, basically, in the transmission of kinetic energy from solvent particles or molecules to the suspended microparticles via multiple collisions that, as we will see later, produces defects in the final microstructure due to the continuous rearrangement of particles. Taking into account the main interactions that particles suffer (magnetic and repulsive forces and Brownian motion), the equation that drives the particle motion is, adequately, the **Langevin** equation:



$$m_i \ddot{\vec{r}}_i = \sum_j \vec{F}_{ij} - \gamma_i \dot{\vec{r}}_i + \vec{f}_i \quad (24)$$

where m_i and γ_i are the mass and friction coefficient with the solvent of the particle, \vec{F}_{ij} is the interaction force between particles i and j (core repulsion plus dipolar interaction), and \vec{f}_i the Brownian force that fulfils the fluctuation-dissipation theorem. No hydrodynamic particle–particle interaction is considered.

Normalization of equations

Before running simulations it is important to carry out the normalization of equations in order to make easier the computation process. Quantities such as the value of the Boltzmann constant ($O(10^{-23})$), the particle radius ($O(10^{-6})$), or the particle mass ($O(10^{-15})$), are too small and are not adequate from a computational point of view, hence its use can be translated in large computational times. In order to prevent this effect, we normalize all the equations by:

$$\text{length} \sim a, \text{ mass} \sim m \text{ and energy} \sim k_B T$$

where a is the average particle radius, m is the average particle mass, k_B is the Boltzmann constant and T is the temperature ($k_B T$ is the thermal energy). Then, for example, U_0 (Equation26) would be normalized by $a^3 \cdot k_B T$ and the mean square displacement by a^2 .

As an important discussion, the stability and the time evolution of the structure will be determined not only by the magnetic field intensity but by the thermal energy that the random motion introduces: for low magnetic fields, the thermal energy overcomes the potential magnetic energy and columnar aggregates are not stable or directly, they do not form. Other important action that the Brownian motion realizes is the random redispersion before running simulations: to equate initial conditions in each simulation, firstly particles are placed in an ordered network and then left to redisperse via Brownian motion, which is introduced in the equations of motion as a random parameter in a certain numerical range. Once particles are well dispersed, an external magnetic field is applied and then the system begins to **equilibrate** until the **potential magnetic energy reaches a plateau value with time** indicating the stabilization of the system. In addition to the effect of Brownian motion in the structuration of the system and its dynamics, there is another important factor which clearly determines the final structure and the resulting measurements, **the particle size distribution**. It is well known that monodisperse systems can crystallize under certain conditions so therefore, it would be reasonable to use polydisperse systems to try to simulate the real behavior of MR fluids. Indeed, in our real system, carbonyl iron particles are very polydisperse confirming the necessity to include polydispersity in the simulations. As we are going to see later, polydispersity plays an important role in the evolution of the structure and it will be seen that a low polydispersity index can **avoid crystallization**. It must be kept in mind that the polydispersity in the system is very small and despite this fact, we observe differences with respect to the monodisperse system. Our criterion to calculate the polydispersity index is $PDI = \frac{\sum_{i=1}^N \sqrt{(a_i - a)^2}}{N}$

where N is the number of particles and a_i is the radius of particle i . In the case



of a monodisperse system, $PDI = 0$. Deviations from this value indicate the high or low polydispersity of the system.

Real particles, such as carbonyl iron particles, do not penetrate each other and this effect must be introduced in computational methods. They behave as particles that are not easily deformable, i.e. **quasi-hard spheres** and hence we try to simulate this kind of repulsion to **prevent particle overlapping**. For this purpose we take as a repulsive force an exponential function with this form:

$$\vec{F}_{ij}^{rep} = -\frac{3U_0}{16a^4} \exp\left(-100 \frac{|\vec{r}_{ij}| - (a_i + a_j)}{a_i + a_j}\right) \hat{r} \quad (25)$$

where $|\vec{r}_{ij}|$ is the distance between particles i and j and U_0 is the **magnetic control parameter** defined as:

$$U_0 = 4\pi\mu_0\mu_{cr}\beta_M^2 a_i^3 a_j^3 H_0^2 \quad (26)$$

We notice that the particle radius has a subscript because of the option of a polydisperse system, where particles have different sizes. As we will see later, the definition of U_0 will be essential. Also we could model the repulsion by using other kinds of functions such as power-law functions but it has been shown that the exponential repulsion better simulates the real behavior, corroborated by studying differences between the two final structures under the influence of both repulsions²⁸. A conventional repulsion-attraction potential in magnetic systems has the shape which is shown in Figure 14. Regarding both the

magnetic and repulsion forces, Equations (22) and (25), respectively, one can understand the repulsion-attraction mechanisms and can extract two basic conclusions: if particles are in the same horizontal plane ($\theta = 90^\circ$), they will absolutely repel each other; on the other hand, if particles are aligned in the magnetic field direction ($\theta = 0^\circ$), the attraction will be a maximum. Looking at the scheme of Figure 14, it is clear that when particles are very close to each other (near to contact), the repulsive force strongly dominates and particles repel. Moving towards larger distances, the attractive interaction grows and repulsive force suffers a fast decrease. Therefore, the repulsive force only contributes to avoid overlapping and its effect at medium/large distances is negligible. Hence, this approach to reproduce the real repulsion between particles is not too far from reality.

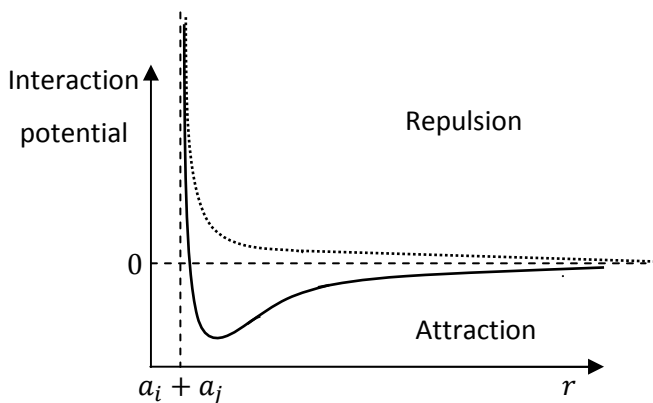


FIG. 14 Interaction potential between magnetic particles. The dashed line corresponds to particles in a plane perpendicular to magnetic field and the continuous line to particles in different planes. The vertical dashed line marks the distance where two hard spheres would collide.



To study the evolution of the structure towards the equilibrium, in addition to the potential magnetic energy we calculated other parameters (order parameters) such as the **average number of neighbors per particle**. This shows the number of particles which are in the immediate environment of a particle, defined as the sphere centered in the center of such particle with a certain radius (cut-off radius). Also this average number of neighbors indicates that the system is equilibrated by reaching a plateau with time. As a way to better understand this order parameter, a simple scheme is shown in Figure 15, for two cases: single width particle chains and thick columns. In the figure, r_c refers to the cut-off radius of the neighbors sphere. As we can see, the red particle would have only two close neighbors contrary to the green particle that has six close neighbors. In MR systems, there is a mix of these structures and due to that, an average over all of the particles is required to take this parameter as an effective parameter. Simply by taking the total number of close neighbors and then dividing by the number of particles within the system this parameter is calculated.

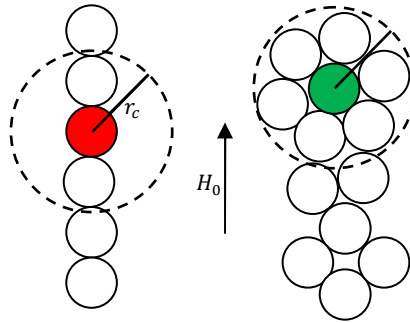


FIG. 15 Number of close neighbors for two probe spheres in two different columnar aggregates. The red particle has two neighbors (single width particle chain) and the green particle (thick columnar aggregate), six neighbors.

It was mentioned before the potential magnetic energy as a structural parameter which determined the equilibrium state. It is well known that magnetic interactions in MR fluids are very complex but a good first approach is to suppose that particles interact like **magnetic dipoles**, whose magnetic moments only depend on the external magnetic field, neglecting multipolar interactions. The total magnetic force on a particle can be calculated by adding all contributions from the other particles in the system, using the Equation (22) for each pair of particles. The average potential magnetic energy is calculated as follows:

$$E_{mag} = \frac{1}{N} \sum_{i \neq j}^N U_0 \left(\frac{1}{|\vec{r}_{ij}|} \right)^3 (1 - 3 \cos^2 \theta) \quad (27)$$



where N is the total number of particles that, in our case it is **1000**, and θ is the angle between the direction of the magnetic field and the vector \vec{r}_{ij}^* .

In our simulations we consider $N = 1000$ particles, with a flat distribution of radii between $0.9a$ and $1.1a$, giving a $PDI = 0.05$. The volume fraction is always $5 \text{ vol}\%$ and the parameter U_0 is changed from 0 to values up to 100. The system was equilibrated prior to applying the magnetic field (as quasi hard spheres), and then equilibrated again in the external field. Further simulation details are given in the sections Part III and Appendix A, which are devoted to simulations. In Figure 16 the evolution of the potential magnetic energy and the average number of neighbors per particle as a function of the magnetic control parameter is shown. Data points correspond to plateau values in the representation of these parameters as a function of time. The control parameter and the potential magnetic energy are **normalized** and due to this fact there are no units in the figure. Also in Figure 16, there are two snapshots of the microstructure in simulations: at off-field state and at a normalized value of $U_0 = 60$.

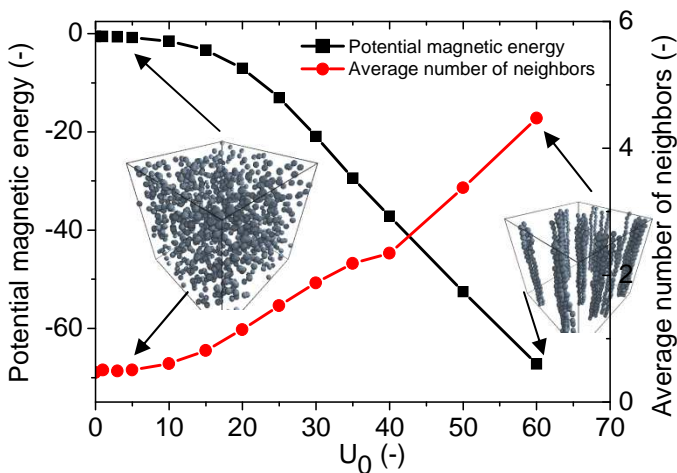


FIG. 16 Black squares correspond to the potential magnetic energy and red circles to the average number of neighbors per particle. The off-field state clearly shows the random disorder of particles. On the other hand, thick columnar aggregates are shown in the snapshot at $U_0 = 60$.

In static conditions, as it is our case, it was mentioned above that there was a competition between magnetic and Brownian forces and such competition determines the stability of the structure. To evaluate each contribution, as in the case of the Mason number which plays an important role in dynamic conditions, there is a parameter that shows the balance of both Brownian and magnetic forces, the **lambda parameter**, λ , defined as follows²⁹:

$$\lambda = \frac{\pi\mu_0\mu_{cr}\beta_M^2 a^3 H_0^2}{2k_B T} \quad (28)$$



As we can see, this parameter is clearly a balance between the magnetic interaction and the thermal motion, evaluated by the temperature T (usually 25 °C in experiments) and the Boltzmann constant $k_B = 1.38065 \cdot 10^{-23} \text{ J/K}$. Therefore, λ gives an estimation about the predominant force: for sufficient large values of this parameter, magnetostatic interactions dominate over Brownian motion, leading to form columnar aggregates; if the value of λ is sufficiently small, thermal motion dominates and structures are not possible, as it occurs in the case of dilute MR fluids (0.1 vol% – 5 vol%). The use of λ in static conditions is justified because Brownian motion is non-negligible, contrary to the case of dynamic conditions, where hydrodynamic forces completely dominate at low magnetic field values in dilute suspensions. Once the system is in equilibrium, a wide range of possibilities to study the structure and the dynamics under no flow conditions opens up. Referring to the structural aspect, we used both the average number of neighbors and the potential magnetic energy to characterize the structure, but there are other interesting magnitudes that lead to further understand the structural conformation. That is the case of **the particle pair distribution function, the static structure factor and the crystallization order parameter.**

First of all, **the radial particle pair distribution function, $g(r)$** , gives information about how density varies through the system as a function of the radial distance from a reference particle. Therefore, this function provides an idea of how matter is distributed in space and its calculation is easy: the method consists in counting the number of particles in a spherical shell centered in a reference particle. In Figure 17 an illustrative scheme to understand the sense of this function is shown.

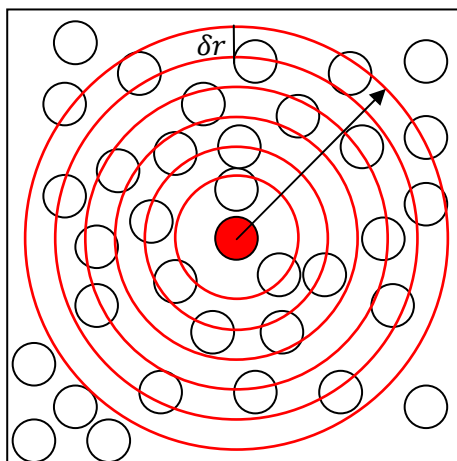


FIG. 17 Calculation of $g(r)$. The thickness is the same for each shell and the distribution extends throughout the simulation box. The calculation of the distribution function results from an average over all particles.

In our MR systems, it is important to remark that under the presence of a magnetic field, the system is no longer isotropic and the radial distribution function has to be divided into its parallel and perpendicular to the external field components to study the matter distribution. On the other hand, the Fourier transform of the pair distribution function, the **structure factor**, $S(\vec{q})$, basically, is a mathematical tool to interpret interference patterns of incident radiation on a system. By means of this factor one can understand the scatter mechanisms of a certain material and find how is the internal structure (columnar distribution, etc.). This factor is defined as follows³²:



$$S(\vec{q}) = \left\langle \left(\sum_{i=1}^N \cos \vec{q} \cdot \vec{r}_i \right)^2 + \left(\sum_{i=1}^N \sin \vec{q} \cdot \vec{r}_i \right)^2 \right\rangle \quad (29)$$

where \vec{q} is the wave vector restricted to $\vec{q} = \frac{2\pi}{L}(n_x, n_y, n_z)$, with n_i integer numbers and L is length of the side of the cubic simulation box (we will see in more detail this aspect later). Finally, the **crystallization order parameter**, Q_l , gives us information about how crystalline is the system, i.e. how the structure is close or far from a crystallized state. The definition has this expression³⁰:

$$Q_l = \sqrt{\frac{4\pi}{2l+1} \sum_{m=-l}^l \left| \frac{1}{N} \sum_{k=1}^N \sum_{j=1}^{n_k} Y_{lm}(\theta_j, \Phi_j) \right|^2} \quad (30)$$

where N now is the total number of bonds between nearest neighbors, l is an integer, n_k is the number of nearest neighbours of a particle k , and Y_{lm} are the spherical harmonics that depend on the angles in spherical coordinates θ_j and Φ_j . We mentioned above that introducing polydispersity avoids crystallization and thanks to the three parameters that we have shown before, it is possible to discern exactly in which state is the system. As we are going to see in the next chapters, the crystallization order parameter has higher values in the case of monodisperse systems, indicating a possible crystalline order. As an illustrative way, in Figure 18 two snapshots corresponding to the monodisperse and polydisperse systems are shown. The normalized value of U_0 is 60 and these

snapshots correspond to the equilibrium state. In light of these results, it has become clear that the influence of the polydispersity is really important in the equilibrium state as we can see in the figure: thicker and ordered columnar aggregates are observed in the case of the monodisperse system, unlike in the case of the polydisperse system, where structures are apparently less rigid and thin and a clear particle order is not observed.

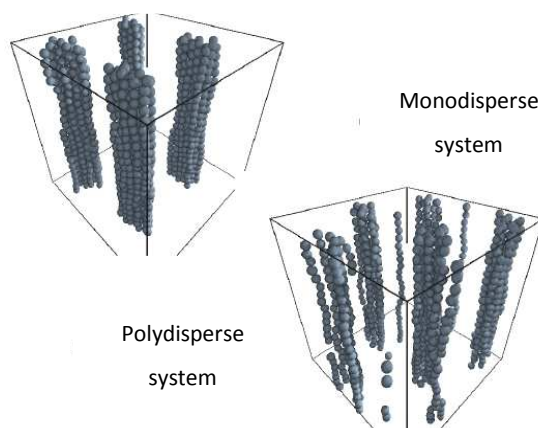


FIG. 18 Snapshots of a monodisperse and a polydisperse system at $U_0 = 60$.

At this point we have to distinguish between rheological experimental tests and the system dynamics in simulations: while in experiments the MR fluid is subjected to several kinds of deformations, i.e. external stresses are applied, in simulations the dynamics in the equilibrium state (without external stresses) is studied by taking into account only magnetic and Brownian forces, which have



an internal character. Even so, by means of some physical magnitudes it can be built a bridge between microscopic results and macroscopic interpretation.

Once the structural aspect is clear, it is the moment to tackle the **dynamics in the equilibrium state**. In this state, structure continues evolving because of the **Brownian motion** but, in average, the system is in equilibrium and the potential magnetic energy and the average number of neighbors reach a constant plateau value. We are going to study those changes in this state. For this, we study the **stress correlation function, the bond correlation function and the mean square displacement**. The first one has a clear physical meaning: the stress correlation function indicates how the system relaxes the stress provoked by a fluctuation and to do that, this function studies the correlation between the **stress tensor components** during time. This is a measure about the stability or rigidity of the structure or in other words, this is a measure of the **stress relaxation time**. Before showing the expression of the stress correlation function it is important to remark that we will only take into account the non-diagonal components of the stress tensor because we are interested only in the shear stress and deformation. First, we calculated the non-diagonal components of the microscopic stress tensor by using the following equation³¹:

$$\sigma_{\alpha\beta} = \sum_{i=1}^N m_i v_{i,\alpha} v_{i,\beta} - \sum_{i<j} r_{ij,\alpha} F_{ij,\beta} \quad (31)$$

where m_i is the particle mass, $v_{i,\alpha}$ is the α^{th} component of velocity of particle i , $r_{ij,\alpha}$ the α^{th} component of the vector position between particles i and j and $F_{ij,\beta}$ refers to the β^{th} component of the total force between the particle pair (magnetic + repulsive force). Looking at the later expression one can see that

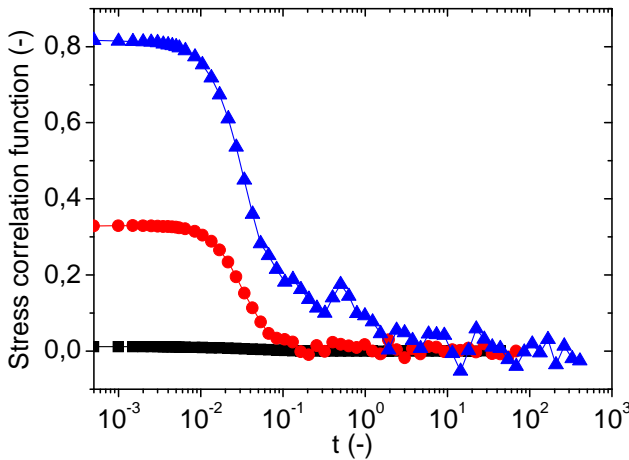
the calculation of the stress tensor involves two components: the kinetic part which refers to the particle motion itself and the part which corresponds to the effect of the forces acting on particles. The stress correlation function is defined as:

$$C_{\sigma\sigma}(t) = \frac{1}{k_B TV} \sum_{\alpha < \beta} \langle \sigma_{\alpha\beta}(t) \sigma_{\alpha\beta}(0) \rangle \quad (32)$$

In this expression, V refers to the simulation box volume and t is the time. $\langle \dots \rangle$ indicates an ensemble average. As we mentioned above, this equation studies the time correlation between non-diagonal components of the microscopic stress tensor, starting the correlation from $t = 0$. In light of that, lower values of the function would indicate that stress tensor components would be totally decorrelated and this would mean that the system behaves as a very low viscous fluid, i.e. stress relaxation time is really short or zero. When the initial values of the stress correlation function increase, this means that the system is approaching a solid-like state and the stress relaxation time grows, the decorrelation is slower. In fluids, more or less viscoelastic, the stress correlation function falls to zero but, in solids, this function decreases up to a long-time plateau. By applying the **Fourier transform** ($\tilde{C}_{\sigma\sigma}(\omega)$) to the stress correlation function it is possible to calculate a macroscopic magnitude, the **complex modulus**, $G(\omega) = i\omega\tilde{C}_{\sigma\sigma}(\omega)$ ³² and then, the viscoelastic moduli, $G(\omega) = G' + iG''$, which are easily measurable in the lab by a conventional dynamic oscillatory shear test as mentioned previously. This means that we are able to connect the microscopic measurements (stress tensor components) with macroscopic measurable magnitudes (viscoelastic moduli).



Another important function in the study of the system dynamics is the **bond correlation function**. This is very similar to stress correlation function but refers to the evolution of the neighbors of a given particle during time, i.e. this function evaluates how many particles are close neighbors of a probe particle and how many particles are still close neighbors after a time interval. As a way to better understand this: if the system is a crystal, for example, this function would be a constant because the internal structure does not evolve and particles remain in its place. For a Newtonian fluid, this function would decay fast to zero. For viscoelastic fluids, we would have a combination of these two extreme states. In Figure 19 conventional curves for the stress correlation function and the bond correlation function are shown at different values of the magnetic control parameter U_0 .



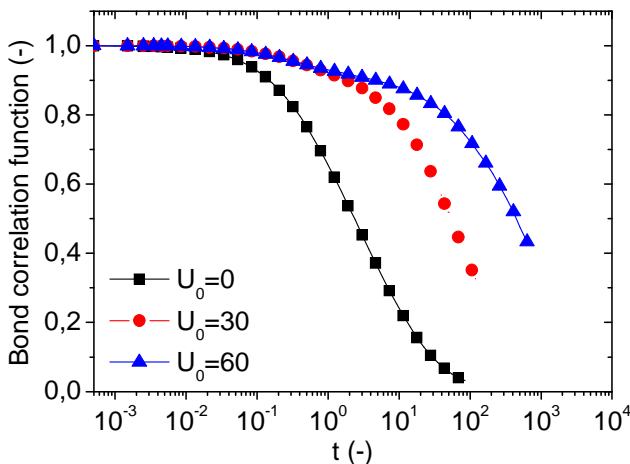


FIG. 19 The upper graph corresponds to the stress correlation function as a function of time; in the bottom, the time evolution of the bond correlation function for a polydisperse system.

Finally, we study the **mean square displacement** in the equilibrium state. This magnitude provides us information about the particle motion within the system. The particle can stay in several situations, for example, particles can move through the bulk or can be arrested within a dense structure. Both cases could be determined studying the mean square displacement. The conventional representation of this magnitude is versus time (Figure 20). The expression is:

$$\langle \Delta r(t)^2 \rangle = \frac{1}{N} \sum_{i=1}^N \Delta r_i(t)^2 \quad (33)$$



where $\Delta r_i(t)^2$ refers to the square of the difference between the initial and actual positions of the particle. Basically, this magnitude evaluates the absolute displacement of particles during a certain time.

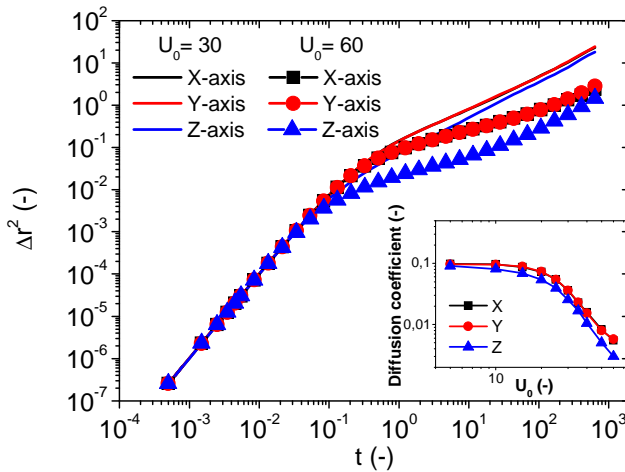


FIG. 20 Mean square displacement in three coordinates axis as a function of time for two different control parameter values. Diffusion coefficients as a function of U_0 in the inset.

Typical results of the MSD are shown in Figure 20. At short times we can observe in the figure that the particle moves in the ballistic regime. At larger times, the particle begins to suffer collisions with other particles and the trend changes, and the particle begins to be arrested within a certain structure: particle has close neighbors that difficult its free motion until diffusion is reached at long times. In the inset, the diffusion coefficients are shown. These are calculated as the long time slopes of the mean square displacement and have the following expression:

$$D = \log_{t \rightarrow \infty} \frac{1}{6t} \langle |\vec{r}(t) - \vec{r}(0)|^2 \rangle \quad (34)$$

We observe that these coefficients decay when the control parameter U_0 increases: when the magnetic field is more intense, columnar aggregates are more stable and thicker and particles inside these structures have its motion more and more limited.

References

- ¹Foundations of Colloidal Science, vol. I, Robert J. Hunter, Oxford Science Publications, 1987.
- ²Berkovsky, B. M. and Bashtovoy, V., Magnetic fluids and applications handbook. Begell house, inc. New York, Wallingford (UK), 1996.
- ³Papisov, M. I, Bogdanov, A., Jr., Schaffer, B., Nossiff, N., Shen, T., Weissleder, R. and Brady, T.J., Colloidal magnetic resonance contrast agents: effect of particle surface on biodistribution, *J. Magn. and Magn. Mat.* **122**, p. 383.
- ⁴Magnetoviscous Effects in Ferrofluids, Stefan Odenbach, Springer 2002.
- ⁵J. de Vicente, D.J. Klingenberg, and R. Hidalgo-Álvarez, *Soft Matter*, **7**, 3701, 2011.
- ⁶J. Rabinow, *AIEE Trans.*, **67**, 1308–1315, 1948.
- ⁷D. J. Klingenberg, *AIChE J.*, **47**, 246–249, 2001.
- ⁸M. Heine, J. de Vicente and D. J. Klingenberg, *Phys. Fluids*, **18**, 023301. 4, 2006.
- ⁹B. N. Reinecke, J. W. Shan, K. K. Suabedissen and A. S. Cherkasova, *J. Appl. Phys.*, **104**, 023507, 2008.
- ¹⁰J. Liu, G. A. Flores and R. Sheng, *J. Magn. Magn. Mater.*, **225**, 209–217, 2001.
- ¹¹W. Kordonski and D. Golini, *J. Intell. Mater. Syst. Struct.*, **13**, 401–404, 2002.



- ¹²S. Jha and V. K. Jain, *Int. J. Mach. Tool Manufact.*, **44**, 1019–1029, 2004.
- ¹³W. I. Kordonski, A. B. Shorey and M. Tricard, *J. Fluids Eng.*, **128**, 20–26, 2006.
- ¹⁴F. Donado, J. L. Carrillo and M. E. Mendoza, *J. Phys.: Condens. Matter*, **14**, 2153–2157, 2002.
- ¹⁵K. J. Solis and J. E. Martin, *Appl. Phys. Lett.*, **97**, 034101, 2010.
- ¹⁶D. H. Read and J. E. Martin, *Anal. Chem.*, **82(5)**, 2150–2154, 2010.
- ¹⁷D. H. Read and J. E. Martin, *Adv. Funct. Mater.*, **20(10)**, 1577–1584, 2010.
- ¹⁸D. H. Read and J. E. Martin, *Anal. Chem.*, **82(16)**, 6969–6975, 2010.
- ¹⁹Rheophys: The Deformation and Flow of Matter, Patrick Oswald, Cambridge University Press 2009.
- ²⁰James, David F., *Boger Fluids, Annual Review of Fluid Mechanics*, vol. **41**, Issue 1, pp.129-142.
- ²¹J. R. Stokes, *Swirling flow of viscoelastic fluids*. Research Collections (UMER), 1998.
- ²²J.D. Jackson, *Classical Electrodynamics*, John Wiley & Sons, NY, 1975.
- ²³R. M. Bozorth, *Ferromagnetism*, van Nostrand, Toronto, Canada, 1951.
- ²⁴F.W. Sears and M. W. Zemansky, *University Physics*, second edition, Addison-Wesley. Reading. MA. 1962.
- ²⁵P. J. Rankin, *The Rheology of Electric- and Magnetic- Field Activated Suspensions*, UMI, University of Wisconsin, 2000.
- ²⁶J. M. Ginder, L. C. Davis, *Appl. Phys. Lett.* **65**, 3410-3412, 1994.
- ²⁷D. J. Klingenberg, F. van Swol and C. F. Zukoski, *J. Chem. Phys.*, 1989, **91**, 7888.
- ²⁸R. E. Rosensweig, *Ferrohydrodynamics*, Dover, New York, 1997.
- ²⁹P. J. Steinhardt, D. R. Nelson and M. Ronchetti, *Phys. Rev. B: Condens. Matter*, 1983, **28**, 784.
- ³⁰M. P. Allen and D. J. Tildesley, *Computer Simulation of Liquids*, Clarendon Press, Oxford, 1986.



³¹R. G. Larson, *The Structure and Rheology of Complex Fluids*, Oxford University Press, Oxford, 1999

³²D. Chandler, *Introduction to Modern Statistical Mechanics*, Oxford University Press, 1987.





PART I-EFFECT OF THE PARTICLE MORPHOLOGY

Title of the manuscript:

Dynamic Magnetorheology of Sphere- and Rod-based MR-Fluids

Authors:

J. de Vicente¹, J.P. Segovia-Gutiérrez¹, E. Andablo-Reyes¹, F. Vereda¹, and R.
Hidalgo-
Álvarez¹

Affiliation

¹ Departamento de Física Aplicada, Facultad de Ciencias, Universidad de
Granada, Granada E-18071, Spain

Published

The Journal of Chemical Physics, **131**, 194902 (2009)



Abstract

The effect of particle shape in the small amplitude oscillatory shear behavior of magnetorheological (MR) fluids is investigated from zero magnetic field strengths up to **800 kA/m**. Two types of MR fluids are studied: the first system is prepared with spherical particles, and a second system is prepared with rod-like particles. Both types of particles are fabricated following practically the same precipitation technique, and have the same intrinsic magnetic and crystallographic properties. Furthermore, the distribution of sphere diameters is very similar to that of rod thicknesses. Rod-based MR fluids show an enhanced MR performance under oscillatory shear in the viscoelastic linear regime. A lower magnetic field strength is needed for the structuration of the colloid and, once saturation is fully achieved, a larger storage modulus is observed. Existing sphere- and rod-based models usually underestimate experimental results regarding the magnetic field strength and particle volume fraction dependences of both storage modulus and yield stress. A simple model is proposed here to explain the behavior of microrod-based MR fluids at low, medium and saturating magnetic fields in the viscoelastic linear regime in terms of magnetic interaction forces between particles. These results are further completed with rheomicroscopic and dynamic yield stress observations.



I. INTRODUCTION

Magnetorheological (MR) fluids are well known because of their magnetic-field tunable rheological properties. In the absence of a magnetic field, MR fluids typically behave as Newtonian fluids. However, under the application of a magnetic field particles aggregate to form chain-like structures aligned in the direction of the field. As a consequence, magnetized MR fluids present a yield stress and highly elastic response¹.

Typical MR fluids are formulated by dispersing magnetizable spheres in a non magnetic medium. The effect of magnetic field and particle volume fraction in their rheological response has been largely studied in the past and a collapse is generally found in terms of the Mason number². However, up to now the influence of particle shape has been scarcely studied, the reason for this probably being the lack of suitable non-spherical magnetic particles having appropriate size; particles should be large enough so that magnetic forces overcome thermal motion and small enough in order to prevent sedimentation.

Basically, the influence of particle shape on MR response stems from the fact that a spheroid whose major axis is aligned with the magnetic field and has the same intrinsic magnetic properties and volume as a spherical particle, will have a greater induced magnetic moment due to its smaller demagnetization factor in that direction. As a consequence, stronger fluids are expected to be prepared using anisotropic particles. Apart from this, other advantages are as follows: (i) lower volume fractions are required for the column like aggregates to connect the gap in a rheometer, (ii) better stability against sedimentation because of hindered settling, (iii) easy re-dispersion because of the formation of a less compacted sediment once the magnetic field is absent.



Shaw and coworkers^{3,4} were probably the first to investigate the effect of particle shape in electrorheological (ER) fluids in an attempt to improve the rheological properties of the fluid. They showed that using poly(p-phenylene-2,6-benzobisthiazole) rodlike particles it is possible to enhance the dielectric interaction of the particles as well as their mechanical interaction. Yabing and Wen⁵ presented experimental results on the effect of particle shape on dried and water activated ER fluids under both DC and AC fields. Their results for water activated fluids were explained due to surface effects; a lower ER effect is observed for anisotropic particles in contrast to the findings by Kanu and Shaw. Watanabe et al.⁶ analyzed the orientational distributions and rheological properties of magnetic spherocylinders subjected to a simple shear flow. Tsuda et al.⁷ studied the yield stress vs. electric field dependence for spheres and whisker suspensions. For whisker suspensions, the yield stress was clearly larger, although the slope of the yield stress vs. electric field curve decreased from 2 to 1.3. The observed enhancement of ER performance for whisker suspensions electrified under oscillatory shear can be explained by the column thickening induced by oscillatory shear. Yin and coworkers⁸ prepared nano-fibrous polyaniline (PANI) particles by a modified oxidative polymerization in aniline in acid solution. These particles were later dispersed in solution and investigated with rheological techniques. Both steady state and oscillatory responses were larger for nano-fibrous particles than spherical ones. Bell and coworkers showed that MR fluids utilizing nonspherical magnetic particles exhibit enhanced rheological properties as well as greater stability^{9,10,11}.

Early 2007 our group developed a procedure to prepare highly elongated micron-sized magnetite particles by magnetic field-induced self-assembly¹². These particles were then anticipated to be of great interest in MR fluid

formulations. An important advantage of this method is that it makes possible to prepare both spheres and microrod particles of the same material (in this case magnetite) and with the same electrokinetic, intrinsic magnetic and crystallographic properties. Furthermore, the resulting distribution of sphere diameters is very similar to that of rod thicknesses.

Typical rheological experiments found in the literature are carried out under steady state conditions. However, physical information drawn from such tests is rather poor compared to what can be obtained from a spectromechanical analysis. This kind of test allows us to separate elastic and viscous contributions to the rheological performance, and can reveal relaxation phenomena present in the microstructure without destroying it. To date, no conclusive studies of the field-dependent moduli of MR-materials have been reported.

In this work we report below, we investigated the effect of particle shape in the MR performance of model magnetic colloids. Experiments were carried out in oscillatory shear flow using a parallel plate torsional magneto-rheometer under the presence of a wide range of magnetic fields up to ~ 800 kA/m.

II. EXPERIMENTAL

A .Synthesis of MR-fluids

Both types of particles were fabricated following the method described by Sugimoto and Matijević¹³. Briefly, the method relies in the precipitation of $\text{Fe}(\text{OH})_2$ and its subsequent oxidation at 90°C in the presence of KNO_3 . The main difference between the fabrication process of the rods and the spheres was that, in the case of the rod-like particles, the reactant mixture was cured in a flat



flask that was placed inside the gap of a permanent magnet ($B \sim 400 \text{ mT}$) as that depicted in ref. 14. For both spheres and rods, a first solution (sol. no. 1) was prepared with doubly distilled water and the required amounts of KOH and KNO_3 . This solution was purged with N_2 for at least 1 hour. A second solution (sol. no. 2) of $\text{FeSO}_4 \cdot 7\text{H}_2\text{O}$ was prepared with doubly distilled water that had also been previously purged for at least 1 hour with N_2 . The concentrations of the solutions were adjusted so that in the final reactant mixture there was a concentration of $\text{Fe}(\text{OH})_2$ of 0.025 M an excess of Fe^{2+} in solution of 0.005 M and a concentration of KNO_3 of 0.20 M . One of the difficulties we had to overcome for the preparation of the MR fluids was the low yield of the reaction. For the concentrations given above, we obtained less than 2 mg of magnetite per mL of reactant mixture, whereas the preparation of the MR fluids required a relatively large amount of magnetite. For instance, a MR fluid with a magnetite content of $5 \text{ vol}\%$ in volume requires approximately 258 mg of magnetite per mL of fluid. This difficulty was especially severe for the rod-like particles because of the limited volume of reactants that could be cured inside the magnet.

The reactant mixture inside the magnet was cured for 70 minutes. It had been established in the past¹² that under the conditions described above this curing time was sufficient for the full growth of the magnetite rods. Therefore, after 70 minutes the reaction flask was emptied and refilled with the proper volumes from stocks of solutions no. 1 and no. 2, which were purged with N_2 for as long as needed.

Spheres were fabricated using a reactant mixture with identical concentrations as those mentioned above, but curing it in 250 mL screw-cap flasks in the absence of any magnetic fields. These particles were cured for 4 hours.

After the curing process, both spheres and rods were washed with doubly distilled water at least 8 times, and then stored in absolute ethanol. A permanent magnet was used during the washing process to accelerate sedimentation of the particles and facilitate the decantation of the supernatant. For the preparation of the MR suspensions, particles were dried at 40 °C in air for approximately 8 hours or until no further weight loss due to ethanol evaporation was detected.

The preparation of the suspensions consisted of the following steps: (i) magnetite and silicone oil (20 $mPa \cdot s$) were mixed in a polyethylene container; (ii) the mixture was stirred first by hand, and then in an ultrasonic bath; (iii) step (ii) was repeated several times, and finally, the sample was immersed in a Branson sonifier (model 450) to ensure the required final homogeneity. The gradual homogenization of the samples was confirmed by the disappearance of the aggregates initially observed in the container bottom. Using this preparation procedure, the resulting suspensions, at a given volume fraction, were found to be reproducible from the point of the rheological tests results.

The fragmentation of rod-like particles during shearing tests was found not to be significant. To investigate this point, suspensions were prepared varying the time they were subjected to ultrasounds using a different preshear. Negligible differences in the rheological response were observed suggesting that particles fragmentation is not likely.



B. Microscopic characterization

A Motic B3 optical microscope was used to investigate the structure at large magnetic fields. A rheomicroscope (MCR, Anton Paar, Austria) was employed to see the evolution of the structure at low and medium magnetic fields during rheological tests. The rheomicroscope was employed with a parallel plate measuring configuration (40 mm diameter, 300 μm gap). The upper plate is free to rotate at a commanded velocity. In this case, the lower plate is made of glass and is maintained immobile. The microscope objective looks from below in reflective light mode. A CCD camera captures the image which is later processed in a PC.

C. Rheological characterization

Dynamic oscillatory properties of the MR-fluids were measured at 25°C using a parallel-plate magneto-rheometer (MCR Anton Paar, Austria). The diameter of the plates was 20 mm and the plate separation was fixed at 300 μm . The magnetic field was applied normal to the direction of flow. All plates used for magnetorheological characterization were made of titanium with the exception of rheomicroscope tests, which were obtained using the glass disk mentioned in section II B.

First, the viscoelastic linear region was determined. Storage and loss moduli were measured as a function of strain at a frequency $f = 1 \text{ Hz}$, in the presence of the following magnetic fields: 0 kA/m, 175 kA/m, 353 kA/m, 530 kA/m, 707 kA/m and 884 kA/m. Then, magnetosweeps were carried out at a strain

amplitude $\gamma_0 = 0.003 \%$ (well within the viscoelastic linear region in all cases) and a frequency $f = 1 \text{ Hz}$ according to Laeuger et al.¹⁵

The experimental procedure is summarized as follows: (i) precondition at a constant shear rate $\dot{\gamma} = 200 \text{ s}^{-1}$ during 30 seconds, (ii) suspension is left to equilibrate for 1 minute, (iii) constant dynamic-mechanical shear conditions are preset (both frequency and amplitude are kept constant) and magnetic field is gradually increased from 0.175 to 884 kA/m (logarithmically increased at a rate of 10 points per decade). In all cases experiments were repeated at least three times with fresh new samples.

Dynamic yield stress measurements were carried out in controlled shear rate mode. In a first step a preshear is applied in the absence of a magnetic field. Then, the magnetic field is turned on without any shear applied yet. After 30 seconds of equilibration the shear rate starts to increase from 0.01 s^{-1} to 500 s^{-1} . Dynamic yield stress is obtained from curve fitting using the Bingham model at large shear rates. The yield stress is obtained by extrapolation of the curve to zero shear rate. It is important to observe that different model functions usually produce different yield point values¹⁶. We chose this procedure because it is frequently used in the MR fluids literature¹⁷.

III. THEORY

A. Sphere-based MR-fluids

At low magnetic fields, dipolar interactions dominate between magnetisable particles in non magnetic media. In this case, a quadratic dependence is usually observed for the yield stress and the storage modulus, both as functions of the



magnetic field strength. The model by Martin and Anderson¹⁸ predicts the following dependence of the storage modulus:

$$G' = 2.11k_3\phi\mu_0\beta^2H^2 \quad (1)$$

where $\beta = \frac{\mu_{sph} - 1}{\mu_{sph} + 2}$, $k_3 = \left(1 - \frac{k}{4} - \frac{k^2}{8}\right)^{-1}$, $k = 1.202\beta$

Here, ϕ is the particle volume fraction, μ_0 is the magnetic permeability of vacuum, H is the internal magnetic field in the suspension (see the Appendix A for its calculation), and μ_{sph} is the relative magnetic permeability of the spheres.

The model by de Vicente et al.¹⁹ assumes a different hydrodynamic interaction. According to these authors the storage modulus can be written as:

$$G' = 1.76\phi\mu_0\beta^2H^2 \quad (2)$$

At medium magnetic fields, poles in the particles begin to saturate. In this case, a quadratic dependence is no longer observed. Ginder²⁰ proposed the following equation:

$$G' = 3\phi\mu_0M_sH \quad (3)$$

where M_s is the saturation magnetisation of the particles. At large fields, particles are completely saturated. In this case, both yield stress and storage modulus are constant with the field. From a finite element calculation, Ginder obtained the following result²⁰:

$$G' = 0.3\phi\mu_0 M_s^2 \quad (4)$$

B. Rod-based MR-fluids

As a first approximation, acicular and rod-like particles can be modelled mathematically by prolate spheroids. The magnetic dipolar moment of a solid spheroid dispersed in a non magnetic medium can be written as²¹:

$$m = V\mu_0 \frac{\mu_{rod} - 1}{1 + (\mu_{rod} - 1)N_D} H \quad (5)$$

where $V = \frac{1}{6}\pi d_1 d_2^2$ is the volume of the particle, d_1 and d_2 are the length and width of the spheroids respectively, μ_{rod} is the relative magnetic permeability of the spheroid, and N_D is the demagnetizing factor of the spheroid. In this work, the permeability of both microsphere, μ_{sph} , and microrod, μ_{rod} , magnetite particles was calculated from the Frohlich-Kennelly equation²² with $\mu_{sph,i} = \mu_{rod,i} = 15$ and $M_s = 490 \text{ kA/m}$ (the hysteresis curve at room temperature corresponding to these particles can be found elsewhere¹²). The length and width of the spheroids are given by $d_1 = 6900 \text{ nm}$ and $d_2 =$



560 nm (see Ref.12). From Eq.(5), the dipolar interaction force between two spheroids is given by:

$$\vec{F} = -\frac{1}{3}\pi d_1^2 \mu_0 \left[\frac{\mu_{rod} - 1}{1 + (\mu_{rod} - 1)N_D} \right]^2 H^2 \vec{f} \quad (6)$$

where

$$\vec{f} = \left(\frac{d_2}{2r} \right)^4 \left[(3 \cos^2 \theta - 1) \hat{r} + \sin 2\theta \hat{\theta} \right] \quad (7)$$

and θ and r are the tilt angle and the centre-to-centre distance respectively (see Figure 1).

Assuming that these two dipoles are aligned in a head-to-tail configuration, as expected for spheroids due to the contribution of the shape anisotropy energy, the horizontal component of the force required to separate them is given by:

$$F_H = -\frac{1}{3}\pi d_1^2 \mu_0 \left[\frac{\mu_{rod} - 1}{1 + (\mu_{rod} - 1)N_D} \right]^2 H^2 \left(\frac{d_2}{\alpha d_1} \right)^4 \left[\frac{\cos^4 \theta}{16} (4 \sin \theta \cos^2 \theta - \sin^3 \theta) \right] \quad (8)$$

where the centre-to-centre distance between dipoles is $r = \frac{\alpha d_1}{\cos \theta}$. As a first approximation, the storage modulus in the viscoelastic linear region can be obtained from:

$$G' = \lim_{\theta \rightarrow 0} \frac{N_c F_H / S}{\theta} \quad (9)$$

where $\frac{N_c}{S} = \frac{6\phi}{\pi d_2^2}$ is the number of chains per unit surface. Substituting Eq.(8)

in Eq.(9) we get:

$$G' = \frac{\phi}{2\alpha^4} \left(\frac{d_1}{d_2} \right)^{-2} \mu_0 \left[\frac{\mu_{rod} - 1}{1 + (\mu_{rod} - 1)N_D} \right]^2 H^2 \quad (10)$$

On the other hand, the maximum force allowed is given by:

$$F_{H,\max} = \frac{1}{3} \pi \frac{d_2^4}{\alpha^4 d_1^2} \mu_0 \left[\frac{\mu_{rod} - 1}{1 + (\mu_{rod} - 1)N_D} \right]^2 H^2 f_m \quad (11)$$

where $f_m = \max \left[\frac{\cos^4 \theta}{16} (4 \sin \theta \cos^2 \theta - \sin^3 \theta) \right] = 0.057$

If we assume that spheroids aggregate to form single-width chains upon the application of the magnetic field, basically, the yield stress in a suspension of



magnetized spheroids depends on the number of chains per unit surface, and the maximum force which is given by Eq.(11).


$$\tau_y = \frac{N_c F_{H,\max}}{S} \quad (12)$$

Substituting Eq.(11) in Eq.(12) we get an equation for the yield stress in rod suspensions as a function of the storage modulus:

$$\tau_y = 4G' f_m \quad (13)$$

As observed from Eq.(10) and Eq.(13), the internal magnetic field dependence of both the yield stress and modulus is found to be quadratic at low fields. As a first approximation, at large magnetic fields, saturation of the particles comes into play through magnetic permeability μ_{rod} . Even though Eq.(5) is strictly valid at low fields, in the limit of large fields the equation reduces to $m = \mu_0 M_s V$ which is valid for two saturated spheroids. As a consequence, Eq.(5) will be used here for the whole magnetic field range investigated.

Yield stress and storage modulus scale as a power of -2 on d_1/d_2 for large enough aspect ratios (where N_D asymptotically approaches zero). In the case of aspect ratios lower than approximately 5, the aspect ratio dependence is more complicated because of the demagnetization factor. Interestingly, a strong dependence is observed with α , which basically represents the interparticle distance in the aggregate cf. Figure 1.



Models reported above assume that particles aggregate forming single-width chains aligned in the direction of the magnetic field. However, this assumption is far from being reasonable for typical concentrations used in the formulation of MR fluids. In Figure 2(c) we show a photograph of typical structures induced by the presence of a magnetic field in a microrod based MR fluid at 5 *vol%*. As observed, thick columnar structures exist instead of single width chains. Realistic models should consider thick aggregates and this is not easy to model because of multipolar interactions, interparticle friction and the presence of other short range forces appearing at small distances.

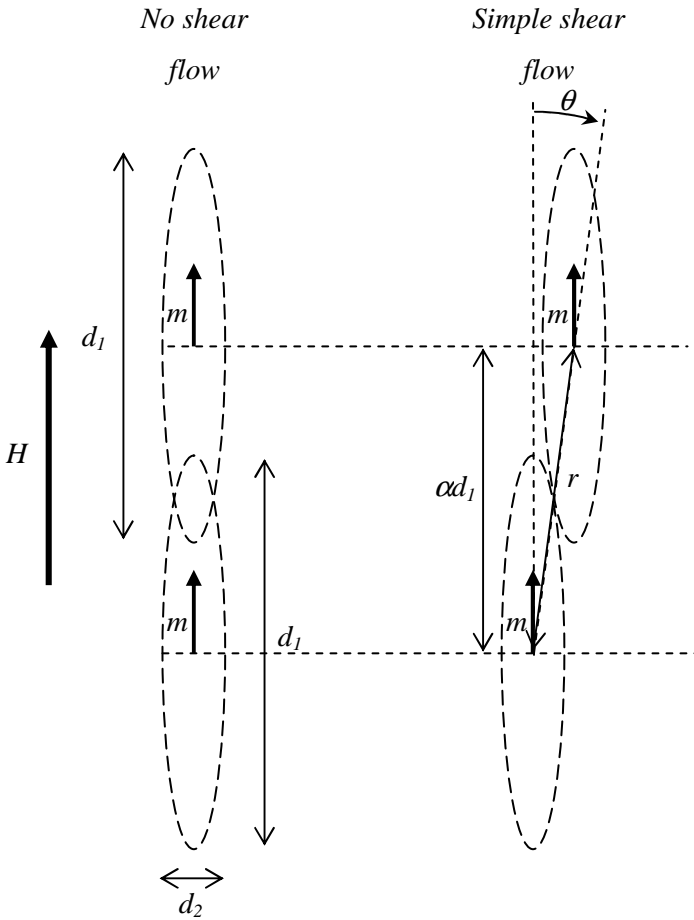


FIG. 1. Schematic representation showing the shape and orientation of the anisotropic structures in the presence and absence of a steady shear flow.

Recently, a “column structure” model has been developed by Bossis and coworkers²³ to explain the shear stress in magnetorheological fiber based

suspensions. In this model, fibers overlap each other in the aggregate at the same overlap length b_0 . When the suspension is strained, the fibers slip along each other and the columns extend and tilt. This model takes into account three interactions that contribute to the total stress: particle-field magnetic interactions (τ_{field}), solid friction ($\tau_{friction}$) and magnetic interactions between the fibers ($\tau_{magnetic}$). Furthermore, the model can be adapted to predict storage modulus by taking the limit to low displacement angles:

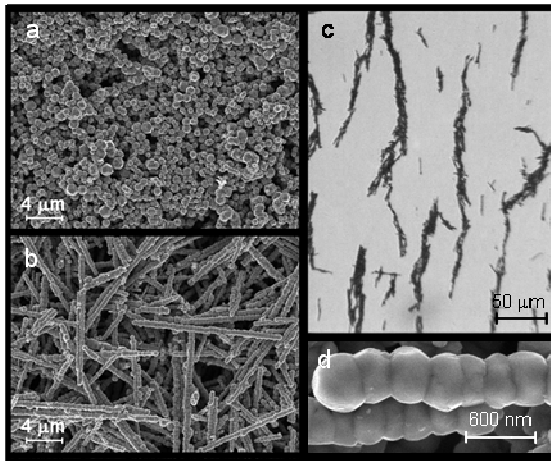


FIG. 2. Characteristic SEM micrographs of magnetite spheres (a) and rods (b) used for the preparation of the magnetorheological suspensions. Typical structure induced by the magnetic field in rod based MR fluids (c). Detail of rod-like particles (d).

$$\begin{aligned}
 G' &= \lim_{\theta \rightarrow 0} \frac{\tau_{field} + \tau_{friction} + \tau_{magnetic}}{\theta} \approx \\
 &\approx \left[\frac{\phi}{2} \frac{(\mu_{rod} - 1)^2}{\mu_{rod} + 1} \mu_0 H(\theta = 0)^2 \right] \lim_{\theta \rightarrow 0} \frac{\tilde{\tau}_{field} + \tilde{\tau}_{friction} + \tilde{\tau}_{magnetic}}{\theta} \quad (14a)
 \end{aligned}$$



where each contribution to the stress can be obtained as follows:

$$\tilde{\tau}_{field} = \sin 2\theta \cos^2 \theta \quad (14b)$$

$$\tilde{\tau}_{friction} = \frac{\xi}{2} \sin^2 2\theta \quad (14c)$$

$$\tilde{\tau}_{magnetic} = -\frac{G(\theta)}{16} \left(\frac{d_2}{d_1} \right)^2 \sin 2\theta \left[(\mu_{rod} + 1) \cos^2 \theta + \frac{4 \sin^2 \theta}{\mu_{rod} + 1} \right] \quad (14d)$$

Here, $G(\theta) = [\beta - \xi(d_2/d_1)] / [\beta + (d_2/d_1)^2]^{3/2}$, with $\beta = 1 - (1 - \beta_0) / \cos \theta$, where $\beta_0 = b_0/d_1$ and ξ represents the friction coefficient. In the case of small angles, structures are slightly perturbed and according to this model only particle-field interactions prevail. A simplified equation results:

$$G' = \phi \mu_0 \frac{(\mu_{rod} - 1)^2}{\mu_{rod} + 1} H^2 \quad (15)$$

IV. RESULTS AND DISCUSSION

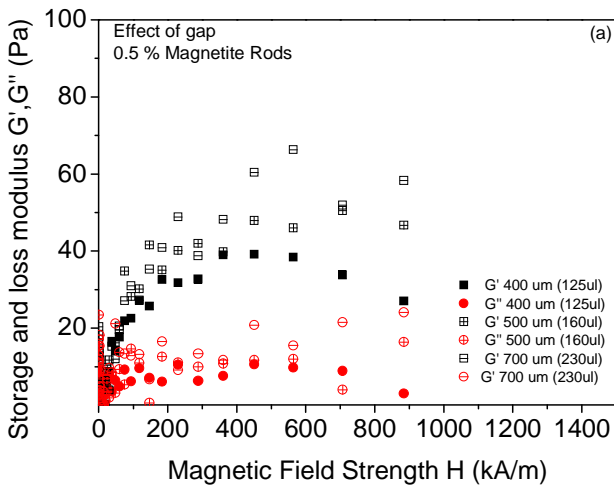
Micrographs of typical magnetite spheres and rods are shown in Figure 2(a) and Figure 2(b) and (d) respectively. Apart from their different morphology, no other differences regarding their crystalline structure or intrinsic magnetic properties were found.¹²

However, a number of comments should be made regarding the size and morphology of the magnetite particles used in this study. We measured the diameter of over 500 magnetite spheres, and obtained a value of $680 \pm 150 \text{ nm}$. For the rod-like particles, the average cross section was $560 \pm 120 \text{ nm}$ and the average length was $6900 \pm 3800 \text{ nm}$. The uncertainties indicated above correspond to the standard deviation of each population. Note the large uncertainty of the rod length measurement, which is indicative of their very inhomogeneous length. Furthermore, the rod-like particles are actually linear arrays of individual particles that fused together (see Figure 2(d)) during growth. This leads to a relatively rough texture that constitutes a major difference from the ideal spheroids of our model.

Preliminary experiments were run in order to ascertain which is the effect of gap distance in the plate-plate configuration. It is well known that the MR response may depend on gap distance since the mechanical response is strongly dependent on the number of columns per unit surface^{24,2}. As a consequence, measuring at large gap distances may result in a negligible MR response due to the lack of gap-spanning structures.



In Figure 3(a) we present experimental results corresponding to microrod-based suspensions at 0.5 vol% measured at different gap distances. As observed, similar results are obtained suggesting that the effect of gap distance is not relevant in this system. Small discrepancies may arise from gaps that are not correctly filled. In the experiments whose results we report below, we used a gap distance of 300 μm . Such distance requires a small sample amount, while it ensures continuum rheology and a small enough gap in order to facilitate gapspanning structures.



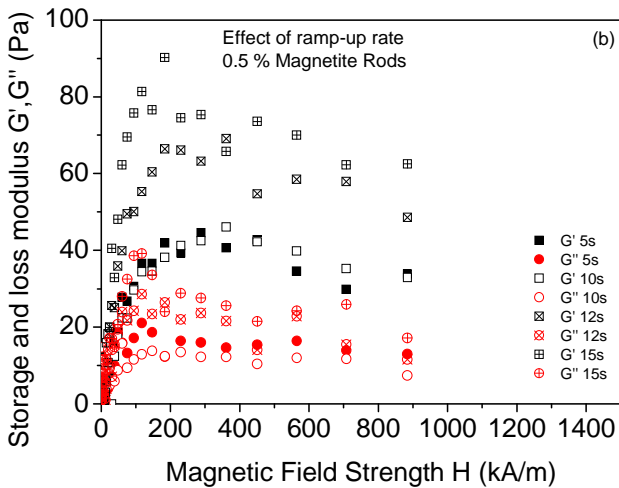
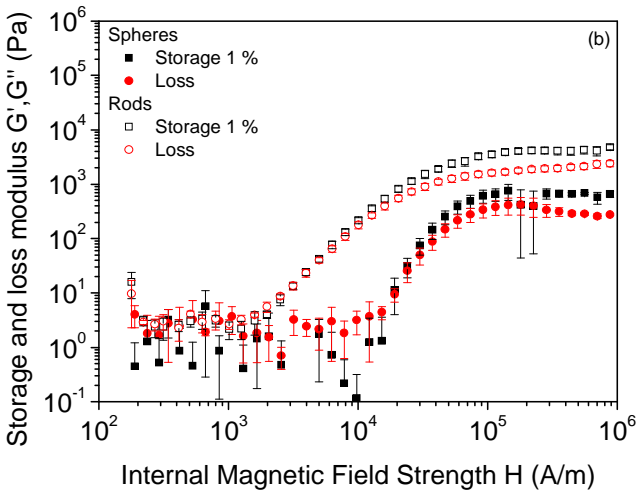
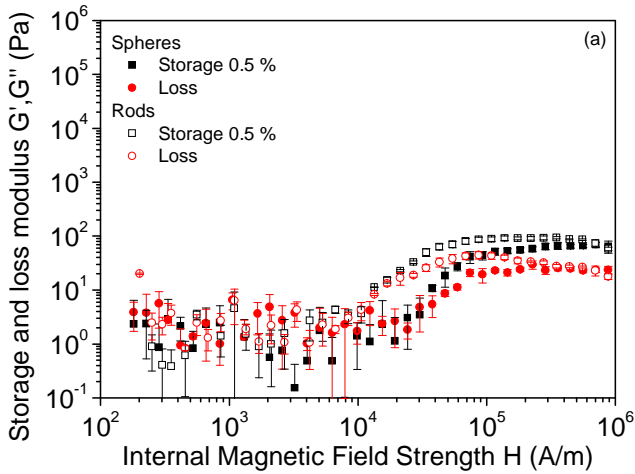


FIG. 3. Effect of experimental conditions in the dynamic moduli. a) Effect of gap distance in the magneto-rheological response for rod-based MR fluids at 0.5 vol%. Integration time 15 s. b) Effect of sweep time in the magneto-rheological response for rod-based MR fluids at 0.5 vol%. Gap 300 μm .

The speed at which the magnetic field is increased may be an important factor in these studies. The rate of increase of the magnetic field had to be conveniently chosen so as to get quasi-equilibrium states. The effect of the rate of increase was investigated, and the results obtained for different rates are shown in Figure 3(b). Here, associated to each curve there is a “integration time” which refers to the data acquisition time spent at every point in the plot. As observed, if measurements are carried out too quickly, the sample is not allowed to relax and a non equilibrium state is explored. For times larger than



12 seconds results do not differ too much. In the following, a rate of increase of 12 seconds is fixed.



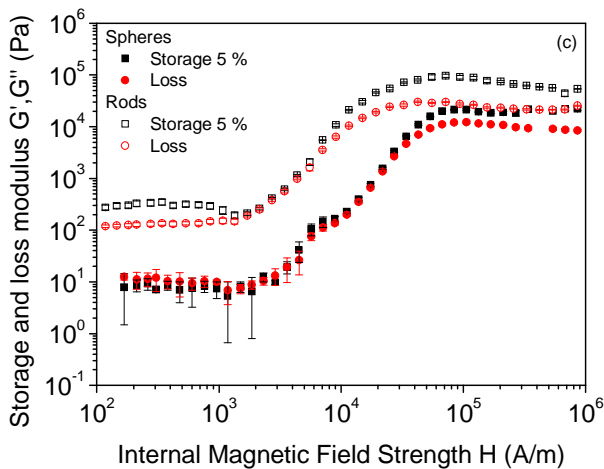


FIG. 4. Internal magnetic field, H , dependence of storage, G' , and loss moduli, G'' , for sphere and rod-based MR fluids at 0.5 vol% (a), 1 vol% (b) and 5 vol% (c).

Averaged magnetosweep curves are presented in Figure 4(a), 4(b) and 4(c) for volume fractions of 0.5 vol%, 1 vol% and 5 vol% respectively. Lower volume fractions were difficult to investigate because of the sensitivity limitation of the rheometer. Larger volume fractions are also difficult to be investigated due to the low yield of the synthesis routes. As observed, regardless of the internal magnetic field strength, the storage modulus, G' , is larger than the loss modulus, G'' .

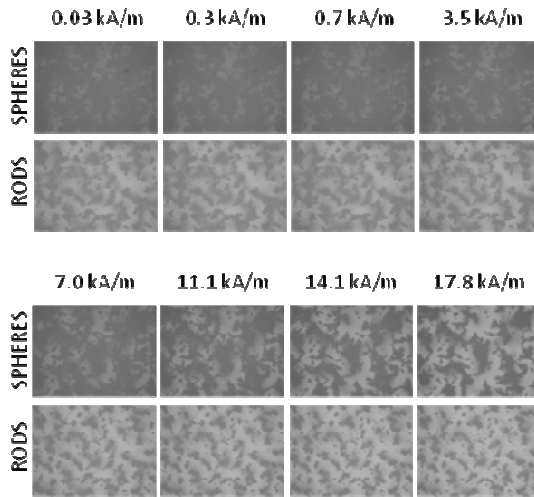


FIG. 5. Structure evolution of a 1 vol% suspension of magnetite spheres and microrods in a 20 mPa s silicone oil contained between 40 mm diameter glass parallel plates (300 μm gap), as the magnetic flux density is increased from 0.03 kA/m to 17.8 kA/m during a magnetosweep test. The magnetic field is perpendicular to the paper.

This suggests some degree of structuration in the colloid. For magnetic fields larger than 1 – 10 kA/m, both moduli increase at least two orders of magnitude. This finding is in agreement with a magnetically induced chain-like structure in the colloid (cf. Figure 5); in the presence of a magnetic field, particles aggregate to align in the direction of the magnetic field. Interestingly, rod-based magnetorheological fluids show a much larger elastic and viscous response when compared to sphere-based fluids. By increasing the particle volume fraction, a stronger MR response is observed. Interestingly, 5 vol% microrod based MR fluids present a non negligible low field storage modulus plateau (cf. Figure 4(c)) which is associated to hindered settling in the rod-based suspension as compared to the sphere-based MR fluids with the same particle

content. Such behaviour has been observed by Bell and coworkers in the past¹⁰. In summary, three regions are clearly observed in magnetosweep curves.

(I) At low magnetic fields, both moduli are nearly constant. Particles become magnetized but interparticle magnetostatic interactions are still too weak to promote the formation of gap-spanning aggregates. In this region, a slight decrease in G' is observed at the largest fields and particle volume fractions, probably associated to some particle arrangement which favours oil to flow in between the dispersed particles (cf. Figure 4(c)). For low particle contents, some noise is found as a result of limited torque resolution of the rheometer.

(II) At medium magnetic fields, both moduli strongly increase as a consequence of the appearance of strong magnetic interactions between the particles. Particles aggregate and motion is partially impeded. Note that for solid contents of 0.5 vol% and 1 vol% the increase of the moduli clearly starts at lower fields in the case of the rod-based suspensions.

(III) At high magnetic fields, the structuration is fully achieved and particle arrangement prevents plate motion. This is manifested by constant moduli.

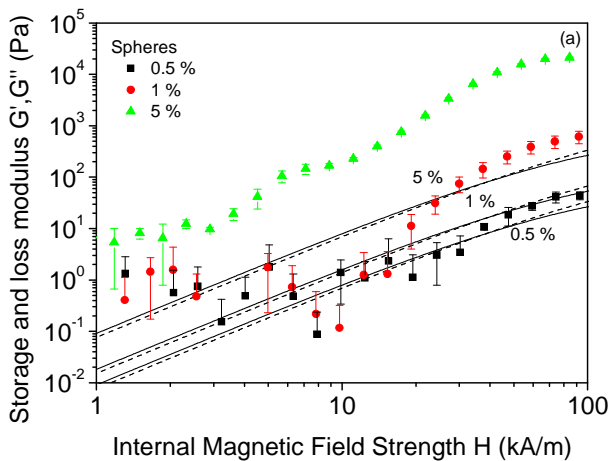
These results were further corroborated from rheomicroscope observations. In Figure 5 we show snapshots corresponding to the typical structures observed in 1 vol% magnetorheological fluids at different external magnetic fields during the magnetosweep test described above using the microscope. For comparison, photographs corresponding to sphere and rod based MR fluids are shown. At low magnetic fields aggregates do not exist or they are loose enough for a dark image to be obtained. However, upon increasing the magnetic field thick aggregates appear. Interestingly, in the case of sphere-based MR fluids a critical magnetic field for the formation of the thick aggregates exists around 10 kA/m,



whereas rod-based MR fluids do not show any critical field in the range investigated, only a slight column width decrease is observed as the magnetic field increases. The fact that the aggregates of the rod-based fluids are visible in the microscope at lower fields is a sign of an earlier structuration, and must be related to the increase of the dynamic moduli that was also observed at lower fields (see Figure 4).

In Figure 6(a) we show the results corresponding to low field responses of the sphere-based MR fluids. As observed, theoretical models, Eq.(1) and Eq.(2), satisfactorily predict a quadratic field storage modulus dependence at low particle volume fractions. However, models significantly underestimate experimental results for particle volume fractions larger than 0.5 vol%. This is expected since models assume single width particle chains and this is not the kind of structure observed at such concentrations, cf. Figure 2(c) and Figure 5. Also, other short-range interactions seem to have relatively large contributions to the moduli. The low magnetic field region has been largely investigated in the literature. However, particle volume fraction dependence varies between different authors. A detailed study by Claracq et al.²⁵ found a 1.65 ± 0.50 power law exponent for the dynamic moduli versus particle volume fraction dependence in carbonyl iron based MR fluids. Unfortunately, they did not report on the three volume fractions used for the fitting. It is important to remark that lower particle contents are not accessible with our rheometer due to limited torque resolution. Including multipolar contributions to the MR response would result in a better agreement with experimental data as reported by Klingenberg²⁶ (in the case of yield stress) and de Vicente et al.¹⁹ (in the case of storage modulus).

In Figure 6(b) we present medium field (30 kA/m) storage modulus as a function of particle volume fraction for the two systems investigated. In all cases, the storage modulus for microrods is larger than the storage modulus of spheres. This is expected from the smaller critical field strength associated to the sudden increase in storage moduli (see Table I) which results from a lower demagnetization energy for axisymmetric particles oriented with the field when compared to their spherical counterparts. Such a lower N_D results in a larger internal magnetic field in the rodlike particle and hence in a larger magnetic moment, a stronger interparticle magnetostatic interaction and enhanced field induced torque.



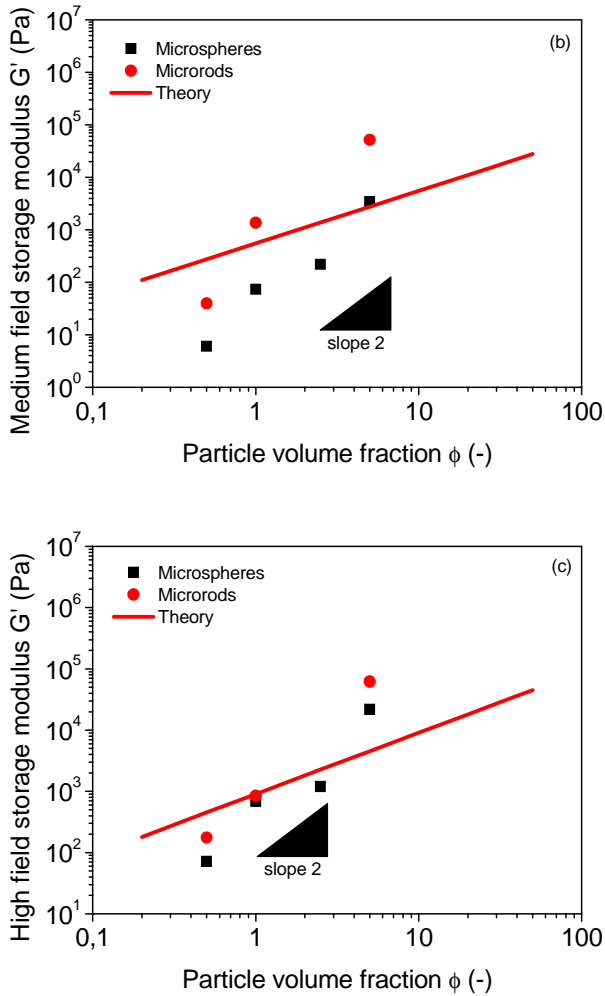


FIG. 6. Particle volume fraction, ϕ , dependence of small amplitude oscillatory shear moduli. a) Low field response and quadratic field theories for sphere-based MR fluids. Solid lines correspond to Eq.(1). Dashed lines correspond to Eq.(2). b) Medium field

response and Ginder's theoretical predictions -solid line, Eq.(3)- for sphere-based MR fluids. External magnetic field 30 kA/m . c) High field response and Ginder's theoretical predictions , solid line, Eq.(4), for sphere-based MR fluids.

It is worth to remark that this finding may be of interest in the case of low field MR applications. Observing the results for the critical field in Table I it is important to make some comments on the $5 \text{ vol}\%$ results. The critical field of 3.1 kA/m for microrod based MR fluids at $5 \text{ vol}\%$ is actually greater than that of the sphere based fluid at the same concentration. This is the opposite of what was observed for lower volume fractions, and a consequence of the much larger off-field storage modulus for that particle concentration.

TABLE I. Critical field strength (kA/m) associated to the increase in storage modulus.

<i>vol</i> %	Microspheres	Microrods
0.5	24.4	1.06
1	13.6	2.0
5	2.8	3.1

The solid line in Figure 6(b) corresponds to the predictions of Eq.(3) for spheres. Even though this model predicts the order of magnitude correctly, it fails at explaining the experimental dependence of G' on particle volume fraction. By linear fitting experimental data of sphere based MR fluids, a slope of 2.5 ± 0.3 is obtained. Power law exponents for spheres and rods at medium and saturating fields are shown in Table II.



Measurements of the storage modulus for spheres and microrods at saturation are shown in Figure 6(c). Smaller differences are now appreciated between rods and spheres as expected because the storage modulus in this region mainly depends on squared saturation magnetization (see Eq.(4)). In agreement with results presented in Figure 6(b), a slope larger than one for G' vs. ϕ dependence is observed both for sphere and rod-based fluids (see Table II). This is in contrast to analytical models that predict a storage modulus proportional to particle concentration and to the square of the saturation magnetization of the particles. Even though the correct order of magnitude is captured, the particle content dependence requires further investigations, especially at larger concentrations.

Even though theories intended to model the behaviour at saturation (Eq.(3) and (4)) typically predict yield stresses that compare quite favourably with the experimental data of carbonyl iron at 50 vol%^{27,28}, the theoretical storage modulus is greatly exceeded by the experimental results. In this work we show that the particle volume fraction effect is not trivial. The discrepancies are likely due to the fact that the models presented here treat only the stresses resulting from magnetic interactions and not those associated with other interactions such as van der Waals, steric, etc, which are expected to come into play at large particle contents specially for nonisotropic magnetic particles where entropic repulsion is significant at low fields. All theories considered in this manuscript assume that magnetic interaction forces are always more important than other forces that may also be present in a magnetorheological fluid. As a consequence, only magnetic contributions to the stress are considered. However, conventional magnetorheological suspensions usually contain a very large amount of particles that under the presence of a magnetic field eventually

come into very close contact. At very short interparticle distances, other forces apart from magnetostatic ones may be relevant and should be considered in a more detailed analysis. Of outstanding interest is van der Waals attraction which could lead to the formation of much stronger structures than those expected from a simple analysis only including magnetic forces.

TABLE II. Power law exponent, α , according to $G' \propto \phi^\alpha$ in sphere and rod based MR fluids at medium (30 kA/m) and saturating fields.

	Medium fields	Large fields
Microspheres	2.5 ± 0.3	2.2 ± 0.4
Microrods	2.9 ± 0.6	2.6 ± 0.1

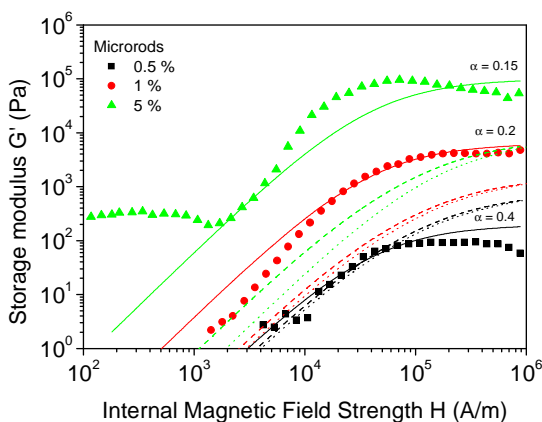


FIG. 7. Comparison between experimental results and theoretical predictions for the storage modulus, G' , of rod-based MR fluids. Solid lines represent microrod model predictions at $N_D = 0.015$ and different α values (Eq.(10)). Dotted lines correspond to



full Kuzhir model predictions (Eq.(14)) with $b_0 = 2500nm$ and $\xi = 0$. Dashed lines correspond to approximated Kuzhir model predictions (Eq.(15)) $\mu_{rod,i} = 15$, $M_s = 490$ kA/m and $\theta \approx 0^\circ$.

In Figure 7 we present results corresponding to the microrod based models described in section III B. On the one hand, the proposed model , Eq.(10), satisfactorily captures both the medium field increase in storage modulus and the plateau at saturation through a magnetic field-dependent permeability. Best fit α values increase with decreasing particle content as expected from larger interparticle distances. On the other hand, column structure models (dashed lines) underpredict experimental results at large particle contents. This finding is in agreement with Kuzhir et al.²³ results on yield stress measurements. To further understand the effect of interparticle distance in the proposed model, dynamic yield stress measurements were carried out on sphere- and microrod-based fluids. Figure 8 includes the most relevant results for suspensions at three different volume fractions. As observed, the proposed model satisfactorily explains dynamic yield stresses at the lowest fields investigated for a fixed $\alpha = 0.3$.

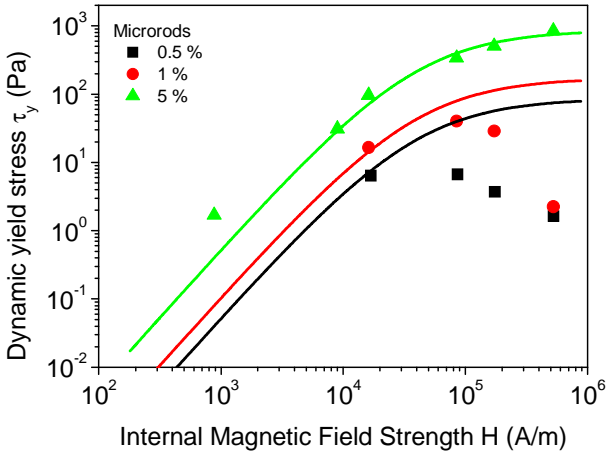


FIG. 8. Dynamic yield stress, τ_y , as a function of the internal magnetic field, H , for microrod based MR fluids. Solid lines represent the predictions of the microrod based model (Eq.(13)) with $\alpha = 0.34$ for the three concentrations investigated. The decrease at high fields corresponding to 0.5 and 1 vol% suspensions is ascribed to the sedimentation and/or migration of the largest aggregates.

This is consistent with the fact that interparticle distances, right at the moment in which aggregates break, are expected to be the same for any particle concentration in the suspension. As expected, dynamic yield stresses at large fields reach a plateau at 5 vol%. The observed decrease at 0.5 and 1 vol% concentration is possibly due to sedimentation of the larger aggregates even though the rheometer is rotating²⁹. Another possible explanation would be the particle/aggregate migration towards regions with large magnetic field gradients. Due to the design of the magnetorheological cell, the magnetic field is not homogeneous everywhere between the plates. Low particle density regions



are expected just at the center and at the rim. Actually, this magnetic field gradient has proved recently to be useful for confining ferrofluids in a simulated face seal³⁰.

V. CONCLUSIONS

In summary, rod-based MR fluids show an enhanced MR performance under oscillatory shear. Firstly, a lower magnetic field strength is needed for the structuration of the colloid. Secondly, once the saturation is fully achieved, a larger elastic modulus is observed in rod-based suspensions as compared to sphere-based MR fluids. Existing sphere-based models satisfactorily capture the order of magnitude of storage modulus but fail to predict the particle volume fraction dependence. By concentrating the microrod-based MR fluids, a larger saturation storage modulus is obtained, but also a larger value for the off-field storage modulus is observed. Taking the off-field modulus as the baseline, and for relatively low solid contents (0.5 vol% and 1 vol%), the critical field for structuration was significantly smaller for rod-based suspensions than for their sphere-based counterparts. At larger concentrations (5 vol%) this behavior reverses, which seems to be related to the larger off-field storage modulus at that concentration. In spite of the fact that magnetorheological models reported in the literature neglect loss modulus values, these are demonstrated to strongly depend on magnetic field strength. The microscopic rod-based model proposed satisfactorily captures the dependence of G' vs. the internal magnetic with one fitting parameter. This model was satisfactorily tested with steady state measurements.



ACKNOWLEDGEMENTS

This work was supported by MEC MAT 2006-13646-C03-03 and MEC MAT 2009-14234-C03-03 projects (Spain), by the European Regional Development Fund (ERDF) and by Junta de Andalucía P07-FQM-02496, P07-FQM-03099 and P07-FQM-02517 projects (Spain).



APPENDIX A. Calculation of the internal magnetic field in magneto-rheological suspensions

In general, the internal magnetic field depends on the external magnetic field, H_0 , and magnetic permeability of the suspension, $\mu(H)$ through:

$$H = \frac{H_0}{\mu(H)} \quad (\text{A.1})$$

Considering a mean field Maxwell-Garnett theory, the permeability of the suspension can be written as a function of the particle volume fraction, ϕ , and the magnetic contrast factor, β :

$$\begin{aligned} \mu(H) &= \frac{1 + 2\phi\beta}{1 - \phi\beta} \quad ; \\ \beta &= \frac{\mu_{sph}(H_{sph}) - 1}{\mu_{sph}(H_{sph}) + 2} \end{aligned} \quad (\text{A.2})$$

where the magnetic field strength in the sphere is written as:

$$H_{sph} = \frac{3\mu(H)H}{\mu_{sph}(H_{sph}) + 2\mu(H)} \quad (\text{A.3})$$

being, $\mu_{sph}(H_{sph}) = 1 + \frac{\mu_{sph,i}}{1 + \frac{\mu_{sph,i}}{M_s} H_{sph}}$ with $\mu_{sph,i}$ the initial magnetic

permeability of the spheres. In order to obtain the internal field in a suspension of spheres, Eq.(A.1-A.3) are simultaneously solved by numerical iteration.

In the case of magnetic microrod suspensions, the internal magnetic field is written as:

$$H = \frac{H_0}{\mu_{\parallel} \cos^2 \theta + \mu_{\perp} \sin^2 \theta} \quad (\text{A.4})$$

where θ is the strain angle, and $\mu_{\parallel} = 1 + \phi(\mu_{rod} - 1)$ and $\mu_{\perp} = \frac{1 + \phi \frac{\mu_{rod} - 1}{\mu_{rod} + 1}}{1 - \phi \frac{\mu_{rod} - 1}{\mu_{rod} + 1}}$

are the permeability components along the major and minor microrod axes.

Here,

$$\mu_{rod}(H_{rod}) = 1 + \frac{\mu_{rod,i}}{1 + \frac{\mu_{rod,i}}{M_s} H_{rod}} \quad (\text{A.5})$$

where $\mu_{rod,i}$ is the initial magnetic permeability of the microrods, and the magnetic field strength in the rod is given by:

$$H_{rod} = H \sqrt{\cos^2 \theta + \sin^2 \theta \left(\frac{1 + \frac{\mu_{\perp} - 1}{2}}{1 + \frac{\mu_{rod} - 1}{2}} \right)^2} \quad (\text{A.6})$$

Eq.(A.4-A.6) are simultaneously solved by numerical iteration to obtain the internal field in the magnetic microrod suspension.


REFERENCES

- ¹G. Bossis, O. Volkova, S. Lacis, and A. Meunier, Magnetorheology: fluids, structure and rheology, in: O. Odenbach (Ed.), Ferrofluids, Springer, Germany, 2002, pp 202-230.
- ²J. de Vicente, M.T. López-López, J.D.G. Durán, and F. González-Caballero, Rheol. Acta **44**, 94 (2004).
- ³R.C. Kanu, and M.T. Shaw, Int. J. Mod. Phys. B **10**, 2925 (1996).
- ⁴R.C. Kanu, and M.T. Shaw, J. Rheol. **42**, 657 (1998).
- ⁵Q. Yabing, and W. Wen, J. Phys. D: Appl. Phys. **35**, 2231 (2002).
- ⁶T. Watanabe, M. Aoshima, and A. Satoh, J. Colloid Interface Sci. **302**, 347 (2006).
- ⁷K. Tsuda, Y. Takeda, H. Ogura, and Y. Otsubo, Colloids Surf., A **299**, 262 (2007).
- ⁸J. Yin, X. Zhao, X. Xia, L. Xiang, and Y. Qiao, Polymer **49**, 4413 (2008).
- ⁹R.C. Bell, E.D. Miller, J.O. Karli, A.N. vavreck, and D.T. Zimmerman, Int. J. Mod. Phys. B **21**, 5018 (2007).
- ¹⁰R.C. Bell, J.O. Karli, A.N. vavreck, D.T. Zimmerman, G.T. Ngatu, and N.M. Wereley, Smart Mater. Struct. **17**, 015028 (2008).

- ¹¹G.T. Ngatu, N.M. Wereley, J.O. Karli, and R.C. Bell, *Smart Mater. Struct.* **17**, 045022 (2008).
- ¹²F. Vereda, J. de Vicente, and R. Hidalgo-Álvarez, *Langmuir* **23**, 3581 (2007).
- ¹³T. Sugimoto, and E. Matijević, *J. Colloid Interface Sci.* **74**, 227 (1980).
- ¹⁴F. Vereda, J. de Vicente, and R. Hidalgo-Álvarez, *Colloids Surf., A* **319**, 122 (2008).
- ¹⁵J. Laeuger, K. Wollny, H. Stettin, and S. Huck, A new device for the full rheological characterization of magneto-rheological fluids, in: *Proceedings of the ERMR2004, Beijing, China, 2005*, pp. 370–376.
- ¹⁶T.G. Mezger, *The rheology handbook*, 2nd edition, Vincentz, Coatings compendia, 2006.
- ¹⁷G. Bossis, P. Khuzir, S. Lacis, and O. Volkova, *J. Magn. Mater.* **258**, 456 (2003).
- ¹⁸J.E. Martin, and R.A. Anderson, *J. Chem. Phys.* **104**, 4814 (1996).
- ¹⁹J. de Vicente, M.T. López-López, J.D.G. Durán, and G. Bossis, *J. Colloid Interface Sci.* **282**, 193 (2005).
- ²⁰J.M. Ginder, L.C. Davis, and L.D. Elie, *Int. J. Mod. Phys. B* **10**, 3293 (1996).
- ²¹S.S. Dukhin, *Dielectric properties of disperse systems*, in: E. Matijević (Ed.), *Surface and Colloid Science*, vol 3, Wiley-Interscience, 1971, New York.
- ²²D.C. Jiles, *Introduction to magnetism and magnetic materials*, Chapman & Hall, London, 1991.
- ²³P. Kuzhir, M.T. López-López, and G. Bossis, *J. Rheol.* **53**, 127 (2009).
- ²⁴B.J. de Gans, N.J. Duijn, D. van den Ende, and J. Mellema, *J. Chem. Phys.* **113**, 2032 (2000).
- ²⁵J. Claracq, J. Sarrazin, and J.P. Montfort, *Rheol. Acta* **43**, 38 (2004).
- ²⁶D.J. Klingenberg, PhD Thesis, University of Illinois, Urbana-Champaign, 1988.
- ²⁷A.J. Parziale, and P.D. Tilton, *AIEE Trans* **69**, 150 (1950).



- ²⁸J.M. Ginder, *Encyclopedia of Applied Physics* **16**, 487 (1996).
- ²⁹D.J. Klingenberg, J.C. Ulicny, and A. Smith, *Appl. Phys. Lett.* **86**, 104101 (2005).
- ³⁰E. Andablo-Reyes, J. de Vicente, and R. Hidalgo-Álvarez, Thin film rheology of ferrofluids, in: F. Martínez-López, J. de Vicente, A. Martín-Rodríguez and M.A. Rodríguez-Valverde (Eds.), *III Reunión Ibérica de Coloides e Interfases (RICI)*, and *VIII Reunión del Grupo especializado de Coloides e Interfases (GECI)*, University of Granada, 2009, Granada (Spain).



Title of the manuscript

Effect of particle shape in magnetorheology

Authors

Juan de Vicente¹, Fernando Vereda¹, Juan Pablo Segovia-Gutiérrez¹, María del Puerto Morales², Roque Hidalgo-Álvarez¹

Affiliation

¹ Departamento de Física Aplicada, Facultad de Ciencias, Universidad de Granada, Granada E-18071, Spain

² Instituto de Ciencia de Materiales de Madrid, CSIC, C) Sor Juana Inés de la Cruz 3, 28049 Cantoblanco, Madrid, Spain

Published

Journal of Rheology, **54(6)**, 1337-1362 (2010)

**Abstract**

Magnetorheological (MR) properties were investigated for sphere, plate and rod-like iron particles in suspension under the presence of magnetic fields to ascertain the effect of particle shape in MR performance. A novel two-step synthesis route for micrometer sized iron particles with different morphologies is described in detail. Small-amplitude dynamic oscillatory and steady shear flow measurements were carried out in the presence of external magnetic fields. Finite element method calculations were performed to explain the effect of particle shape in the magnetic field induced yield stress. Compared to their sphere and plate counterparts, rod-like particle based MR fluids present a larger storage modulus and yield stress. The effect of particle shape is found to be negligible at large particle content and/or magnetic field strengths.

I. INTRODUCTION

Magneto-rheological (MR) fluids are typically prepared by dispersing magnetizable spherical microparticles in a non magnetic medium. Because of the large -magnetic multidomain- particle size, structuration is achieved in the presence of an external field. This structure is able to support shear stresses, presenting large field dependent viscoelastic moduli and a yield stress¹⁻³. Up to now, most of the studies reported in the literature deal mainly with spherical particles and a wide range of synthesis routes exist to prepare them within the ideal size range of $100\text{ nm} - 10\ \mu\text{m}$ diameter⁴. Increasing the size of the particles typically increases the MR response but the particles tend to settle rapidly. Smaller particles settle more slowly but Brownian motion hinders magnetic field induced structuration, eventually resulting in a superparamagnetic colloidal ferrofluid when particle size approaches 10 nm ⁵.

Many attempts have been made in the past to improve the MR response in the mesoscale particle size, especially by addition of thickeners and stabilisers that may promote stronger and more kinetically stable structures⁶⁻⁸, and by incorporation of magnetic additives that may form physical networks and/or bridge the gaps between particles increasing the magnetic permeability of the composites⁹⁻¹¹. Since the magnetic particles dispersed in a conventional MR fluid come into close contact under the application of magnetic fields, particle shape is reasonably expected to determine the field induced structure at rest and also the aggregates break-up, friction and dissipation mechanisms under shear. Furthermore, a greater induced magnetic moment is expected for non-spherical particles due to their smaller demagnetization factor in their long direction.



The effect of particle shape on the rheological performance of field-responsive fluids has been explored in the past. Kanu and Shaw (1996, 1998) investigated the effect of particle shape in electrorheological (ER) fluids in an attempt to improve the rheological properties of the fluid^{12,13}. They showed that by using poly(p-phenylene-2,6-benzobisthiazole) rod-like particles it is possible to enhance the dielectric interaction between the particles as well as their mechanical strength. Qi and Wen (2002) presented experimental results on the effect of particle shape on dried and water activated ER fluids under both DC and AC fields¹⁴. Their results for water-activated fluids were explained in terms of surface effects; a lower ER effect was observed for anisotropic particles in contrast to the findings by Kanu and Shaw. Satoh (2001) and Watanabe *et al.* (2006) computed the rheological properties and the orientational distributions of particles of a highly dilute colloidal dispersion composed of ferromagnetic spherocylinders under a simple shear flow^{15,16}. Chin *et al.* (2001) added Co- γ -Fe₂O₃ and CrO₂ magnetic needle-like particles to the formulation of conventional MR fluids, which provided improved stability against rapid sedimentation⁷. Furthermore, additive-containing MR suspensions exhibited a larger yield stress, especially at the largest magnetic fields investigated (0.64 kOe). By addition of titanate whiskers in electric field responsive fluids, Yin and Zhao (2006) observed a yield stress increase of two orders of magnitude¹⁷. Tsuda *et al.* (2007) studied the yield stress *versus* electric field dependence for spheres and whisker suspensions¹⁸. For the later, the yield stress was clearly larger. The slope of the yield stress *versus* electric field curve decreased from 2 to 1.3 from spheres to whiskers. Yin *et al.* (2008) prepared a nano-fibrous polyaniline electrorheological fluid by means of a modified oxidative polymerization in acid aqueous solution¹⁹. The resulting fluid possessed significantly improved stability and stronger ER effect compared to spherical

polyaniline ER fluids. López-López *et al.* (2009) used polyol techniques to prepare 60 μm long cobalt microfibers. Steady shear flow tests suggested an enhanced field induced effect for suspensions of magnetic fibers²⁰.

A generalised problem that arises from previous works on non-spherical magnetic particles is the difficulty to ascertain the effect of particle shape in isolation from other parameters. This difficulty arises because preparation routes normally differ for each material under study, which results in very broad size distributions and in magnetic particles with different chemical composition and hence magnetic characteristics. In many cases the typical particle size also changes, making it even more difficult to interpret the results because the effect of particle size is not well understood either²¹.

Recently, some studies have appeared regarding well defined non-spherical magnetic particles in the mesoscale range, in particular for micro-wires and micro-rods^{22,23}. Bell *et al.* (2008) used template-based electrodeposition using anodized alumina membranes to fabricate iron microwires with a diameter of 260 nm and lengths of 5.4 μm and 7.6 μm . By precipitation and magnetic field-induced self assembly under constant uniaxial fields, de Vicente *et al.* (2009) prepared magnetite rod-like particles with average diameter and length of 560 nm and 6.9 μm respectively. These works showed that MR performance is significantly improved for elongated magnetic particles under small-amplitude shear and simple steady shear flows, hence suggesting that particle shape strongly affects the structuration under an external field.

To the best our knowledge, a study on the effect of particle shape in MR performance, a study in which only shape changes while the rest of the



parameters are kept practically constant, is missing in the literature. Very scarce and ill-connected information exists in the literature and is mostly concerning sphere, rod, wires and fiber-like magnetic particles. As far as we know, magnetic plate-like particles based MR fluids have never been prepared nor investigated yet from a rheological perspective. The preparation of one- two- and three-dimensional microparticles of the same magnetic material, having well defined rod-like, plate-like and sphere-like morphologies may be helpful, from a fundamental and practical point of view, for the design of advanced MR fluids with a better performance.

In this work we describe a simple procedure to prepare micron-sized spheres, plates and rods of the same material and hence very similar intrinsic magnetic responses. The material chosen is iron mainly because iron-based MR fluids are extensively studied in MR technology²⁴ and a very large MR response is observed due to its large low-field magnetic permeability and saturation magnetization compared to ferrites²³ and cobalt-based²⁰ MR fluids²⁵. Furthermore, the chemistry of pure iron and that of iron oxides are both very well known and many methods exist for iron particle functionalization and surface treatment²⁶.

This manuscript is structured as follows: firstly we describe the experimental section, which includes the synthesis of iron microparticles -having spherical, plate-like and rod-like shape-, the preparation of MR fluids including these particles, the rheological essays carried out for their mechanical characterization, and finally their magnetic properties. Next we show preliminary results of finite element method calculations of model magnetic structures with non spherical shape. In the following section we report on the

characterization of the particles and the mechanical study of the suspensions prepared. Results of small-amplitude oscillatory and simple steady shear flow tests, together with yield stress measurements, are presented.

II. EXPERIMENTAL

A. Synthesis and characterization of colloidal sphere-, plate- and rod-like magnetic particles

A.1. Magnetite and hematite precursors

Magnetite spheres and rods were fabricated following a procedure previously described in the literature^{23,27}. The chemistry involved in the fabrication of both types of particles is the same²⁸, and relies in the precipitation of $\text{Fe}(\text{OH})_2$ upon the mixing of $\text{FeSO}_4 \cdot 7\text{H}_2\text{O}$ (reagent grade, Sigma-Aldrich, Germany) with KOH (chemically pure, Panreac, Spain) in aqueous solution, and in the curing of that precipitate at 90°C in the presence of KNO_3 (reagent grade, Scharlau, Spain). The concentrations of reactants were adjusted to produce **0.025 moles** of $\text{Fe}(\text{OH})_2$ per liter of the mixture, an excess concentration of $\text{Fe}^{2+}_{(\text{aq})}$ of **0.005 M** and a concentration of KNO_3 of **0.20 M**. Rod-like particles were obtained by curing the reactants in the presence of a DC magnetic field of approximately **400 mT**, whereas the absence of this field during the curing process resulted in spherical particles. After the curing process, the black magnetic precipitate obtained in both cases was washed with doubly-distilled water. A permanent magnet was used to keep the precipitate while the supernatant was discarded. The particles were finally stored in ethanol.

Hematite plates were prepared according to the process described by Sugimoto and coworkers²⁹. Basically, equal volumes of solutions of $\text{FeCl}_3 \cdot 6\text{H}_2\text{O}$ (2 M)



(Extra pure, Scharlau, Spain) and NaOH (8 M) (analysis grade, Panreac, Spain), were mixed and stirred with a magnet for 10 minutes. A volume of 12 mL of that mixture was then placed in a teflon-lined autoclave with a total capacity of approximately 24 mL. The autoclave was placed in an oven that had been previously heated to 180 °C, and the mixture was maintained at that temperature for 2 hours. After that time the autoclave was left to cool at ambient temperature. The resulting suspension had a reddish color. Particles were washed by allowing them to settle and pipetting the supernatant. This process was repeated 4 times, and particles were finally stored in ethanol. Powder samples of the magnetite and hematite precursors were obtained by drying at 40 °C aliquots of the corresponding suspensions in ethanol.

A.2. Iron particles

The sphere, plate and rod-like precursors were then reduced to metal iron by exposing them to a hydrogen atmosphere under optimum conditions of temperature, time and hydrogen^{30,31}. First the sample was heated at 400 °C during two hours under nitrogen flow to eliminate any water. Then, reduction of the iron oxide particles was carried out at 400 °C during 4 hours under a hydrogen flow of 40 Lh⁻¹. Once the sample had cooled, nitrogen gas wetted with ethanol was passed through the sample for 5 hours in order to passivate the surface. Stable iron particles coated with an oxide layer were finally obtained without the addition of any extra element.

A.3. Particle characterization

Electron microscopy was used to study the morphology, size and size distribution of both the precursors and the final iron particles. Samples were prepared by drying droplets of the suspensions in ethanol on top of a glass slide, and coating the resulting powder with a thin (ca. 20 nm) graphite coating. These samples were examined in a LEO Gemini 1530 field emission scanning electron microscope in a secondary electron (SE) mode.

The phases present in the samples were identified by powder X-ray diffraction (XRD) measurements using a Philips 1710 diffractometer and the Cu K α radiation. X-ray patterns were collected between $2\theta = 5^\circ$ and $2\theta = 70^\circ$.

The magnetic characterization of the powders was carried out in a vibrating sample magnetometer (MLVSM9 MagLab 9T, Oxford Instruments). Coercive field and saturation magnetization values were obtained from the hysteresis loops recorded at room temperature. Saturation magnetization values were evaluated by extrapolating to infinite magnetic field the experimental results obtained in the high field range where the magnetization linearly decreases with $1/H$.

B. Preparation of MR fluids

The preparation of the suspensions consisted of the following steps: (i) the magnetic powder (iron or magnetite with the appropriate particle morphology) and silicone oil (Sigma-Aldrich, 20 mPa·s) were mixed in a polyethylene container; (ii) the mixture was stirred first by hand, and then in an ultrasonic



bath; (iii) step (ii) was repeated several times, and finally, the sample was immersed in a Branson sonifier (model 450) to ensure the required final homogeneity. The gradual homogenization of the samples was confirmed by the disappearance of the aggregates initially observed in the container bottom.

C. Magnetorheological characterization

Dynamic oscillatory properties of the MR-fluids were measured at 25 °C using a parallel-plate configuration in a MCR 501 Anton Paar magneto-rheometer. The diameter of the plates was 20 mm and the plate separation was fixed at 300 μm . A DC magnetic field was applied normal to the velocity gradient and vorticity vectors. Firstly, the viscoelastic linear region was determined. Storage and loss moduli were measured as a function of strain at a frequency $f = 1 \text{ Hz}$, in the presence of a magnetic field. Then, magnetosweeps were carried out at a strain amplitude $\gamma_0 = 0.003 \%$ (well within the viscoelastic linear region in all cases) and a frequency $f = 1 \text{ Hz}$. The experimental procedure can be summarized as follows: (i) precondition at a constant shear rate $\dot{\gamma} = 200 \text{ s}^{-1}$ during 30 seconds, (ii) the suspension was left to equilibrate for 1 minute with the magnetorheometer's magnetic field off, (iii) constant dynamic-mechanical shear conditions were preset (both frequency and amplitude are kept constant) and the magnetic field was gradually increased from 185 A/m to 884 kA/m (logarithmically increased at a rate of 10 points per decade). In all cases experiments were repeated at least three times with fresh new samples.

Steady shear flow tests were carried out at 25 °C using the same measuring device mentioned above. The experimental procedure is summarized as follows:

(i) precondition at a constant shear rate $\dot{\gamma} = 200 \text{ s}^{-1}$ during 30 seconds, (ii) the suspension was left to equilibrate for 1 minute in the presence of a magnetic field, (iii) shear stress was logarithmically increased from 0.1 Pa at a rate of 10 points per decade, (iv) finally shear stress was decreased from the maximum value to zero in order to ascertain any thixotropic behavior. Again, experiments were repeated at least three times with fresh new samples. The yield stress in the MR fluids was determined using two different approaches. The first one consists in the determination of the so-called static yield stress as the stress corresponding to the onset of flow in double logarithmic representations of stress *versus* shear. A second method to determine the yield stress is to fit the Bingham plastic equation to a rheogram in lin-lin representation. The latter procedure results in the so-called Bingham yield stress. Even though there are other more appropriate methods to measure the yield stress, these two approaches are frequently used in the MR literature^{32,50,20}.

D. Magnetic properties of the MR fluids

The effect of particle shape in the magnetic hysteresis curves of the suspensions was ascertained using a Quantum Design (San Diego, CA) MPMS-XL 5.0 Tesla magnetometer. The initial magnetization of the sample was measured from $H = 0$ to $H = 4000 \text{ kA/m}$. The external magnetic field was subsequently swept from $+4000$ to -4000 kA/m and then back to $+4000 \text{ kA/m}$. Measurements were carried out at room temperature.

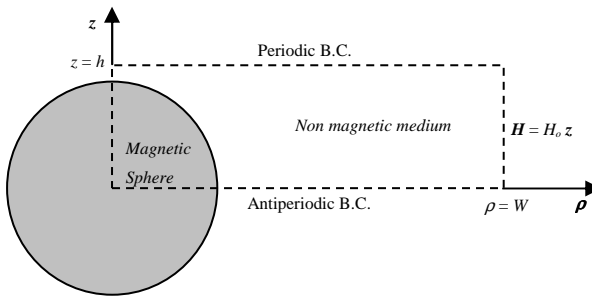


FIG. 1 Schematic representation of the axisymmetric problem solved using FEMM. The computational area is outlined with a dashed line. The magnetic character of the particles was introduced with a $B = B(H)$ relationship given by the Fröhlich-Kennelly equation³⁴, with relative initial magnetic permeability of 40 and saturation magnetization of 1550 kA/m. The density of iron is assumed to be $\sim 7.8 \text{ g/cm}^3$.

III. FINITE ELEMENT METHOD CALCULATIONS

The Finite Element Method Magnetics (FEMM) software [D. C. Meeker, Finite Element Method Magnetics, Version 4.2 (15 Jul 2009 Build), <http://www.femm.info>] was employed to calculate the magnetostatic force acting on a given microparticle as a function of interparticle gap distance, both for spheres and rod-like particles, and for various field strengths. No calculations were carried out for the plates because in the case of three-dimensional problems the software is limited to axial symmetry. A general configuration solved using FEMM consisted of an infinite chain of particles exposed to a uniform magnetic field. Particle geometry was chosen to resemble our iron particles: we considered chains of spheres of $0.7 \mu\text{m}$ of diameter and chains of spherocylinders of the same diameter and an aspect ratio of 8 (cf Section IV.A).

The magnetic character of the particles was introduced with a $B=B(H)$ relationship given by the Frölich-Kennelly equation³⁴, with relative initial magnetic permeability of 40 and saturation magnetization of 1550 kA/m (see Section IV.C.1). This Frölich-Kennelly equation was multiplied by factor of 0.47 to correct for particle porosity.

The problem solved using FEMM is graphically depicted in Figure 1 for the case of the spherical particles. The infinite chain was created by applying periodic boundary conditions on the top boundary and antiperiodic boundary conditions in the bottom boundary of the computational region, which is depicted with a dashed line. Because of the axial symmetry of the problem, the computational region is a cylinder with a radius W and a height h . A uniform field H_0 along the z axis was imposed by fixing its value on the outer surface ($\rho=W$) and moving this surface far enough from the particle, i.e. moving it to a point from which any further removal of this surface has no effect on the calculated fields near the particle.

The force acting on a given particle due to the particles above was calculated by integrating the magnetic field strength due to the particles, $H-H_0$, on the top plane of the computational region³⁶.

$$F = \frac{\mu_0}{2} \int_0^W [H_{z=h}(\rho) - H_0] 2\pi\rho d\rho \quad (1)$$

where μ_0 is the magnetic permeability of free space.



Eq. (1) follows from the calculation of the force using the Maxwell stress tensor (\mathbf{T}) for the field due to the particles ($H - H_0$). The total force acting on a particle would be given by the evaluation of $\mathbf{n} \cdot \mathbf{T}$ over any surface that encloses the particle, where \mathbf{n} is the normal to that surface⁵.

FIG. 2 SEM photographs corresponding to A) magnetite spheres, B) hematite plates, C) magnetite rods, D) iron spheres, E) iron plates, and F) iron rods.

If $\mathbf{n} \cdot \mathbf{T}$ is evaluated over the surface of a cylinder that totally surrounds the particle, the contribution of the lateral surface of the cylinder would vanish because of the axial symmetry of the problem, whereas the contribution of the top and bottom planes would cancel each other because the net force acting on the particle is zero. The contribution of the top plane could be considered the force due to the particles above the particle of interest.

IV. RESULTS AND DISCUSSION

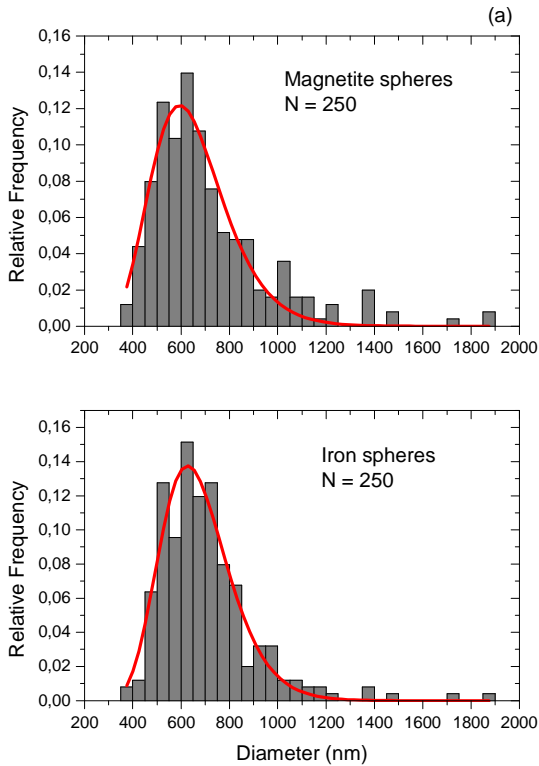
A. Particle characterization

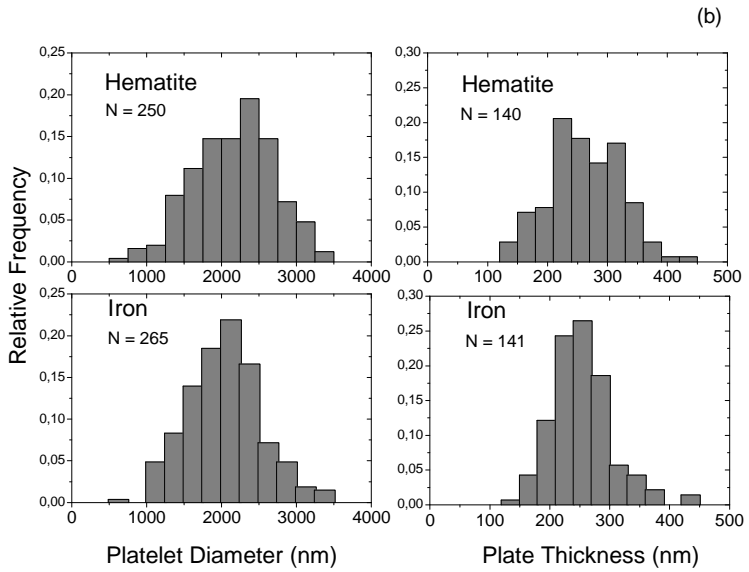
In Figure 2 we show SEM photographs corresponding to the three types of particles obtained before (A-C) and after (D-E) reduction. As can be observed, particle shape is preserved even though irregularities appear on the surface due to the porosity induced by the reduction process. This porosity must result from the loss of oxygen from the lattice of the iron oxides and the associated change of density, which increases from that of the iron oxides (ca. 5 g/cm^3) to that of metallic iron (7.8 g/cm^3). Furthermore, the histograms shown in Figure 3 reveal that the average sizes and the size distributions are also preserved during the reduction of the iron oxide particles. Interestingly, in all cases the typical particle size is of the order of a micrometer, and hence large enough for MR applications. In particular, since the magnetic dipolar moment in the particles grows with the cube of their radius and thermal Brownian motion is negligible for this range of sizes, strong magnetically-induced structures are expected.

The effect of the porosity of the iron particles on the mechanical properties of the final MR dispersions is not well understood and is beyond the scope of this article, but it should be noted that this porosity affects equally the three morphologies that we studied. Concretely, taking 5.25 g/cm^3 and 5.17 g/cm^3 as the densities of hematite ($\alpha\text{-Fe}_2\text{O}_3$) and magnetite (Fe_3O_4) respectively, it can be seen that the volumetric iron content is nearly the same: $65.8 \times 10^{-3} \text{ mol/cm}^3$ for hematite and $67 \times 10^{-3} \text{ mol/cm}^3$ for magnetite. Since the volume of the particles was preserved after their complete reduction to iron, it follows that the porosity of the iron particles is almost the same independently of whether the precursor was magnetite or hematite. The



density of our iron particles can then be estimated to be in the vicinity of 3.7 g/cm^3 , which implies a porosity (volume of voids divided by volume of particle) of approximately **0.53**.





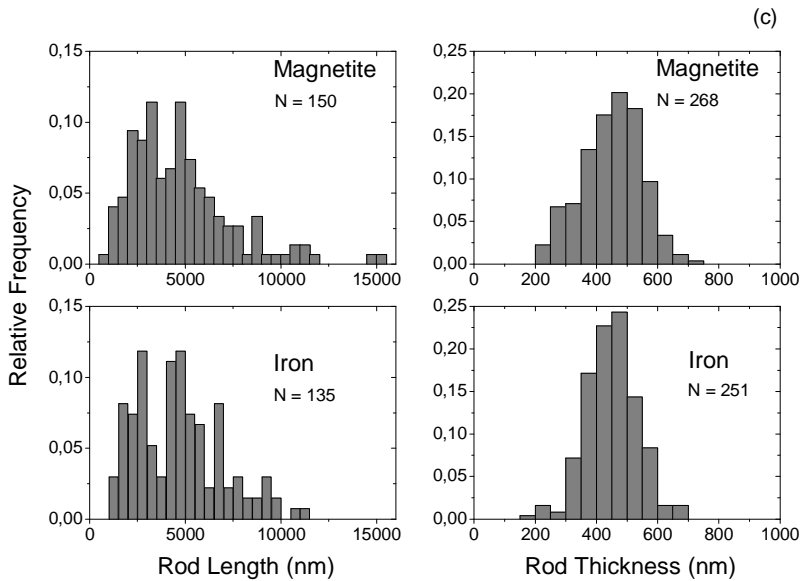


FIG. 3 Histograms corresponding to spheres, plates and rods. The solid lines represent a log-normal fit where the mean diameters of the magnetite and the iron particles are found to be $631 \pm 10 \text{ nm}$ and $658 \pm 10 \text{ nm}$ respectively. N stands for the number of particles used for the statistical analysis.

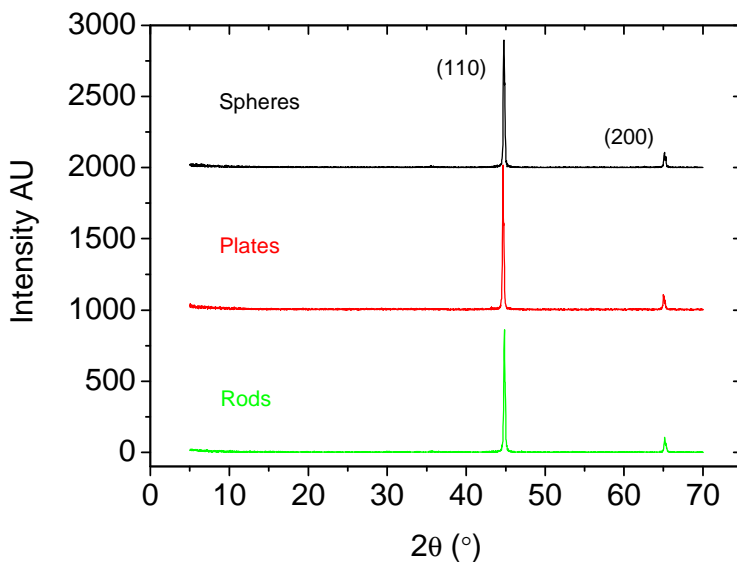


FIG. 4 X-ray diffraction spectra of the metal iron particles. Characteristic peaks for pure iron are observed for the three different particles. Lattice planes of iron are indicated in () brackets.

It should also be noted that in this work the concentration of the colloidal suspensions is given in terms of volumetric percentage of solid (iron) content. When suspensions were prepared, the mass of the solid phase was measured and the density of metallic iron was then used to calculate the volume of that phase.

X-Ray results are shown in Figure 4. As observed, the reduction process promotes the formation of iron particles. Minor peaks corresponding to iron oxides at around 35° were not observed, in contrast to smaller iron particles



prepared by a similar route or by electrodeposition²². These results suggest that particles are truly passivated by a very thin surface oxide layer that is negligible in comparison to the metal iron core. In all cases the crystallite size was much smaller than the size of the particle as an indication of the polycrystalline character of the particles.

Magnetic measurements at low temperature (Figure 5a) after cooling in the presence of a magnetic field show no hysteresis shift. Therefore, exchange anisotropy coming from the core-shell (metal/oxide) type structure was not observed, further supporting the presence of a very thin oxide surface layer.

Magnetic properties of the particles at room temperature were also ascertained. In Figure 5b we show the hysteresis cycles corresponding to the three systems investigated. As observed, a typical sigmoidal M versus H dependence is found, which is characteristic of multidomain magnetic particles. Low values of M_r/M_s (remnant magnetization over saturation magnetization) are typical of highly interacting systems and multidomain particles where magnetization rotation takes place by wall motion. A summary of the most important magnetic magnitudes extracted from Figure 5b is shown in Table I. Usually, saturation magnetization and permeability decreases when increasing the oxidation degree of the particle³³. In this case, since X-ray analysis and low temperature magnetic measurements suggest that the oxide layer is negligible; other sources are required to explain such data.

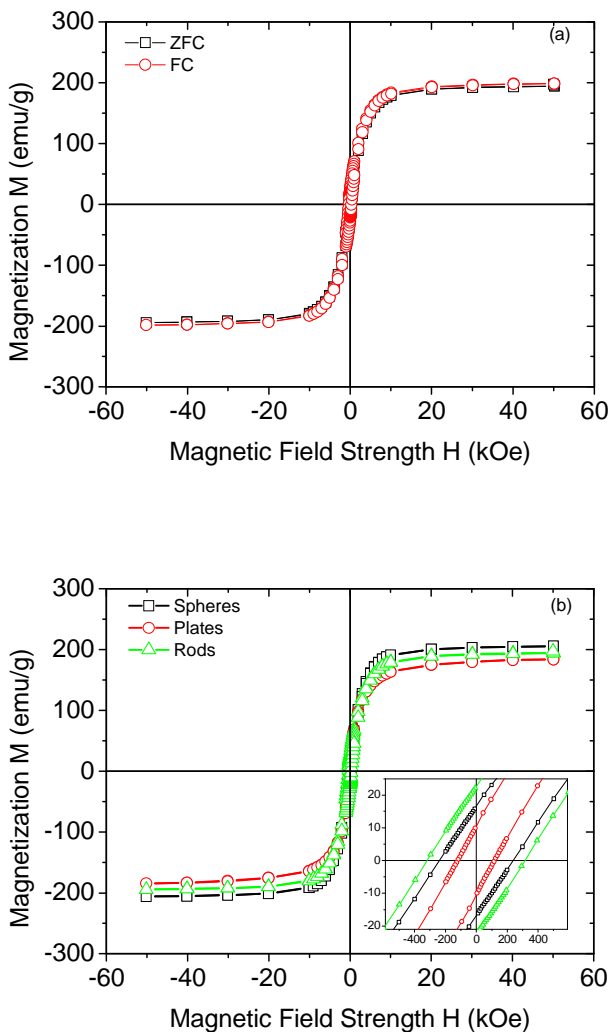


FIG. 5 a) Magnetisation curves after Zero Field Cooled and Field Cooled corresponding to rod-like particles (**19.3 mg**). Temperature: **5 K**. Magnetic field: **5 T**. b) Magnetic hysteresis curve for iron spheres, plates and rods.



It is well known that particle size strongly affects the coercive field but a reduction in saturation magnetization has only been observed for nanometer size particles³⁸. Such decrease in M_s can be explained by the presence of non magnetic impurities resulting from the synthesis. It should be noted that we employed magnetic separation during the washing process of the magnetite particles but not during the washing of the hematite particles. Finally, since the formation mechanism is different in the case of plates, structural defects may be present in this sample giving rise to a lower saturation magnetization.

TABLE I. Magnetic properties of synthesized iron particles. Assuming an iron density of 7.8 g/cm^3 , the averaged best fit curve to Fröhlich-Kennelly equation provides an initial relative magnetic permeability of **40** and saturation magnetization of **1.550 kA/m**.

	Spheres	Plates	Rods
Saturation magnetization (emu/g)	205	183	193
Coercive field (Oe)	240	120	325
Remnant magnetization (emu/g)	16.8	10.5	22.5

Coercive field changes from one sample to the other. Assuming that shape anisotropy is the driving mechanism for coercivity, particles having smaller demagnetization factor in the longest direction should present larger coercivities. According to this, the expected order for coercivity is rod > plate > sphere. However, plates present the smallest coercivities, which may further indicate that magnetization inversion occurs by domain wall motion and that differences in the coercivity exhibited by the different samples may result from small differences in the microstructure of the samples, or in the case of the

plates from the presence of non magnetic material coexisting with magnetic material. Magnetic interactions are also expected to affect the magnetic behavior of the particles, mainly the remnant magnetization and coercivity values. Those interactions are expected to be stronger for the anisometric particles.

To sum up, by means of the fabrication of the three types of iron-oxide particles and their subsequent reduction to iron, we obtained a set of particles of the same chemical composition (metallic iron), comparable typical size ($\sim 1 \mu\text{m}$), almost identical porosity and surface roughness, and very similar magnetic properties, so that the only relevant difference between them was their morphology.

B. Small-amplitude oscillatory shear magnetorheology

Viscoelastic moduli are probably the most important rheological material functions of MR fluids. From a fundamental point of view, they provide quantitative information about the magnetically induced structures in a wide range of time and frequency domains. From a practical point of view, many promising applications of MR fluids, as is the case of mechanical dampers, involve operation in dynamic conditions and thus oscillatory perturbations. As a consequence, the first tests to be described here concern small-amplitude oscillatory shearing.

Furthermore, MR response is well known to depend on a variety of parameters, the most relevant one being the magnetic field strength. Hence, we investigated

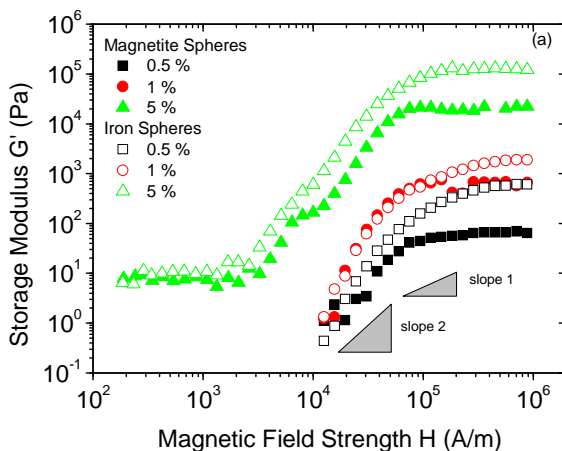


the magnetic field dependence of viscoelastic moduli for MR fluids prepared with particles having different shape.

It should be mentioned that all the rheological functions measured for our samples and reported and commented below are much smaller than those of typical commercial MR fluids. The reason for this is the very low (compared to commercial MR fluids) particle concentrations of our fluids.

B.1. Magnetite and iron spherical particles

Averaged small-amplitude oscillatory shear magnetosweep³⁹ curves at a constant strain amplitude ($\gamma_0 = 0.003\%$) and excitation frequency ($f = 1\text{ Hz}$) are presented in Figure 6a for volume fractions of 0.5 vol%, 1 vol% and 5 vol%. Three regimes are typically found when performing a magnetosweep test^{23,40}. At low fields, structures are weak and do not span between the plates.



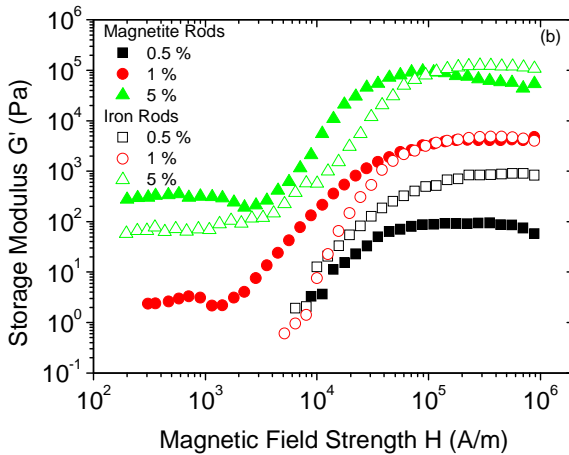


FIG. 6 Small-amplitude oscillatory shear magnetosweep curves corresponding to sphere (a) and rod-based (b) MR fluids. Particles with different magnetic properties were investigated at three different volume fractions. Due to lack of instrumental sensitivity, data below 1 Pa usually appeared scattered and as a consequence it is not shown in the figures.

As a consequence, the elasticity of the sample, if it exists, is hard to be measured. Upon increasing the magnetic field strength, the average length of the structures increases and the storage modulus rises up by more than two orders of magnitude. At large enough magnetic fields the particles magnetically saturate and the storage modulus levels off. As observed, iron-based suspensions typically show larger storage modulus than magnetite suspensions, which is expected from the larger saturation magnetization of iron. Interestingly, for the two lowest volume fractions the storage modulus starts to increase at the same magnetic field regardless of the material used. Larger



volume fractions result in an upwards shift of the curves, which is indicative of a stronger viscoelastic behavior.

Theoretical models available in the literature qualitatively explain the behavior observed. In general, a quadratic dependence with the magnetic field is observed at low field values ($G' \propto H^2$). Upon increasing the magnetic field the particles begin to saturate at the poles hence decreasing the power law exponent ($G' \propto H$)⁴¹. At very large magnetic fields particles are fully saturated and the storage modulus becomes constant. A quantitative agreement is hardly found in the literature mainly because the volume fraction dependence is not linear, in contrast with the predictions of simple width chain models. Typically, theoretical predictions overestimate experimental results at low volume fractions and underestimate experimental results at high volume fractions^{42,23}.

B.2. Magnetite and iron rod-like particles

A first insight on the effect of particle shape comes from Figure 6b. Here we show results relative to the effect of magnetic field on storage modulus for rod-like particle based MR fluids prepared with either magnetite or iron as bulk material. Curves are qualitatively similar to those shown in Figure 6a. A larger modulus is measured for iron based MR suspensions at 0.5 vol%. Interestingly, the difference between iron and magnetite particles is significantly reduced (compared to results presented in Section IV.B.1 above) due to shape anisotropy, especially at the largest volume fraction investigated. Another interesting feature is the fact that the sudden increase of storage modulus is delayed to larger fields in the case of iron-based microrods. This feature is

possibly due to a larger interparticle friction inhibiting the field-induced ordering (cf Figure 2).

B.3. Sphere, plate and rod-like iron particles

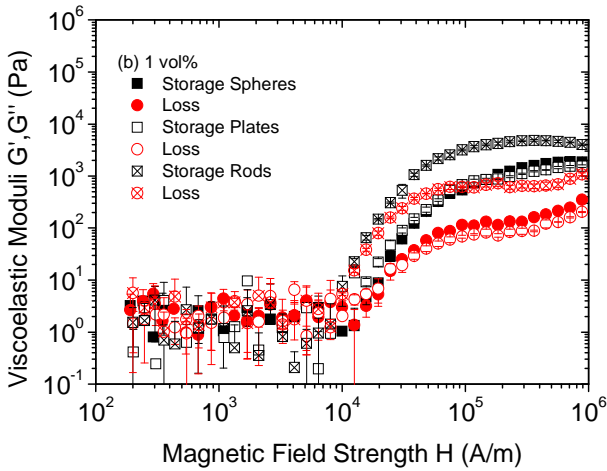
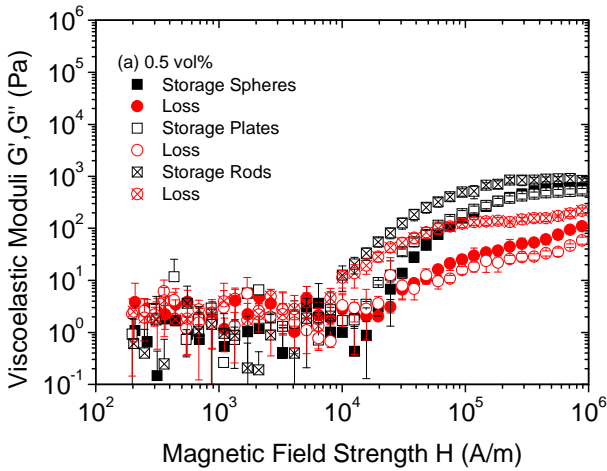
In Figure 7 we show magnetosweep results for spherical, plate-like and rod-like iron particle based MR fluids. It is clearly observed that rod-like particle based MR fluids are stronger than any of the other systems we investigated. However, for the larger concentration investigated and/or for large magnetic fields, negligible differences exist between the three morphologies studied. This finding could be explained assuming a well defined macroscopic structure whose microscopic detail is not relevant in the suspension mechanical behavior. It is also worth remarking that plate and sphere-based suspensions behave very similarly in small-amplitude oscillatory shear in spite of the very different particle shape.

C. Steady shear flow magnetorheology

As observed in Section IV.B, negligible differences exist in the linear viscoelastic rheological behavior of MR fluids containing particles of different shape at 5 vol%. As a consequence, the steady shear flow of MR fluids having a 1 vol% concentrations was investigated to highlight the differences. Results from a typical steady shear flow experiment are shown in Figure 8. The flow curves corresponding to plate and rod-based MR fluids are included in Figure 8a for two magnetic fields (17.7 and 265 kA/m). The most important differences are observed at the lowest fields, where rod particles develop a larger stress compared to plates. However, at the largest fields investigated the flow curves



are very similar independently of the particle shape, which is in agreement with results from small-amplitude oscillatory



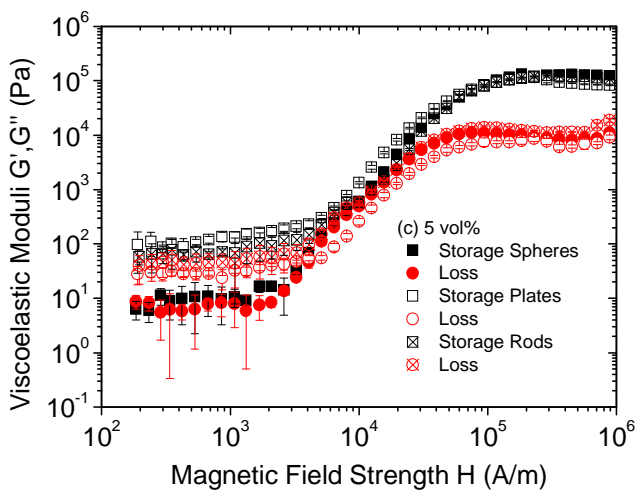


FIG. 7 Magnetic field dependence of storage and loss moduli for iron spheres, plates and rods. a) 0.5 vol%, b) 1 vol%, and c) 5 vol%; squares, G' ; circles, G'' ; closed symbol, spheres; open symbol, plates; crossed symbol, rods.

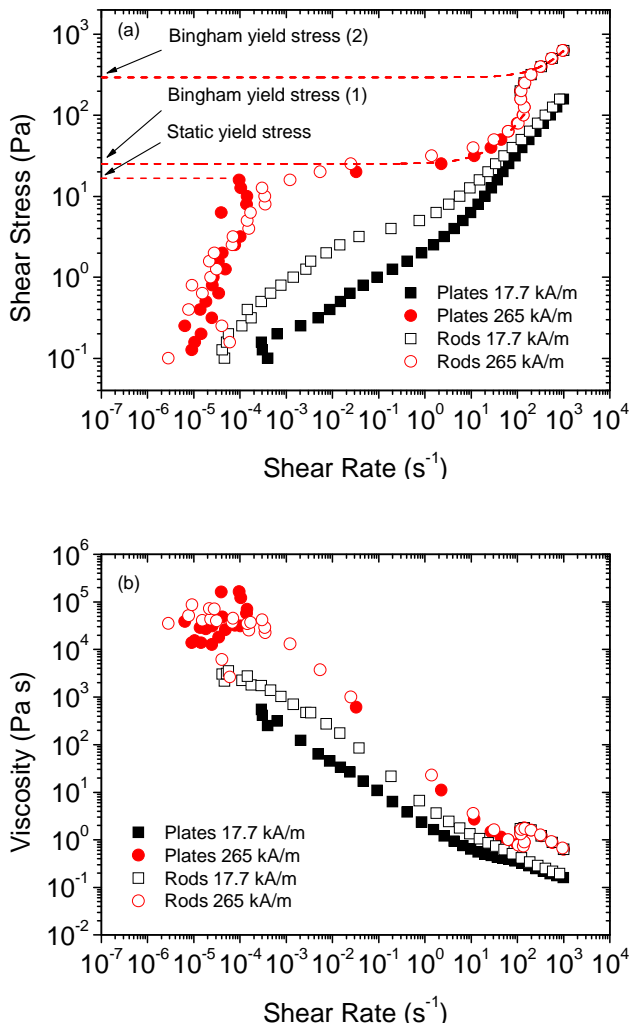


FIG. 8 Typical ramp-up shear flow curves for plate and rod-based MR fluids at 1 vol%. a) rheogram, b) viscosity curve.

shear experiments. In the presence of strong enough magnetic fields, MR fluids behave as plastic materials presenting a yield stress that is manifested by the appearance of a plateau value at medium shear rate values (cf. Fig 8a). In Figure 8b we show typical viscosity curves corresponding to the same plate and rod-based MR fluids. Regardless of the magnetic field strength applied, a clear shear thinning is observed as a consequence of structure degradation because of the shearing forces. At large shear rates an occurrence of shear thickening behavior is found in spite of the low concentration of the samples studied. More detailed information on this atypical behavior is included in Table II. As observed, this phenomenon is only found at large enough magnetic fields. The larger the magnetic field, the larger the shear rate and stress associated to the increase in viscosity. The three types of particles investigated showed such increase in viscosity at large shear rates. However, it is interesting to note that this phenomenon was not observed in the case of smooth carbonyl iron particles with the same magnetic properties and similar size as the iron particles used here (results not shown for brevity). This may suggest that interparticle friction may be at the heart of this finding. Nevertheless, more experiments should be carried out to investigate any dependence of the critical shear rate/stress for the onset of shear thickening on the gap of the measuring geometry.

TABLE II. Onset of the viscosity increase at high shear observed in rheograms like those shown in Figure 8.

Spheres		Plates		Rods	
Shear	Shear	Shear	Shear	Shear	Shear
Stress (Pa)	rate	Stress (Pa)	rate	Stress (Pa)	rate
	(s^{-1})		(s^{-1})		(s^{-1})



17.7	-	-	-	-	-	-
kA/m						
53.0	26	50	-	-	-	-
kA/m						
88.4	39	66	58	60	49	60
kA/m						
176.8	71	135	83	94	89	66
kA/m						
265.3	107	248	114	147	102	151
kA/m						

A similar anomalous shear flow behavior was described by Yin *et al.* (2008) in the case of granular polyaniline particles¹⁹. Results were then explained in terms of an insufficient time for the broken fibrillated structures to reform by the external field at high shear, hence the hydrodynamic forces dominating the flow. In Figure 8a we show the results of the fitting to the Bingham equation below and above the critical shear rate, even though only the former will be considered in the following analysis.

C.1. Scaling behavior with the Mason number

Under a steady shear flow, typical dominant contributions acting on a conventional MR fluid are only magnetostatic and hydrodynamic forces. These two interactions are typically grouped in the so called Mason number, which can be defined as:

$$Mn = \frac{8\eta_c \dot{\gamma}}{\mu_0 \mu_{sr} \beta^2 H^2} \quad (2)$$

where η_c is the viscosity of the continuous medium, $\dot{\gamma}$ is the shear rate, μ_{sr} is the relative magnetic permeability of the suspending medium, $\beta = (\mu_p - \mu_{sr}) / (\mu_p + 2\mu_{sr})$ is the magnetic contrast factor, μ_p is the relative magnetic permeability of the particles, and H is the magnetic field strength in the suspension. This definition comes from the balance between stokesian hydrodynamic and dipolar magnetostatic forces acting on a particle, and agrees with other definitions given in previous works within a numerical coefficient⁴³⁻⁴⁶. At low Mn , magnetic forces are dominant and gap-spanning structures exist between confining surfaces. On the contrary, at large Mn , structures are expected to be broken because hydrodynamic forces overcome magnetostatic forces. Since the particle volume fraction investigated here was very low ($\phi = 0.01$), the internal magnetic field could be assumed to be simply the applied external magnetic field. As a consequence μ_{sr} and β were easily calculated from a Fröhlich-Kennelly equation³⁴ for the M versus H dependence for the particles. From the fit to this equation, the relative initial permeability of the solid phase is found to be 40 and their saturation magnetization 1550 kA/m (assuming the density of iron is ca. 7.8 g/cm³). Results for μ_{sr} and β for a range of magnetic fields investigated are shown in Table III.



TABLE III. Suspension relative magnetic permeability and magnetic contrast factor corresponding to the three samples investigated. These values are considered in the calculation of the Mason number for the scaling under steady shear flow.

H (kA/m)	μ_{sr}	β
17.7	1.0273	0.902
53.0	1.0257	0.849
88.4	1.0243	0.803
176.8	1.0213	0.706
265.3	1.0190	0.630

As a first approximation, magnetic field-induced structures in a MR fluid can be modeled as chains with the width of a single particle. Several models exist in the literature for moderate shear rates (i.e. in the shear thinning region of Figure 8b) under steady shear flow^{45,47,48,32}, all of them predicting a viscosity versus Mason number scaling according to:

$$\frac{\eta - \eta_{\infty}}{\eta_c \phi} = CMn^{-1} \quad (3)$$

where ϕ is the particle volume fraction and η_{∞} is the high shear viscosity.

Rearranging in Eq. (3) for the case of small Mason numbers, assuming that $\eta \gg \eta_{\infty}$, we obtain the following expression for the shear viscosity as a function of Mn :

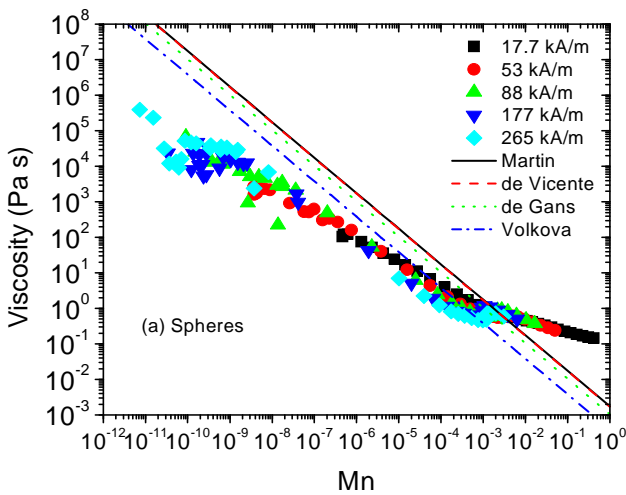
$$\eta \approx \frac{\eta_c \phi C}{Mn} \quad (4)$$

where C is a constant that depends on the details of the microscopic model considered, $C = 8.82$ ⁴⁵, $C = 8.485$ ⁴⁷, $C = 5.25$ ⁴⁸, and $C = 1.91$ ³².

In Figure 9 we show results for steady shear flow tests on sphere, plate and rod based MR suspensions for a wide range of magnetic fields that are mostly within the magnetic linear regime (cf. Figure 5). Interestingly, all curves taken at different magnetic field collapse, suggesting that, for a given particle volume fraction, magnetostatic and hydrodynamic forces dominate the problem whereas other forces such as interparticle friction or short ranged van der Waals attractions are negligible. The only exception is the rod-based MR fluids, for which the collapse is not as good as that observed for spheres and plates. More interesting is the fact that, regardless of particle shape, viscosity curves are very similar and do nearly collapse. This further suggests that the effect of particle shape is not relevant under shear flow. Bearing in mind that Eq. (4) is only applicable at intermediate Mason numbers, from the inspection of Figure 9 it seems clear that our experimental data is better explained by the model proposed by Volkova *et al.* (2000)³². It is well known that theoretical predictions overestimate experimental results in the case of both sphere-based conventional MR fluids⁴⁷ and inverse ferrofluids⁴⁸. The model by Volkova *et al.* (2000) takes into account a more refined hydrodynamic interaction than the usual stokesian approximation. By using a better hydrodynamic description, theoretical predictions are in better accordance with experiments. It is also important to remark here that these chain models assume that aggregates are



fully free to rotate and consequently viscosity should always decrease with the Mason number regardless of the range of Mason number considered. The plateau observed at low Mason number can also be theoretically predicted if chain-like aggregates interconnect the plates⁴⁵. However, due to the scatter of our measurements at such low deformations, it is not possible to withdraw any further conclusion.



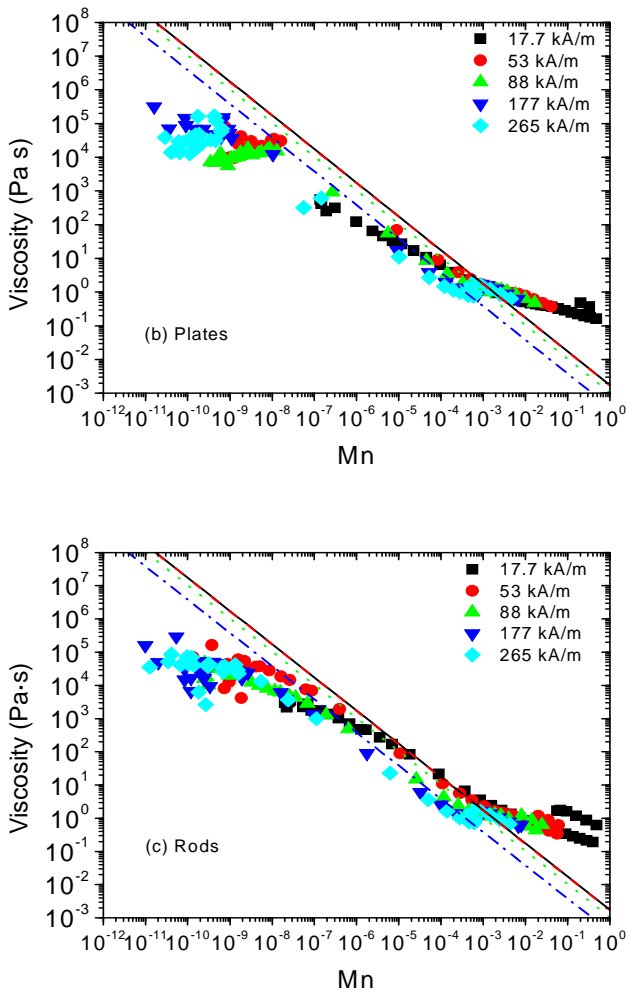


FIG. 9 Shear viscosity as a function of Mason number for a wide range of magnetic fields and three different particle shapes. a) spheres, b) plates and c) rods. Lines correspond to theoretical models at low and moderate Mason numbers: black solid line⁴⁵; red dashed line⁴⁷; green dotted line⁴⁸; blue dash-dotted line³².

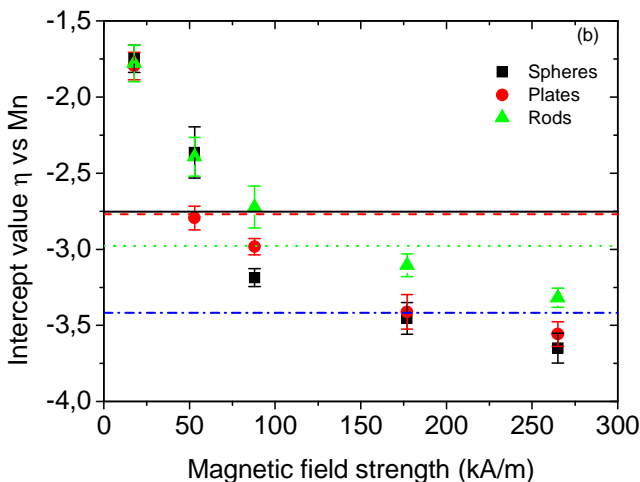


FIG. 10 Slope and intercept values for linear fits to the scaling curves shown in Figure 9 in the interval range between $Mn = 10^{-8}$ and $Mn = 10^{-4}$. Lines correspond to theoretical models at low and moderate Mason numbers: black solid line⁴⁵, red dashed line⁴⁷, green dotted line⁴⁸ blue dash-dotted line³².

A longstanding debate exists on the slope of the double logarithmic representation of η versus Mn under steady shear flow regime. Micromechanical models assuming single width chain aggregates do predict a -1 slope that to the best of our knowledge has never been found experimentally. Most experimental data available in the literature have an absolute slope value smaller than 1 [de Gans *et al.* (1999)⁴⁸, 0.8–0.9; Volkova *et al.* (2000)³², 0.74–0.87; Felt *et al.* (1996)⁴⁹ 0.74–0.83]. For completeness, we show in Figure 10 slopes and intercept values obtained from linear fits to the experimental data of Figure 9, in the range between $Mn = 10^{-8}$ and Mn

◆

$= 10^{-4}$. The slope approaches -1 for the largest magnetic fields investigated, in agreement with previous works by de Gans *et al.* (1999)⁴⁸, Volkova *et al.* (2000)³² and Felt *et al.* (1996)⁴⁹. More interestingly, it does not significantly change with particle shape except at low fields, where the slope for rods is smaller than that for the other morphologies. Intercept values also depend on the magnetic field. Actually, a given micromechanical model is found to fit the experimental data better than the other models in a particular range of magnetic field intensities, whereas in a different region one of the other models might provide the best fit. This may be at the heart of the diversity of explanations for the steady shear flow behavior of MR fluids. Of course, the model by Volkova³² is again the one that better agrees with experiments at largest fields. For fields larger than 300 kA/m , particles do magnetically saturate and hence a plateau is expected for large fields in Figure 10.

Results obtained for ramp-down curves do behave similarly to those shown in this section. Slight changes are observed that may be due to the well known formation of shear cylindrical layers under the presence of external magnetic fields^{37,51,52,53}.

The strength of a MR fluid is undoubtedly its main characteristic since this property can be externally controlled by the application of magnetic fields. The strength is usually manifested as a frequency constant storage modulus under small-amplitude oscillatory shear test and also by the appearance of both a static and dynamic yield stress. To obtain a better understanding of this phenomenon, yielding behavior is now analysed in more detail below.



C.2. Yielding

The yield stress is probably one of the most important properties envisaged for applications of MR fluids⁵⁴. As can be seen in Figure 8, a yielding behavior of the magnetized MR fluids is clearly observed, this yielding being the result of structure collapse under the application of large enough shear stresses. The yielding is manifested by the stress plateau in Figure 8a and the ~ -1 slope observed in Figure 8b. In order to quantify the strength of these structures under shear flow, both static and dynamic yield stresses were obtained from the rheograms carried out under stress-controlled conditions in the presence of external magnetic fields.

The static yield stress is estimated here as frequently done in MR literature by extrapolating the shear stress versus shear rate plots in double logarithmic representations. Basically, the static yield stress corresponds to the value of the stress in the plateau in Figure 8a. The magnetic field dependence of this yield stress is shown in Figure 11. In all cases a power-law dependence is approximately found (see Table IV) in agreement with other authors for sphere and elongated particles¹⁹. A local saturation model by Ginder *et al.* (1996) predicts a power law dependence of $3/2$ in the case of spheres⁴¹. Experimental data obtained here suggest a value of 1.58 ± 0.19 , which is in good agreement with Ginder's finite element calculations. As observed in Table IV, anisotropic particles result in a significantly smaller slope. Qualitatively, similar results were obtained for spherical and elongated polyaniline particles by Yin *et al.* (2008)¹⁹, and aluminum borate sphere and whisker-like particles by Tsuda *et al.* (2007)¹⁸. As observed, rod-like particle based MR fluids present the largest static yield stress regardless of the magnetic field intensity applied. However, the larger the

magnetic field, the smaller the difference between the yield values for different morphologies, in agreement with the small-amplitude oscillatory shear results shown in Figure 7.

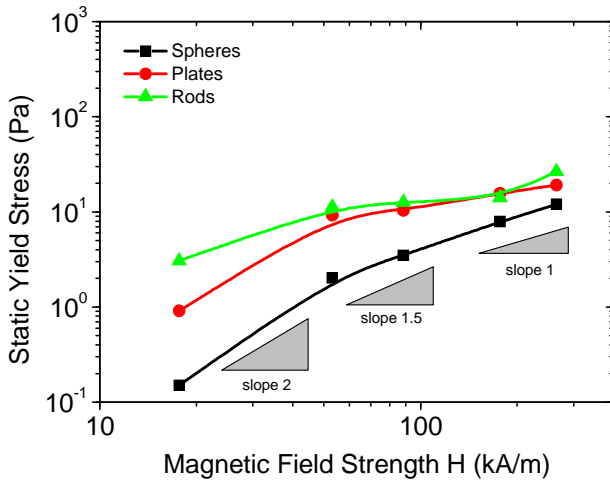


FIG. 11 Effect of particle shape in the static yield stress of MR fluids at different magnetic field strengths. Lines are plotted to guide the eye.

Results shown in Figure 11 can be understood after inspection of the magnetization curve of the suspensions. In Figure 12 we show magnetization *versus* magnetic field strength for iron-based suspensions. As observed, spheres do magnetize at a slower rate compared to plates and rods, both of which magnetize in a similar way. These findings are in good agreement with the static yield stress observations (for a given applied field, the larger the magnetization the larger the static yield stress) and can be qualitatively explained in terms of



the demagnetization factor associated to the different particle geometries. The demagnetization factor of a sphere is 0.333, whereas that associated with the long direction (symmetry axis) of a prolate spheroid with an aspect ratio of 8 can be calculated to be 0.028^{55} . In the case of an oblate spheroid, also with an aspect ratio of 8, the demagnetization factor associated with any direction perpendicular to its symmetry axis is 0.085. It seems clear that non-spherical particles tend to align with their long direction parallel to the applied external field, and that as this field is increased they experience a larger internal field due to their lower demagnetization factors, which results in a faster magnetization process and in a stronger structuration for fields below saturation.

Further insight on the yielding behavior can be obtained by using Finite Element Methods. Finite element calculations were carried out for infinite chains of particles whose size and shape was chosen to resemble those in our sphere-based and rod-based suspensions. Calculations shown in Figure 13 suggest that when the chains are exposed to a uniform magnetic field, the magnetostatic interparticle force is larger in the case of the spherocylinders than in the case of the spherical particles. The calculations also show that as the uniform field increases and particle magnetization comes near to saturation, the force between spherical particles approaches that between spherocylinders. This behavior agrees qualitatively well with that observed for the static yield stress in our suspensions (see Figure 11).

TABLE IV. Slopes corresponding to linear fits for static and dynamic yield stresses as a function of the magnetic field strength from Figure 11 and Figure 14, respectively.

	Static	Dynamic
Spheres	1.58 ± 0.19	0.84 ± 0.06
Plates	1.07 ± 0.25	0.77 ± 0.04
Rods	0.71 ± 0.13	0.68 ± 0.05

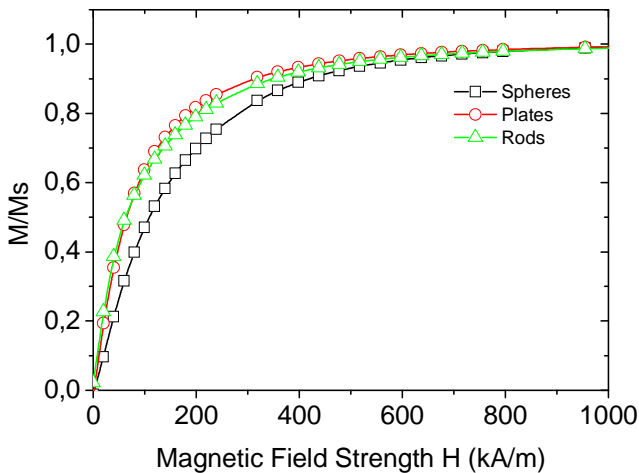


FIG. 12 Initial magnetic hysteresis curves for iron based MR suspensions at 1 vol% up to 1000 kA/m. Magnetization data are normalized by the saturation value for a comparative discussion. Lines are plotted to guide the eye.



The static yield stress suffers from important criticisms in the sense that it is not well defined because it strongly depends on factors such as the surface roughness of the plates or the formation of a wall slip layer⁵⁶. In some cases it is a better option to gauge the strength of the MR fluid through the dynamic yield stress, which is basically the stress needed to continuously separate the particles against attractive magnetic forces in the low shear rate limit³.

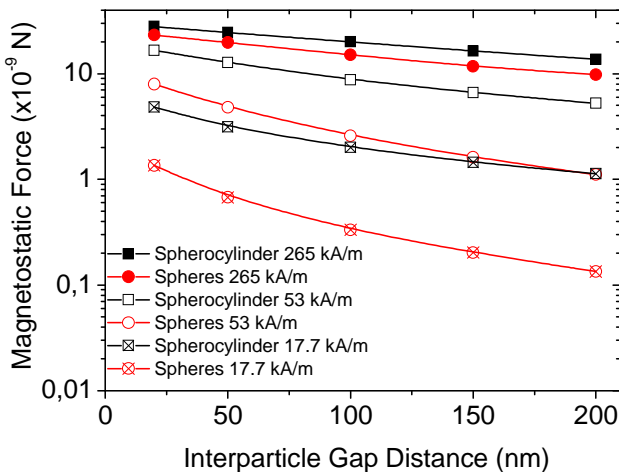


FIG. 13. Force acting on a given particle due to particles above (or below), as a function of interparticle gap, for chains of spherical particles and chains of spherocylinders in a uniform external field. This force was calculated using the FEMM software and is presented for three values of the external field that correspond to data points shown in

Figure 11.

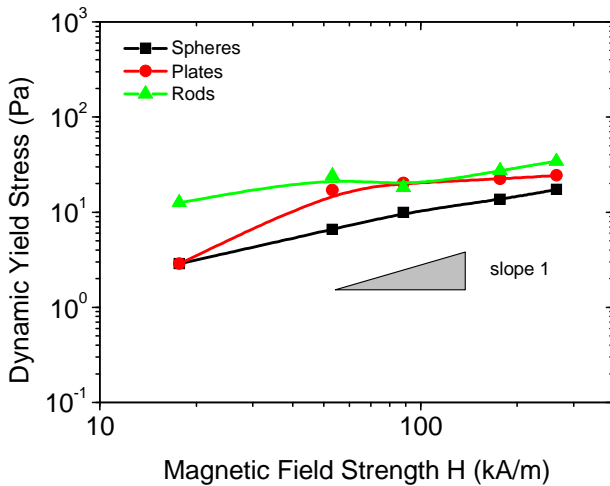


FIG. 14 Dynamic yield stress as a function of magnetic field obtained by fitting the Bingham equation for low shear rates. Lines are plotted to guide the eye.

Since the rheograms measured for iron based MR suspensions (cf. Figure 8) suggest the occurrence of shear thickening behavior at high shear, it would be possible to consider two differentiated dynamic yield stresses corresponding to low and large values of the shear stress. However, only extrapolations at low stresses were considered here. Dynamic yield stresses are plotted in Figure 14. They were found to be larger than their static counterparts in agreement with experiments by López-López *et al.* (2009)²⁰. Again, the smallest yield stresses correspond to sphere-based MR fluids. More interesting is the fact that the slope of the dynamic yield stress versus magnetic field curves depends on particle shape and that values significantly lower than two are found (see Table IV).



V. CONCLUSIONS

The effect of particle shape in MR performance was studied using iron-based MR fluids. In particular, spherical, plate-like and rod-like magnetic particles were investigated.

A novel two-step synthesis route was developed to obtain micron-sized iron particles with three very different morphologies covering one- two- and three-dimensional materials. The first step basically consisted in a wet chemical precipitation. This method allowed us for the fabrication of iron oxide particles having sphere, plate and rod shapes. Oxides obtained at this stage were later reduced to pure iron and surface passivated under controlled experimental conditions. Resulting iron particles have relative initial magnetic permeability of 40 and saturation magnetization of 1550 kA/m . These values are well within the largest among magnetic materials normally employed in MR technology.

In a next step, MR fluids were prepared by dispersing iron particles in silicone oil. Rod-based MR fluids typically presented a larger storage modulus. Plates and spheres did show a very similar storage *versus* magnetic field strength dependence. Interestingly, at large particle concentration and/or large magnetic fields applied, negligible differences exist between the three morphologies studied under small-amplitude oscillatory shear magnetosweep tests.

Steady shear flow behaviour was satisfactorily captured by the Mason number. A master curve was obtained in all cases for spheres, plates and rods. Only for the later, the collapse was slightly worse suggesting that other forces apart from magnetostatic and hydrodynamic ones may be present under flow.

Experimental results were qualitatively explained in terms of the model proposed by Volkova *et al.* (2000)³². The viscosity *versus* Mason number slope asymptotically approached -1 for large magnetic fields.

Ramp-up stress controlled experiments were carried out to determine the yield stress. The stronger structures were formed by rod-like particles, and the weaker ones were obtained in the case of sphere-based MR fluids. Again, the yield stress did not significantly depend on particle shape for large magnetic fields applied. Yield stress observations were in good qualitative agreement with initial magnetization versus magnetic field strength curves for MR suspensions and Finite Element Method calculations.

To sum up, MR fluids prepared with non-spherical particles exhibited a stronger structuration that was apparent in their higher storage modulus and higher yield stress. Such stronger structuration, however, was less noticeable for larger particle concentrations and for larger applied fields. Under steady flow conditions, i.e. once the initial structures have been broken, no relevant differences were observed between the morphologies that we studied. The fact that non-spherical particles magnetize more easily when their long axis is aligned with the external field accounts for the formation of stronger structures at fields below saturation. When particles of different morphologies experience the same magnetization (i.e. when they saturate), differences become smaller.



ACKNOWLEDGEMENTS

The authors would like to thank Dr. F. Galisteo-González for providing the Bool2k software used for the generation of particle-size distributions from electron microscopy micrographs. The authors are also grateful to Prof. Enrique Colacio for supplying the autoclave in which the hematite plates were fabricated. This work was supported by MICINN MAT 2009-14234-C03-03 and MAT 2010-15101 projects (Spain), by the European Regional Development Fund (ERDF) and by Junta de Andalucía P07-FQM-02496, P07-FQM-03099 and P07-FQM-02517 projects (Spain). J. P. Segovia-Gutiérrez acknowledges financial support by the “Ministerio de Educación: Becas del Programa de Formación del Profesorado Universitario (FPU)” (AP2008-02138).

REFERENCES

- ¹Rankin, P. J., J. M. Ginder, and D. J. Klingenberg, “Electro- and magnetorheology,” *Curr. Opin. Colloid In.* **3**, 373-381 (1998).
- ²Klingenberg, D. J., “Magnetorheology: applications and challenges,” *AIChE* **47**, 247-249 (2001).
- ³Bossis, G., O. Volkova, S. Lacis, and A. Meunier, “Magnetorheology: Fluids, Structures and Rheology,” in: S. Odenbach (Ed) *Ferrofluids. Magnetically controllable fluids and their applications* (Lecture notes in Physics; 594; Springer-Verlag 2002) pp 202-230.
- ⁴Phule, P. P., “Synthesis of novel magnetorheological fluids,” *MRS Bulletin*, **August**, 23-25 (1998).
- ⁵Rosensweig, R. E., *Ferrohydrodynamics* (Dover Publications Inc., New York, 1997).

- ⁶Bombard, A. J. F., L. S. Antunes, and D. Gouvêa, "Redispersibility in magnetorheological fluids: surface interactions between iron powder and wetting additives," *J. Phys. Conf. Series* **149**, 012038 (2009).
- ⁷Chin, B. D., J. H. Park, M. H. Kwon, and O. Ok. Park, "Rheological properties and dispersion stability of magnetorheological (MR) suspensions," *Rheol. Acta* **40**, 211-219 (2001).
- ⁸de Vicente, J., M. T. López-López, F. González-Caballero, and J. D. G. Durán, "Rheological study of the stabilization of magnetizable colloidal suspensions by addition of silica nanoparticles," *J. Rheol.* **47(5)**, 1093-1109 (2003).
- ⁹López-López, M. T., J. de Vicente, G. Bossis, F. González-Caballero, and J. D. G. Durán, "Preparation of stable magnetorheological fluids based on extremely bimodal iron–magnetite suspensions," *J. Mater. Res.* **20(4)**, 874-881 (2005).
- ¹⁰Park, B. J., I. B. Jang, H. J. Choi, A. Pich, S. Bhattacharya, and H. –J. Adler, "Magnetorheological characteristics of nanoparticle-added carbonyl iron system," *J. Magn. Magn. Mater* **303**, 290-293 (2006).
- ¹¹Wereley, N. M., A. Chaudhuri, J. –H. Yoo, S. John, S. Kotha, A. Suggs, R. Radhakrishnan, B. J. Love, and T. S. Sudarshan, "Bidisperse magnetorheological fluids using Fe particles at the nanometer and micron scale," *J. Intel. Mat. Syst. Str.* **17**, 393-401 (2006).
- ¹²Kanu, R. C., and M. T. Shaw, "Studies of ER fluids featuring rodlike particles," *Int. J. Mod. Phys. B* **10**, 2925-2932 (1996).
- ¹³Kanu, R. C., and M. T. Shaw, "Enhanced electrorheological fluids using anisotropic particles," *J. Rheol.* **42**, 657-670 (1998).
- ¹⁴Yabing, Q., and W. Wen, "Influences of geometry of particles on electrorheological fluids," *J. Phys. D: Appl. Phys.* **35**, 2231-2235 (2002).



- ¹⁵Satoh, A., "Rheological properties and orientational distributions of dilute ferromagnetic spherocylinder particle dispersions," *J. Colloid Interf. Sci.* **234**, 425-433 (2001).
- ¹⁶Watanabe, T., M. Aoshima, and A. Satoh, "Rheological properties and particle behaviours of a nondilute colloidal dispersion composed of ferromagnetic spherocylinder particles subjected to a simple shear flow: Analysis by means of a mean-field approximation for the two typical external magnetic field directions," *J. Colloid Interf. Sci.* **302**, 347-355 (2006).
- ¹⁷Yin, J., and X. Zhao, "Titanate nano-whisker electrorheological fluid with high suspended stability and ER activity," *Nanotechnology* **17**, 192-196 (2006).
- ¹⁸Tsuda, K, Y. Takeda, H. Ogura, and Y. Otsubo, "Electrorheological behaviour of whisker suspensions under oscillatory shear," *Colloids Surf. A* **299**, 262-267 (2007).
- ¹⁹Yin, J., X. Zhao, X. Xia, L. Xiang, and Y. Qiao, "Electrorheological fluids based on nano-fibrous polyaniline," *Polymer* **49**, 4413-4419 (2008).
- ²⁰López-López, M. T., P. Kuzhir, and G. Bossis, "Magnetorheology of fiber suspensions. I. Experimental," *J. Rheol.* **53(1)**, 115-126 (2009).
- ²¹de Gans, B. J., N. J. Duin, D. van den Ende, and J. Mellema, "The influence of particle size on the magnetorheological properties of an inverse ferrofluid," *J. Chem. Phys.* **113**, 2032-2042 (2000).
- ²²Bell, R. C., J. O. Karli, A. N. Vavreck, D. T. Zimmerman, G. T. Ngatu, and N. M. Wereley, "Magnetorheology of submicron diameter iron microwires dispersed in silicone oil," *Smart Mater. Struct.* **17**, 015028 (2008).
- ²³de Vicente, J., J. P. Segovia-Gutiérrez, E. Andablo-Reyes, F. Vereda, and R. Hidalgo-Álvarez, "Dynamic rheology of sphere- and rod-based magnetorheological fluids," *J. Chem. Phys.* **131**, 194902-1-10 (2009).
- ²⁴Bozorth, R. M., *Ferromagnetism* (IEEE Press, New York, 1978).

- ²⁵Craik, D. J., *Magnetic Oxides* (John Wiley & Sons, London, 1975).
- ²⁶Vereda, F., J. de Vicente, and R. Hidalgo-Álvarez, "Influence of a magnetic field on the formation of magnetite particles via two precipitation methods," *Langmuir* **23**, 3581-3589 (2007).
- ²⁷Sugimoto, T., and E. Matijević, "Formation of uniform spherical magnetite particles by crystallization from ferrous hydroxide gels," *J. Colloid Interf. Sci.* **74**, 227-243 (1980).
- ²⁸Sugimoto, T., A. Muramatsu, K. Sakata, and D. Shindo, "Characterization of hematite particles of different shapes," *J. Colloid Interf. Sci.* **158** 420-428 (1993).
- ²⁹Mendoza-Reséndez, R., M. P. Morales, and C. J. Serna, "Reduction mechanism of uniform iron oxide nanoparticles to metal used as recording media," *Mater Sci. Eng.* **23**, 1139-1142 (2003).
- ³⁰Mendoza-Reséndez, R., O. Bomati-Miguel, M. P. Morales, P. Bonville, and C. J. Serna, "Microstructural characterization of ellipsoidal iron metal nanoparticles," *Nanotechnology* **15**, S254-258 (2004).
- ³¹Volkova, O., G. Bossis, M. Guyot, V. Bashtovoi, and A. Reks, "Magnetorheology of magnetic holes compared to magnetic particles," *J. Rheol.* **44**, 91-104 (2000).
- ³²de Vicente, J., G. Bossis, S. Laci, and M. Guyot, "Permeability measurements in cobalt ferrite and carbonyl iron powders and suspensions," *J. Magn. Magn. Mater.* **251**, 100-108 (2002b).
- ³³Jiles D., *Introduction to Magnetism and Magnetic Materials* (Chapman & Hill, London, 1991).
- ³⁴Meeker, D.C., *Finite Element Method Magnetics, Version 4.2* (15 Jul 2009 Build), <http://www.femm.info>
- ³⁵Ginder, J. M., and L.C. Davis, "Shear stresses in magnetorheological fluids: role of magnetic saturation," *Appl. Phys. Lett.* **65**, 3410-3412 (1994).



- ³⁶de Vicente, J., F. González-Caballero, G. Bossis, and O. Volkova, "Normal force study in concentrated carbonyl iron magnetorheological suspensions," *J. Rheol.* **46(5)**, 1295-1303 (2002a).
- ³⁷Morales, M. P., S. Veintemillas-Verdaguer, M. I. Montero, C. J. Serna, A. Roig, Ll. Casas, B. Martínez, and F. Sandiumenge, "Surface and internal spin canting in γ -Fe₂O₃ nanoparticles," *Chem. Mater* **11**, 3058-3064 (1999).
- ³⁸Wollny, K., J. Laeuger and S. Huck, "Magneto sweep – A new method for characterizing the viscoelastic properties of MR fluids," *Applied Rheology* **12(1)**: 25-31 (2002).
- ³⁹Ramos, J., J. de Vicente, and R. Hidalgo-Álvarez, "Small-amplitude oscillatory shear magnetorheology of inverse ferrofluids," *Langmuir* **26(12)**, 9334-9341 (2010).
- ⁴⁰Ginder, J. M., L. C. Davis, and L. D. Elie, "Rheology of magnetorheological fluids: models and measurements," *Int. J. Mod. Phys. B* **10**, 3293-3303 (1996).
- ⁴¹de Vicente, J., M. T. López-López, J. D. G. Durán, and G. Bossis, "A slender-body micromechanical model for viscoelasticity of magnetic colloids: Comparison with preliminary experimental data," *J. Colloid Interf. Sci.* **282**, 193-201 (2005).
- ⁴²Marshall, L., C. F. Zukoski, and J. Goodwin, "Effects of electric fields on the rheology of non-aqueous concentrated suspensions," *J. Chem. Soc., Faraday Trans.* **85**, 2785-2795 (1989).
- ⁴³Klingenberg, D. J., and C. F. Zukoski IV, "Studies on the steady-shear behavior of electrorheological suspensions," *Langmuir* **6**, 15-24 (1990).
- ⁴⁴Martin J. E., and R. A. Anderson, "Chain model of electrorheology," *J. Chem. Phys.* **104 (12)**, 4814-4827 (1996).
- ⁴⁵Ulicny, J. C., M. A. Golden, C. S. Namuduri, and D. J. Klingenberg, "Transient response of magnetorheological fluids: Shear flow between concentric cylinders," *J. Rheol.* **49**, 87-104 (2005).

- ⁴⁶de Vicente, J., M. T. López-López, J. D.G. Durán, and F. González-Caballero, "Shear flow behavior of confined magnetorheological fluids at low magnetic field strengths," *Rheol. Acta* **44**, 94-103 (2004).
- ⁴⁷de Gans, B. J., H. Hoekstra, and J. Mellema, "Non-linear magnetorheological behaviour of an inverse ferrofluid," *Faraday Discuss.* **112**, 209–224 (1999).
- ⁴⁸Felt, D. W., M. Hagenbuchle, J. Liu, and J. Richard, "Rheology of a magnetorheological fluid," *J. Intel. Mat. Syst. Str.* **7**, 589-593 (1996).
- ⁴⁹de Vicente, J., J. D. G. Durán, A. V. Delgado, F. González-Caballero, and G. Bossis, "Effect of magnetic hysteresis of the solid phase on the rheological properties of MR fluids," *Int. J. Mod. Phys. B* **16**, 2576-2582 (2002c).
- ⁵⁰Cutillas, S., G. Bossis, and A. Cebers, "Flow-induced transition from cylindrical to layered patterns in magnetorheological suspensions," *Phys. Rev. E* **57**, 804–811 (1998).
- ⁵¹Henley, S. and F. E. Filisko, "Flow profiles of electrorheological suspensions: An alternative model for ER activity," *J. Rheol.* **43**, 1323–1336 (1999).
- ⁵²Vieira, S. L., L. B. Pompeo Neto, and A. C. F. Arruda, "Transient behavior of an electroheological fluid in shear flow mode," *J. Rheol.* **44**, 1139–1149 (2000).
- ⁵³Bossis, G., P. Kuzhir, S. Lacis, and O. Volkova, "Yield stress in magnetorheological suspensions," *J. Magn. Magn. Mater* **258**, 456-458 (2003).
- ⁵⁴Shine, A.D. and Armstrong, R.C., "The rotation of a suspended axisymmetric ellipsoid in a magnetic field", *Rheol. Acta* **26**, 152-161 (1987).
- ⁵⁵Barnes, H. A., "The yield stress – a review or πάντα ρεῖ - everything flows?," *J. Non-Newtonian Fluid Mech.* **81**, 133-178 (1999).



**Title of the manuscript**

On the Effect of Particle Porosity and Roughness in Magnetorheology

Authors

Fernando Vereda¹, Juan de Vicente¹, Juan P. Segovia-Gutiérrez¹, Roque Hidalgo-Alvarez¹

Affiliation

¹ Departamento de Física Aplicada, Facultad de Ciencias, Universidad de Granada, Granada E-18071, Spain

Published

Journal of Applied Physics, **110**, 063520 (2011)



Abstract

We report a study on the mechanical properties of magnetorheological (MR) fluids prepared with porous iron particles with rough surfaces. These particles were obtained by reducing a magnetite precursor in a H_2 atmosphere at $400\text{ }^\circ\text{C}$. Small-amplitude dynamic oscillatory and steady shear flow measurements were carried out in the presence of external magnetic fields. Results were compared with those obtained for MR fluids prepared with conventional solid carbonyl iron particles of comparable size. We found significant differences between the rheology of both types of suspensions and, more importantly, we found that simple available models can predict quantitatively those differences as long as the average density of the particles is known and is used to calculate their effective volume magnetization and the real volume fraction of the MR fluids prepared with them. By doing so, we obtained for both the porous iron suspensions and the solid iron suspensions a single master curve of the dimensionless storage modulus at saturation $[G'_{sat}/\mu_0 M_S^2]$ as a function of volume fraction (ϕ), and a good collapse of the viscosity versus Mason number curves, as well as of the yield stress versus applied field curves. Particle porosity is thus an important factor in MR fluids and should be considered in their design and modeling. Finally, the porous iron suspensions also exhibited an atypical thickening behaviour that was not observed in the solid iron analogues and that we tentatively ascribe to the rougher surface of the porous particles.



I. INTRODUCTION

Magnetorheological (MR) fluids are typically prepared by dispersing magnetizable microparticles in a non-magnetic medium. In the presence of a magnetic field, these particles are sufficiently large for the magnetostatic interparticle interactions to be much greater than their thermal energy, so that large aggregates connecting confining surfaces appear within the suspension. The structure formed by the aggregates can withstand shear stresses, presenting field-dependent viscoelastic moduli and a yield stress.¹

We recently developed a versatile method for the preparation of micron-sized, iron particles with different shapes by chemical reduction of iron oxides at high temperature². It turned out that the resulting particles presented a porosity that could be easily estimated, as the volume was preserved in the reduction process, and were therefore ideal systems to evaluate the influence of particle porosity in magnetorheology. Interestingly, MR fluids are usually prepared in the laboratory by dispersing a known mass of the solid phase in a known volume (or mass) of a liquid carrier. It may happen that particles have voids, i.e. that they are hollow³ or relatively porous², which would affect particle density and average particle volume magnetization. If this fact remains unknown during the preparation of the suspensions, porosity can lead to miscalculations of the particle volume fraction or to an average particle volume magnetization that is lower than that assumed from the dry powder magnetization measurements. The goal of this study was to compare the main magnetorheological properties under shear (yielding and viscoelasticity) of porous particle-based MR fluids with those of MR fluids prepared with solid particles of the same material and a



similar size. We also wanted to verify if properly accounting for the porosity of the particles could quantitatively explain the differences observed.

According to the physical mechanism for the field-driven structuration of MR fluids, it is also expected a profound effect of the particle surface roughness in the MR response. In fact, the effect of particle roughness and friction in the structuration of MR fluids was discussed by J. E. Martin and co-workers⁴, and interparticle friction has been considered in some models⁵ and simulations⁶ aimed to describe mechanical properties of MR fluids. However, there are few experimental studies dedicated to the effect of particle surface roughness. Recently, Son and co-workers⁷ reported an enhanced magnetic response of MR fluids prepared with particles of “petal like morphology”, and ascribed their larger magnetic response to the rugged surface of the particles and the concomitant interparticle friction. Because our porous particles also had a rough surface, another goal of this article was to determine the effect of particle surface roughness on the properties of the MR fluids prepared with them.

II. MATERIALS AND METHODS

A. Fabrication of porous iron particles

Porous iron particles were obtained by the chemical reduction of magnetite particles. The fabrication of the magnetite precursor has been described previously⁸ and was based on the work of Sugimoto and Matijevic⁹. The method relies in the mixing of $\text{FeSO}_4 \cdot 7\text{H}_2\text{O}$ and KOH in aqueous solution, which results in the formation of a green precipitate, and in the subsequent curing of that precipitate at 90 °C in the presence of KNO_3 . The resulting black precipitate is then washed with doubly distilled water using magnetic decantation. The final

wash was done with ethanol to facilitate the drying of the powder, which was carried out at 40 °C in air.

The reduction of the magnetite powder to iron has also been described previously.¹⁰ The sample was first heated at 400 °C for 2 h under nitrogen flow to eliminate any adsorbed water. Then, reduction of the iron oxide particles was carried out at 400 °C for 4 h under a hydrogen flow of 40 L h⁻¹. Once the sample had cooled, nitrogen gas wetted with ethanol was passed through the sample for 5 h in order to passivate the surface²

B. Particle characterization (SEM, particle size, magnetometry, X-ray)

Electron microscopy was used to study the morphology, size, and size distribution of

both the precursor and the final iron particles. Samples were prepared by drying droplets of the suspensions in ethanol on top of a glass slide and coating the resulting powder with a thin (approximately 20 nm) graphite coating. These samples were examined in an LEO Gemini 1530 field emission scanning electron microscope in a secondary electron mode.

The phases present in the samples were identified by powder X-ray diffraction measurements using a Philips 1710 diffractometer and the Cu K α radiation. X-ray patterns were collected between $2\theta = 5^\circ$ and $2\theta = 70^\circ$.

The magnetic characterization of the dry powders and the MR fluids were carried out in a vibrating sample magnetometer (MLVSM9 MagLab 9T, Oxford Instruments) at room temperature. The applied magnetic field was swept between +4000 kA/m and -4000 kA/m. Saturation magnetization values



were evaluated by extrapolating to infinite magnetic field the experimental results obtained in the high field range where the magnetization linearly decreases with $1/H$.

C. Preparation of MR fluids

MR fluids were prepared with either our porous iron particles or commercial solid iron particles (HQ carbonyl iron, BASF).

The preparation of the MR suspensions consisted of the following steps: (i) the appropriate mass of iron microparticles and volume of silicone oil ($20 \text{ mPa} \cdot \text{s}$, Sigma-Aldrich) were mixed in a polyethylene container; (ii) the mixture was stirred first by hand, and then in an ultrasonic bath; (iii) step (ii) was repeated several times and, finally, the sample was immersed in a Branson sonifier (model 450) to ensure the required final homogeneity. The gradual homogenization of the samples was confirmed by the disappearance of the aggregates initially observed in the container bottom.

For the comparison between MR fluids prepared with either porous or solid iron particles, we prepared suspensions with both the same concentration of magnetizable material, i.e. with the same mass concentration of iron, as well as with the same particle volume fraction. We estimated that the density of the porous particles was 0.47 times that of bulk iron (see Section III A below). It follows that for the same gravimetric content of iron, the suspensions prepared with the porous particles had a larger particle volume fraction (approximately twice as many particles) because of their lower density.

Table I provides a list of the mass concentrations of the MR fluids used in this study, and of the corresponding particle volume fraction (ϕ) for the porous iron and solid iron suspensions. The iron content was low because of two reasons: the relatively small yield of the synthesis processes, and the fact that we were mostly interested in a range of ϕ in which the growth of MR parameters with ϕ is expected to be linear, which would facilitate the quantitative comparison between the two types of particles.

TABLE I. Gravimetric iron concentrations and the equivalent particle volume fractions for the porous iron and the solid iron suspensions used in this study.

Mass concentration of iron (mg cm^{-3}) ^a	Volume fraction (ϕ) of solid iron particles ($D = 7.87 \text{ g cm}^{-3}$) ^a	Volume fraction (ϕ) of porous iron particles ($D \approx 3.74 \text{ g cm}^{-3}$) ^a
39.3	0.005	0.011
78.7	0.010	0.021
165	0.021	-
393	0.05	0.11
787	0.10	-

^a Concentrations are given per volume of suspension.

D. MR fluid characterization

Dynamic oscillatory properties of the MR fluids were measured at 25 °C using a parallel-plate magneto-rheometer (MCR Anton Paar). The diameter of the plates was 20 mm and the plate separation was fixed at 300 μm . The magnetic filed H mentioned throughout the manuscript was supplied by the magneto-rheometer



coils, and had been calibrated in the gap between the plates with no sample filling that gap. This magnetic field was applied normal to the direction of flow. Firstly, the linear viscoelastic region was determined. Storage and loss moduli were measured as a function of strain at a frequency $f = 1 \text{ Hz}$, in the presence of the following magnetic fields: 0 A/m , 175 kA/m , 353 kA/m , 530 kA/m , 707 kA/m and 884 kA/m . Then, magnetosweeps were carried out at a strain amplitude $\gamma_0 = 0.003 \%$ (well within the linear viscoelastic region in all cases) and a frequency $f = 1 \text{ Hz}$. The experimental procedure is summarized as follows: (i) precondition at a constant shear rate $\dot{\gamma} = 200 \text{ s}^{-1}$ during 30 s in the absence of any magnetic field, (ii) suspension was left to equilibrate for 1 minute, (iii) constant dynamic-mechanical shear conditions were preset (both frequency and amplitude are kept constant) and the magnetic field was gradually increased from 175 to 884 kA/m (logarithmically increased at a rate of 10 points per decade). In all cases experiments were repeated at least three times with fresh new samples.

Steady shear flow tests were carried out at $25 \text{ }^\circ\text{C}$ using the same measuring device mentioned above. The experimental protocol can be summarized as follows: (i) precondition at a constant shear rate $\dot{\gamma} = 200 \text{ s}^{-1}$ for 30 s in the absence of any magnetic field, (ii) the suspension was left to equilibrate for 1 min in the presence of a magnetic field, and (iii) with the field still applied, shear stress was logarithmically increased from 0.1 Pa at a rate of 10 points per decade, until a relatively large shear rate (ca. 800 s^{-1}) was reached. Higher rates could result in sample ejection. Again, experiments were repeated at least three times with fresh new samples.

E. Calculation of static and dynamic yield stresses

The yield stress in the MR fluids was determined using two different approaches. The first one consists in the determination of the so-called static yield stress as the stress corresponding to the onset of flow in double logarithmic representations of stress versus shear rate. A second method to determine the yield stress is to fit the Bingham plastic equation to a rheogram in lin-lin representation. The latter procedure results in the so-called Bingham yield stress. Even though there may be other more appropriate methods to measure the yield stress, these two approaches are frequently used in the MR literature.¹

III. RESULTS AND DISCUSSION

A. Particle size and morphology. Particle porosity

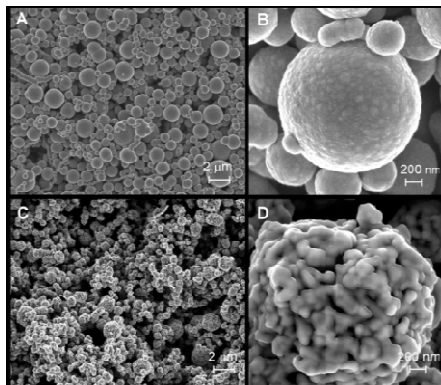


FIG. 1 SEM micrographs of the two types of particles used for the preparation of the MR fluids. Solid carbonyl iron (A and B) and porous iron particles obtained from the reduction of a magnetite precursor (C and D).



It can be seen in micrographs A and C of Figure 1 that the two types of particles have a comparable size. Size distributions of the solid carbonyl iron particles can be found in the literature. The diameter distribution given by Bombard et al.¹¹, which was measured by laser light scattering, peaks somewhere between 0.6 and 0.7 μm , whereas that reported by Hydutsky et al.¹², obtained by measuring the diameter of many particles in SEM micrographs, has the maximum at 0.77 μm . The actual size distribution of the porous particles is shown in Figure 2. The diameter (d) distribution of the porous particles can be fit to a log-normal distribution:

$$f(d) = \frac{A}{d \sigma \sqrt{2\pi}} \exp \left[-\frac{\left(\ln d/d_0 \right)^2}{2\sigma^2} \right] \quad (1)$$

with parameters $d_0 = 658 \text{ nm}$ and $\sigma = 0.219$. The fitted curve shown in Figure 2 peaks at 628 nm .

The composition of the porous particles was inferred from X-ray diffraction. All the peaks of the X-ray diffraction spectrum [not shown here for brevity, see de Vicente et al.² of the powder after the reduction process are ascribed to metallic iron. Remarkably, none of the peaks corresponding to the spinel structure of magnetite were visible after the reduction process.

One of the most important features of the porous iron particles is that their size distribution is almost identical to that measured for the magnetite precursor², which means that particle size was practically preserved during the reduction

process. This is intimately related to the porosity of the particles: the fact that a given particle maintains its original volume while its chemical composition changes from Fe_3O_4 to pure Fe, as stated in the previous paragraph, giving away all its oxygen (i.e. losing some mass) leads to the formation of voids. The preservation of particle size also allowed for a simple estimation of particle porosity as follows. The volumetric iron content of magnetite is $6.70 \times 10^{-2} \text{ moles/cm}^3$. If this iron remains in the same volume previously occupied by magnetite, the density of the particles after reduction will be 3.74 g/cm^3 . Since the density of bulk iron is 7.87 g/cm^3 , the relative volume of the porous particles that is occupied by metallic iron is 0.47 and thus the porosity (volume of voids divided by the total volume of particle) is 0.53. Both the porosity of and the surface roughness can be qualitatively appreciated in the micrographs B and D of Figure 1. It is also clear that the porous particles have a qualitatively rougher surface than the solid iron particles. Furthermore, the shapes of the particles shown in those micrographs are representative of the two types of particles: solid carbonyl iron particles are spherical, whereas the porous particles exhibit a more irregular morphology. This morphology is a consequence of the reduction process and of the fact that the magnetite precursor was mainly formed by particles in the shape of rhombic dodecahedral crystals³ and not spheres.

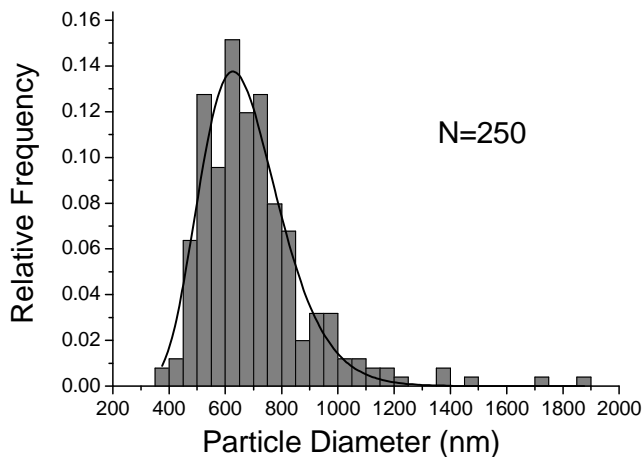


FIG. 2 Diameter distribution of the synthesized porous iron particles.

Because of their lower density, porous particles will occupy a larger volume of the suspension than solid particles for the same iron content. Also, the average volumetric magnetization of a porous particle will be smaller than that of a solid particle.

B. Magnetization of particles and fluids

The magnetization curves for the two iron powders are shown in Figure 3(A). Both types of particles exhibit almost identical saturation magnetization. We obtained values of $205 \text{ A m}^2 \text{ kg}^{-1}$ and $209 \text{ A m}^2 \text{ kg}^{-1}$ for the saturation magnetization of the solid iron and the porous iron powders respectively. The main difference between the magnetization curves is the fact that the magnetization of the solid iron increases more rapidly, reaching saturation at a

lower applied field. This must be the consequence of the different microstructure of both types of particles. Figure 3B shows the magnetization curves for two MR fluids prepared with the two types of particles. The iron content for both fluids is 78.7 mg/mL . Again, the saturation magnetization is practically the same and the fluid prepared with the solid iron particles reaches saturation at lower fields.

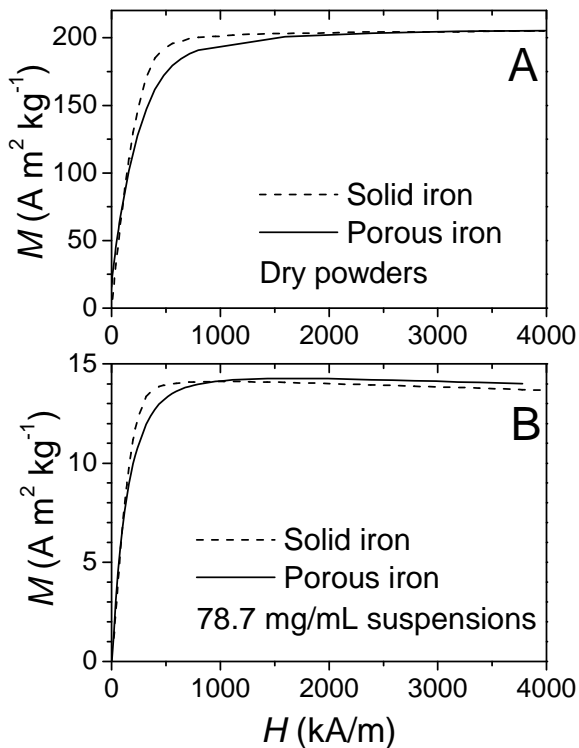


FIG. 3 Mass magnetization of the dry powders (A) and suspensions with 78.7 mg/mL of iron (B).



C. Magnetorheology

C.1. Dynamic oscillatory shear

Small-amplitude oscillatory shear tests are a powerful tool to evaluate the viscoelastic behavior of MR fluids in the linear regime. On the one hand, the elastic properties are typically described by the storage modulus (G'), which is directly related to the strength of the structures formed in the suspensions. On the other hand, the viscous properties are determined by the loss modulus (G''), which accounts for the energy dissipation.

Figure 4 shows the results of small-amplitude oscillatory shear magnetosweeps for suspensions prepared with either porous or solid iron, and with iron concentrations of 39.3, 78.7 and 393 mg/mL (corresponding to solid iron particle volume fractions of 0.005, 0.01 and 0.05 respectively.) At low iron concentrations (39.3 and 78.7 mg/mL) G' starts increasing at practically the same field for both types of suspensions and the solid particle suspensions exhibit larger G' at saturation. This is expected, since we are comparing suspensions with the same mass of iron, which implies that the particle volume fraction of the porous iron based suspension is approximately twice that of the solid iron suspension ($\phi_{\text{porous}} \approx 2 \phi_{\text{solid}}$), whereas the average volumetric magnetization of each porous particle will be approximately half that of a solid particle $M_{\text{porous}} \approx M_{\text{solid}}/2$. Simple micromechanical chain-like models¹³ predict that G' at intermediate fields scales as $G'_{\text{med}} \approx 3\phi\mu_oM_sH$, while G' at saturation is $G'_{\text{sat}} \approx 0.3\phi\mu_oM_s^2$. Therefore, when $M_{\text{porous}} \approx M_{\text{solid}}/2$ and $\phi_{\text{porous}} \approx 2\phi_{\text{solid}}$ one would expect $G'_{\text{solid}} \approx G'_{\text{porous}}$ at medium fields and $G'_{\text{solid}} \approx 2G'_{\text{porous}}$ at saturation. The values of G' that we measured for our

suspensions with iron contents of 39.3 and 78.7 mg/mL are in good agreement with these predictions: the storage modulus for both types of suspensions are practically the same at intermediate fields, and the ratio G'_{solid} / G'_{porous} at saturation is equal to 1.9 and 2.1 at iron concentrations of 39.3 and 78.7 mg/mL respectively.

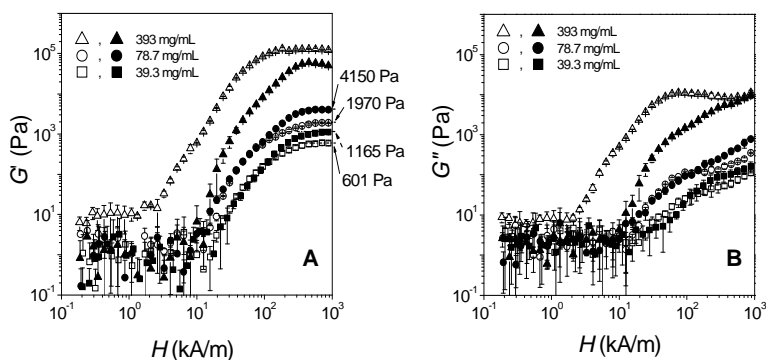


FIG. 4 Small-amplitude oscillatory shear magnetosweep curves for suspensions prepared with porous iron (open symbols) or solid iron (solid symbols) with the same gravimetric iron content. A: storage modulus (G'). B: loss modulus (G'').

The curves for the suspensions with the highest iron content (393 mg/mL) show more clearly the effect of porosity: even though the gravimetric concentration of iron was the same in both suspensions, the porous iron based suspension exhibits at low fields a larger storage modulus. More importantly, the field-induced structuration of this suspension starts at lower fields than for its solid iron counterpart, and the G' of the porous iron suspension at saturation



is about twice as large as that of the solid iron suspension. Please note that experiments were repeated three times with fresh samples and the curves shown in Figures 4 and 5 include error bars. The fact that the particle volume fraction of the porous iron suspension was approximately twice that of the solid iron suspension can account for these observations. This was also the case for suspensions with 39.3 and 78.7 *mg/mL* of iron content, but apparently at such small concentrations the contribution of the volume fraction to G' at saturation was closer to being linear (as predicted by micromechanical chain-like models), and at larger concentrations an increase faster than linear is expected because of the presence of thick columnar structures and/or non-affine motion of the aggregates.¹

The loss modulus (G'') is associated with energy dissipated under flow. Results of measurements of the loss modulus of our suspensions are presented in Figure 4(B). Once the magnetic field is large enough, the loss moduli are clearly smaller than the storage moduli. Even though a complete understanding of the loss modulus in MR fluids is still missing in the literature, expected contributions to the viscous dissipation are the liquid carrier viscosity, and dissipation due to the field-induced aggregates. It is apparent that in our suspensions the latter dominates, since the storage moduli increase with the field, and the field dependence of G'' resembles that of G' .

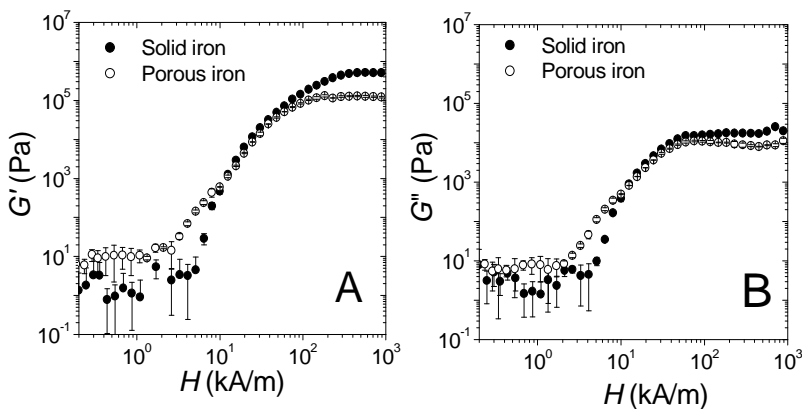


FIG. 5 Small amplitude oscillatory shear magnetosweep curves for suspensions prepared with porous iron (open circles) or solid iron (solid circles) with the same particle volume fraction ($\phi = 0.10$). A: storage modulus. B: loss modulus.

Since the dependence of G' on ϕ is hard to predict as ϕ grows, it seemed reasonable to compare suspensions with the same ϕ . Figure 5(A) shows G' as a function of the magnetic field for two suspensions with $\phi = 0.10$. Note that the curves for the porous particle suspension with $\phi = 0.10$ shown in Figure 5(A) are the same curves shown in Figure 4 with an iron content of 393 mg/mL . Since ϕ is the same for both suspensions but $M_{\text{solid}} \approx 2M_{\text{porous}}$, chain-like models predict that at saturation $G'_{\text{solid}} \approx 4G'_{\text{porous}}$. Note that the values we obtained are again in good agreement with this prediction: 125 kPa and 516 kPa for the porous iron suspension and the solid iron suspension respectively.



It is also noticeable in Figure 5(A) that the porous particle suspension exhibits a larger G' before structuration, and that it starts the structuration at lower fields. We believe this may be caused by the roughness of the porous particles. Surface roughness can affect the MR properties either by a mere enhancement of mechanical friction or by facilitating the coupling of the magnetic field between particles. The latter would result in a more efficient magnetization of the particles and therefore in the formation of aggregates (structuration) at lower fields, as we observed. The contributions of roughness and volume fractions are intimately related, since roughness plays a more important role at higher concentrations due to the proximity among particles and to the formation of thicker columnar aggregates.

Once again, it can be seen in Figure 5(B) that at large enough fields the storage moduli of the two suspensions is larger than the loss moduli, and that dissipation associated with the field-induced structuration is the dominating contribution.

The fact that chain-like micromechanical models predict correctly the ratio between the two storage moduli of the two types of suspensions at saturation as long as their particle volume fraction is matched suggests that G'_{sat} is truly proportional to M_s^2 . Further insight on the dependence of G'_{sat} on ϕ can be obtained by plotting G'_{sat} and $G'_{sat}/(\mu_0 M_s^2)$ versus ϕ (see Figure 6). A reasonably good collapse of the curves corresponding to the two types of suspensions was obtained when G'_{sat} was divided by $\mu_0 M_s^2$. The saturation magnetization was calculated by multiplying the gravimetric saturation magnetization measured for the dried powders (Figure 3(A)) by the density of the particles: 7.87 and 3.74 g/cm^3 for the solid and the porous particle

respectively. The quality of the collapse further supports our estimations for the density of the porous particle being half the density of iron and for their volumetric magnetization being also half that of iron. It also confirms that G'_{sat} is proportional to M_s^2 and, more importantly, that for both types of particles G'_{sat} depends in the same fashion on ϕ in the range of ϕ of our measurements ($0.005 < \phi < 0.10$). By visual inspection of the bottom graph of Figure 6, we can conclude that the increase of G'_{sat} with ϕ is only linear at the smallest volume fractions investigated, whereas for $\phi > 0.02$ the growth of G'_{sat} is significantly faster than $\sim \phi$, as was observed in the data presented in Figure 4.

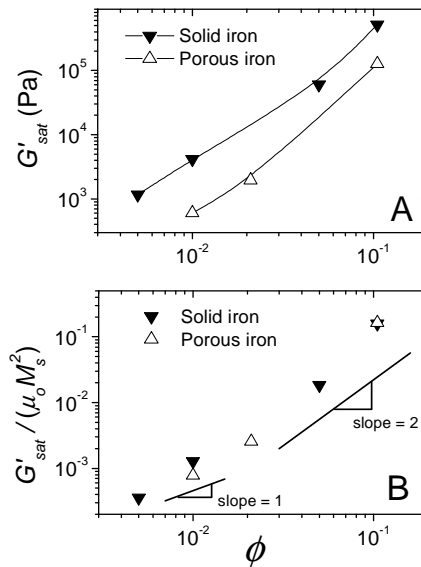


FIG. 6 Storage modulus at saturation, G'_{sat} , (A) and scaled storage modulus at saturation, $G'_{sat} / (\mu_0 M_s^2)$, (B) as a function of volume fraction for both types of particles. Solid circles: solid iron. Open circles: porous iron. Lines in A are a guide to the eye.



C.2. Steady shear

In the steady shear flow tests the MR suspension is first left to structure in the presence of a constant magnetic field and an increasing shear stress is applied subsequently while the field is maintained on. This stress eventually leads to the rupture of the structures and to the onset on flow, therefore providing information about both the strength of the field-induced structures as well as the flow properties of the suspension. The magnetic fields at which the shear flow tests were carried out were chosen in the 20 – 300 kA/m range. We were especially interested in probing this region because it was where most of the field-induced change of the viscoelastic moduli had been observed.

Shear stress versus shear rate curves obtained from the steady shear tests were first used to obtain the static and the dynamic yield stresses. Both parameters give an idea on the strength of the field-induced structures in the suspensions. The static yield stress can be understood as the stress needed to start the flow of the suspension, whereas the dynamic yield stress is the stress needed to continuously separate the particles against attractive magnetic forces¹⁴. The former was obtained from the plateau observed in the double logarithmic representation of the shear stress vs. shear rate curves, whereas the second was estimated by fitting a Bingham plastic equation to the lin-lin representation of the same curves². All values of the dynamic yield stress presented in Table II and in Figure 7 where obtained from fits in a range of shear rate between 5 and 50 s^{-1} . The values obtained for the static and the dynamic yield stresses for suspensions with the same iron content (78.7 mg/mL) are summarized in Table II.

TABLE II. Values of the static yield stress and the dynamic yield stress obtained from the ramp-up shear flow rheograms for both the porous particle and the solid particle based suspensions.

H (kA/m)	Static Yield Stress (Pa)		Dynamic Yield Stress (Pa)	
	Solid Iron ^a	Porous Iron ^a	Solid Iron ^a	Porous Iron ^a
17.7	0.5	0.2	2.5±0.2	1.5±0.3
53.0	4.0	2.0	9.8±0.6	4.4±0.2
88.4	10.5	4.0	18.6±0.2	6.9±0.2
176.8	20.0	7.9	36±1	12.1±0.5
265.3	31.6	12.0	60±3	16.4±0.5

^a Iron content in both types of suspensions was 78.7 mg/mL.

The field dependence of the yield stresses is shown in Figure 7(A) and 7(B). The curves for the two different types of particles have very similar slopes, although some trends are observed: slopes for static yield stresses are in general larger than those for the dynamic yield stresses, and slopes for the $\phi = 0.021$ solid iron suspensions are also larger than those for the other two suspensions. In the case of intermediate fields, local saturation models predict a yield stress that scales as $\tau_0 \approx \phi \mu_0 M_s^{1/2} H^{3/2}$ ^{13,14} eventually becoming field strength-independent at saturation. As expected, experimental data shown in Figure 7(A) and 7(B) follow the 3/2 prediction in the field range investigated. It can be seen both in Table II and in Figure 7 that for an iron concentration of 78.7 mg/mL, the solid iron suspension exhibits a stronger structuration despite its lower particle content. This is the result of the larger volumetric magnetization of the solid particles, and is in agreement with the results of the small-amplitude



oscillatory shear tests reported in the previous section for the same gravimetric iron concentration. We show in Figure 7(C) and 7(D) the result of scaling the yield stresses with respect to ϕ and $\mu_0 M_p^2(H)$, the latter term being proportional to typical interparticle magnetostatic forces of the system. In this expression M_p is the average particle magnetization. M_p can be obtained from magnetization measurements of dry powder samples, or by measuring the suspension magnetization at a given field and dividing it by ϕ . We tried both methods for the calculation of M_p and in both cases obtained reasonably good collapses of the stress vs. field curves. The M_p values used to generate the graphs shown in Figure 7(C) and 7(D) were obtained from dry powder magnetization curves. The collapse was significantly poorer when we divided the yield stress by $\phi \mu_0 M_s^{1/2}$, as suggested by the Ginder model for intermediate fields mentioned above.

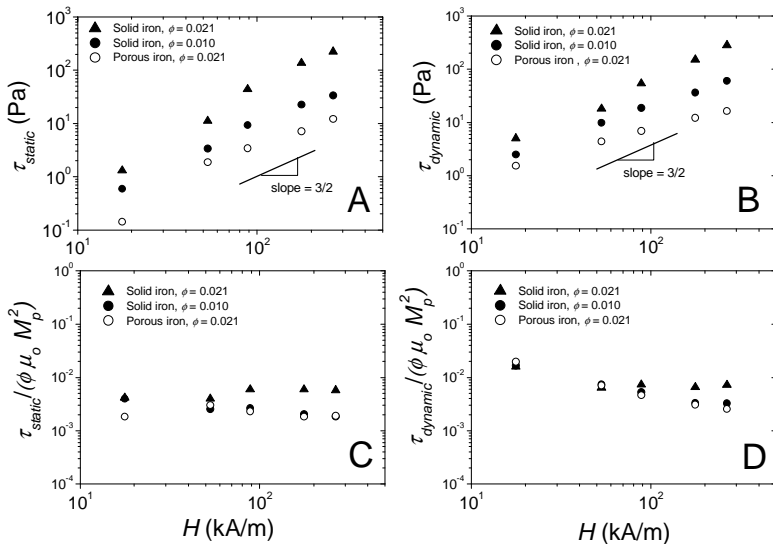


FIG. 7 Top: Dependence of the static yield stress (A) and the dynamic yield stress (B) on the applied field for porous and solid iron suspensions. Note that one of the solid iron suspensions had the same mass concentration as the porous iron suspension (that with $\phi = 0.01$), whereas the other solid iron suspension was prepared with the same particle volume fraction as the porous iron suspension ($\phi = 0.021$). Bottom: scaled static (C) and dynamic (D) yield stresses. The range of four orders of magnitude in the y-axis has been preserved to facilitate the comparison with the data before scaling.

Regarding the flow behaviour of our MR fluids, viscosity (η) versus shear rate ($\dot{\gamma}$) curves in a log-log representation are shown in Figure 8(a) for suspensions with the same volume fraction of particles ($\phi = 0.021$) and for several field strengths. The viscosity of the suspensions is clearly a function of the field



strength and the shear rate. In general viscosities of the solid iron suspensions are higher for the same field and shear rate. The same data is represented as a function of the Mason number (Mn) in Figure 8(b). A few expressions can be found in the literature^{15,16} for this number, which is basically the ratio between hydrodynamic and magnetostatic forces. We used the expression provided by Klingenberg et al.¹⁷:

$$Mn = \frac{F_{Hyd}}{F_m} = \frac{9}{2} \frac{\eta_c \dot{\gamma} \phi^2}{\mu_o \mu_c M^2} \quad (2)$$

where η_c is the viscosity of the continuous medium (0.020 Pa s), ϕ is the particle volume fraction of the suspension (0.021), μ_o is the vacuum permeability, μ_c is the relative permeability of the continuous phase and M is the measured magnetization of the suspension. Note that $M\phi^{-1}$ is the average particle magnetization (M_p) mentioned above. M_p can then be calculated from magnetization curves of dry powder samples (Figure 3(A)) or from curves of suspensions like those shown in Figure 3(B). Dry powder magnetization curves were used to obtain the curves shown in Figure 8(b), although the quality of the collapse was similar when the calculation of Mn was based on the magnetization of suspensions.

The relatively good collapse of all the $\eta(Mn)$ curves for $Mn > 10^{-9}$ indicates that for the volume fraction that we studied, magnetostatic and hydrodynamic forces dominate the flow behavior. The fact that curves corresponding to both porous and solid particles collapse together is also interesting, and supports again that our estimation that the density of the porous particles was

approximately 0.5 that of the solid particles is reasonable. This estimation was necessary to prepare suspensions of the same particle volume fraction.

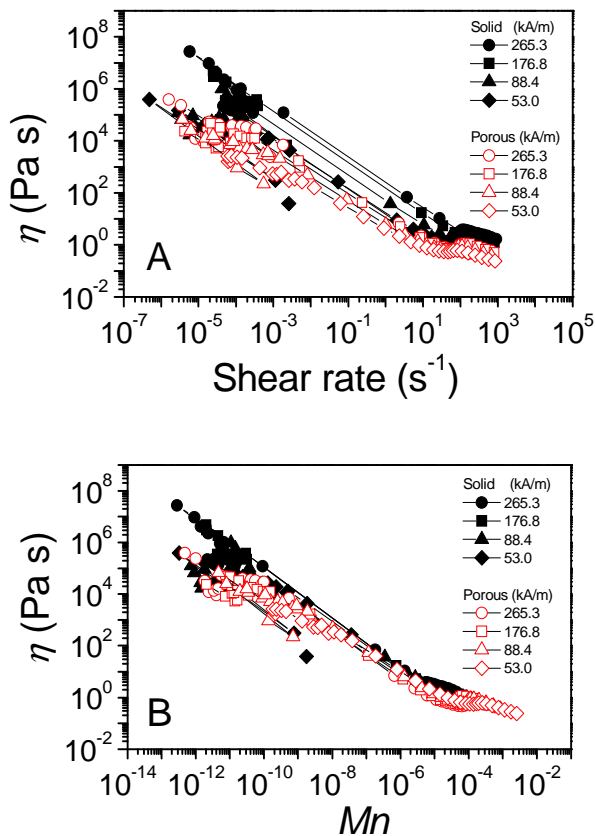


FIG. 8. Viscosity curves for the two types of suspensions at four different field strengths. A: viscosity as a function of the shear rate. B: viscosity as a function of the Mason number, Mn (see Eq. 1). Suspensions had the same particle volume fraction ($\phi = 0.021$).



Perhaps the most striking difference between the two types of MR fluids is the fact that for the suspensions prepared with porous particles there is a shear thickening (i.e. a flow-induced increment of the viscosity) regime. The presence of the shear-thickening regime is evident in the viscosity curves obtained for the porous particle suspension (Figure 9, bottom). Such shear thickening behaviour was not observed in the suspensions prepared with solid particles (Figure 9, top). Because the occurrence of shear thickening seems to be very ubiquitous in the flow of suspended solids as long as the appropriate shear rate range is reached¹⁸, it is possible that in our experiments such rate was reached for the porous particle suspensions but not for the solid particle suspensions. In fact, Lootens *et al.*¹⁹ studied suspensions prepared with rough-surface silica particles, and found that roughness decreased the shear rate at which thickening occurred.

At the heart of the current picture on shear thickening is the fact that at high shear hydrodynamic forces lead to the formation of hydroclusters – ‘transient concentration fluctuations that are driven and sustained by the applied shear field’¹⁸. Hydroclusters are associated with large stress fluctuations that lead to high dissipation rates and high shear viscosity. It happens that particles in hydroclusters can be at very short distances from each other - typical separation between particles in hydroclusters has been estimated to be in the order of nanometers¹⁸ - which can make particles’ surfaces roughness a key factor in shear thickening. Hoffman²⁰ proposes a model in which particles can cluster and/or reach physical contact, so that ‘lubrication forces and frictional forces are most likely involved in the shear thickening process.’

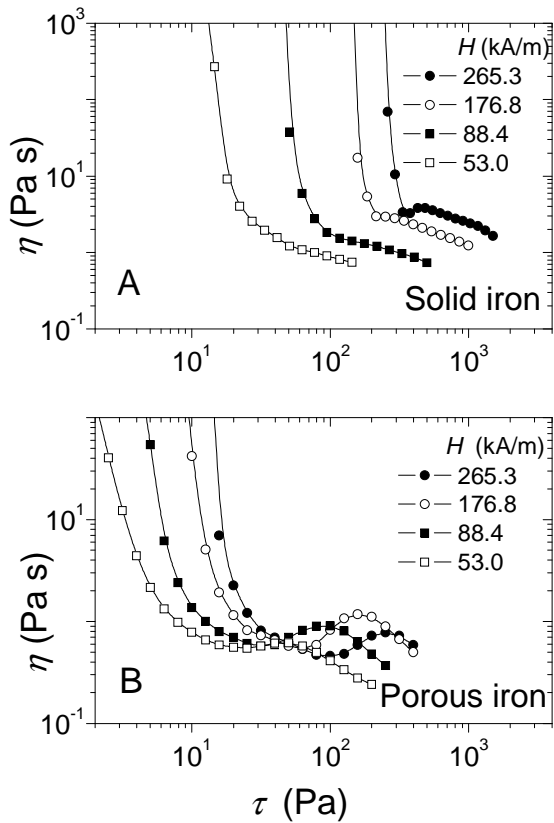


FIG. 9 Viscosity (η) as a function of shear stress (τ) for suspensions prepared with solid particles (A) and porous iron particles (B). Particle volume fraction was the same ($\phi = 0.021$) for both types of suspensions.

Figure 10 shows the critical shear stresses, i.e. the shear stress at which thickening starts, and the stress at which thinning is resumed as a function of applied field. The thickening regime started at a higher stress as the field



intensity was increased. Brown *et al.*²¹ have shown that this is a general behaviour in suspensions in which the source of a yield stress can be controlled, such as magnetorheological fluids and suspensions of hard spheres at high concentrations. As the source of the yield stress is manipulated and the yield stress increases, the critical yield stress also increases. If the yield stress is increased above a given threshold, it could mask completely the thickening region.

For our porous iron suspension the stress that marks the end of the shear thickening behaviour increases with the applied field, whereas for the suspensions presented by Brown *et al.*²¹ that stress remains constant. However, we have only four data points in the curves of Figure 10 and more points are needed to draw conclusions on a definite trend.

It is also interesting that our suspension exhibited shear thickening at a particle volume concentration of 0.021. In general, shear thickening also occurs in dilute suspensions²² but is hard to observe, and in fact most of the reported data that we have found has been taken on suspensions with much larger concentrations^{18,23}. We have only come across two reports on shear thickening on MR fluids, and the particle volume fractions were 0.20²¹ and 0.25²⁴

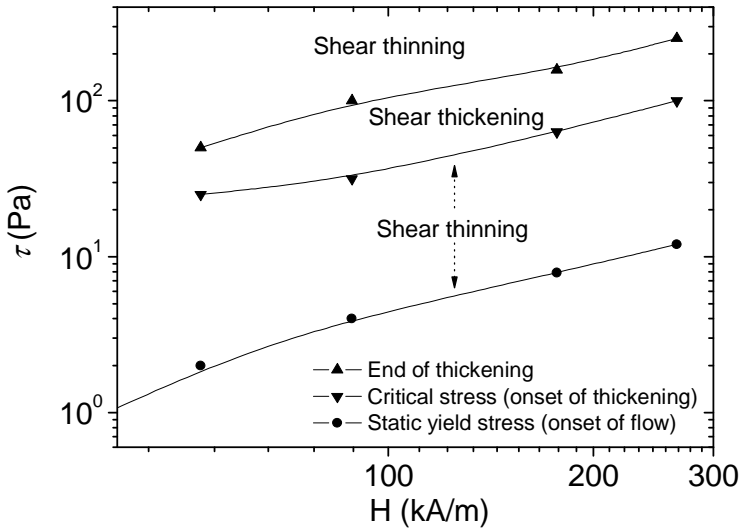


FIG. 10 Shear stresses that mark the onset of flow (static yield stress), the onset of shear thickening (critical stress) and the end of the shear thickening for different field strengths and for a porous iron suspension with a particle vol. concentration of $\phi = 0.021$. The boundaries of the shear thickening region are given by the local minima and maxima of the curves shown in Figure 9 (bottom).



IV. CONCLUSIONS

We carried out a comparative study between the rheology of MR fluids prepared with porous iron particles and that of MR fluids prepared with solid iron particles.

We found that suspensions that have the same mass concentration of iron, that were prepared with particles of very similar size, and that have practically identical magnetization curves, may have a very different rheological behaviour. The reason behind that different behaviour was particle porosity. Voids within particles lead to a density smaller than that of the bulk material and to an average volume magnetization also smaller than that of the bulk material. Because of the lower density of the porous particles, for the same mass content porous particles occupy a larger volume fraction.

More importantly, we have shown that porous particles can be modelled reasonably well if the appropriate corrections are made, i.e. if the right particle volume concentration and an effective volume magnetization are estimated. By doing this, the rheological parameters of the porous iron suspensions were satisfactorily related to those of the more conventional solid iron suspensions. Concretely, a single master curve of the dimensionless storage modulus at saturation [$G'_{sat}/(\mu_0 M_s^2)$] as a function of volume fraction (ϕ) was obtained from experimental data of the two types of particles. This also confirmed that G'_{sat} is proportional to M_s^2 and that for both types of particles G'_{sat} depends in the same fashion on ϕ . The increase of G'_{sat} with ϕ was generally faster than linear even at small volume fractions. We were also able to collapse together the yield stress versus H curves by scaling the yield stresses with respect to ϕ

and $\mu_0 M_p^2$, the latter term being proportional to the typical interparticle magnetostatic forces of a system. Furthermore, we could account for the influence of particle porosity in the flow behavior of the MR fluids by using a Mason number that also takes into account the average particle magnetization (M_p) at different fields¹⁷ for the calculation of the magnetostatic forces. This Mason number led to a good collapse the viscosity curves of the solid iron suspensions and the porous iron suspensions.

Interestingly, the term ($\mu_0 M^2$) was involved in the scaling of the three rheological parameters we studied, which confirms that magnetostatic forces determine to a great extent the mechanical properties of MR fluids. It was also interesting to verify that despite the inhomogeneous nature of the porous particles, the properties of MR suspensions prepared with them can be predicted reasonable well by assuming an average particle magnetization.

Finally, we have detected an atypical thickening behaviour in relatively diluted porous iron suspensions ($\phi = 0.021$) that was not observed in the solid counterparts and that may be caused by the rougher surface of the porous particles.



ACKNOWLEDGEMENTS

Fernando Vereda is especially grateful to the “Programa de reincorporación de doctores de la U. de Granada.” The authors would like to thank Prof. F. Galisteo-González for providing the Bool2k software used for the generation of particle-size distributions from electron microscopy micrographs. This work was supported by MICINN MAT 2010-15101 project (Spain), by the European Regional Development Fund (ERDF) and by Junta de Andalucía P07-FQM-02496 project (Spain). J. P. Segovia-Gutiérrez acknowledges financial support by the “Ministerio de Educación: Becas del Programa de Formación del Profesorado Universitario (FPU)” (AP2008-02138).

REFERENCES

- ¹ J. de Vicente, D.J. Klingenberg, and R. Hidalgo-Alvarez, *Soft Matter* **7**, 3701-3710 (2011).
- ² J. de Vicente, F. Vereda, J.P. Segovia-Gutiérrez, M.P. Morales, and R. Hidalgo-Álvarez, *J. Rheol.* **54**, 1337-1362 (2010).
- ³ F. Vereda, B. Rodríguez-González, J. de Vicente, and R. Hidalgo-Álvarez, *J. Colloid Interface Sci.* **318**, 520-524 (2008).
- ⁴ J.E. Martin, K.M. Hill, and C.P. Tigges, *Phys. Rev. E* **59**, 5676-5692 (1999).
- ⁵ M.T. López-López, P. Kuzhir, and G. Bossis, *J. Rheol.* **53**, 115 (2009).
- ⁶ J. de Vicente and J. Ramírez, *J. Colloid Interface Sci.* **316**, 867-876 (2007).
- ⁷ Y.-H. Son, J.-K. Lee, Y. Soong, D. Martello, and M. Chyu, *Appl. Phys. Lett.* **96**, 121905 (2010).
- ⁸ F. Vereda, J. de Vicente, and R. Hidalgo-Álvarez, *Langmuir* **23**, 3581-3589 (2007).
- ⁹ T. Sugimoto and E. Matijević, *J. Colloid Interface Sci.* **74**, 227-243 (1980).
- ¹⁰ R. Mendoza-Reséndez, O. Bomati-Miguel, M.P. Morales, P. Bonville, and C.J. Serna, *Nanotechnology* **15**, S254-S258 (2004).
- ¹¹ A.J.F. Bombard, M. Knobel, M.R. Alcantara, and I. Joekes, *J. Intell. Mater. Syst. Struct.* **13**, 471-478 (2002).
- ¹² B.W. Hydutsky, E.J. Mack, B.B. Beckerman, J.M. Skluzacek, and T.E. Mallouk, *Environ. Sci. Technol.* **41**, 6418-6424 (2007).
- ¹³ J. Ginder, L. Davis, and L. Elie, *Int. J. Mod. Phys. B* **10**, 3293-3303 (1996).
- ¹⁴ G. Bossis, O. Volkova, and A. Meunier, *Lect. Notes Phys.* **594**, 202-230 (2003).
- ¹⁵ J.E. Martin, *Phys. Rev. E* **63**, 011406 (2000).
- ¹⁶ O. Volkova, S. Cutillas, and G. Bossis, *Phys. Rev. Lett.* **82**, 233-236 (1999).
- ¹⁷ D.J. Klingenberg, J.C. Ulicny, and M.A. Golden, *J. Rheol.* **51**, 883-893 (2007).



- ¹⁸ N.J. Wagner and J.F. Brady, *Phys. Today* **62**, 27-32 (2009).
- ¹⁹ D. Lootens, H. van Damme, Y. Hémar, and P. Hébraud, *Phys. Rev. Lett.* **95**, 268302 (2005).
- ²⁰ R.L. Hoffman, *J. Rheol.* **42**, 111-123 (1998).
- ²¹ E. Brown, N.A. Forman, C.S. Orellana, H. Zhang, B.W. Maynor, D.E. Betts, J.M. DeSimone, and H.M. Jaeger, *Nat. Mater.* **9**, 220-224 (2010).
- ²² J. Bergenholtz, J.F. Brady, and M. Vivic, *J. Fluid Mech.* **456**, 239-275 (2002).
- ²³ B.J. Maranzano and N.J. Wagner, *J. Chem. Phys.* **114**, 10514-10527 (2001).
- ²⁴ Y. Tian, J. Jiang, Y. Meng, and S. Wen, *Appl. Phys. Lett.* **97**, 151904 (2010).

**PART II-YIELD STRESS AND THE EFFECT OF PARTICLE
CONCENTRATION**

Title of the manuscript

Non-linear viscoelasticity and two-step yielding in magnetorheology: a colloidal
gel approach to understand the effect of particle concentration

Authors

J. P. Segovia-Gutiérrez¹, C.L.A. Berli², J. de Vicente¹

Affiliation

¹ Departamento de Física Aplicada, Facultad de Ciencias, Universidad de
Granada, Granada E-18071, Spain

² *INTEC (UNL-CONICET), Güemes 3450, 3000 Santa Fe, Argentina*

Published

Journal of Rheology, **56(6)**, 1429-1448 (2012)

**Abstract**

The yielding behavior of conventional magnetorheological (MR) fluids is revisited for a wide range of magnetic fields and particle concentrations under a colloidal gel perspective. A two-step yielding behavior is found at intermediate magnetic fields ($\sim 10 \text{ kA/m}$) that can be explained as a transition from a strong-link to a weak-link (or transition) regime upon increasing the particle concentration in the MR fluid. This two-step yielding behavior is reminiscent of the classical concepts of static (frictional) and dynamic (Bingham) yield stress. By relating macroscopic elastic properties to a scaling fractal model we could identify the prevalent gelation regime in MR fluids.

I. INTRODUCTION

Magnetorheological (MR) fluids are field-responsive colloidal suspensions with tunable rheological properties. The presence of an external magnetic field induces string-like particulate structures in the direction of the field. This microstructure greatly affects the bulk rheology, either increasing the shear viscosity (at low volume fractions and low fields) or developing a yield stress accompanied by a viscoelastic behavior (at large field strength)¹⁻³. Traditionally, the control over the rheology of MR fluids is essentially achieved by adjusting either the particle volume fraction or the interparticle magnetic interaction force.

With no additives, magnetic particles employed in the formulation of conventional MR fluids are rather strongly attractive (even in the absence of external fields). Hence, similarly to other aggregating suspensions, in the absence of an external magnetic field the rheological properties of MR fluids slightly increase when increasing the volume fraction at low values, and abruptly increase once the concentration is larger than a critical or threshold volume fraction (ϕ_c) corresponding to the formation of a space-filling particle network (Figure 1). It has been reported in the literature that ϕ_c is basically independent of the external field strength, and is a characteristic parameter related to the suspension itself evidencing a sort of first-order phase transition (i.e. percolation transition)⁴. As a consequence, isolated clusters exist below ϕ_c while aggregated and percolated structures exist above ϕ_c , hence resulting in very different rheological behaviors when exploring the volume fractions below and above this critical concentration^{4,5}.



Obviously, another important quantity in magnetorheology concerns the magnetic field strength. This is so because the interparticle magnetic interaction force depends on the external field². On the one hand, the effect of magnetic field strength in MR performance below ϕ_c has been described in terms of a directional gelation model⁶. Initially the zero shear viscosity grows with the field strength up to a certain point when the loss factor becomes independent on the excitation frequency (the so-called gelation point). Next, at some critical value H_c , a yield stress appears and the storage modulus G' becomes higher than the loss modulus G'' (Figure 1). On the other hand, the effect of magnetic field strength in suspensions above ϕ_c has been extensively documented mainly because most of MR fluids' applications involve volume fractions of the order of 30 vol% and hence well above ϕ_c ^{7,2}. The physics behind the rheological behavior of MR fluids operating below or above ϕ_c and/or H_c is definitely different (cf. Figure 1), but, surprisingly, in spite of its importance, there are very few systematic works, if any, where both magnetic field strength and particle volume fraction are varied in a wide range. On the one hand, the effect of magnetic field strength seems to be reasonably well understood. At small field strengths, the yield stress and the storage modulus are predicted to be essentially proportional to the magnetic field strength squared^{7,8}.

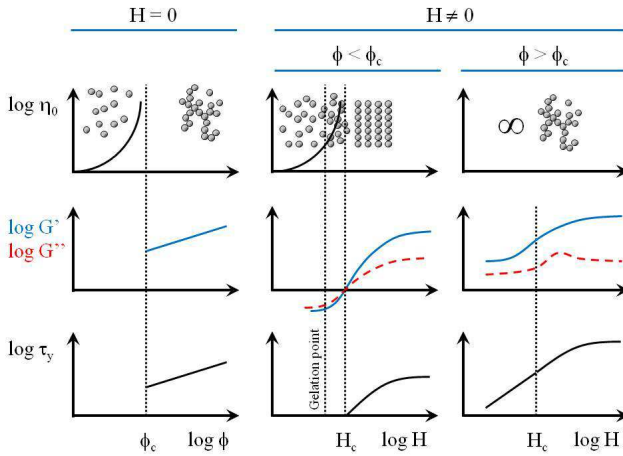


FIG. 1 Schematics of the magnetic field strength and particle concentration dependence of the low shear viscosity η_0 , storage and loss moduli (G' and G'') and yield stress τ_y in magnetorheology.

As the applied field strength increases and the magnetization begins to saturate, the yield stress will increase sub-quadratically with the external field strength, $\tau_y = \sqrt{6}\phi\mu_0M_s^{1/2}H_0^{3/2}$, eventually becoming field strength-independent at large field strengths, $\tau_y = 0.086\phi\mu_0M_s^{9/2}$. Similarly, for intermediate magnetic field strengths, Ginder *et al.* (1996)⁹ predicted that $G' = 3\phi\mu_0M_sH_s$. The nonquadratic dependence on the field strength arises as the particle magnetization begins to saturate near the poles in chainlike aggregates. At large field strengths where the particles' magnetization is completely saturated, the storage modulus becomes independent of field strength, and is given by $G' = 0.3\phi\mu_0M_s^2$.



On the other hand, there is very limited number of thorough studies on the effect of particle concentration. Micromechanical models based on the fibrillation model (i.e., gap-spanning single particle-width chains) predict a yield stress and elastic (storage) modulus that increase linearly with the number of chains, that is to say, with the volume fraction². This prediction has been experimentally confirmed in the case of diluted MR fluids at low fields where interchain interactions are ignored. Felt *et al.* (1996)¹⁰ claimed a linear increase of the dynamic (Bingham) yield stress with volume fraction in the range $0.014 < \phi < 0.12$. Unfortunately, these authors only investigated three volume fractions. The dynamic yield stress was also found to increase roughly linearly with the particle concentration in the case of electrorheological fluids in the range $0.1 < \phi < 0.2$ ¹¹. Rankin *et al.* (1999)¹² found that the dynamic yield stress in MR greases also has an approximately linear relation with the volume fraction in the range $0.02 < \phi < 0.25$. Unfortunately, only four data were taken for the fitting. In general, more data points are needed to draw any further conclusion. In most cases, a more rapid than linear increase with volume fraction is observed for more concentrated conventional MR fluids that is thought to be associated with thick columnar structures and/or non-affine motion of the aggregates². For example, Volkova *et al.* (2000)¹³ showed that static (frictional) and dynamic yield stresses increase faster than linear in the range $0.1 < \phi < 0.4$. Also, Chin *et al.* (2001)¹⁴ found that only at low volume fractions $\phi < 0.2$ a linear relation was found. As volume fraction increased, the dynamic yield stress increased faster than linear. A faster than linear increase of the dynamic yield stress has been also measured in ER fluids¹⁵.

More exotic behaviors have also been reported in the literature and some of them in contradiction with each other. Using conventional MR fluids in

dimethylpolysiloxane, Fujita *et al.* (2000)¹⁶ reported a yield stress that increases as volume fraction increases and saturates for volume fractions larger than 30 vol%. In the case of inverse ferrofluids, Volkova *et al.* (2000)¹³ also demonstrated that after an initial increase, both static and dynamic yield stresses saturate at $\phi = 0.3$, and even decrease with the volume fraction. Linear chain models fail to predict the saturation with volume fraction, however, the yield stress dependence with volume fraction calculated with macroscopic models show an increase at low concentrations, reaches a maximum at 30 vol% and then decreases at higher volume fractions¹³.

In this work, we report a comprehensive study on the non-linear (yielding) behavior in gelled (i.e. fully percolated, $H > H_c$) model conventional MR fluids prepared by dispersing magnetizable carbonyl iron particles in a non-magnetic liquid medium. The yielding behavior is investigated as a function of particle volume fraction in a wide range to explore both regions below and above ϕ_c .

II. MATERIALS AND METHODS

Additive-free MR fluids were prepared by carefully mixing carbonyl iron powder (HQ grade from BASF; diameter $\sim 800\text{nm}$) in silicone oil (20 mPa s, Sigma-Aldrich) to get suspensions having well defined volume fractions ranging from 0.5 vol% to 50 vol% (metallic iron density 7.8 g/cm^3). Carbonyl iron particles (grade HQ, BASF) were chosen for this study because they are frequently used in the formulation of MR fluids^{7,2}. It is well known that additive-free MR fluids are not kinetically stable and experience sedimentation. However, we decided not to include additives in the recipe in order to keep the fluids as simple as possible. It is also important to remark that the magnetic field employed in the rheology tests was sufficiently large for the structuration of the suspension, and always



applied from the beginning of the test. Under these conditions, the occurrence of sedimentation is not expected to be a problem. The preparation of suspensions consisted of the following steps: (i) magnetic powder and silicone oil were mixed in a polyethylene container; (ii) the mixture was stirred first by hand, and then in an ultrasonic bath; (iii) step (ii) was repeated several times to ensure the required final homogeneity.

A MCR 501 (Anton Paar) magnetorheometer was employed to investigate the rheological properties of MR fluids under shearing flows. Non-magnetic (titanium-based) parallel plates of diameter 20mm were used. The commanded gap was set as $300\mu\text{m}$. An external magnetic circuit was used to generate uniaxial DC magnetic fields of the order of $\sim 100\text{kA/m}$ in the gap between the plates [Wollny *et al.* (2002)]. To achieve a reasonably uniform radial magnetic flux density profile, we studied the effect of sufficiently small magnetic field strengths ($\leq 300\text{kA/m}$)¹⁸. As usual, magnetic field strengths reported in this manuscript refer to the maximum plateau value corresponding to radial magnetic flux density profiles provided by the manufactures of the magnetocell¹⁹. Results presented below are always averages over at least three separate runs with fresh new samples. Preliminary experiments at different gap distances demonstrate that slippage effects can be discarded. All experiments were run at $25\text{ }^\circ\text{C}$.

III. LINEAR RHEOLOGICAL RESPONSE UNDER MAGNETIC FIELDS

The linear viscoelastic behavior of the MR fluids was investigated as a function of the magnetic field strength for a wide range of particle volume fractions. The strain amplitude was fixed at **0.003 %** and the excitation frequency was **1 Hz**.

Typical magnetosweep curves in the linear viscoelastic regime are shown in Figure 2. Interestingly, two well differentiated scenarios are found depending on the particle concentration in the suspension. On the one hand, for particle volume fractions below **10 vol%**, the viscoelastic moduli are found to be negligible for magnetic field strengths below **10 kA/m**. In fact, the torque at these very low moduli/field values was below the lower limit of the torque transducer and this is the reason for the scatter in the data. For larger fields, the storage modulus (G') becomes larger than the loss modulus (G'') and both moduli increase towards a final plateau at large fields close to the saturation of the dispersed particles. On the other hand, for particle concentrations larger than **10 vol%**, non-negligible moduli are measured even at low fields suggesting that for these suspensions ϕ_c is somewhere close to **10 vol%**. Actually, for concentrations larger than **20 – 30 vol%**, the storage modulus overpasses the loss modulus at low fields. As expected, upon increasing the magnetic field strength the storage modulus reaches a saturating value that in this case does not differ much when changing the particle concentration. Interestingly, the loss modulus reaches a local maximum and then decreases towards a final plateau value.

In summary, results presented in Figure 2 suggest that for carbonyl iron-based conventional MR fluids the percolating transition (gelation threshold²⁰) appears at $\phi_c \sim \mathbf{10\ vol\%}$ and that $H_c \sim \mathbf{10\ kA/m}$. Well below the percolating transition ϕ_c

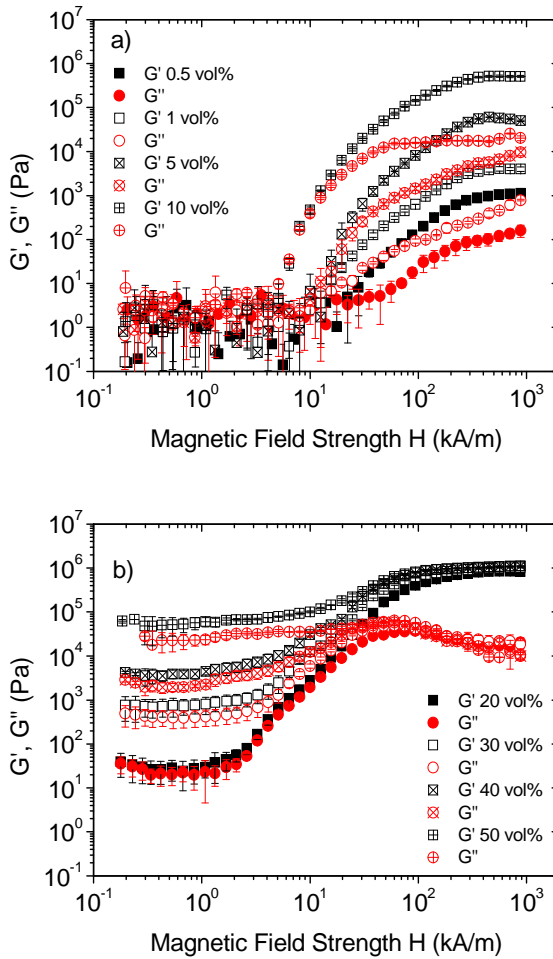


FIG. 2 Magnetic field strength dependence of storage G' and loss moduli G'' (in the linear viscoelastic region) for conventional MR fluids. a) particle concentrations below 10 vol%. b) particle concentration above 10 vol%. Strain amplitude $\gamma_0 = 0.003\%$ and frequency $f = 1$ Hz.

and for magnetic fields smaller than H_c aggregates are expected to be short and consequently not connecting the gap. As a result, energy is completely dissipated under shear and the storage modulus is negligible. This statement is reinforced by the fact that the yield stress of the sample was found to be negligibly small. On the other hand, for magnetic fields larger than H_c percolated field-induced structures should exist for all the particle concentrations investigated (0.5 vol% – 50 vol%).

In the following we will focus our attention to magnetic fields above the gel point H_c , by using the criterion of the crossover of G' and G'' mentioned above. Nevertheless, it is worth noting that yield stress values from steady shear flow measurements of the same suspensions (data not shown here) indicate that the critical values H_c and ϕ_c are closely related each other, and vary inversely. In other words, the higher H_c , the lower ϕ_c , in agreement with the scenario described by Trappe *et al.* (2001)²¹ for aggregating colloids.

IV. YIELDING BEHAVIOR FROM SIMPLE SHEAR FLOW TESTS

Yield stress measurements in MR fluids are typically obtained using steady shear flow tests via extrapolation at low shear rates^{13,2}.

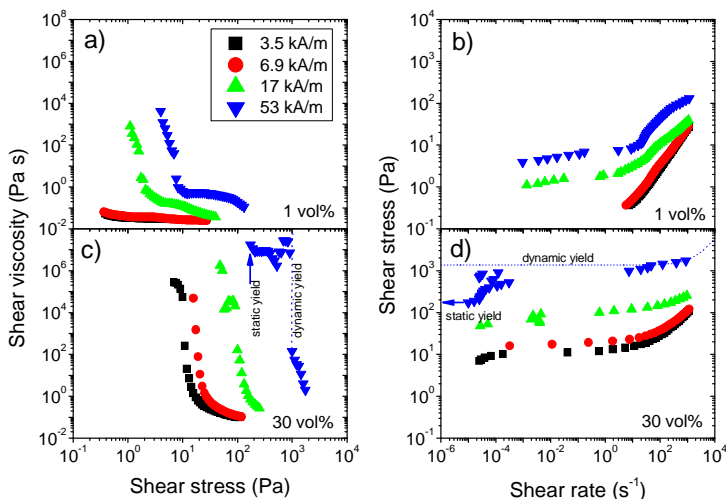


FIG. 3 Steady shear flow curves for MR fluids at two different volume fractions: a) and b) **1 vol%**; c) and d) **30 vol%**. Note the non-monotonic behavior observed for the most concentrated MR fluid for magnetic fields larger than H_c .

In Figure 3 we show typical results obtained for MR fluids at **1 vol%** and **30 vol%** in the presence of different magnetic fields from **3.5 kA/m** to **53 kA/m**. Care was taken to favor that the sheared sample had reached a steady state. Accordingly, every point in the Figure 3 is an average during 30 seconds. We employ two different representations to show the onset of yielding. In the first representation (Figs. 3a and 3c) we show the shear stress dependence of the shear viscosity. Here, the yield stress is associated to the sharp drop in the viscosity when increasing the stress. On the other hand, the yield stress is given by the low-shear shear stress plateau in shear stress versus

shear rate representations (cf. Figs. 3b and 3d). Of course, both yield stresses are the same independently of the method employed.

MR fluids with a particle content below ϕ_c (e.g. 1 vol% in Figure 3) clearly show the typical behavior with a yield stress that increases with the magnetic field strength for $H > H_c$. This finding has been extensively found in the literature and in some cases a good scaling behavior with the average particle magnetization has been reported²². On the other hand, more concentrated MR fluids with particle concentration larger than ϕ_c (e.g. 30 vol% in Figure 3) seem to exhibit two yielding processes for intermediate fields, larger than H_c (17 kA/m and 53 kA/m). It is interesting to remark here that these results were highly reproducible both using stress and strain controlled modes, and smooth and rough surfaces. In all cases, wall slip did not occur as demonstrated by measuring at different gap thicknesses.

V. YIELDING BEHAVIOR FROM DYNAMIC OSCILLATORY SWEEPS

A more accurate determination of the yielding behavior results from unsteady dynamic oscillatory shear tests^{23,24}. In Figure 4 we show the strain amplitude sweep tests for different particle volume fractions in the presence of a magnetic field strength of 53 kA/m.

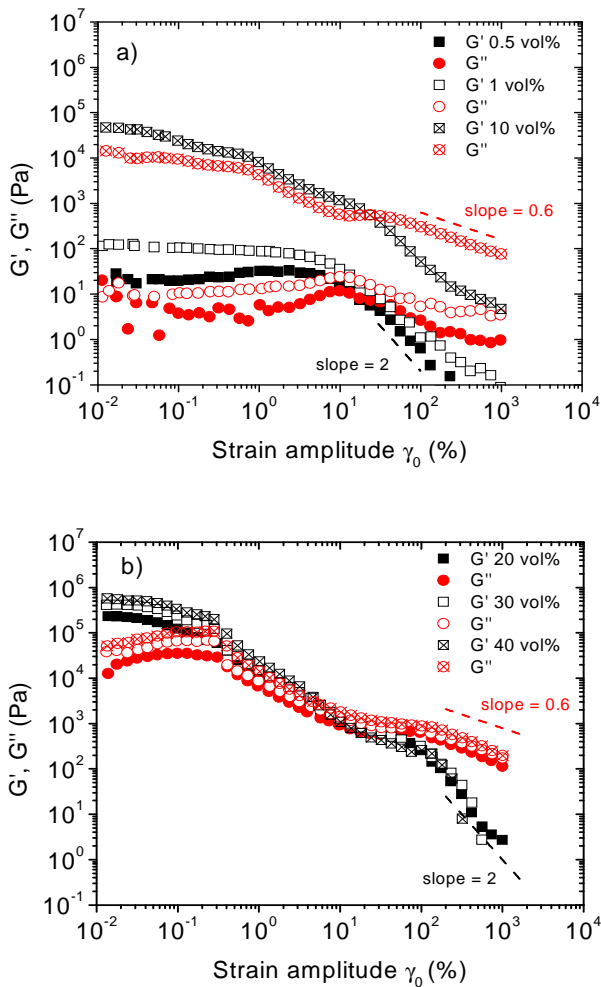


FIG. 4 Dynamic strain amplitude sweep tests with storage modulus G' (squares) and loss modulus G'' (circles) as a function of the strain amplitude at $\omega = 1 \text{ rad/s}$. a) volume fractions below **10 vol%**, b) volume fractions above **10 vol%**. Magnetic field strength **53 kA/m**.

Experiments are grouped in two figures for better clarity. Results for volume fractions up to 10 *vol%* are included in the Figure 4a, while those for volume fractions larger than 10 *vol%* are shown in Figure 4b. While dilute MR fluids experience a dramatic change in the viscoelastic properties when increasing the volume fraction (see Figure 4a), more concentrated MR fluids exhibit a very similar behavior very slightly dependent on the particle content (see Figure 4b). These findings are in agreement with magnetosweep tests reported in Figure 2. As expected, MR fluids investigated clearly operate well above the gelation threshold ($H > H_c$) even for a particle volume fraction as low as 0.5 *vol%*. This is so because the magnetic field strength is already very large (if compared to the thermal Brownian motion) resulting in the anisotropic connectivity of the field-induced structures and a storage modulus significantly larger than the loss modulus at low strains (cf Figure 2). Similar results to those reported in Figure 4 are obtained for magnetic field strengths in the range from 17 to 265 *kA/m* (not shown here for brevity).

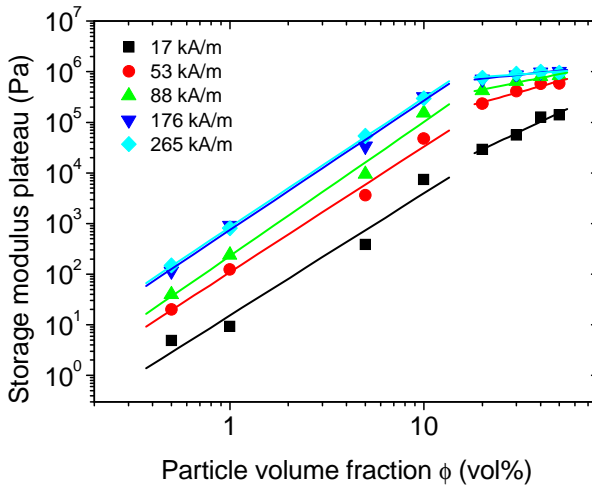


FIG. 5 Low strain storage modulus as a function of particle volume fraction ($0.5 \text{ vol}\%$ – $50 \text{ vol}\%$) for different magnetic field strengths (0 kA/m – 265 kA/m). The lines represent power law fits of the data (see Table I).

As stated in sections above, for fields larger than 10 kA/m , the storage modulus overpasses the loss modulus and this means that the samples are well above the so-called gel point⁶. Hence, the scaling with volume fraction is expected to be no longer of the percolation type but rather is affected mainly by the structure of the individual aggregates^{25,20,26,27}. Accordingly, a convenient way to explore the scaling behavior is to interrogate the particle volume fraction dependence of the low strain storage modulus and the yield strain.

A. Low strain storage modulus

Let us begin reporting the low strain storage modulus dependence. The low strain G' plateau value as obtained from strain amplitude sweeps (Figure 4) is typically used to quantify the elastic character of colloidal MR gels. In the absence of external magnetic fields the storage modulus is negligible below 10 vol%. This finding reinforces the idea that the percolation transition in these MR fluids is around $\phi_c = 10 \text{ vol}\%$. Presumably, this limiting value of 10 vol% should depend on the ratio between the size of the system (i.e. the gap thickness of the rheometer tools) and the typical particle size^{28,29}. As a consequence, different formulations in the MR fluid would give a different ϕ_c . For particle contents larger than 10 vol% the MR fluids display a strong volume fraction dependence of the storage modulus. A power law $G' \sim \phi^n$ with exponent $n = 4.15 \pm 0.30$ is able to fit the data. Experimental values of 2.4 to 4.4 have been reported in the literature³⁰. The magnitude of the power law exponent is believed to be related to interconnectedness and space filling ability of the network microstructure³¹. Hence, this high power in ϕ is indicative of a compact coagulated structure.

For magnetic fields larger than 10 kA/m the storage modulus increases and tends towards a quasi-plateau at large concentrations (Figure 5). Interestingly, two well differentiated regions can be observed where G' exhibits a power-law behavior and can be fitted to the form $G' \sim \phi^n$. The best fit results for n are summarized in Table I. Below a particle concentration of 10 vol%, n value remains approximately constant (~ 2.5) independently of the magnetic field applied. This value is significantly larger than the theoretical predictions under the assumption of single-width particle chains models that predict a scaling with



ϕ^2 , and still larger than classical theories for strong 3-dimensional particulate gels that predict a scaling with ϕ^2 ^{32,33}.

TABLE I. Slopes corresponding to linear fits for low strain storage modulus and yield strain γ_{1L} as a function of particle volume fraction in the gel regime ($H > H_c$) from Figure 5 and Figure 7a, respectively. (*) negative slope.

H(kA/m)	Low strain storage modulus		Yield strain, γ_{1L}	
	$\phi < 10$ vol%	$\phi > 10$ vol%	$\phi < 10$ vol%	$\phi > 10$ vol%
17	2.4 ± 0.3	1.8 ± 0.3	-1.35 ± 0.04	*
53	2.48 ± 0.18	1.06 ± 0.18	-1.35 ± 0.04	0.4 ± 0.5
88	2.7 ± 0.2	0.76 ± 0.12	-1.35 ± 0.04	0.7 ± 0.3
176	2.55 ± 0.12	0.39 ± 0.04	-1.35 ± 0.04	1.4 ± 0.3
265	2.55 ± 0.02	0.26 ± 0.10	-1.35 ± 0.04	2.6 ± 0.2

Above a particle concentration of 10 vol%, n depends on the magnetic field strength. With increasing the field strength, the n value decreases from a value close to 2 to a value of 0.26.

B. Limiting strain/stress for linearity

Upon increasing the strain amplitude, MR fluids eventually yield exhibiting a clear decay in G' associated to the appearance of higher harmonics in the stress signal (see Figure 4). As frequently done, we interpret the onset of nonlinearity to be the breaking of the weakest bonds in the gel-like network. Interestingly, depending on the particle content, G'' exhibits either only one or two peaks

with increasing the strain amplitude that are indicative of a maximum dissipation of energy during the period of destroying the elastic structure. Dilute MR fluids (below 10 vol%) reveal a single yielding process associated to a single peak in G'' around a strain amplitude of $\gamma_0 = 10\%$ as commonly reported in the literature of dilute MR fluids and also predicted by macroscopic and microscopic micromechanical models with $\gamma_0 \sim 50\%$ and $\gamma_0 \sim 30\%$, respectively². Significantly, the peak in G'' occurs when G' drops below G'' meaning that local yielding coincides with macroscopic yielding. More concentrated MR fluids (above 10 vol%) show a complex rheological response with two distinct yielding processes (two peaks in G'') similarly to attractive glasses and colloidal depletion gels with intermediate volume fraction³⁴. In attractive glasses the two yielding processes are associated with the breaking of interparticle bonds at small strains ($\sim 4\%$) and with the limit of elastic cage deformations (i.e. breaking of topological constraints) at large strains ($\sim 50\%$)³⁵. On the other hand, in depletion colloidal gels the first yield point is presumably due to the breaking of bonds between interconnected clusters ($\sim 5\%$) while the second one is attributed to the breaking of clusters into smaller constituents ($\sim 100\%$)³⁶.

A more convenient representation of the dynamic oscillatory strain amplitude sweep data is to plot the strain dependence of the in-phase (elastic) component of the total stress $G'\gamma_0$ ³⁷. Interestingly, this kind of representation highlights the two key factors determining the strength of the MR fluid (i.e. the cohesive energy of the flocs $E_c \sim \frac{1}{2} G' \gamma_{1L}^2$): on the one hand, the attractive force between particles (i.e. storage modulus G') and on the other hand, the strain level at which the structure persists without losing its rigidity (i.e. the limiting strain for linearity γ_{1L}). As a way of example, in Figure 6 we show the results for the lowest and largest fields investigated in this study (17 and 265 kA/m). The

maxima or shoulders of the elastic stress provide a quantitative way of localizing the shear yield point(s).

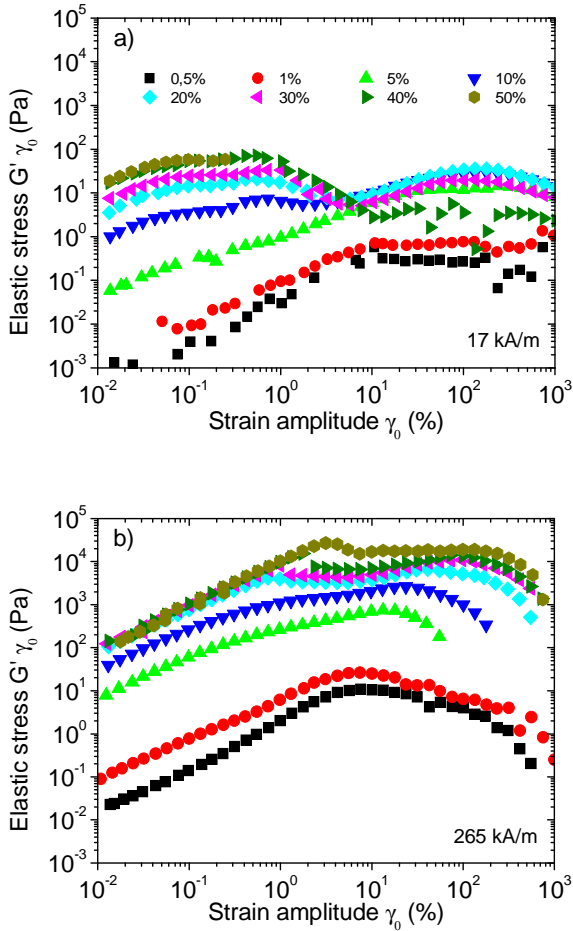


FIG. 6 Elastic stress $G'\gamma_0$ as a function of strain amplitude γ_0 for different particle concentrations from 0.5 vol% to 50 vol%. a) 17 kA/m, b) 265 kA/m.

Actually, this approach has been used in other glassy materials to illustrate the progressive structural breakdown and demonstrated the existence of two yielding processes in attractive glasses and colloidal gels^{38,39,35,40,34,36}. As observed in Figure 6, yield stresses strongly depend on magnetic field strength and particle concentration. For low and medium fields, yield strengths are of similar magnitude $(G'\gamma_0)_{max} \sim \vartheta(10^2 Pa)$ as other experiments reported in literature on weakly flocculated gels, although the maxima are attained at exceedingly small strain values³⁸. Figure 6 reveals that a single yielding process is only present for volume fractions well below 10 vol% independently of the magnetic field. If the particle content increases, a two yielding process is clearly observed. Also, the linear region is very small indeed in the case of low magnetic fields especially at the largest volume fractions investigated.

B.1. Yield strain

Next, we consider the dependence of the two yield points, as well as the crossing point between G' and G'' (so-called flow point⁴¹), on the particle volume fraction and discuss the corresponding yield strains and yield stresses (Figs. 7 and 8). The first yield strain was determined following two approaches: i) from the point beyond which G' deviates more than 10% from its maximum plateau value γ_{1L} (cf Figure 4) and ii) from the first maximum in elastic stress versus strain representations γ_1 (cf Figure 6). Their dependence with particle volume fraction and magnetic field strength is comparable. Also, the limiting strain for linearity obtained for our MR fluids (ranging from $\sim 0.01\%$ to $\sim 1\%$) was about the same level as reported in the literature for MR and ER fluids^{42,38,43,6,44,45}.

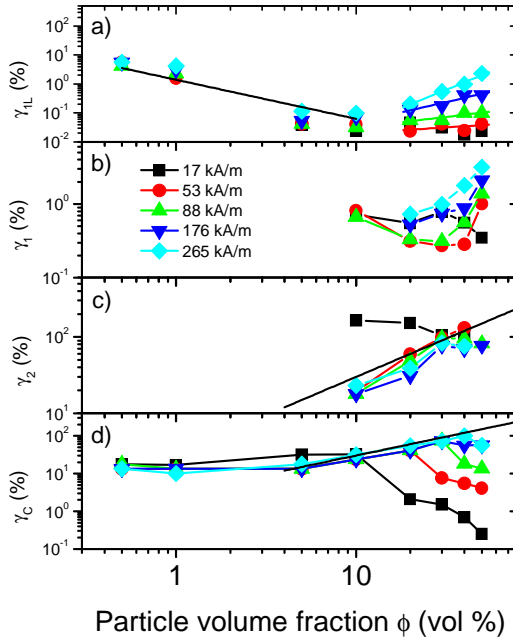



FIG. 7 Yield strains as a function of particle concentration taken from dynamic strain sweeps. a) Limit of the linear viscoelastic region γ_{1L} , b) first yield strain γ_1 , c) second yield strain γ_2 , d) crossover yield strain γ_c ($G' = G''$). The straight lines have power law exponents reported in Table I. Straight lines in c) and d) are exactly the same with a power law exponent of 1.

As observed in Figure 7, there are two well differentiated regions. Below 10 vol% the yield strain strongly decreases with a slope of -1.35 ± 0.04 (see Table I) independently of the magnetic field. This is possibly due to the lower particle densities and the higher structural and bonding flexibility that allows



elongation and stretching before bonds break similarly to depletion gels³⁶. In this region, the MR fluid becomes stiffer with increasing concentration hence showing a large modulus (cf Figure 5), but starts to break at smaller strain as the observable linear region shrinks with increasing particle concentration (ie. stronger gels also are more brittle). However, above 10 *vol%* the yield strain either remains constant at a low value for small fields, or increases as a power law for larger fields. We will come back to this point in Section VI. For the moment, it is worth to remark here that the behavior of our MR fluids at the lowest magnetic fields investigated very closely resembles the behaviour of 3D depletion gels investigated by Koumakis and Petekidis (2011)³⁶.

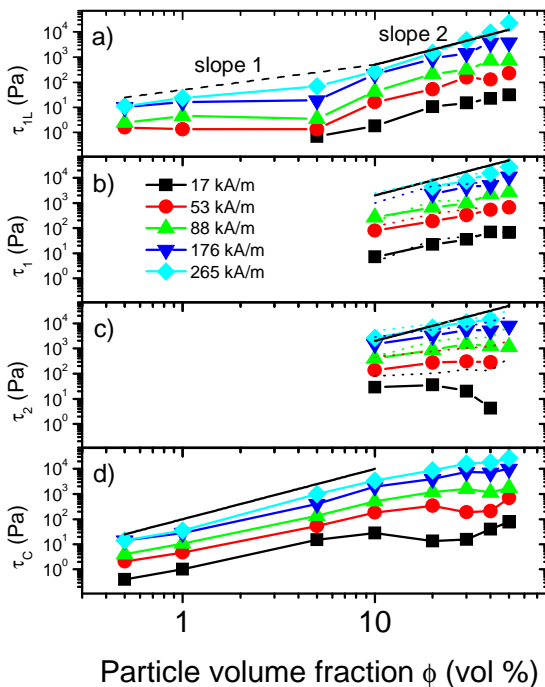


FIG. 8 Stresses corresponding to the yield strains of Figure 7. a) Limit of the linear viscoelastic region τ_{1L} , b) first yield stress τ_1 , c) second yield stress τ_2 , d) crossover yield stress τ_c ($G' = G''$). The straight lines have a power law exponent of 1.0 (dashed line) and 2.0 (solid line). Dotted lines correspond to static (Figure b) and dynamic (Figure c) yield stress measurements under steady shear flow tests.

The second yield strain γ_2 is found to increase with increasing the particle concentration as expected because particle caging should reinforce as concentration increases. Only for the lowest field investigated the second yield

strain decreases. This apparently surprising result for the lowest field can be explained if cages turn into clusters due to attractions as the volume fraction decreases. Hence, the second yield strain should increase with decreasing particle content because of the enhanced flexibility of interconnected clusters³⁶. Of course, the second yielding process disappears at particle concentrations below 10 vol% in agreement with a critical concentration of $\phi_c = 10 \text{ vol}\%$.

MR fluids show a liquid-like behavior ($G'' > G'$) for strain amplitudes larger than the crossover strain γ_c . This crossover strain amplitude is expected to have an intermediate behavior between γ_{1L} (or γ_1) and γ_2 when increasing the particle concentration ($\gamma_{1L} \sim \gamma_1 < \gamma_c < \gamma_2$). As a consequence, for the lowest particle concentration investigated $\gamma_c \sim \gamma_{1L} \sim 10 \%$, while for the largest concentrations investigated $\gamma_c \sim \gamma_2$ (see Figure 7). Actually, for low particle concentrations, aggregates are expected to be both scarce and floppy and by simply breaking some intra-aggregate bonds the suspensions may flow. On the contrary, for more concentrated MR fluids it is necessary to break not only inter-aggregate bonds but also intra-aggregate links to make the suspension flow resulting in the observed power law increase of γ_c (exponent of 1) for concentrations larger than 10 vol%. It is interesting to observe that γ_c remains essentially constant ($\gamma_c \sim 10 \%$) for particle concentrations below 10 vol%. This suggests that in this concentration range, MR fluids are increasingly brittle but do shear melt ($G'' > G'$) at the same strain amplitude. The reason for this is unknown yet. Finally, decreasing branches in γ_c are presumably associated to flow instabilities as G' reverses to lower stresses when increasing the strain amplitude. An extreme example is the yielding behavior of MR fluids at 17 kA/m.



B.2. Yield stress

The yield stresses corresponding to the various yield strain points discussed above are plotted in Figure 8. For a given particle volume fraction, these are expected to be the multiplication of the low shear storage modulus by the yield strain ($\tau = G'\gamma$). As a consequence, the stresses involved in the first yield point do linearly increase up to a particle concentration of 10 *vol%*. In this region, the effect of magnetic field is manifested through the field dependence of the storage modulus as the yield strain is not sensitive to the field in this concentration range. For a particle concentration larger than 10 *vol%* the first yield stress increases with ϕ following a power law dependence with an exponent of 2.0 that is independent of the magnetic field applied in spite of the fact that both the storage modulus and yield strain strongly depend on the magnetic field applied (see Figs. 5 and 7, respectively). These results are in good agreement with previous experimental data reported in the literature where an intermediate slope between 1 and 2 has been claimed in a very wide volume fraction range spanning from 0.1 to 50 *vol%*. Remarkably, here we show that a closer look to the volume fraction dependence reveals two well differentiated regions. It is also interesting to note that there is a good correlation between the first yield stress and the static yield stress obtained from steady shear flow tests exemplified in Figure 3 (cf. dotted lines in Figure 8b).

The second yield stress exhibits a more complex behavior. The field dependence of the second yield stress comes from the field dependence of the storage modulus. The only exception being the lowest field investigated because in this case not only the modulus but also the second yield strain depends on the field strength. As a consequence, the slopes of these curves change when changing

the field. It is also interesting to note that there is a reasonably good correlation between the second yield stress and the so-called dynamic (Bingham) yield stress values extrapolated from rheograms to zero shear rate (cf. dotted lines in Figure 8c). These Bingham yield stresses were found to depend on the square of the volume fraction in many colloidal^{46,47,33}.

The crossover yield stress represents the transition between the viscoelastic solid at low strain and the viscoelastic liquid at high strain. As observed in Figure 8d, a power law exponent of two is obtained as a function of the volume fraction.

VI. COLLOIDAL GEL DESCRIPTION

Generally speaking, the link between the structural properties of colloidal gels and their macroscopic rheological behavior is provided by a so-called scaling theory. Basically, the structures in MR fluids are highly disordered, but similarly to other colloidal gels, there is experimental evidence that in certain length scales and at sufficiently low volume fractions they are self-similar and can be described in terms of fractal geometry⁴⁸. Fractal models assume that the structure of the gels is constituted by a collection of closed packed fractal clusters of colloidal particles which during gelation aggregate with each other. Pioneering work in this field was carried out by Brown and Ball (1985)²⁵. They formulated a power-law relationship of the elastic modulus to the solid volume fraction. This formulation was experimentally verified by Sonntag and Russel (1987)⁴⁹ and Buscall *et al.* (1988)⁵² among others. Then, Shih *et al.* (1990)²⁰ and Wu and Morbidelli (2001)²⁶ extended the models by Brown and Ball (1985)²⁵



including previous contributions by Kantor and Webman (1984)⁵¹ and Buscall *et al.* (1988)⁵².

In general, depending on the strength of the links between the aggregates in comparison to that of the aggregates, we can distinguish two limiting rheological regimes, namely, strong-link regime and weak-link regime reminiscent of the scaling theory for polymeric systems (Figure 9)²⁶. The strong-link regime is achieved with very big flocs while the weak-link regime results from the formation of small flocs. At low particle concentration, well inside the strong-link regime, the links between aggregates (inter) are stronger than the intrinsic elasticity of the aggregates (intra). As a consequence, the breaking of bonds occurs within an aggregate. On the contrary, at high particle concentration, the so-called weak-link regime prevails that is dominated by the elasticity of the aggregates rather than the interlinks between aggregates. The scaling (power law behaviour) for both the storage modulus G' and the limit of linearity (i.e. yield strain) γ_{1L} with respect to the particle concentration ϕ is dictated by the fractal nature of the colloidal flocs. The forms of the equations for the strong-link regime (SLR) are:

$$G'_{SLR} \sim \phi^{(d+x)/(d-d_f)} \quad (1a)$$

$$\gamma_{1L,SLR} \sim \phi^{-(1+x)/(d-d_f)} \quad (1b)$$

whereas the equations for the weak-link regime (WLR) read as follows:

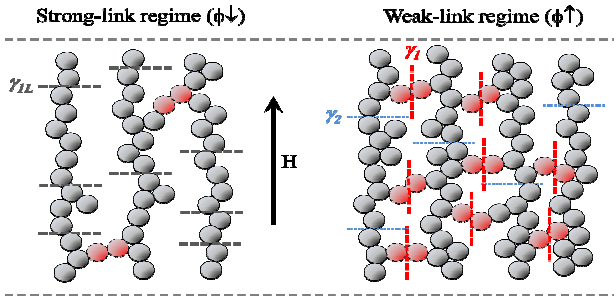


FIG. 9 Structure representation of a gelled MR fluid for $H > H_c$. Dashed lines represent the weakest bonds in the field-induced structures. Red dotted spheres represent the secondary structure reported in Pan and McKinley (1997)³⁸. Left; $\phi < \phi_c$, strong-link regime. Right; $\phi > \phi_c$, weak-link regime.

$$G'_{WLR} \sim \phi^{(d-2)/(d-d_f)} \quad (2a)$$

$$\gamma_{1L,WLR} \sim \phi^{1/(d-d_f)} \quad (2b)$$

Here d is the Euclidean dimension ($d = 3$), d_f is the fractal dimension of the flocs, and x is the backbone fractal dimension of the flocs ($1 < x < d_f$)²⁰. On the one hand, the fractal dimension d_f is a parameter that describes the spatial distribution of mass within the network. On the other hand, the parameter x is that fraction of the aggregate that sustains the applied load. It is difficult to estimate and is usually assumed to be in the range $x \in [1, 1.3]$ ^{27,53}. Both strong- and weak-link extreme situations have been verified by experiments using various gelation systems^{20,54,55,56,57}.



Of course, the strong- and weak-link regimes described by Shih *et al.* (1990)²⁰ represent two extreme situations. In practice, intermediate situations have been reported in the literature, in the so-called transition regime (TR), where both inter-aggregate and intra-aggregate links contribute to the gel's overall elasticity^{55,56}. Expressions for G' and γ_{1L} in this intermediate situation were developed by Wu and Morbidelli (2001)²⁶:

$$G'_{TR} \sim \phi^{\beta/(d-d_f)} \quad (3a)$$

$$\gamma_{1L,TR} \sim \phi^{(d-\beta-1)/(d-d_f)} \quad (3b)$$

where $\beta = (d - 2) + (2 + x)(1 - \alpha)$ and α is a microscopic elastic constant in the range $\alpha \in [0,1]$. As expected, equations for the transition regime reproduce correctly the limiting scenarios; for the strong-link regime $\alpha = 0$, whereas for the weak-link regime $\alpha = 1$.

As shown in sections above, in the absence of magnetic fields, conventional MR fluids reported in this manuscript exhibit a power law dependence of both the storage modulus and yield strain on the volume fraction for $\phi > 10 \text{ vol}\%$: $G' \sim \phi^{4.15 \pm 0.30}$ and $\gamma_{1L} \sim \phi^{-0.91 \pm 0.21}$, respectively. It is well known that the exponent of the volume fraction dependence of the storage modulus is related to the structure through the fractal dimension of the clusters and also related to the mechanism of particle aggregation. For example, experiments and simulations show that the exponent should be 4.5 ± 0.2 for a reaction-limited (slow) aggregation (RLA) process and 3.5 ± 0.2 for a diffusion-limited (fast) cluster-cluster aggregation (DCA) process^{50,27}. Using the model developed by

Wu and Morbidelli (2001)²⁶, and assuming a fractal dimension of backbones $x = 1.3$ we estimated a value of $\alpha = 0.527$ and a fractal dimension $d_f = 2.383$, the later being very close to the reaction-limited aggregation (RLCA) model prediction $d_f = 2.1$ suggesting that the MR fluid, in the absence of magnetic fields, behaves similarly to conventional transition gels (see Table II)^{55,56}. Interestingly, these results suggest that other interparticle interactions apart from purely magnetostatic forces exist that are relevant in the absence of magnetic fields. As previously emphasized in the Introduction section, these findings are in good agreement with microscopic observations in very similar (conventional) MR fluids reported in the MR literature. Also, similar values for the power-law exponent (4.0 ± 0.5) for the elastic modulus were obtained in silica and polystyrene latex suspensions⁵⁰ and fumed silica dispersions⁵⁸.

TABLE II. Evaluated microscopic parameters at $x = 1.3$ ($/ x = 1.0$) using Wu and Morbidelli model (2001)²⁶ for conventional MR fluids. α microelasticity constant and d_f fractal dimension.

	α	d_f	Gel type	
>10 vol% no field	0.527	2.383	Transition gel	
<10 vol% all fields	0	1.32	Strong-link gel	
>10 vol%	17 kA/m	0.697 / 0.667	1.889 / 1.889	Transition gel
	53 kA/m	0.863 / 0.849	1.63 / 1.63	Weak-link gel
	88 kA/m	0.988 / 0.986	1.63 / 1.63	Weak-link gel
	176 kA/m	1.171 / 1.188	1.883 / 1.883	Weak-link gel
	265 kA/m	1.248 / 1.273	2.301 / 2.301	Weak-link gel



The behavior of MR fluids under the presence of magnetic fields is more complex. Samples below 10 vol% do behave similarly, independently of the magnetic field strength. Using the corresponding equations for the strong-link regime we obtain $x = 1.269$ and $d_f = 1.319$, while using the model by Wu and Morbidelli (2001)²⁶ we obtain $\alpha = 0$ and a fractal dimension $d_f = 1.32$ —under the assumption of $x = 1.3$, as otherwise is frequently done in the literature²⁶—(Table II). As observed, the fractal dimension estimated from the two models is very similar indeed. The similar results obtained under the application of the two fractal models indicate that the system is in the strong-link regime. Besides, the small value of the fractal dimension is in agreement with a much smaller cluster size²⁷, if compared to the fractal dimension obtained in the absence of magnetic fields, and also in agreement with the formation of one-dimensional elongated structures in the direction of the field⁵⁹.

More concentrated suspensions (> 10 vol%) under the presence of magnetic fields do exhibit an interesting behavior. Using the corresponding relations for the weak-link regime to estimate d_f one obtains unrealistic values as they are different when obtained from G' and γ_{1L} data. However, when using Wu and Morbidelli (2001)²⁶ model remarkable results are found. Results contained in Table II show that either choosing $x = 1$ or $x = 1.3$ do not provide much difference. For the weakest field investigated, $\alpha = 0.697$ and $d_f = 1.889$ suggesting that in this case inter- and intrafloc links are comparable, and then we are in the transition regime. This justifies the failure of the application of the weak-link model ($\alpha = 1$). Upon increasing the field, α increases up to a value very close to $\alpha = 1$ (for fields ≥ 88 kA/m) while the fractal dimension still remains close to $d_f = 1.7$ independently of the field strength applied. Only for

the largest fields investigated d_f increases possibly due to the much larger cluster size²⁷.

A priori, any colloidal gel may cross over from the strong-link regime to the weak-link regime with increasing particle concentration and this seems to be the case in conventional MR fluids under the presence of an external magnetic field from the inspection of Figs. 5 and 7a. This is manifested by the appearance of two regions. On the one hand, for low concentrations, G' increases with particle content, while γ_{1L} decreases with particle content. On the other hand, for large particle contents, G' still increases but more slowly than in the strong-link regime, and γ_{1L} increases with concentration. Accordingly, MR fluids operating in the strong-link regime (below 10 vol%) do exhibit a single yielding process (γ_{1L}) that is associated to intracluster bond breaking. On the contrary, MR fluids operating in the weak-link regime (above 10 vol%) do exhibit a two yielding process (γ_1 and γ_2) that are associated to the breaking of bonds between interconnected clusters and to the breaking of clusters into smaller constituents, respectively.

The explanation above seems to be coherent with the fact that micromechanical models available in MR literature are only valid at low particle concentration². This is expected because only for low particle concentrations it is feasible to assume that bond breaking first occurs inside the aggregate. Also, for large enough concentrations, the first yielding process is compatible with the existence of a secondary structure resulting from many-body interactions, and comprised of short chains tilted with respect to the field direction³⁸. This secondary structure originates a nonuniform distribution of local strain that is at the heart of the exceedingly low values of γ_{1L} and γ_1 .



Finally, it is worth to remark that the application of colloidal gel scaling theories in magnetorheology has limitations. First, original fractal gel models did not take into account the field strength-dependent, long-range and anisotropic feature of the magnetic interactions between particles. As a consequence, special care has to be taken when drawing conclusions. Second, inherent to the theory is the fact that the interactions between particles are assumed to be independent of particle concentration. In general, it has been documented that clusters may swell in dilute suspensions if the interparticle interaction has a particle-concentration dependence^{20,60}. Unfortunately, strictly speaking, this is not the case for MR fluids where interparticle magnetic forces enhance due to multipolar effects upon increasing the concentration. Consequently, this suggests that we are far from the ideal case where the volume fraction and strength of attraction could be varied independently. Third, the fractal gel models do have an upper and lower concentration bound. The lower bound is limited by the maximum size of the growing flocs and the upper bound is determined by the shrinking range of the fractal scaling region with concentration²⁹. Generally speaking, fractal models can be applied only for low enough particle concentrations –even though the fractal scaling behavior has been observed at high volume fractions as well⁵²–. At large volume fractions the number of particles per cluster are in fact so small that the use of fractal models can no longer be justified and more advanced theoretical models would be needed^{26,61}.

VII. CONCLUSIONS

We have conducted an extensive experimental research on model magnetorheological fluids having a wide range of particle concentrations and

submitted to a wide range of uniaxial DC magnetic field strengths. These experiments show that most of the inconsistencies found in MR fluid literature regarding particle concentration dependences can be explained under a colloidal gel perspective well above the gelation threshold ($H > H_c$). For typical particle contents employed in the formulation of conventional MR fluids, the elastic behavior of the field-induced gels is not determined by the scaling of the percolation transition as it might be near the gelation threshold⁶² but is instead dominated by the fractal nature of the colloidal flocs.

Considering the structure of the field-induced gel network as a collection of closed-packed fractal flocs of colloidal particles, two different scenarios are found depending on the particle concentration. On the one hand, for low enough particle volume fractions in the strong-link regime the storage modulus increases with increasing the concentration while the yield strain decreases with increasing the particle content. On the other hand, for large particle concentrations, well in the weak-link regime, both the storage modulus and yield strain increase when increasing the particle concentration. The crossover concentration ($\phi_c \sim 10 \text{ vol}\%$) from the strong-link regime to the weak-link regime does not depend on the magnetic field strength but is expected to depend on the ratio between the gap thickness and particle size. We demonstrate that the existence of a crossover concentration has severe consequences in the yielding behavior of MR fluids both under steady and dynamic oscillatory shearing flows. A single yielding process only appears when the concentration is below ϕ_c . For larger particle contents, a two-step yielding process comes up that reveals similarities to the rheology of attractive colloidal glasses and depletion colloidal gels, and resembles the classical static and dynamic definitions for the yield stress.



We have demonstrated that by using a colloidal gel scaling theory it is possible to extract structural information that otherwise is difficult to be obtained because MR fluids are opaque and conventional light scattering techniques are not easily applied. Surprisingly, very few papers have treated MR fluids as physical gels, in spite that MR fluids are simple fluids amenable to be used as prototypes of the directional gel transition of colloidal gels. The rheological fractal model developed by Wu and Morbidelli (2001)²⁶ is successfully employed to the case of MR fluids in the presence of magnetic fields. Its use is twofold: i) from the rheological data it is possible to extract structural information of the aggregates such as the fractal dimension, and ii) assuming the backbone fractal dimension, one can compute the corresponding α value and identify the gelation regime prevailing in the system.

Results presented in this work are believed to have implications in the formulation of effective MR fluids containing the optimal amount of magnetic material according to the desired application and hence reducing costs.

ACKNOWLEDGEMENTS

This work was supported by MAT-2010-15101 project (MICINN, Spain), by the European Regional Development Fund (ERDF) and by Junta de Andalucía P11-FQM-7074 and P10-RNM-6630 projects (Spain). J.P.S.-G. acknowledges financial support by the “Ministerio de Educación: Becas del Programa de Formación del Profesorado Universitario (FPU)” (AP2008-02138).

**REFERENCES**

- ¹Klingenberg, D. J., "Magnetorheology: applications and challenges," *AIChE journal*, **47(2)**, 246-249 (2001).
- ²de Vicente, J., D. J. Klingenberg and R. Hidalgo-Álvarez, "Magnetorheological Fluids: A Review," *Soft Matter* **7**, 3701-3710 (2011).
- ³Berli, C. L. A., and J. de Vicente, "A structural viscosity model for magnetorheology," *Appl. Phys. Lett.* in press.
- ⁴Hao, T., Y. Chen, Z. Xu, Y. Xu, and Y. Huang, "Percolation transition in electrorheological fluids," *Chin. J. Polym. Sci.* **12**, 97-105 (1994).
- ⁵Hao, T., and Y. Xu, "Microstructure-confined mechanical and electric properties of the electrorheological fluids under the oscillatory mechanical field," *J. Colloid Interf. Sci.* **185**, 324-331 (1997).
- ⁶Chin, B. D., and H. H. Winter, "Field-induced gelation, yield stress, and fragility of an electro-rheological suspension," *Rheol. Acta* **41**, 265-275 (2002).
- ⁷Park B. J., F. F. Fang, and H. J. Choi, "Magnetorheology: materials and application," *Soft Matter* **6**, 5246-5253 (2010).
- ⁸Ramos, J., D. J. Klingenberg, R. Hidalgo-Álvarez and J. de Vicente, "Steady Shear Magnetorheology of Inverse Ferrofluids," *J. Rheol.* **55(1)**, 127-152 (2011).
- ⁹Ginder, J. M., L. C. Davis, and L. D. Elie, "Rheology of magnetorheological fluids: models and measurements," *Int. J. Mod. Phys. B* **10**, 3293-3303 (1996).
- ¹⁰Felt, D. W., M. Hagenbuchle, J. Liu, and J. Richard, "Rheology of a magnetorheological fluid," *J. Intel. Mat. Syst. Str.* **7**, 589-593 (1996).
- ¹¹Goodwin, J. W., G. M. Markham, and B. Vincent, "Studies on model electrorheological fluids," *J. Phys. Chem. C* **101**, 1961-1967 (1997).
- ¹²Rankin, P. J., A. T. Horvath, and D. J. Klingenberg, "Magnetorheology in viscoplastic media," *Rheol. Acta* **38**, 471-477 (1999).



- ¹³Volkova, O., G. Bossis, M. Guyot, V. Bashtovoi, and A. Reks, "Magnetorheology of magnetic holes compared to magnetic particles," *J. Rheol.* **44(1)** 91-104 (2000).
- ¹⁴Chin, B. D., J. H. Park, M. H. Kwon, and O. O. Park, "Rheological properties and dispersion stability of magnetorheological (MR) suspensions," *Rheol. Acta* **40**, 211-219 (2001).
- ¹⁵Rankin, P. J., and D. J. Klingenberg, "The electrorheology of barium titanate suspensions," *J. Rheol.* **42(3)**, 639-656 (1998).
- ¹⁶Fujita, T., K. Yoshimura, Y. Seki, G. Dodbiba, T. Miyazaki, and S. Numakura, "Characterization of magnetorheological suspensions for seal," *J. Intel. Mat. Syst. Str.* **10**, 770-774 (2000).
- ¹⁷Wollny, K., J. Lauger, and S. Huck, "Magneto sweep - a method for characterizing the viscoelastic properties of magneto-rheological fluids," *Appl. Rheol.* **12**, 25-31 (2002).
- ¹⁸Laun, H. M., G. Schmidt, and C. Gabriel, "Reliable plate-plate MRF magnetorheometry based on validated radial magnetic flux density profile simulations," *Rheol. Acta* **47**, 1049-1059 (2008).
- ¹⁹Laeuger, J., K. Wollny, H. Stettin, and S. Huck, "A new device for the full rheological characterization of magneto-rheological fluids," *Int. J. Mod. Phys. B* **19**, 1353-1359 (2005).
- ²⁰Shih, W-H., Shih, W.Y., Kim, S-I., Liu, J., and I.A. Aksay, "Scaling behavior of the elastic properties of colloidal gels," *Phys. Rev. A* **42(8)**, 4772-4779 (1990).
- ²¹Trappe, V., V. Prasad, L. Cipelletti, P. N. Segre, and D. A. Weitz, "Jamming phase diagram for attractive particles," *Nature* **411**, 772-775 (2001).
- ²²Klingenberg, D. J., J. C. Ulicny, and M. A. Golden, "Mason numbers for magnetorheology," *J. Rheol.* **51**, 883-893 (2007).

- ²³de Vicente, J., F. González-Caballero, G. Bossis, and O. Volkova, "Normal force study in concentrated carbonyl iron magnetorheological suspensions," *J. Rheol.* **46(5)**, 1295-1303 (2002).
- ²⁴Laun, H. M., C. Gabriel, and Ch. Kieburg, "Magnetorheological fluid (MRF) in oscillatory shear and parameterization with regard to MR device properties," *J. Phys: Conf. Series* **149**, 012067 (2009).
- ²⁵Brown, W. D., and R. C. Ball, "Computer simulation of chemically limited aggregation," *J. Phys. A* **18**, L517-L521 (1985).
- ²⁶Wu, H., and M. Morbidelli, "A model relating structure of colloidal gels to their elastic properties," *Langmuir* **17**, 1030-1036 (2001).
- ²⁷Marangoni, A. G., "The nature of fractality in fat crystal networks," *Trends in Food Science & Technology* **13**, 37-47 (2002).
- ²⁹Yanez, J. A., E. Ilaar, and L. Bergstrom, "Viscoelastic properties of particles gels," *Journal of Colloid and Interface Science* **209**, 162-172 (1999).
- ³⁰Macosko, C. W. "Rheology: principles, measurements and applications," Wiley-VCH: New York, 1994, page 457.
- ³¹Tadros, Th. F., "Correlation of viscoelastic properties of stable and flocculated suspensions with their interparticle interactions," *Advances in Colloid and Interface Science* **68**, 97-200 (1996).
- ³²Russell, W. D., D. A. Saville, and W. R. Schowalter, *Colloidal dispersions*, Cambridge University Press, United Kingdom, 1989. Chapter 14.
- ³³Larson, R. G., *The Structure and Rheology of Complex Fluids*, Oxford University Press, New York, 1999. Chapter 7.
- ³⁴Laurati, M., S. U. Egelhaaf, and G. Petekidis, "Nonlinear rheology of colloidal gels with intermediate volume fraction," *J. Rheol.* **55(3)**, 673-706 (2011).



- ³⁵Pham, K. N., G. Petekidis, D. Vlassopoulos, S. U. Egelhaaf, P. N. Pusey, and W. C. K. Poon, "Yielding of colloidal glasses," *Europhysics Letters* **75(4)**, 624-630 (2006).
- ³⁶Koumakis, N., and G. Petekidis, "Two step yielding in attractive colloids: transition from gels to attractive glasses," *Soft Matter* **7**, 2456-2470 (2011).
- ³⁷Yang, M. -C., L. E. Scriven, and C. M. Macosko, "Some rheological measurements on magnetic iron-oxide suspensions in silicone oil," *J. Rheol.* **30**, 1015-1029 (1986).
- ³⁸Pan, X. -D., and G. H. McKinley, "Structural limitation to the material strength of electrorheological fluids," *Appl. Phys. Lett.* **71(3)**, 333-335 (1997).
- ³⁹Pai, V. B., and S. A. Khan, "Gelation and rheology of xanthan/enzyme-modified guar blends," *Carbohydr. Polym.* **49**, 207-216 (2002).
- ⁴⁰Pham, K. N., G. Petekidis, D. Vlassopoulos, S. U. Egelhaaf, W. C. K. Poon, and P. N. Pusey "Yielding behavior of repulsion- and attraction-dominated colloidal glasses," *J. Rheol.* **52**, 649-676 (2008).
- ⁴²Weiss, K. D., J. D. Carlson, and D. A. Nixon, "Viscoelastic properties of magneto- and electrorheological fluids," *J. Intell. Mater. Syst. Struct.* **5**, 772-775 (1994).
- ⁴¹Mezger, T. G., *The Rheology Handbook*, 2nd ed. Vincentz, Germany, 2006.
- ⁴³Parthasarathy, M., and D. J. Klingenberg "A microstructural investigation of the nonlinear response of electrorheological suspensions. 1. Start-up of steady shear flow," *Rheol. Acta* **34**, 417-429 (1995).
- ⁴⁴Claracq, J., J. Sarrazin, and J. P. Montfort, "Viscoelastic properties of magnetorheological fluids," *Rheol. Acta* **43**, 38-49 (2004).
- ⁴⁵de Vicente, J., M. T. López-López, J. D. G. Durán, and G. Bossis, "A slender-body micromechanical model for viscoelasticity of magnetic colloids: comparison with preliminary experimental data," *J. Colloid Interf. Sci.* **282**, 193-201 (2005).

- ⁴⁶Buscall, R., J. W. Goodwin, M. W. Hawkins, and R. H. Ottewill, "Viscoelastic properties of concentrated lattices, Part 1.- Methods of examination," *J. Chem. Soc. Faraday Trans. 1*, **78**, 2873-2887 (1982).
- ⁴⁷Goodwin, J. W., in *Colloid Science*, ed. D. H. Everett (Specialist Periodical Report, The Chemical Society, London, 1976), **Vol. II**, p. 242.
- ⁴⁸Mandelbrot, B. "The fractal geometry of nature," W. H. Freeman: New York, 1982.
- ⁴⁹Sonntag, R. C., and W. B. Russell, "Elastic properties of flocculated networks," *Journal of Colloid and Interface Science* **116**, 485-489 (1987).
- ⁵¹Kantor, Y., and I. Webman, "Elastic properties of random percolating systems," *Phys. Rev. Lett.* **52**, 1891-1894 (1984).
- ⁵²Buscall, R., P. D. Mills, J. W. Goodwin, and D. W. Dawson, "Scaling behaviour of the rheology of aggregate networks formed from colloidal particles," *J. Chem. Soc. Faraday Trans* **84**, 4249-4260 (1988).
- ⁵³Song, F., L. -M. Zhang, J. -F. Shi, and N. -N. Li, "Viscoelastic and fractal characteristics of a supramolecular hydrogel hybridized with clay nanoparticles," *Colloids and Surfaces B: Biointerfaces* **81**, 486-491 (2010).
- ⁵⁴Marangoni, A. G., and D. Rousseau, "Is plastic fat rheology governed by the fractal nature of the fat crystal network?," *J. Am. Oil. Chem. Soc.* **73**, 991-994 (1996).
- ⁵⁵Hagiwara, T., H. Kumagai, T. Matsunaga, "Fractal analysis of the elasticity of BSA and beta-lactoglobulin gels," *J. Agric. Food. Chem.* **45**, 3807-3812 (1997).
- ⁵⁶Ikeda, S., E. A. Foegeding, and T. Hagiwara, "Rheological study on the fractal nature of the protein gel structure," *Langmuir* **15**, 8584-8589 (1999).
- ⁵⁷Narine, S. S., and A. G. Marangoni, "Relating structure of fat crystal networks to mechanical properties: a review," *Food Research International* **32**, 227-248 (1999).




⁵⁸Khan, S. A., and N. J. Zoeller, "Dynamic rheology of flocculated fumed silica suspensions," *J. Rheol.* **37**, 1225-1235 (1993).

⁵⁹Domínguez-García, P., and M. A. Rubio, "Three-dimensional morphology of field-induced chain-like aggregates of superparamagnetic microparticles," *Colloids Surf. A* **358**, 21-27 (2010).

⁶⁰de Gennes, P. G., "Scaling concepts of polymer physics," Cornell University Press, Ithaca, New York, 1979.

⁶¹Vermant, J., and M. J. Solomon, "Flow-induced structure in colloidal suspensions," *J. Phys.: Condens. Matter* **17**, R187–R216 (2005).

⁶²Zimmerman, D. T., R. C. Bell, J. A. Filer II, J. O. Karli, and N. M. Wereley, "Elastic percolation transition in nanowire-based magnetorheological fluids," *Appl. Phys. Lett.* **95**, 014102 (2009).

**Title of the manuscript**

Average particle magnetization as an experimental scaling parameter for the yield stress of dilute magnetorheological fluids

Authors

F. Vereda¹, J. de Vicente¹, J. P. Segovia-Gutiérrez¹, R. Hidalgo-Alvarez¹

Affiliation

¹ Departamento de Física Aplicada, Facultad de Ciencias, Universidad de Granada, Granada E-18071, Spain

Published

Journal of Physics D: Applied Physics, 44(2011), 425002 (2011)



Abstract

We propose an experimental parameter for the scaling of the yield stress (τ_y) of magnetorheological (MR) fluids: the average particle magnetization $\langle M_p \rangle$ as estimated from magnetization curves of the MR suspensions. When τ_y was expressed as a function of this scaling parameter, the curves for MR suspensions prepared with particles of different saturation magnetization and even different morphology collapsed together. In addition, the collapse worked reasonably well for a wide range of magnetic fields: from weak fields below which the sensitivity of our magnetorheometer could not detect the τ_y to fields close to particle saturation. The collapse failed for particles of a highly anisotropic morphology, which must be indicative of non-magnetostatic contributions to the yield stress.

I. INTRODUCTION

Conventional magnetorheological (MR) fluids are suspensions of relatively large (ca. $1 \mu m$) magnetizable particles in a non-magnetic liquid carrier. Because of the size of the particles, the magnetic forces typically overcome particle thermal agitation upon the application of an external magnetic field. This leads to a structuration within the suspension and to a dramatic change in its mechanical properties that can be regarded as a transition from a liquid to a nearly solid state¹.

The yield stress τ_y is one of most relevant properties in the characterization and design of MR fluids. It is the minimum stress needed for the onset of flow, and is therefore an indication of the strength of the field-induced structure. Because of practical reasons, research has traditionally focused on the prediction of the

dependence of the yield stress on the external magnetic field (H). Such dependence can be expressed as a power law ($\tau_y \sim H^n$). However, due to the non-linearity of the magnetization of dispersed materials, different exponents (n) are expected for weak, intermediate and strong external fields. It is well established that the yield stress is proportional to H^2 at small fields, and that it reaches a plateau (i.e., becomes field-independent) once particle magnetization saturates. In the saturation regime the stress scales with the square of the saturation magnetization of the particles². For intermediate fields, Ginder *et al.*³ and Bossis *et al.*⁴ predicted that τ_y would be proportional to $H^{3/2}$. Such dependence has been observed experimentally^{5,6}, although other reports are inconsistent with that prediction⁷.

In this letter we present an experimental parameter that has been successfully used for the scaling of mostly all that yield stress data collected by our group in the past few years⁸ for a variety of dilute MR fluids. Such parameter seems to capture well the external field dependence, is easily accessible, and should be useful for experimentalists and engineers dedicated to magnetorheology.

Scaling functions are particularly useful in science because they can gather together the dependences of a given physical property on several variables. Furthermore, they usually provide physical insight into the forces or interactions that are relevant to the phenomenon under study. The two most frequently used scaling parameters in magnetorheology (and electrorheology) are probably the coupling parameter (λ)⁹ and the Mason number (Mn)¹⁰. The former parameter, λ is the balance between the magnetostatic energy and the thermal energy of the system. In the absence of flow, the equilibrium structure of a MR fluid can be determined by the particle volume fraction (ϕ) and λ ⁹. Another important parameter in magnetorheology is Mn . When MR fluids are subjected



to a flow, the dependence of the fluid viscosity on the shear rate and the magnetic field strength can be collapsed into a single function of Mn , which is basically the ratio between the hydrodynamic drag and the magnetostatic forces acting on the particles. In addition to λ and Mn , a number of examples of yield stress scaling functions in electrorheology and magnetorheology can be found in the literature¹¹⁻¹³.

In λ and Mn both the magnetostatic energy (in λ) and magnetostatic forces (in Mn) are usually calculated within the frame of the fixed point-dipole approximation, and are proportional to the square of the magnetic moment (m) induced in each particle. It is also common^{1,7,14,15} to calculate m as a function of the external field H and the magnetic contrast factor β

$$m \propto \beta H \quad (1)$$

where β is given by $(\mu_p - \mu_f) / (\mu_p + 2\mu_f)$, and μ_p and μ_f are the relative permeabilities of the particles and the fluid carrier, respectively.

The point-dipole approximation and the linear dependence of m with m and H work reasonably well for small fields and for wide separations between particles. For intermediate fields, β becomes field dependent. Some authors use experimental magnetization curves for the particles, or $M(H)$ curves calculated from the Fröhlich–Kennelly equation, to calculate $\mu_p(H)$ and thus introduce the dependence of β on H . For finite separations H and β vary with position in the vicinity of the particles, and m is no longer proportional to βH .

An alternative approach is to express m as a function of an average volumetric particle magnetization $\langle M_p \rangle$:

$$m = V \langle M_p \rangle \quad (2)$$

Both the typical energy and magnetostatic force would be then proportional to $\langle M_p \rangle^2$, where $\langle M_p \rangle$ as a function of H can be obtained dividing the measured suspension magnetization by the volume fraction¹⁶:

$$\langle M_p(H) \rangle = \frac{M_{Suspension}(H)}{\phi} \quad (3)$$

The calculation of the average particle magnetization from magnetization curves of the suspensions was proposed by Klingenberg and co-workers¹⁶, who used it for the calculation of Mn and the collapse of flow curves. Finite-element calculations carried out by these authors showed a better scaling of the interparticle magnetic force with respect to $\langle M_p \rangle^2$ than with respect to $(\beta H)^2$. The calculations also showed that the scaling was valid over a wide range of $\langle M_p \rangle$.

The yield stress is proportional to the forces needed to break field-induced structures¹. If other short range interactions are negligible (friction, Van der Waals), the forces needed to break the structures are expected to be intimately related to the magnetostatic forces, so that we expected the yield stress to be also proportional to $\langle M_p \rangle^2$.

The experimental parameter chosen to scale the yield stress was thus $\langle M_p(H) \rangle$, which was calculated from magnetization curves taken either from powder



samples or from the suspensions. In the latter case eq. (3) was used to relate the suspension magnetization to the average particle magnetization.

II. MATERIALS AND METHODS

The properties of the different types of particles used for the preparation of the MR fluids are summarized in table 1. Representative micrographs of those particles are presented in Figure 1. As can be seen, we used particles of iron and magnetite, with several different average particle magnetization saturations (that of bulk iron, porous iron and magnetite), and three basic shapes (spheres, plates and rods).

TABLE I. Relevant physical properties of the different types of particles used for the preparation of the MR fluids.

	Shape	Typical size ^a (μm)	$M_{\text{Particle}}^{\text{Saturation}}$ (kA/m) ^c
Commercial solid iron particles ^b	Spherical	0.76 ± 0.40	1600
Porous iron spheres	Spherical	0.7 ± 0.2 [8]	766 [8]
Porous iron plates	Plate-like	Diameter: 2.1 ± 0.5 [8] Thickness: 0.25 ± 0.05 [8]	671 [8]
Porous iron rods	Rod-like	Diameter: 0.45 ± 0.08 [8] Length: 4.7 ± 2.2 [8]	707 [8]

Solid magnetite spheres	Spherical	0.68±0.15[17]	475 [18]
		Diameter: 0.56±0.12	
Solid magnetite rods	Rod-like	[17]	475 [18]
		Length: 7±0.4	

- a) Average plus or minus standard deviation obtained for sets with at least 150 particles.
- b) HQ carbonyl iron (BASF).
- c) Saturation magnetization of the particles was obtained from dry powder samples, assuming a density of 5170 kg m^{-3} and 7800 kg m^{-3} for magnetite and iron respectively, and estimating⁸ that the density of the porous iron particles was 0.47 times that of bulk iron.

The MR fluids were prepared by dispersing a given type of particles in 20 *mPa·s* silicon oil (Sigma-Aldrich). Particle volume content (ϕ) was always low, ranging from 0.5 % to 2.1 %, mainly because we wanted to work with dilute dispersions for which the yield stress is expected to depend linearly on ϕ .

Rheology experiments were carried out in an MCR Anton Paar magnetorheometer (MRD 180) in a parallel plate configuration. The diameter of the plates was 20 mm and the plate separation was fixed at 300 μm . The magnetic field was applied normal to the direction of flow. The experimental protocol of the steady shear flow tests can be divided in three steps: (i) precondition at a constant shear rate $\dot{\gamma} = 200 \text{ s}^{-1}$ for 30 s in the absence of any magnetic field, (ii) the suspension was left to equilibrate for 1 min in the presence of a magnetic field, and (iii) with the field still applied, shear stress was logarithmically increased from 0.1 *Pa* at a rate of 10 points per decade.

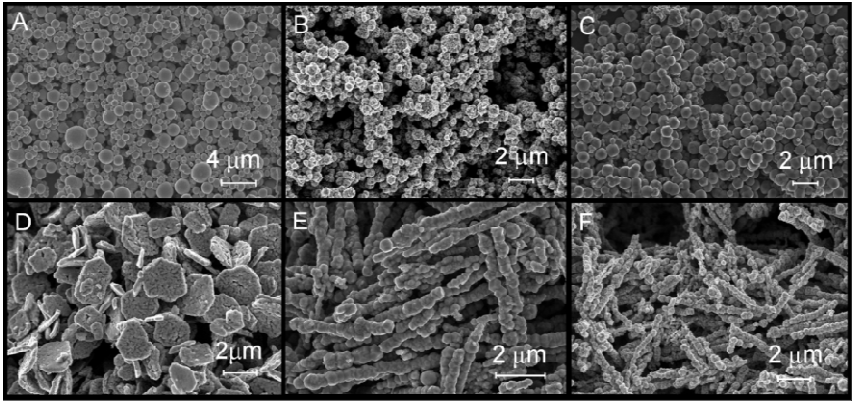


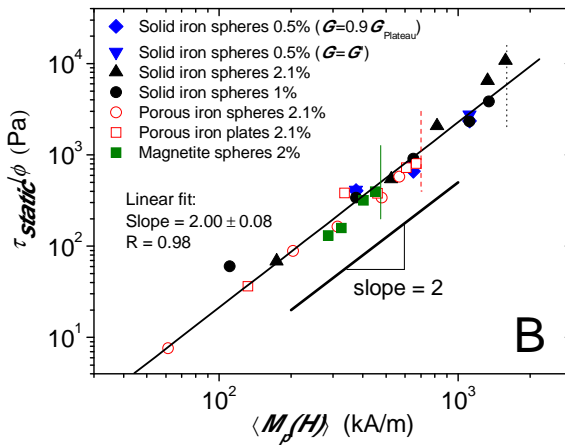
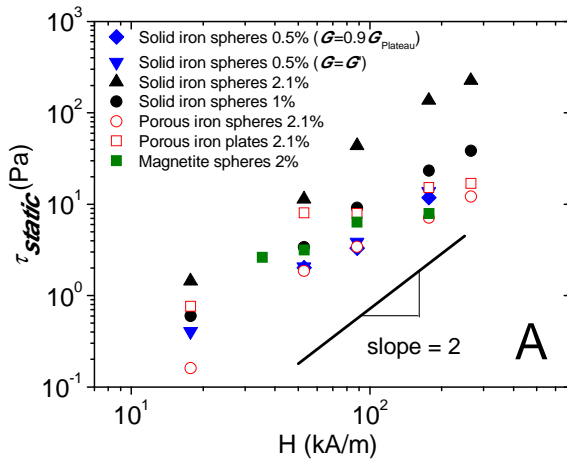
FIG. 1. Scanning electron micrographs of the different types of particles used for the preparation of the MR fluids: A: commercial carbonyl iron spheres; B: porous iron spheres; C: magnetite spheres; D: porous iron plates; E: magnetite rods; F: porous iron rods.

The static yield stress (τ_{static}) was obtained from double logarithmic representations of the stress versus the shear rate. Two linear fits were carried out on data points that precede the onset of flow (rapid increase of stress for a small increase of rate) and on points right after the onset of flow (rapid increase of shear rate for a negligible increase of stress). The point at which the two linear fits intercept was taken as the static yield stress^{19,20}. Yield stress data points were also calculated from small-amplitude oscillatory shear (SAOS) experiments. In those experiments the suspensions were left to equilibrate in the presence of a magnetic field, and the storage and the loss moduli (G' and G'' respectively) were measured as a function of the stress amplitude. For small stress amplitudes (amplitudes within the linear viscoelastic regime) G' is constant, but the continuous increase of the stress eventually results in the

onset of flow, whose revealing feature is a drop of G' and a maximum in G'' . The yield stress can be taken as the stress amplitude at which G'' becomes as large as G' ($G' = G''$ in Figure 2), or as the stress amplitude at which G' has decreased to 0.9 times its low stress plateau value ($G' = 0.9 G'_{plateau}$ in Figure 2). Finally, the dynamic yield stress ($\tau_{dynamic}$) was calculated by fitting the Bingham plastic equation to a typical steady shear flow rheogram in a lin-lin representation.

The contrast factor β as a function of H was calculated from the magnetization curves of powder samples, calculating $\mu_p(H)$ from:

$$\mu_p(H) = \frac{M}{H} + 1 \quad (4)$$



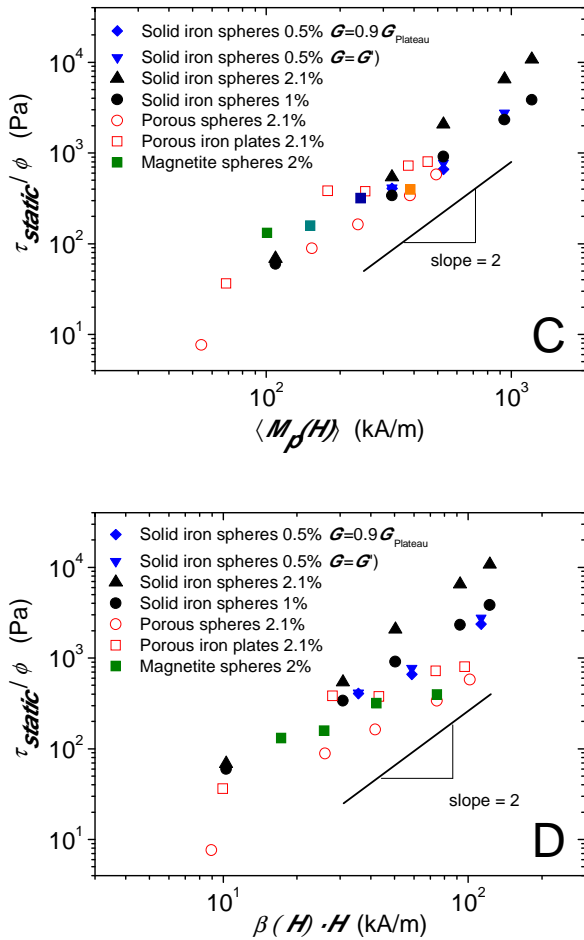


FIG. 2 A: Static yield stress (τ_{static}) versus applied field for MR fluids prepared with different types of particles. B: Scaled static yield stress vs. average particle magnetization $\langle M_p(H) \rangle$, which was calculated from magnetization curves of the suspensions using eq. (3). Vertical lines in B indicate the saturation magnetization of magnetite (solid, 475 kA/m); porous



iron (dashed, ca. 700 kA/m); and solid iron (short dots, 1600 kA/m). C: Same as B, but $\langle M_p(H) \rangle$ was calculated from the magnetization curves of powder samples. D: Scaled static yield stress versus $\beta(H)H$ (see eq. 1). $\beta(H)$ was obtained from magnetization curves of the dry powders. The particle volume content of each suspension is indicated as a percentage in the legends.

III. RESULTS AND DISCUSSION

The yield stress versus the external field for a number of different MR fluids is presented in Figure 2(A). The scaled static yield stress (τ_{static}/ϕ) versus the average particle magnetization, calculated from the magnetization curves of the suspensions using eq. (3), is presented in Figure 2B. As can be seen, the use of $\langle M_p \rangle$ calculated from the magnetization of the suspensions results in an excellent collapse of the curves of the different types of MR fluids. The quality of the collapse is remarkable if we take into account: i) that data come from a collection of MR fluids prepared with particles of different properties; and ii) that for each set of data shown, the external field H was swept from values below which the sensitivity of our rheometer was not enough to detect a yield stress, to values close to the magnetic saturation. Furthermore, a linear fit to all the data points presented in Figure 2B results in a slope of 2.00 ± 0.08 and a relatively large correlation coefficient ($R = 0.98$). This suggests that the static yield stress of dilute MR suspensions scales as:

$$\tau_{static} \propto \phi \langle M_p \rangle^2 \quad (5)$$

The equation of the linear fit shown in Figure 2(B) is:

$$\frac{\tau_{static}}{\phi} = 2.19 \times 10^{-3} \langle M_p \rangle^{2.0} \quad (6)$$

It is important to note that the graphs of Figure 2 include two curves that were obtained from SAOS experiments. The fact that the yield stress calculated from the SAOS data also scales well into the master curve (Graph 2(B)) strengthens the validity of the collapse and rules out the possibility of slipping during our measurements.

Relevant information can also be obtained from the situations in which a poorer collapse was obtained. This happened when we used the volumetric magnetization measured on powder samples (as opposed to suspensions) as the average particle magnetization (Graph C of Figure 2), and when we represented the scaled static yield stress vs. $\beta(H)H$ (see Graph D of Figure 2 and eqs. 1 and 4) as typically done in MR literature^{21,22}. The magnetization process of the powder samples differs from that of the suspensions, mainly because particles in suspension can move more easily and form columnar structures. The magnetization as measured in a suspension provided a better scaling (Graph B as opposed to Graph C in Figure 2) because this magnetization is more representative of the process that actually takes place in the magnetorheometer²³. The poorer collapse when βH was used as the scaling parameter can be explained in terms of the reasons mentioned in the introduction: the non-trivial dependence of β on H , and the fact that for finite separations H and β vary with position in the vicinity of the particles, and m is no longer proportional to βH .



It is also interesting to note that the data collected from the two MR fluids prepared with rod-like particles (both of magnetite and iron) failed to fall on the master curve (see Figure 3). In both cases the deviation from the master curve is greater at lower particle magnetization, and becomes smaller as the particle magnetization grows. There are a number of studies dedicated to the magnetorheology of suspensions of non-brownian elongated particles. When they are compared under similar experimental conditions to MR fluids prepared with spherical particles, several authors have observed a larger yield stress^{8,24,25} and larger storage modulus¹⁷. Our group observed in the past^{8,17} that for MR fluids prepared with rod-like particles: i) those two rheological parameters (τ_y and G') started increasing at lower external fields, which indicated that, compared to the sphere-based fluids, the rod-based fluids underwent structuration at lower fields; and ii) both G' and τ_y were larger for rod-based than for sphere-based MR fluids for small and intermediate fields, but the difference became smaller at larger external fields as particle magnetization approached saturation. The earlier structuration and the larger G' and τ_y of the rod-based MR fluids was attributed to an easier magnetization (i.e. higher susceptibility) of the elongated particles because of their lower demagnetization factor along their long axis. Such easier magnetization, compared to spheres, was actually confirmed by measuring the magnetization of suspensions of iron spheres, rods and plates [8]. Gómez-Ramírez et al.²⁶ also attributed the larger dynamic yield stress observed in suspensions of cobalt microfibres to the enhanced susceptibility of the aggregates of fibres compared to those composed of spheres. The data now presented in Figure 3, however, strongly suggests that the static yield stress of fibre MR fluids is only partially controlled by magnetostatic particle interactions, and that other contributions, such as interparticle friction, must be important particularly at low fields. The data

points for the rod-based MR fluids eventually tend to converge with the master curve, indicating that at larger particle magnetization the contribution of the magnetostatic interactions to the static yield stress overcomes the non-magnetic contributions.

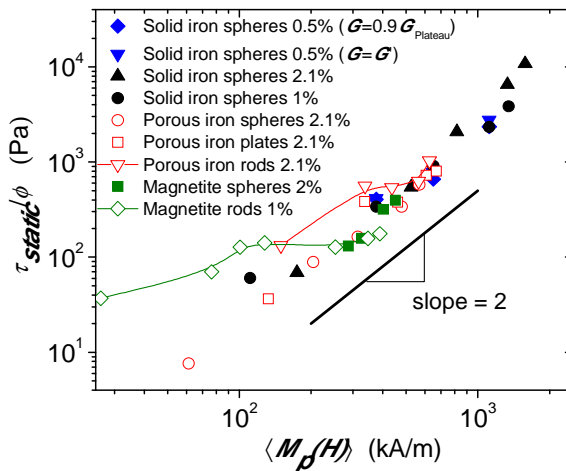


FIG. 3 Scaled static yield stress vs. average particle magnetization $\langle M_p(H) \rangle$, as calculated from magnetization curves of the suspensions using eq. (3) (i.e. same as Figure 2(B)), this time including data corresponding to MR fluids prepared with porous iron rod-like particles and magnetite rod-like particles.

Finally, it is also worth mentioning that when $\tau_{dynamic}$ was considered (Figure 4) the collapse of the curves was also very good, but poorer than in the case of τ_{static} especially at low values of $\langle M_p \rangle$. The static yield stress is the minimum stress required to start the flow, whereas the dynamic yield stress is viewed as the stress needed to continuously break the aggregates that reform by the influence of the field once the flow has started¹. In fact, $\tau_{dynamic}$ was estimated



by extrapolating to zero shear rate the fitting of a Bingham plastic equation, which means that $\tau_{dynamic}$ is determined by a fit to data points of non-negligible shear rate. The static yield stress thus depends almost exclusively on the interparticle magnetic interactions (with the exception of the rod-based MR fluids, as discussed in the paragraph above), which explains the good collapse of the $\tau_{static}(\langle M_p \rangle)$ curves. The poorer collapse of the data points with low values of $\langle M_p \rangle$ in Figure 4, which are precisely the points with the lowest relative contribution of the magnetostatic forces, suggests that $\tau_{dynamic}$ depends on other factors, such as hydrodynamic interactions between particles or aggregates. This is in accordance with the model mentioned above (the dynamic yield stress as the stress needed to continuously break aggregates) and with the fact that points of non-negligible shear rate determine its value.

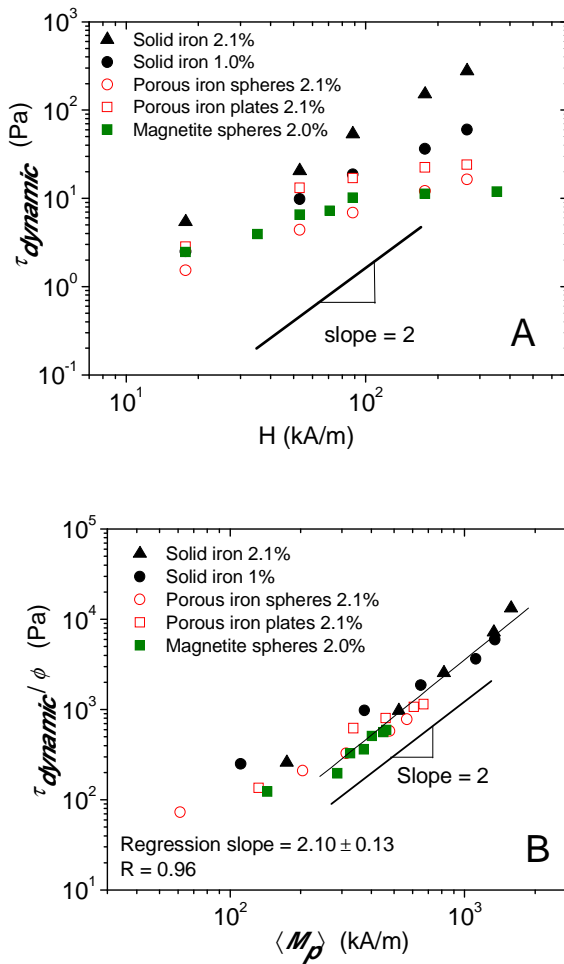


FIG. 4 A: Dynamic yield stress vs. external field. B: Scaled dynamic yield stress versus average particle magnetization. Points with $\langle M_p \rangle$ below 286 kA/m were not used for the fit. The particle volume content of each suspension is indicated as a percentage in the legends.



The equation of the linear fit shown in Figure 4 is:

$$\frac{\tau_{dynamic}}{\phi} = 1.824 \times 10^{-3} \langle M_{Particle} \rangle^{2.1} \quad (7)$$

Data points with $\langle M_p \rangle$ below 286 kA/m were not considered for the linear regression.

IV. CONCLUSIONS

To sum up, in this letter we have shown that the average particle magnetization, as obtained from magnetization measurements of the suspensions, is a good parameter for the scaling of the yield stress (static as well as dynamic) of conventional MR fluids at low particle concentration. We were able to collapse into a single master curve data points taken on suspensions prepared with particles of different saturation magnetization and even morphology. The collapse was reasonably good for a large range of particle magnetizations, whose limits were set by our magnetometer sensitivity and by magnetic saturation. The collapse failed for suspensions prepared with rod-like particles, which was indicative of other contributions (apart from magnetostatic forces) to the yield stress. The existence of these contributions, such as interparticle mechanical friction, is reasonable given the pronounced shape anisotropy of the rod-like particles. The collapse was slightly poorer for dynamic yield stress data than for the static yield stress data, especially at low particle magnetizations. The reason must be again an additional contribution from non-magnetostatic forces, in this case probably hydrodynamic interactions, to the dynamic yield stress.



ACKNOWLEDGEMENTS

Fernando Vereda is especially grateful to the “Programa de reincorporación de doctores de la U. de Granada.” The authors would like to thank Prof. F. Galisteo-González for providing the Bool2k software used for the generation of particle-size distributions from electron microscopy micrographs. This work was supported by MICINN MAT 2010-15101 project (Spain), by the European Regional Development Fund (ERDF) and by Junta de Andalucía P10-FQM-5977 project (Spain). J. P. Segovia-Gutiérrez acknowledges financial support by the “Ministerio de Educación: Becas del Programa de Formación del Profesorado Universitario (FPU)” (AP2008-02138).



REFERENCES

- ¹de Vicente J, Klingenberg DJ and Hidalgo-Alvarez R 2011 *Soft Matter*. **7** 3701–10
- ²Ginder JM and Davis LC 1994 *26 Appl. Phys. Lett.* **65** 3410–2
- ³Ginder J, Davis L and Elie L 1996 *30 Int. J. Mod. Phys. B*. **10** 3293–303
- ⁴Bossis G, Lacis S, Meunier A and Volkova O 2002 *J. Magn. Magn. Mater.* **252** 224–8
- ⁵Phulé PP and Ginder JM 1999 *Int. J. Mod. Phys. B*. **13** 2019–27
- ⁶Rankin PJ, Horvath AT and Klingenberg DJ 1999 *Rheol. Acta*. **38** 471–7
- ⁷Bossis G, Volkova O and Meunier A 2003 *Lect. Notes Phys.* **594** 202–30
- ⁸de Vicente J, Vereda F, Segovia-Gutiérrez JP, M.P. Morales and Hidalgo-Álvarez R 2010 *J. Rheol.* **54** 1337–62
- ⁹Furst EM and Gast AP 2000 *1 Phys. Rev. E*. **62** 6916–25
- ¹⁰Marshall L, Zukoski CF and Goodwin JW 1989 *J. Chem. Soc., Faraday Trans. 1*. **85** 2785–2795
- ¹¹Seo Y 2011 *J. Non-Newtonian Fluid Mech.* **166** 241–3
- ¹²Sung JH, Jang WH, Choi HJ and Jhon MS 2005 *12 Polymer*. **46** 12359–65
- ¹³Choi HJ, Cho MS, Kim JW, Kim CA and Jhon MS 2001 *Appl. Phys. Lett.* **78** 3806
- ¹⁴Martin JE 2000 *27 Phys. Rev. E*. **63** 011406
- ¹⁵Volkova O, Cutillas S and Bossis G 1999 *4 Phys. Rev. Lett.* **82** 233–6
- ¹⁶Klingenberg DJ, Ulicny JC and Golden MA 2007 *J. Rheol.* **51** 883–93
- ¹⁷de Vicente J, Segovia-Gutiérrez JP, Andablo-Reyes E and Vereda F, Hidalgo-Álvarez R 2009 *J. Chem. Phys.* **131** 194902
- ¹⁸Vereda F, de Vicente J and Hidalgo-Álvarez R 2007 *27 Langmuir*. **23** 3581–9
- ¹⁹Mezger TG 2006 *The Rheology Handbook: For Users of Rotational and Oscillatory Rheometers* (Hannover, Germany: Vincentz Network GmbH & Co KG)

-
- ²⁰ Ramos J, Klingenberg DJ, Hidalgo-Alvarez R and de Vicente J 2011 *J. Rheol.* **55** 127–52
- ²¹ Ramos J, de Vicente J and Hidalgo-Álvarez R 2010 *Langmuir*. **26** 9334–41
- ²² de Vicente J, López-López MT, Durán JDG and González-Caballero F 2004 *Rheol. Acta.* **44** 94–103
- ²³ de Vicente J, Bossis G, Lacis S and Guyot M 2002 *J. Magn. Magn. Mater.* **251** 100–8
- ²⁴ Bell R, Karli J, Vavreck A, Zimmerman D, Ngatu G and Wereley N 2008 *Smart Mater. Struct.* **17** 015028
- ²⁵ Kuzhir P, López-López M, Vertelov G, Pradille C and Bossis G 2008 *Rheol. Acta.* **47** 179–87
- ²⁶ Gómez-Ramírez A, Kuzhir P, López-López MT, Bossis G, Meunier A and Durán JDG 2011 *J. Rheol.* **55** 43-67



PART III-BROWNIAN DYNAMIC SIMULATIONS IN MR

FLUIDS

Title of the manuscript

Brownian Dynamic Simulations in magnetorheology and compariso with
experiments

Authors

J.P. Segovia-Gutiérrez¹, J. de Vicente¹, R. Hidalgo-Álvarez¹, Antonio M. Puertas²

Affiliation

¹ Departamento de Física Aplicada, Facultad de Ciencias, Universidad de
Granada, Granada E-18071, Spain.

² Grupo de Física de Fluidos Complejos, Departamento de Física Aplicada,
Universidad Almería, E-04120 Spain.

Published

Soft Matter, **9 (29)**, 6970-6977 (2013)




Abstract

The rheological behaviour of unsheared magnetorheological fluids are studied using Brownian dynamics simulations and experiments. In the simulations, we use monodisperse and polydisperse systems, and study the structure formation and the stress autocorrelation function, that provide the shear moduli and shear viscosity of the system. Whereas the monodisperse system crystallizes, as identified by the pair distribution function, polydispersity hinders crystallization and allows a comparison with the experiments. These are performed with carbonyl iron particles in different Newtonian solvents (silicone oils and a glucose syrup). Special attention is paid to the equilibration of the samples. A rescaling of the viscosity is introduced that collapses data from different systems and shear rates, leaving solely the dependence on the external magnetic field. The simulation data can be collapsed onto the same curve if the magnetic field is also rescaled, due to the approximations involved. The master curve shows the expected quadratic dependence on the external field. The shear moduli from simulations and experiments agree qualitatively; both moduli develop a shoulder at low frequencies, indicating a slow mechanism of stress relaxation connected to structural relaxation.

I. INTRODUCTION

Magnetorheological (MR) fluids are known because of their magnetic field-tunable rheological properties. In the absence of a magnetic field, MR fluids typically behave as Newtonian fluids. However, under the application of a magnetic field, particles aggregates to form chainlike structures aligned in the direction of the field, the so-called magnetorheological effect, first described



more than 60 years ago^{1,2}. In magnetized MR fluids, therefore, the viscosity can increase by several orders of magnitude. For high enough fields MR fluids present a yield stress and highly elastic response. These kind of fluids are very good candidates for a wide range of applications, from mechanical systems such as shock absorbers, brakes and seismic vibration dampers to biomedical applications³, and sound propagation⁴ among others.

Theoretical and experimental characterization of these systems and its rheological properties under different conditions have been widely studied by many researches^{2,5-9}. Furthermore, besides previous experimental and theoretical works, dynamic simulation techniques have played a very important role in understanding the behaviour of MR and, more commonly, ER fluids¹⁰⁻¹⁹. Computational methods have been usually applied to investigate the formation of particle aggregates in presence of static electric or magnetic fields and how the microstructure behaves in small^{13,20} and large¹⁵ amplitude oscillatory shear flows, mainly focusing on the static and dynamic yield stresses. Most of the research efforts have assumed that Brownian motion is negligible¹²⁻¹⁷ but there are also some reports where thermal motion is considered in spite of the large size of the constituents¹⁸. However, most of the works cited previously focus on the solidified system either crystallized, in monodisperse systems, or amorphous.

In this contribution we focus on the rheological behaviour of the equilibrium state in the presence of uniaxial (DC) magnetic fields, up to the formation of rigid structures, i.e. a solid phase. To achieve this goal we make use of both Brownian Dynamic Simulations and experiments.



The dipolar approximation for the particle-particle interaction is taken in the simulations, plus a hard-sphere-like repulsion¹². Under no flow conditions, only competition between dipolar interaction and Brownian force is relevant, and the rheological behaviour is obtained from the microscopic stress tensor. In the range of low magnetic field strengths, thermal motion dominates and weak structures break down continuously. Upon increasing the field strength, we observe the formation of solid columnar structures aligned with the external field, in competition with the Brownian motion; in the case of monodisperse particles, a hexatic crystal phase is reached. In the experiments, carbonyl iron particles were used because of their high and fast magnetic response. We focus on the the region of low magnetic fields and low shear rates, to allow direct comparison with simulations. Viscosities from simulations and experiments can be properly presented to fall onto the same master curve, showing a quadratic dependence with the external magnetic field, as predicted by the theoretical models. The comparison of the shear moduli also shows qualitative agreement. The fluid-solid transition point, however, is poorly defined.

The next section deals with the simulation part of the work; the simulation method as well as the characterization of the structural aspect and the rheology in the equilibrium state in these systems are presented. The next section (Experiments) is concerning to the experimental procedure and results from rheological tests. In Section IV (Discussion) the comparative study between both techniques is shown and finally, conclusions are exposed in the last section (Conclusions).



II. SIMULATIONS

The use of simulations in MR fluids has been usually carried out in the large-particle limit, where Brownian motion can be neglected, simplifying the simulation method. Here, we retain this contribution since we study quiescent systems. This allows us to study the fluid regime in MR fluids, where the magnetic forces are not strong enough to render the system solid. A crucial point in this case is the equilibration of the system, which we monitor using structural parameters, such as the potential magnetic energy and the average number of neighbors per particle, and dynamical ones, particularly the mean squared displacement (MSD), and bond correlation and shear stress correlation functions. We concentrate on the structure and dynamics of the equilibrated systems, and not on the kinetics of structure formation.

As mentioned above, the simulations and experiments are performed at a concentration of 5 vol%. Although typical volume fractions used in mechanical applications are commonly much higher, around 30 – 40 vol%, we use this low volume fraction to reduce the computational time and minimize the effect of magnetic multipolar interactions, while retaining the main driving mechanism for MR effect.

Upon increasing the strength of the dipolar interaction, elongated clusters aligned with the external field form. More intense fields cause the formation of transient columns that span through the system, but the system is still in the fluid state, as observed by the MSD and correlation functions. In particular, the stress correlation function decays to zero, giving a finite viscosity.



A. Simulation Details

We perform Brownian Dynamics Simulations of both monodisperse and polydisperse systems, composed by $N = 1000$ spherical particles. The equation of motion of particle i is given by the Langevin equation:

$$m_i \ddot{\vec{r}}_i = \sum_j \vec{F}_{ij} - \gamma_i \dot{\vec{r}}_i + \vec{f}_i \quad (1)$$

where m_i and γ_i are the mass and friction coefficient with solvent of the particle, \vec{F}_{ij} is the interaction force between particles i and j (core repulsion plus dipolar interaction), and \vec{f}_i is the Brownian force. No hydrodynamic particle-particle interaction is considered. In the case of the monodisperse system, all particles have the same mass, m_0 , radius, a , and friction coefficient γ_0 . On the other hand, in the polydisperse system the particle radius distribution is flat, between $0.9\bar{a}$ and $1.1\bar{a}$, with \bar{a} the average radius, giving a polydispersity index of 5 % as calculated by:

$$PDI = \frac{\sum_{i=1}^N \sqrt{(a_i - \bar{a})^2}}{N} \quad (2)$$

The particle mass is calculated as $m_0(a_i/\bar{a})^3$, and the friction coefficient as $\gamma_0 a_i/\bar{a}$. The system is simulated in a cubic box ($l_x = l_y = l_z = 43.76a$ for the monodisperse system and $l_x = l_y = l_z = 43.92\bar{a}$ for the polydisperse one; in both cases 5 vol%) with periodic boundary conditions in the three

dimensions. The external field is applied along the z -direction, what sets the dipolar interaction:

$$\vec{F}_{12}^{mag} = 3U_0 \left(\frac{1}{|\vec{r}_{ij}|} \right)^4 \left[(3 \cos^2 \theta_{ij} - 1) \hat{r} + \sin 2\theta_{ij} \hat{\theta} \right] \quad (3)$$

where \vec{r}_{ij} denotes the relative position between two particles and θ_{ij} is the angle that \vec{r}_{ij} forms with the magnetic field direction, \hat{r} and $\hat{\theta}$ represent the unit vectors in the direction defined by the pair of particles and the angular vector, respectively. The parameter U_0 sets the strength of the attraction and is given by the physical parameters of the system. In MR fluids, $U_0 = 4\pi\mu_0\mu_{cr}\beta^2 a_i^3 a_j^3 H_0^2$ where H_0 is the modulus of the external magnetic field strength, μ_0 is the magnetic permeability of the vacuum, $\mu_{cr} = \mu_c \backslash \mu_0 \sim 1$ refers to the relative magnetic permeability of the continuous phase and β is the contrast factor:

$$\beta = \frac{\mu_p - \mu_c}{\mu_p + 2\mu_c} \quad (4)$$

where μ_c and μ_p are the magnetic permeabilities of the continuous medium and particles, respectively.

In the simulations, U_0 is the control parameter; and in order to compare with experiments, the magnetic field is calculated using the average radius in the expressions given above.

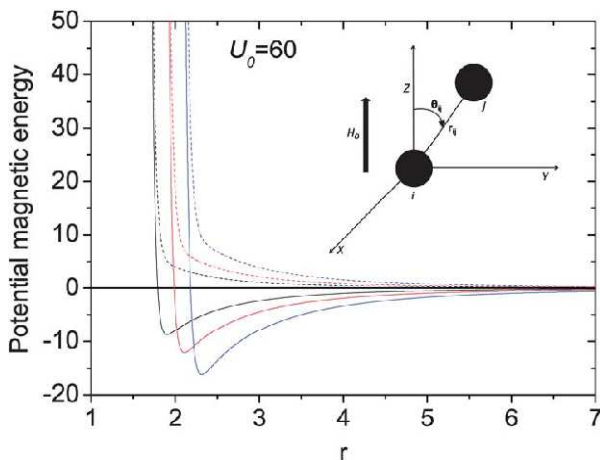


FIG. 1 Total interaction potential between particles of different sizes and with different angles: black lines correspond to $a_i = a_j = 0.9$, red lines to $a_i = a_j = 1$ and blue ones to $a_i = a_j = 1.1$. Continuous lines indicate the interaction with $\theta_{ij} = 0$ and broken lines to $\theta_{ij} = \pi/2$. Inset: schematic representation of the coordinate system, \vec{r}_{ij} and θ_{ij} for the dipolar interaction.

In addition to the dipolar interaction, the core-core repulsion is modeled by the following exponential form:

$$\vec{F}_{ij}^{rep} = -\frac{3U_0}{16a^4} \exp\left(-100 \frac{|\vec{r}_{ij}| - (a_i + a_j)}{a_i + a_j}\right) \hat{r} \quad (5)$$

This functional form of the core-core repulsion correctly describes the lateral attractive interaction between columns^{12,21}.

The equations of motion were integrated using Heun's algorithm²² for the Langevin dynamics. The average particle radius, \bar{a} , average particle mass, \bar{m} , and thermal energy, $k_B T$, are the units of length, mass and energy, respectively. The solvent friction coefficient is set to $\gamma_0 = 10 \sqrt{mk_B T / \bar{a}}$, and the equations of motion were solved with a time step $\delta t = 5 \times 10^{-4} \sqrt{(ma^2) / (k_B T)}$

B. Simulation results

The structure and rheological behaviour of equilibrium states from hard spheres to strongly interacting systems ($U_0 \sim 100$) are studied using suitable parameters, discussed in the following. Equilibration of the system is monitored by structural and dynamical parameters (energy, number of neighbours, pair distribution function, mean squared displacement, bond and stress correlation functions, and viscosity), and the equilibrium values were taken from the long time plateaux. The comparison of the monodisperse and polydisperse systems reveals important differences that ultimately lead to the frustration of crystallization in the polydisperse one. We discuss first the structure and then move on to the rheological behaviour of the equilibrium states.

The mean number of neighbours per particle is presented in the upper panel of Figure 2 as a function of the parameter U_0 ; two particles are considered neighbours when the distance between them is less or equal than $(a_i + a_j + 0.5\bar{a})$. At low U_0 the monodisperse and polydisperse systems agree, whereas the value for the monodisperse system is larger for strong interactions. As expected, polydispersity provokes a less optimal arrangement of the particles. Interestingly, in both cases the number of neighbours is above two, indicating the formation of thick columns and not only single chains; i.e. lateral aggregation of the clusters is taking place. This is confirmed by visual inspection



of the system. At low U_0 , elongated clusters form, that grow and form chains that percolate in the z –direction. At high U_0 , the chains aggregate laterally to form the columns shown in the snapshots for the mono and polydisperse systems.

Despite the larger number of neighbours in the monodisperse system, the energy per particle is larger in the polydisperse system (in absolute value), as shown in the lower panel of Figure 2. The potential energy is calculated as:

$$E_{mag} = \frac{1}{N} \sum_{i \neq j}^N U_0 \left(\frac{1}{|\vec{r}_{ij}|} \right)^3 (1 - 3 \cos^2 \theta) \quad (6)$$

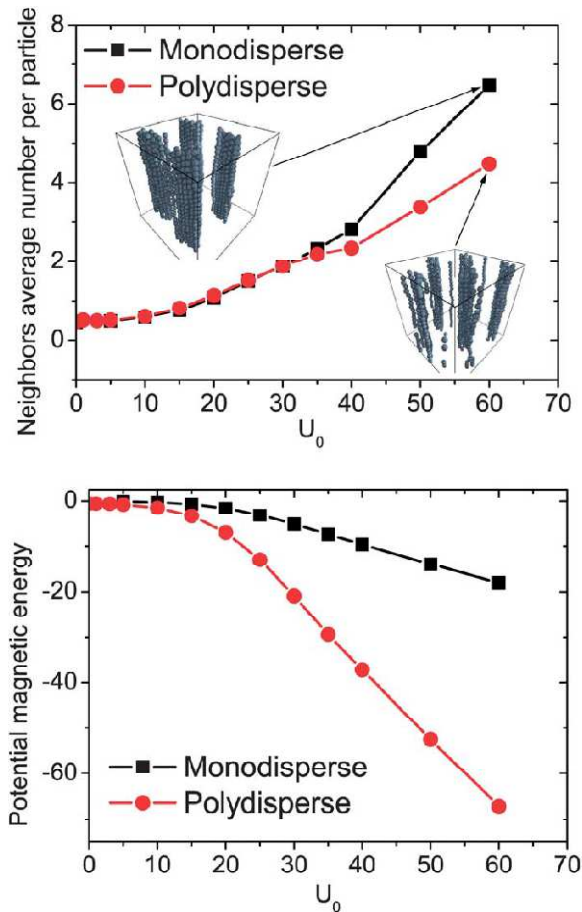


FIG 2. Upper panel: Mean number of neighbours per particle vs. U_0 for both monodisperse and polydisperse systems and two snapshots of the microstructure in each case. Lower panel: Evolution of potential energy with U_0 for both cases.



where $U_0 \propto a_i^3 a_j^3$, as mentioned above. The polydisperse system has a larger energy since the contribution from pairs with big particles is much larger than average particles, and also have more neighbours.

The local structure is studied by means of the pair distribution function. Due to the anisotropy induced by the interaction potential, the contributions to the function parallel and transversal to the external field must be separated. The parallel contribution is shown in Figure 3 for $U_0 = 60$ for the monodisperse and polydisperse systems.

Whereas the monodisperse system shows clear peaks and dips, indicating the long range ordering within the columns, in the polydisperse case the pair distribution function does not show this order.

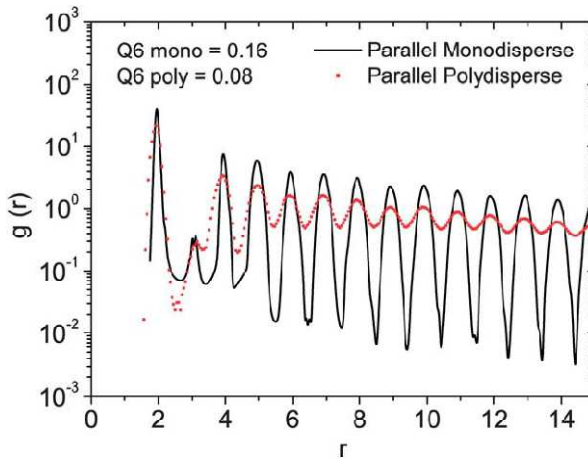


FIG. 3 Pair distribution functions for both monodisperse and polydisperse systems at $U_0 = 60$ in the direction of the magnetic field.

The crystallization order parameter Q_l defined by Steinhardt et al.²³ has been also used to check the local ordering of the particles:

$$Q_l = \sqrt{\frac{4\pi}{2l+1} \sum_{m=-l}^l \left| \frac{1}{N} \sum_{k=1}^N \sum_{j=1}^{n_k} Y_{lm}(\theta_j, \Phi_j) \right|^2} \quad (7)$$

where N is the total number of bonds between nearest neighbours, n_k is the number of nearest neighbours of a particle k , and Y_{lm} are the spherical harmonics that depend on the angles in spherical coordinates θ_j and Φ_j ; the case $l = 6$ is particularly useful in identifying different crystalline structures. The values for Q_6 in the mono and polydisperse systems for $U_0 = 60$ are presented in Figure 3, and indicate that the monodisperse system is crystallized while the polydisperse one is amorphous.

We move now to the study of the rheology of the system. This is based on the auto correlation function of the non-diagonal components of the microscopic stress tensor. This is defined as

$$\sigma_{\alpha\beta} = \sum_{i=1}^N m_i v_{i,\alpha} v_{i,\beta} - \sum_{i<j} r_{ij,\alpha} F_{ij,\beta} \quad (8)$$

where $v_{i,\alpha}$ refers to α^{th} component of the velocity of particle i . The correlation function of the non-diagonal component is calculated as

$$C_{\sigma\sigma}(t) = \frac{1}{Vk_B T} \sum_{\alpha < \beta} \langle \sigma_{\alpha\beta}(t) \sigma_{\alpha\beta}(0) \rangle \quad (9)$$

where the brackets indicate ensemble average and $\sigma_{\alpha\beta}$ refers to a non-diagonal component of the stress tensor; V is the volume of the system and $k_B T$ is the thermal energy. Given the anisotropy of the system, we average this correlation function using the components that contain the z direction, σ_{13} and σ_{23} , and present the results in the upper panel of Figure 4 for different states of the polydisperse system. This function decays to zero in the fluid, as shown, but to a finite value in the solid, and shows a two-step decay in a viscoelastic fluid, which appears as a shoulder for U_0 . The short-time decay is associated to ballistic motion, whereas the long time one corresponds to the structural relaxation. This mechanism relaxes stress for longer times with increasing U_0 , i.e. the system is becoming a solid, as the structure results presented above showed.

The Fourier transform of $C_{\sigma\sigma}(t)$ gives the complex shear modulus, $G(\omega) = i\omega\tilde{C}_{\sigma\sigma}(\omega)$, which is experimentally accessible by dynamic oscillatory shear rheology; $G(\omega) = G' + iG''$, with G' and G'' the storage and loss moduli, respectively. Fluid states are characterized by $G'' > G'$, while in solid ones $G' > G''$. The moduli are presented in the lower panel of Figure 4 for different fluid states, with increasing U_0 . Looking at the region of low frequencies, the energy dissipation dominates ($G'' > G'$) and the conventional quadratic and linear dependence on angular frequency of G' and G'' , respectively, are observed. These behaviours crossover with decreasing frequency, reaching the solid-like or the elastic behaviour ($G' > G''$), where G' becomes constant. Upon increasing U_0 , both G' and G'' grow, indicating that the system becomes more

viscous but also more elastic. More notably, the region with liquid-like character shrinks, and both G' and G'' show a shoulder at low frequencies, signalling the appearance of the mechanism of stress relaxation at longer times mentioned above.

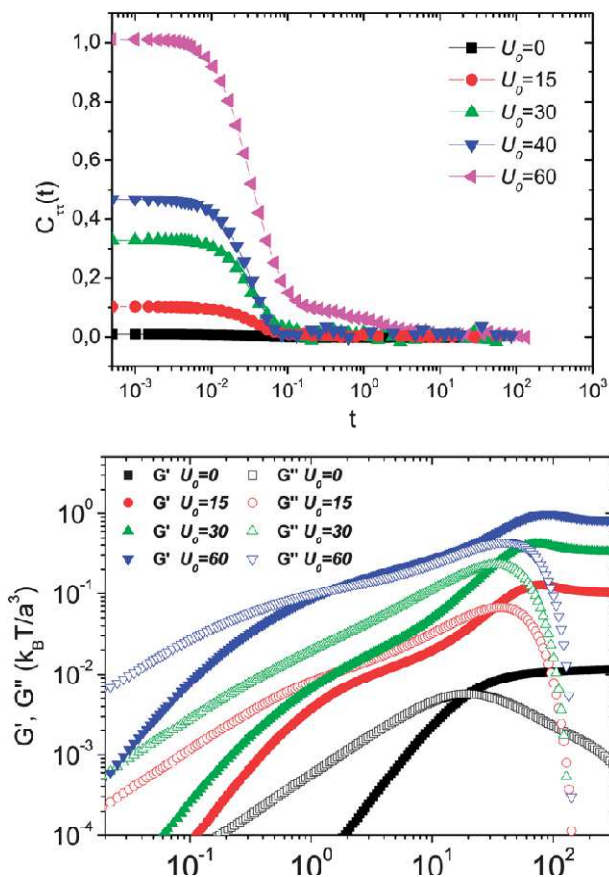


FIG. 4 Upper panel: Stress correlation function for different states, as labeled, in polydisperse systems. Lower panel: Viscoelastic moduli as a function of the angular frequency for four different control parameter values.



This solidification of the system can be noted using the viscosity, which should diverge at the fluid-solid transition point. The viscosity can be calculated using the Green-Kubo relation, $\eta = \int_0^\infty C_{\sigma\sigma} dt$, but computationally, it is more efficient to calculate it using the Einstein relation:

$$\eta = \lim_{t \rightarrow \infty} \eta(t) = \frac{1}{2Vk_B} \lim_{t \rightarrow \infty} \frac{1}{t} \langle \Delta A^2(t) \rangle \quad (10)$$

where $\Delta A(t)$ is defined as follows:

$$\Delta A(t) = A(t+s) - A = \int_s^{t+s} \sum_{\alpha < \beta} \sigma_{\alpha\beta}(t') dt' \quad (11)$$

where the summation is restricted to the 13th and 23th components, as discussed above. Figure 5 presents the evolution of $\eta(t)$ for different states with increasing U_0 . The shear viscosity is read from the long time plateau, which increases with U_0 . The results are presented in Figure 6, together with the diffusion coefficient and the time scale for bond break-up (see below). For the range of U_0 studied here, the viscosity raises more than two decades. Note, however, that since this is a Brownian system, the actual viscosity of the system should be calculated as $\eta_0 + \eta$, where η_0 is the solvent viscosity, $\eta_0 = \frac{\gamma_0}{6\pi}$.

The self diffusion coefficients presented in Figure 6 were obtained from the long time slope of the mean squared displacement of the particles. At low values of U_0 (low magnetic fields) the diffusion coefficients are close to $\frac{1}{\gamma_0} = 0.1$ since particle motion is governed solely by Brownian forces.

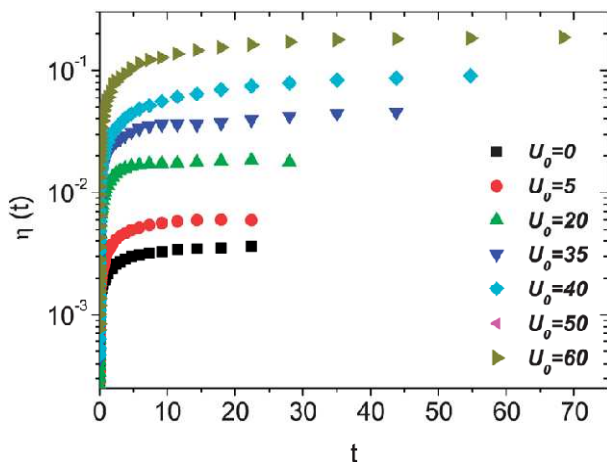


FIG. 5 Evolution of η in several equilibrium states for different values of the control parameter. The viscosities are given by the long time plateaux.

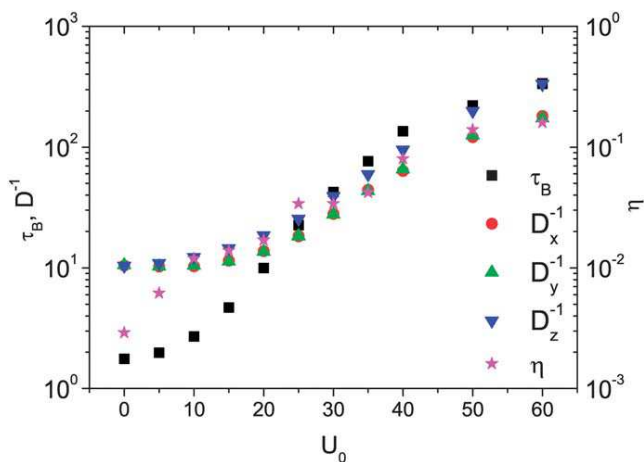


FIG. 6 Dynamic parameters as a function of U_0 viscosity (asterisks), inverse diffusion coefficient in the x -axis (circles), y -axis (up triangle) and z -axis (down triangles), and time scale for bond break-up (squares).



When the magnetic field increases, a deviation from this trend appears, connected with the formation of clusters and columns, and a significant slowing down of the dynamics is observed. Notably, the diffusion coefficient corresponding to the z -axis falls down faster than other coefficients because the magnetic field is parallel to z axis and particles are confined along the vertical columnar aggregates described above. In the x and z axis, the diffusion coefficient also decays when the trapping inside the columns is strong enough, although the interaction itself does not confine it.

This trapping is however transient, as the system is in the fluid states for all the values of U_0 studied here, as noted by the finite viscosity and diffusion coefficient. This can be confirmed by studying the bond correlation function, which is calculated as the fraction of neighbours that a particle retains after time t . This function decays to zero for all the states studied here, as expected for fluid states, but the decay is slower with increasing U_0 . The time when this function decays to 0.5 is defined as τ_B , and is included in Fig. 6. τ_B increases with U_0 over two decades for the range studied. It is interesting to note that above $U_0 \sim 20$ the three dynamic parameters presented in the figure evolve in the same manner, after a trivial rescaling. This value of U_0 corresponds to the point where clusters are observed in the system, i.e. the interaction forces dominate over Brownian motion.

Finally, we wish to note that for the monodisperse system at $U_0 \sim 50$, the mean squared displacement shows long time trapping, i.e. the diffusion coefficient is very small, and the bond correlation function shows a long time plateau and does not decay to zero, i.e. τ_B diverges. These features are connected to crystallization, and are completely absent in the case of the polydisperse

system. Crystallization is a fluid-solid transition, as identified by the dynamic parameters, but the polydisperse system also shows an important increase of the viscosity, albeit at larger magnetic fields.

III. EXPERIMENTS

In this section we show the experimental protocol which was followed to prepare the MR fluids and the rheological techniques employed. Special attention was paid to ensure equilibrated systems prior to running the tests. The low shear viscosity was ascertained by running steady shear flow experiments.

A. Synthesis of the MR fluids

MR fluids were formulated by dispersing carbonyl iron spherical particles with a diameter $d \sim 900 \pm 300 \text{ nm}$ (HQ grade, BASF) --as determined by SEM--, in two Newtonian silicone oils of different viscosities 20 and 500 $\text{mPa} \cdot \text{s}$, Sigma-Aldrich) and in glucose syrup of high viscosity (793 $\text{mPa} \cdot \text{s}$, Cargill), at a particle concentration of 5 *vol%*. This volume fraction was taken in order to directly compare with simulations. To prepare samples we took a carbonyl iron density of 7.87 g/cm^3 and a silicone oil density of 1 g/cm^3 at 25 °C. In the case of samples based on glucose syrup, the density of the solvent was 1.45 g/cm^3 . Homogenization of the suspensions was achieved by dispersing the sample manually (with a spatula) and subjecting the suspension to sonication in an ultrasonic bath (Selecta, 360 W).



B. Rheological characterization

Rheological tests were performed using a stress-controlled rheometer (MCR 501, Anton Paar). On the one hand, a custom-built fixture was designed to get homogeneous fields and to achieve sufficient torque resolution ($0.1 \mu mN$) at low magnetic field strengths (below $10 kA/m$) for the less viscous (oil-based) samples. In this case a glass plate-plate geometry with a diameter of $43 mm$ was combined with a solenoid having 2000 turns. On the other hand, a commercial MRD180 magnetorheology fixture was employed for the glucose syrup-based sample. This involves the use of titanium parallel plates (diameter $20 mm$). A gap of $300 \mu m$ was always chosen as frequently done in the literature⁷.

To ensure that experimental measurements were run in equilibrium, prior to the test, the system was stabilized under magnetic fields during a long period of time ($\sim 2 \times 10^3 s$). To monitor the system stabilization we did perform small-amplitude oscillatory shear time sweeps (Amplitude = 0.01% , Frequency = $1 Hz$). As a way of example, in the upper panel of Figure 7 we show the time evolution of the elastic modulus for the sample based on glucose syrup, for different magnetic fields. These curves demonstrate the slow dynamics of the particles within the glucose syrup:

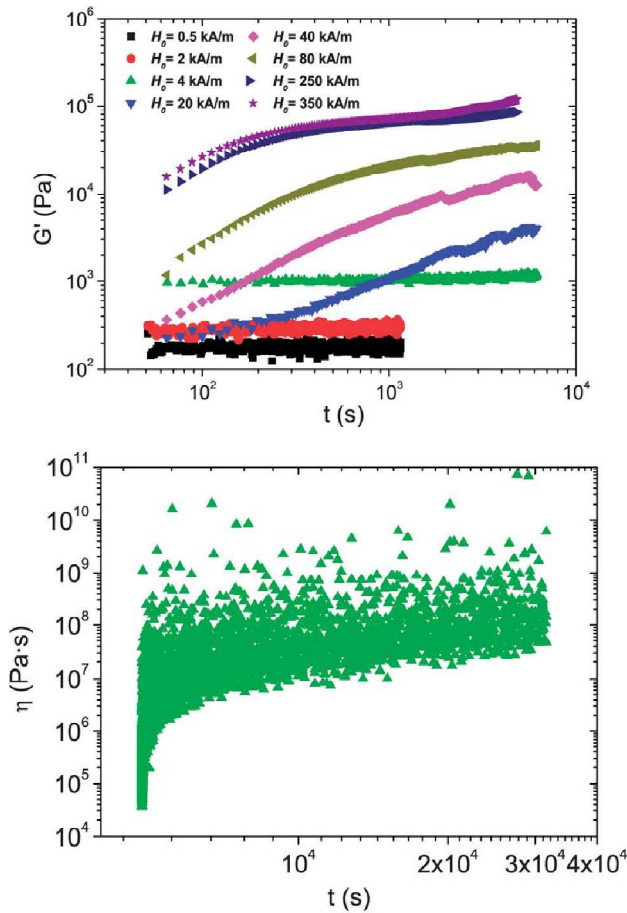


FIG. 7 Upper graph: evolution with time of the elastic moduli for different external magnetic fields for the glucose syrup with particles. Bottom graph: shear viscosity of the glucose syrup sample as a function of time in a conventional creep test. In this case,

$$H_0 = 250 \text{ kA/m} \text{ and the constant stress was } 150 \text{ Pa.}$$

particles need a certain amount of time to form stable structures under a magnetic field. It is also important to remark that whether the system appears



to be equilibrated or not depends on the measuring time scale. With this in mind, the figure reveals that up to 20 kA/m , G' the viscoelastic modulus reaches a clear plateau, i.e. the system is in the fluid state, whereas at high fields, above 250 kA/m , the system shows the typical behaviour of aging (a fast increase at short times followed by a slow growth), i.e. the system is solidifying. The latter was corroborated by measuring the instantaneous shear viscosity in creep tests (lower panel of Figure \ref{estabg}) at a constant shear stress of 150 Pa during a long time period. It is not clear if the states between 20 kA/m and 250 kA/m will reach equilibrium at longer times or not; the transition from fluid to solid is located between these two values.

Stress controlled tests were carried out using both geometries mentioned above and we explored rheological properties over a wide range of magnetic fields, from 0 to 350 kA/m (see Figure 8). This range was limited in the case of samples based on silicone oil due to the difficulty to control the temperature of the external copper coil at fields around 20 kA/m . Furthermore, we took a sufficient time interval length (30 s) over each point to achieve a steady shear viscosity value at low-shear rates. Once the shear viscosity curves are obtained, we are in conditions to calculate the shear viscosity at a convenient shear rate value and in particular at zero shear rate by extrapolation.

Note that all states show a plateau at low shear rates; with increasing magnetic field, this plateau moves to higher viscosities and lower shear rates. This, however, does not indicate that the system is in equilibrium, as discussed previously. As the system ages, the plateau displaces up and to lower shear rates -- the actual value of the plateau, thus, depends on the waiting time^{26,27}.

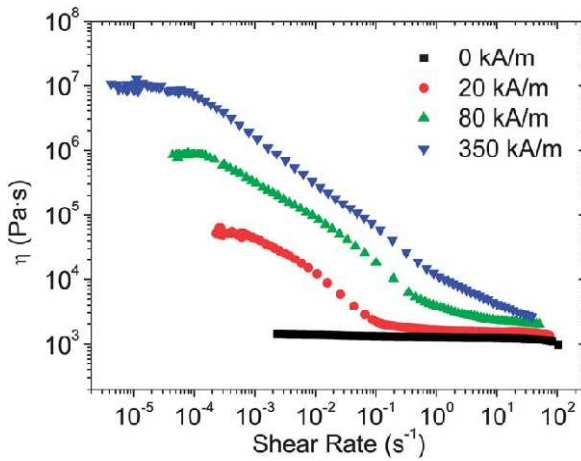


FIG. 8 Conventional stress controlled test results for the sample based on glucose syrup for several magnetic fields.

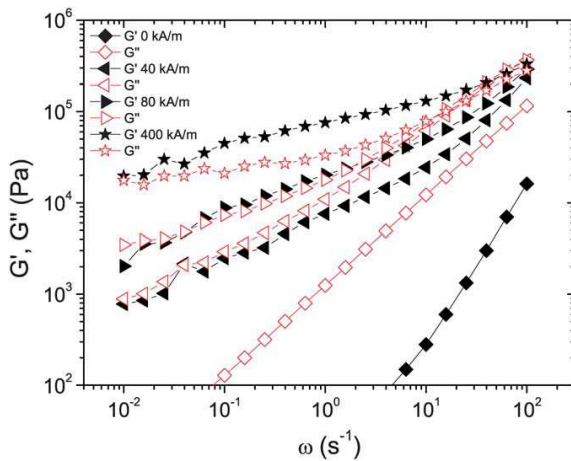


FIG. 9 Storage (G') and loss (G'') moduli for different magnetic fields, as labeled, for the samples based on glucose syrup (Amplitude=0.01 %)



In order to make a direct comparison with the simulations, the storage and loss moduli have been determined experimentally by small-amplitude oscillatory frequency sweeps. This allows also an estimation of the transition point from the fluid to the solid state, given by the crossover from $G'' > G'$ to $G' > G''$, as discussed above. The moduli are presented in Figure 9 for different magnetic fields. The expected linear and quadratic trends with frequency are obtained for G'' and G' , respectively, at low fields, with $G'' > G'$, whereas for large magnetic fields both moduli show a shoulder at low frequencies. Also, for $U_0 \sim 80 \text{ kA/m}$, $G' \approx G''$ in the range of ω presented, giving an estimation of the transition point.

IV. DISCUSSION

To complete this work, in this section we present a comparative study between results from simulations and experimental tests. We focus first on the viscosity, although a direct comparison cannot be performed because: (i) in the simulations it is assumed that particles only interact via magnetic dipolar forces, neglecting the possible remnant magnetization of particles and other interactions (van der Waals, electrostatic, ...); (ii) the solvent viscosity is fixed in the simulations to a low value (since hydrodynamic interactions are not considered, it only introduces a trivial time scale). Due to these reasons, we propose the following rescaling for the viscosity to carry out the comparison:

$$\frac{\eta - \eta_s}{\eta_{H=0} - \eta_s} \quad (12)$$

where $\eta_{H=0}$ corresponds to the shear viscosity at zero magnetic field and η_s is the solvent viscosity. In this way, we correct for the two effects discussed above. We present the shear viscosity using this scaling for different values of the shear rate and different systems in Figure 10. Note that the data indeed collapse onto a master curve for all shear rates and systems, although the bare viscosity depends on both of them. This collapse indicates that the proposed scaling allows a comparison between different systems, probing only the dependence on the external magnetic field.

The comparison between experiments and simulations is shown in Figure 11 To collapse the computational results as shown in the figure, the x -axis was rescaled by a factor 18. The reason for this factor is unclear, but it is not surprising that a scaling factor for the magnetic field is needed. Different possibilities are discussed in the following.

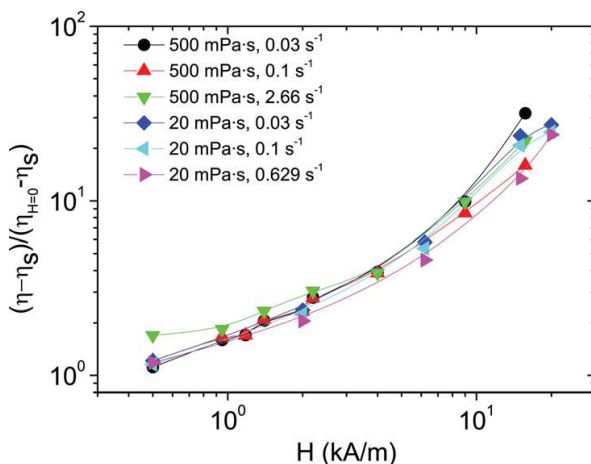


FIG. 10 Normalized viscosities as a function of the magnetic field for different shear rates and systems, as labeled.

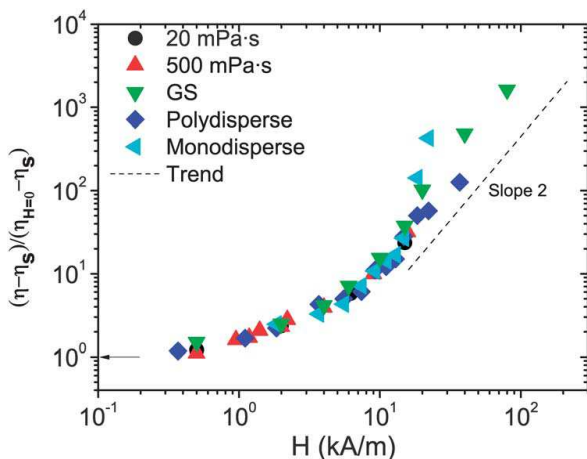


FIG. 11 Comparison between simulations and experiments using the representation proposed in Eq. (12), as a function of the magnetic field. Different symbols represent the rescaled viscosity for different systems, as labeled.

In the simulations the simple dipolar interaction between particles is used, with strength $U_0 = 4\pi\mu_0\mu_{cr}\beta^2a_i^3a_j^3H_0^2$, where it is assumed that the magnetic permeabilities of the particles and solvent (and the contrast factor, β) are constant with the magnetic field. This can be checked using the Fröhlich-Kennelly equation²⁸:

$$\mu_{pr} = \frac{\mu_p}{\mu_o} = 1 + \frac{\chi_i \frac{M_s}{H_0}}{\chi_{i+} \frac{M_s}{H_0}} \quad (13)$$

which models the variation of the magnetic permeability of the particles, μ_p , with the magnetic field. Here

χ_i is the initial magnetic susceptibility and M_s is the saturation magnetization of the particles. We take for our system, $\chi_i = 131$ and $M_s = 1990 \frac{kA}{m}$ ²⁹. The variation of the relative magnetic permeability of the particles directly affects the calculation of the contrast factor, β which, in turn, modifies the real value of H_0 . Despite of that, β remains practically constant (~ 1) over a wide range of magnetic fields (Figure 12, dashed line). The effect on the calculation of H_0 is thus small.

Another possible explanation for the scaling of the magnetic field lies on the effect of the particles on the magnetic field, but due to the low density of particles it is expected to play a minor role. Also, the interaction can have influence from quadrupolar and higher terms, which are neglected since the dipolar interaction is considered as a good approximation. It must be also remembered that the system is polydisperse both in the simulations and experiments, and the average radius is taken to calculate the interaction strength. The polydispersity is, however, different in both systems, log-normal like and much larger in the experimental one.

The viscosity of the monodisperse system is also included in Figure 11. These data are also collapsed onto the same curve, but starts to deviate when crystallization occurs, as discussed previously. The master curve obtained by the collapse of all data can be described by a quadratic dependence of the viscosity on the magnetic field, shown in the figure as a discontinuous line. This functional form is predicted by the particle magnetization model², indicating the validity of the model for the range of magnetic fields studied here.

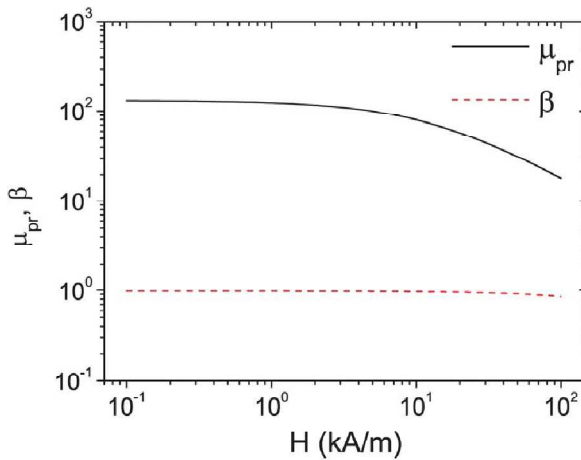



FIG. 12 Evolution of β (dashed line) and μ_{pr} (solid line) as a function of the external magnetic field.

The viscoelastic moduli obtained from simulations and experiments can also be compared qualitatively. Both moduli grow with increasing magnetic field, and develop a shoulder at low frequencies, indicative of the slowing down of the structural relaxation. Whereas the experimental system reaches the point where $G' \approx G''$, giving an estimate of the fluid to solid transition, in the simulations $G'' > G'$ for all states (except at high frequencies).

V. CONCLUSIONS

Brownian dynamic simulations and experimental techniques have been used to study of magnetorheological fluids. We focus on the rheological properties of unsheared systems. The study of the structure of the system shows that thick columns form for moderate field strengths. The monodisperse system crystallizes, while the polydispersity effectively suppresses it. A scaling of the



viscosity is presented that allows comparison of different experimental systems and shear rates. The simulation results, can also be collapsed onto the same master curve, with a suitable scaling of the magnetic field. This scaling is necessary due to the approximations involved in the simulations (dipolar interaction, effective field, polydispersity,...). The master curve where all systems collapse shows a quadratic behaviour with the magnetic field. The shear moduli have also been obtained experimentally and in simulations, and agree qualitatively. Both moduli develop a shoulder at low frequencies upon increasing the external magnetic field. These moduli also give us an estimation of the fluid to solid transition point.

ACKNOWLEDGMENTS

This work was supported by MICINN, MAT 2010-15101 and MAT 2011-28385 projects (Spain) and by Junta de Andalucía and FEDER under projects P09-FQM-4938, P10-FQM-5977, P10-RNM-6630 and P11-FQM-7074. J. P. Segovia-Gutiérrez acknowledges financial support by the "Ministerio de Educación: Becas del Programa de Formación del Profesorado Universitario (FPU)" (AP2008-02138). J. de Vicente and R. Hidalgo-Álvarez thank the financial support received from CEI-Biotic 20F12/16.



REFERENCES

- ¹J. Rabinow, *AIEE Trans.*, 1948, **67**, 1308.
- ²J. de Vicente, D.J. Klingenberg, and R. Hidalgo-Álvarez, *Soft Matter*, 2011, **7**, 3701.
- ³J. Liu, G. A. Flores and R. Sheng, *J. Magn. Magn. Mater.*, 2001, **225**, 209.
- ⁴F. Donato, J. L. Carrillo and M. E. Mendoza, *J. Phys.: Condens. Matter*, 2002, **14** 2153.
- ⁵O. Volkova, S. Cutillas, and G. Bossis, *Phys. Rev. Lett.*, 1999, **82**, 233.
- ⁶Bossis02} G. Bossis, O. Volkova, S. Lacis, and A. Meunier, in *Ferrofluids*, edited by O. Odenbach (Springer, Germany, 2002), pp. 202-230.
- ⁷J. de Vicente, J. P. Segovia-Gutiérrez, E. Andablo-Reyes, F. Vereda, and, R. Hidalgo-Álvarez, *J. Chem. Phys.*, 2009, **131**, 194902.
- ⁸R. Patel and B. Chudasama, *Phys. Rev. E*, 2009, **80**, 012401.
- ⁹P. Kuzhir, M. T. López-López, and G. Bossis, *J. Rheol.*, 2009, **53**, 127.
- ¹⁰G. L. Gulley and R. Tao, *Phys. Rev. E*, 1993, **48**, 2744.
- ¹¹R. Tao and Qi Jiang, *Phys. Rev. Lett.*, 1994, **73**, 205.
- ¹²D. J. Klingenberg, Frank van Swol, and C. F. Zukoski, *J. Chem. Phys.*, 1989, **91**, 7888.
- ¹³D. J. Klingenberg, Frank van Swol, and C. F. Zukoski, *J. Chem. Phys.*, 1991, **94**, 6160.
- ¹⁴G. L. Gulley and R. Tao, *Phys. Rev. E*, 1997, **56**, 4328.
- ¹⁵M. Parthasarathy and D. J. Klingenberg, *J. Non-Newt. Fluid Mech.*, 1999, **81**, 83.

-
- ¹⁶J. de Vicente, F. Vereda, J.P. Segovia-Gutiérrez, M. Del Puerto Morales and R. Hidalgo-Álvarez, *J. Rheol.*, 2010, **54**, 1337.
- ¹⁷J. de Vicente, J. A. Ruiz-López, E. Andablo-Reyes, J. P. Segovia-Gutiérrez and R. Hidalgo-Álvarez, *J. Rheol.*, 2011, **55**, 753.
- ¹⁸M. Heine, J. de Vicente and D.J. Klingenberg, *Physics of Fluids*, 2006, **{bf 18}**, 023301.
- ¹⁹J. E. Martin, *Phys. Rev. E*, 2000, **63**, 011406.
- ²⁰D. J. Klingenberg, *J. Rheol.*, 1993, **37**, 199.
- ²¹M. Mohebi, N. Jamasbi and J. Liu, *Phys. Rev. E*, 1996, **54**, 5407.
- ²²Paul and D. Y. Yoon, *Phys. Rev. E*, 1995, **52**, 2076.
- ²³P.J. Steinhardt, D.R. Nelson, M. Ronchetti, *Phys. Rev. B*, 1983, **28**, 784.
- ²⁴J.P. Segovia-Gutiérrez, J. de Vicente, A.M. Puertas, R. Hidalgo Álvarez, Submitted.
- ²⁵C.L.A. Berli and J. de Vicente, *Applied Physics Letters*, 2012, **101**, 021903.
- ²⁶J.P. Segovia-Gutiérrez, C.L.A. Berli and J. de Vicente, *J. Rheol.*, 2012, **56**, 1429.
- ²⁷P. J. Rankin, Thesis, University of Wisconsin (Madison), (2000).
- ²⁸J. de Vicente, F. González-Caballero, G. Bossis and O. Volkova, *J. Rheol.*, 2002, **46** 1295.





STRONGLY VISCOELASTIC MR FLUIDS

Up to now, the solvents used in the formulation of MR fluids have been Newtonian fluids. In this section, as a complementary part of our work, we are going to study MR fluids based on viscoelastic liquids, specifically Boger fluids. It is worth to remark that this section is far to be complete and only preliminary experimental results will be included.

There are many reasons to explore these new fluids but, in our case, there were mainly two ones which led us to carry out this study: the high viscosity of Boger fluids and its viscoelastic properties. On the one hand, sedimentation process is inherent in MR fluids due to the large particle density and therefore, reducing the settling rate is very important. One possibility is to modify the medium by adding thixotropic agents, surfactants, etc. or, by **changing the solvent**. Then, the high viscosity ($\sim 2 \text{ Pa} \cdot \text{s}$) of Boger fluids plays a relevant role in this sense. On the other hand, intrinsic viscoelastic properties of Boger fluids can introduce new and interesting effects in the rheological response. Therefore, this study leaves the door open for further research.

The formulation of these new MR fluids is the following: as a solid phase, we used silica coated carbonyl iron particles ($d \sim 1 \mu\text{m}$) to prevent degradation of iron in presence of water; a Boger fluid composed by glucose syrup, distilled water, a very small amount of polyacrylamide and sodium azide¹ (to avoid the evolution of microorganisms) was used as the solvent.

To characterize these systems, we performed conventional rheological tests, such as strain amplitude sweep tests, small amplitude oscillatory shear tests or steady shear flow tests. The used devices were both a MCR 501 torsional



rheometer (Anton Paar) with a parallel-plate (20 mm) geometry and a Haake Caber 1 extensional rheometer (Thermo Fisher Scientific).

Boger fluid

The first thing that we did was to characterize the Boger fluid without particles. As in the case of Newtonian fluids, the dissipation of energy dominates ($G'' > G'$) in the rheological response of the Boger fluid. However, the elastic part or the storage modulus (G') in the response is non-negligible, contrary to Newtonian fluids. In Figure 1 viscoelastic moduli of the Boger fluid are shown as a function of the strain amplitude and the angular frequency. In both tests the predominance of the loss modulus (G'') is evident over the entire frequency and strain amplitude ranges.

In steady shear flow tests, the elastic character of the Boger fluid becomes more evident, as we can observe in Figure 2, where the first normal stress difference ($N_1 = \sigma_{11} - \sigma_{22}$; $N_1 = 0$ in Newtonian fluids) is plotted against the shear rate. Also in steady shear flow tests, the appearance of a normal force (F_N) is remarkable. Therefore, despite of the small amount of polyacrylamide in the solvent, this polymer greatly alters the rheological properties of the medium.

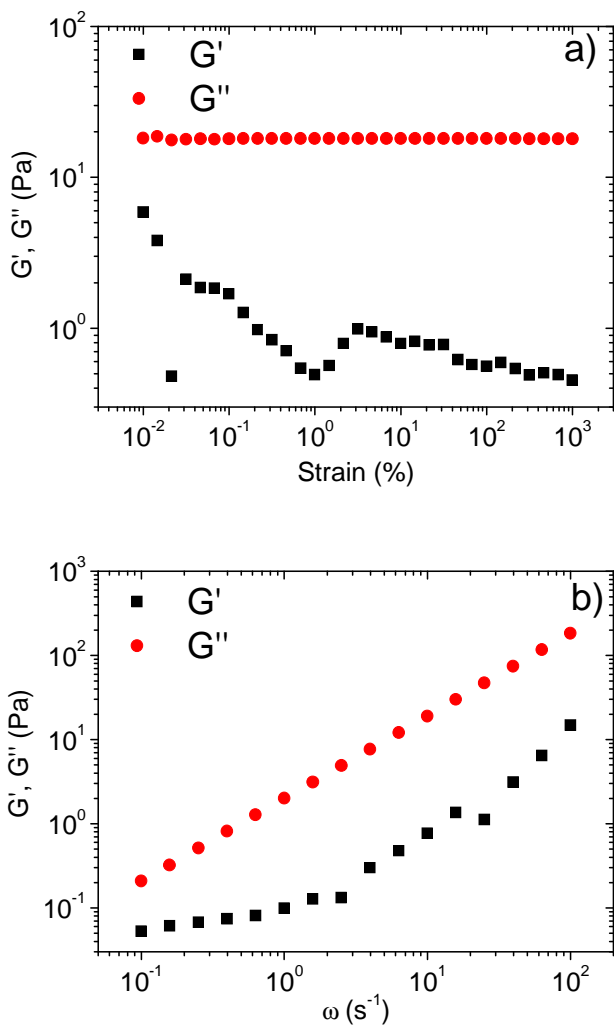


FIG. 1 In a), viscoelastic moduli are presented *versus* the strain amplitude. In b), the moduli are shown as a function of the angular frequency. It is clear the non-negligible value of the storage modulus.

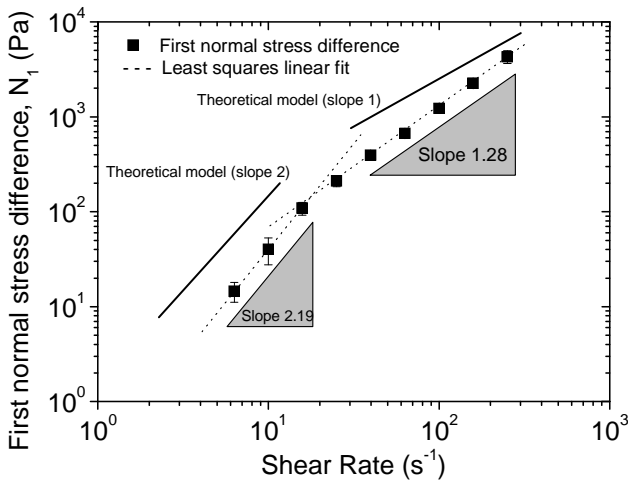


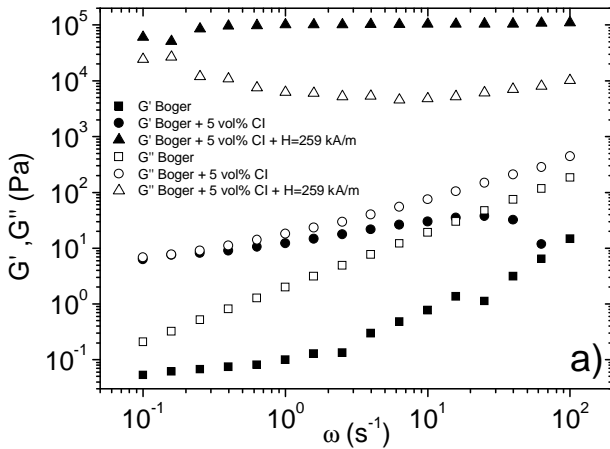
FIG. 2 First normal stress difference as a function of the shear rate. Solid lines represent theoretical predictions¹.

Boger fluid with particles

The next step was to add particles to the Boger fluid. Particle concentrations were 1 and 5 vol% and the system was subjected to a constant magnetic field strength of 259 kA/m. Again, the same experimental procedures were performed. We observed that the presence of particles in the solvent changes the rheological response by conferring more elasticity, even without magnetic field. This particle effect is also observed in the case of MR fluids based on Newtonian solvents.

The storage modulus shows an enhancement when particles are added to the medium and the growth of G' is much more relevant when the system is under the presence of magnetic fields. Not only the storage modulus increases, but

also the loss modulus suffers important changes under those conditions. Due to that, it is possible to observe a clear transition from liquid-like to solid-like state, as we can see in the graph a) of Figure 3. A Boger fluid without particles exhibits a predominant energy dissipation state; at 5 vol%, energy dissipation and storage become almost the same over all the frequency domain ($G' \approx G''$); in presence of a high magnetic field, elastic behavior dominates ($G' > G''$).



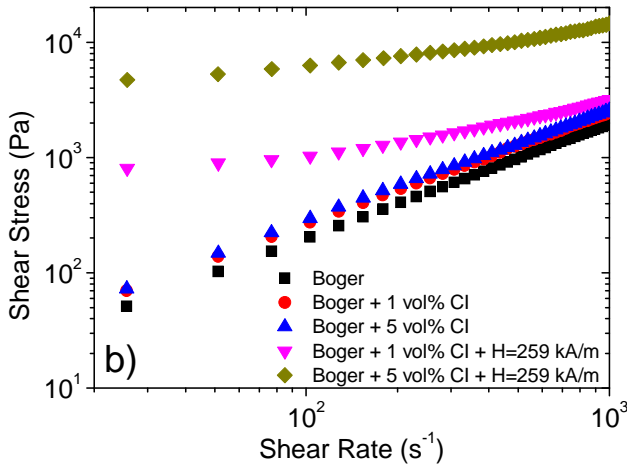


FIG. 3 In the graph a), the viscoelastic moduli are shown *versus* the angular frequency. At b): shear stress-shear rate curves are shown for three different particle concentrations: 0, 1 and 5 *vol%*, with and without magnetic field. **CI** means Carbonyl Iron.

This particle effect also manifests in steady shear flow tests, where the shear stress increases with the particle volume fraction and the magnetic field (see bottom graph in Figure 3).

The normal force was also studied as it is shown in Figure 4. In this figure, apparently there seems to be a contradiction with that has been seen before: the normal force (directly related with the elasticity) decreases when increasing particle concentration and becomes negative in the presence of magnetic fields at 5 *vol%*. This apparent contradiction will be explained later.

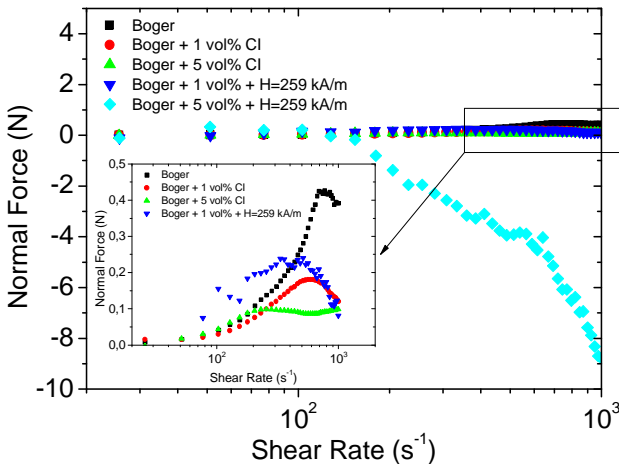


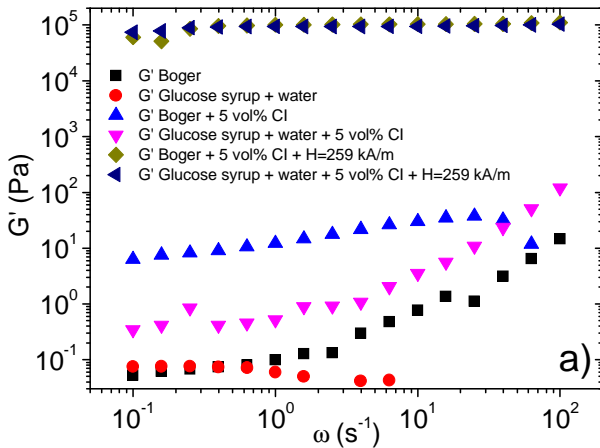
FIG.4 Normal force exerted on the upper plate as a function of the shear rate. The maximum force is achieved by the Boger fluid without particles.

Effect of the polyacrylamide

An essential part of this study is the effect of the presence or absence of polyacrylamide in the solvent. In order to evaluate that effect, we carried out an experimental comparison between the MR fluid based on the Boger fluid and a MR fluid based on a liquid with the same composition and viscosity than the Boger fluid, but without polyacrylamide. Direct comparison of the storage modulus for both systems clearly reflects the effect of the presence of the polymer in the solvent, as we can observe in the graph a) of Figure 5. Without particles, the storage modulus that corresponds to the Boger fluid increases with ω two orders of magnitude, while G' for the Newtonian fluid remains at very low values. At a particle concentration of 5 vol%, both elastic moduli are



non-negligible, and a greater increase is observed in the case of the Newtonian fluid if compared with the MR fluid based on the Boger. It can be explained due to the intrinsic elasticity of the Boger fluid, that makes the storage modulus larger in the region of low frequencies. Finally, under the presence of large magnetic fields, there are no clear differences because magnetostatic forces dominate. Graph b) of Figure 5 corroborates the influence of polyacrylamide.



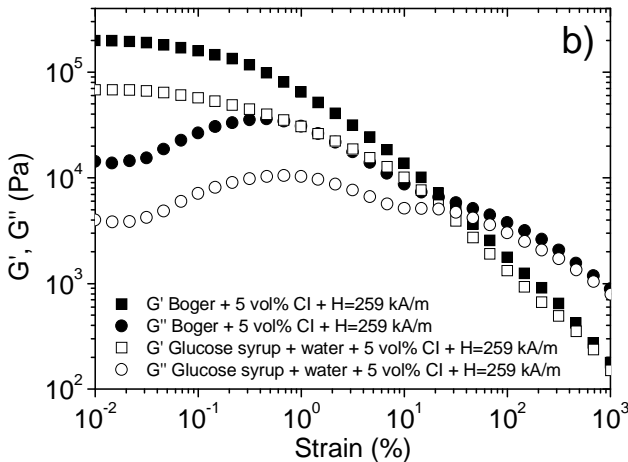


FIG. 5 In the upper graph, storage moduli as a function of the angular frequency are shown in presence and absence of a magnetic field. At the bottom, viscoelastic moduli are shown at a concentration of 5 vol%, under a constant magnetic field strength of 259 kA/m.

In Figure 6, normal force for both MR fluids is shown. In this case, the presence of particles does not affect the response of the MR fluid based on the Newtonian fluid: normal force remains nearly constant and is very close to zero. It is clear that polyacrylamide in the solvent improves the viscoelastic response of MR fluids under different rheological tests. Other factor which also affects the behavior of the system is the presence of particles. We have seen that the normal force, in the case of the Boger fluid, decreases when particles are dispersed in the solvent and additionally, this diminution is greater when the volume fraction increases. On the other hand, the presence of particles in MR fluids based on Newtonian fluids produces an increase in the normal force and,



when the particle volume fraction increases, the normal force also increases. Therefore, the polyacrylamide and the particles somehow interact between them. We mentioned above that carbonyl iron particles were coated with a thin silica layer and it is well known that silica and polyacrylamide interact. The latter implies the plausible adsorption of polymer chains onto silica surface² and this could affect the system elasticity due to the diminution in the number of dispersed polyacrylamide chains. This should be one of the main reasons to explain the decrease in the normal force. However, this effect has not been studied thoroughly in this work yet.

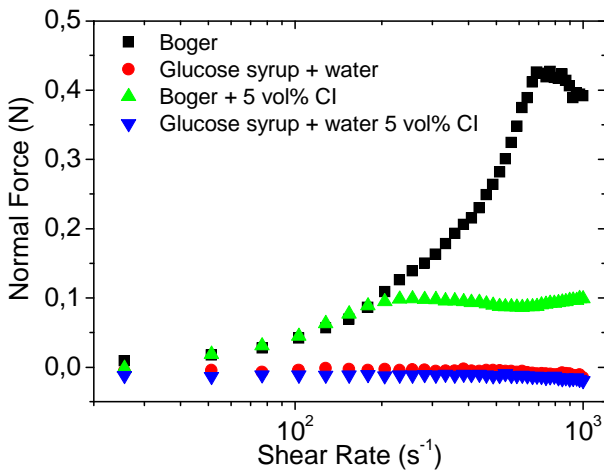


FIG. 6 Normal force *versus* shear rate, with and without particles, for MR fluids based on Newtonian and Boger liquids.

On the other hand, it is also known that polymer chains can break when they are subjected to mechanical stresses. To disperse well the particles in the Boger fluid it is necessary to stir the sample up to its correct homogenization, and this

requires some minutes of stirring. Therefore, stirring the sample may affect the elasticity of the solvent due to the degradation of the polymer chains. Thus, we carried out a systematic study to understand the dependence of the solvent elasticity on the stirring time (see Figure 7).

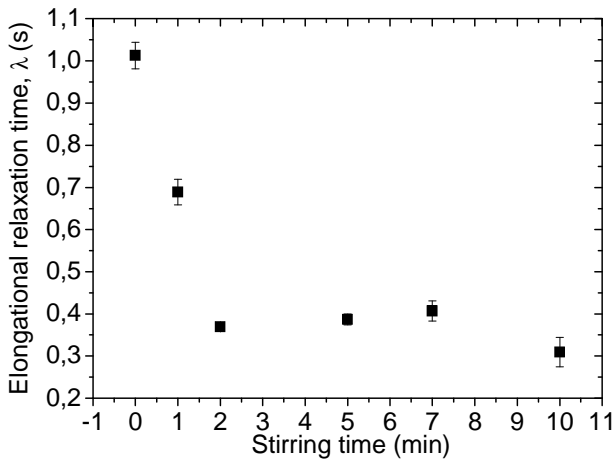


FIG. 7 Elongational relaxation time of the Boger fluid as a function of the stirring time.

In elongational flow experiments, the elastic relaxation time is directly related with the elasticity of the system³. In Figure 7, we notice that the relaxation time decreases when the stirring time increases. This fact can be explained because of the correlation between the polymer chain length and the relaxation time: an increase in the stirring time produces a greater polymer chain degradation and therefore, a decrease in the elongational relaxation time. We can see that up to ~ 5 minutes, there is a sharp drop in the relaxation time and then, a plateau value is achieved. With this, we can now propose a qualitative explanation for the trends observed in Figure 4, where we observe that the curve which



corresponds to 1 vol% shows a larger normal force if compared with the curve at 5 vol%. This fact can be explained by arguing the following: on the one hand, due to the higher particle concentration, the adsorption of polyacrylamide onto silica surface may be more important and this implies the consequent decrease in the elasticity; on the other hand, dispersing less amount of particles requires lower stirring times, so degradation in the polymer chains is less important. Thus, elongational relaxation time is higher.

CONCLUSIONS

As a direct consequence of the high viscosity of the Boger fluid, we considerably can **reduce the particle settling time** if compared the viscosity of the Boger with the corresponding to silicone oils ($\sim 0.02 \text{ Pa} \cdot \text{s}$). Boger fluid itself has enhanced elastic properties with respect to the Newtonian fluid with the same viscosity and implicitly **improves the response of the global system**. The presence of polyacrylamide in the medium, with and without iron particles **clearly improves the viscoelastic properties** (G' and G'' increase) and it would give a higher efficiency in mechanical applications. **The stirring** of the sample reduces the length of polymer chains but the elasticity remains despite of this fact. The effect of stirring is most notable in the case of the normal force. The **adsorption of polyacrylamide onto the silica surface** of iron particles may be important in the diminution of the elasticity, but this effect has not been studied in detail yet.

**REFERENCES**

- ¹J. R. Stokes, *Swirling flow of viscoelastic fluids*. Research Collections (UMER), 1998.
- ²L. T. Lee and P. Somasundaran, *Langmuir*, **5**, 854, 1989.
- ³Campo-Deaño, L. and Clasen, C., *Journal of Non-Newtonian Fluid Mechanics*, **165**, 1688-1699, 2010.





CONCLUSIONS

Within this last section, the main conclusions and reflections of this dissertation are extracted.

First conclusion that should be shown is that magnetorheological fluids are very versatile systems and really good candidates to be considered as **smart materials**. We have seen that under the presence of an **external magnetic field**, rheological properties of these fluids are completely modified and can be controlled. As important modifications: the viscosity increases several orders of magnitude, the elastic behavior of the system overcomes the dissipation process and, if the magnetic field is sufficiently high, **yielding processes** make its appearance.

As a second conclusion, it has become clear from Part I that the particle morphology is determinant in the MR effect and, more specifically the particle anisotropy, where it has been demonstrated that **rod-based MR fluids gives the most efficient and the highest magnetorheological response**, the lower gelation threshold and the highest viscoelastic moduli. In that sense, formulation of MR fluids based on rod-like particles is highly recommended for mentioned applications. Also it is highlighted the influence of the **surface roughness**, which translates in an enhancement in the MR response, so this must also be taken into account in commercial applications. Finally, it is worth to remark that depending on the material in the composition of particles, higher or lower values of the viscoelastic moduli can be achieved because of the intrinsic saturation magnetization of that material. In light of these results, iron



particles present higher viscoelastic moduli and therefore, they are more appropriate for industrial applications.

A third conclusion concerns the effect of **particle concentration** in the MR effect. We have seen that below a certain **particle volume fraction** (Φ_c), magnetorheological response at low magnetic fields (below a **magnetic field threshold** or **gelation threshold**, H_c) is negligible and independent of the particle morphology. Therefore, from an industrial application point of view, it should be fundamental to exceed this value in the preparation of commercial MR fluids. Interestingly, we could observe that theories and interpretations applied to other physical systems such as attractive colloidal glasses and depletion colloidal gels, can extrapolate to our systems because many similarities are present in the rheological behavior, when volume fraction is over the critical particle concentration, Φ_c .

From a fundamental point of view, as a fourth conclusion, we **checked the validity of several theoretical models** which try to explain the storage modulus and yield stress dependence on the magnetic field and the particle concentration. Also a **new theoretical model**, applied to rod-like particles, was proposed and tested, **resulting in a very good agreement with experimental results**, and manifesting the dependence of the storage modulus and the yield stress on the volume fraction (directly linked with the number of gap spanning aggregates), the square of the magnetic field and the relative dimensions of particles. On the other hand, by using a **colloidal gel approach** to understand mechanisms which involve the effect of the particle concentration on the MR effect, we satisfactorily explained the inconsistencies found in the MR fluid literature about this issue.

Also within the fundamental aspects, the **Mason number** reveals that there are two fundamental physical interactions which control the dynamics of sheared MR fluids: the magnetic and the hydrodynamic forces. Additionally, it is shown that in the case of MR fluids based on anisotropic particles (rods or plates), frictional forces between particles play an important role in the total contribution.

As a fifth conclusion, **Brownian Dynamic Simulations** has provided us a more complete vision about the physics behind the MR effect. We have observed the time evolution of the microstructure in a more accurate way and we have corroborated the existence of a minimum magnetic field below which, structures are not stable. Also we studied the internal dynamics of the structure, and we could establish a direct relationship between this internal dynamics and the measurable macroscopic magnitudes such as the viscosity and the viscoelastic moduli, for which we covered regions of very low frequencies that are experimentally inaccessible.

Another important aspect that we studied was the effect of the solvent in the MR response. Conventional MR fluids have to be modified by adding thixotropic agents, etc. to diminish the settling rate of particles. Thus, in our case, we changed the common solvents (silicone oils) for a Boger fluid, as an attempt to improve the particle stability and to introduce new mechanical properties to MR systems. From the results shown above, it is clear that intrinsic properties of the solvent affect the rheological response of MR fluids. Due to the high viscosity of the Boger fluid, the sedimentation process could be slowed down and, additionally, viscoelastic properties of the Boger fluid provide an enhancement in the elastic behavior, even in the off-field state. However, the stirring process



to disperse particles and the plausible adsorption of polyacrylamide onto the silica surface greatly affect to the solvent elasticity. For all that, the development of MR systems based on viscoelastic fluids could be a new line in Magnetorheology.

Therefore, understanding fundamental parameters which control the behavior of MR fluids, one can get a complete vision about these systems and hence, one can have powerful tools to plan and design devices and applications in a better and efficient way. Throughout this dissertation, we have seen the use of theoretical, experimental and computational methods, and this fact clearly shows that the fusion of these three disciplines provides researchers with a broader vision and a wider understanding in MR fluids in particular, and in Science, in general.



CONCLUSIONES

Dentro de esta última sección, las principales conclusiones y reflexiones de esta disertación son expuestas.

La primera conclusión que debería ser expuesta es la de que los fluidos MR son sistemas muy versátiles y que son realmente buenos candidatos para ser considerados como materiales inteligentes. Hemos visto que bajo la presencia de un campo magnético externo, las propiedades reológicas de estos fluidos son completamente modificadas y pueden ser controladas. Como importantes modificaciones: la viscosidad aumenta varios órdenes de magnitud, el comportamiento elástico del sistema domina al proceso de disipación y, si el campo magnético es lo suficientemente intenso, el fenómeno de esfuerzo umbral aparece.

Como segunda conclusión, ha quedado claro que la morfología de las partículas es determinante en el efecto MR y, más específicamente, la anisotropía de las partículas, donde se ha demostrado que los fluidos MR basados en partículas en forma de varilla dan una más eficiente y alta respuesta MR, un menor umbral de gelificación y un efecto viscoelástico. En este sentido, la formulación de los fluidos MR basados en partículas en forma de varilla son altamente recomendables para las aplicaciones mencionadas. También se destaca la influencia de la rugosidad de la superficie, la cual se traduce en un aumento y mejora de la respuesta MR, por lo que esto debe de ser tenido en cuenta, también, en las aplicaciones comerciales. Finalmente, es importante remarcar que dependiendo del material del que estén compuestas las partículas, mayores o menores valores de los módulos viscoelásticos se pueden alcanzar, debido al



valor intrínseco de la magnetización de saturación del material. A la luz de los resultados, las partículas de hierro presentan un mayor efecto viscoelástico y, por tanto, son más apropiadas para las aplicaciones industriales.

La tercera conclusión se refiere al efecto de la concentración de partículas en la respuesta MR. Hemos visto que bajo un cierto valor de la fracción de volumen (Φ_c), el efecto MR a bajas intensidades de campo magnético (por debajo del umbral de campo magnético o umbral de gelificación, H_c) es despreciable e independiente de la morfología de las partículas. Por tanto, desde un punto de vista comercial, sería fundamental exceder este valor en la preparación de fluidos MR. Es notable decir que pudimos observar que las teorías e interpretaciones aplicadas a otros sistemas físicos tales como vidrios coloidales atractivos y geles coloidales, pueden extrapolarse a nuestros sistemas debido a las similitudes presentes en el comportamiento reológico, siempre que la fracción de volumen esté sobre la concentración crítica, Φ_c .

Desde un punto de vista fundamental, como cuarta conclusión, testeamos la validez de varios modelos teóricos que intentan explicar la dependencia con la intensidad del campo magnético y la concentración de partículas del módulo elástico y del esfuerzo umbral. También, un nuevo modelo teórico, aplicado a partículas en forma de varilla, fue propuesto y testeado, resultando en un muy buen acuerdo con los resultados experimentales, y manifestando la dependencia del módulo elástico y del esfuerzo umbral con la fracción de volumen (directamente conectado con el número de agregados que conectan los platos), el cuadrado de la intensidad del campo magnético y las dimensiones relativas de las partículas. Por otro lado, usando una aproximación de gel coloidal para entender los mecanismos envueltos en el efecto de la

concentración de partículas sobre el efecto MR, explicamos satisfactoriamente las inconsistencias encontradas en la bibliografía sobre fluidos MR.

También, dentro de los aspectos fundamentales, el número de Mason revela que hay dos interacciones fundamentales que controlan la dinámica en los fluidos MR bajo cizalla: las fuerzas magnéticas e hidrodinámicas. Además, se muestra que en el caso de fluidos MR basados en partículas anisótropas (varillas y platos), las fuerzas de fricción entre partículas juegan un papel fundamental en la contribución total.

Como quinta conclusión, las simulaciones en Dinámica Browniana nos aportaron una visión más completa sobre la física que hay detrás del efecto MR. Hemos observado la evolución estructural de la micro-estructura de un modo más preciso y hemos corroborado la existencia de un mínimo en el valor del campo magnético, por debajo del cual, la estructura no es estable. También estudiamos la dinámica interna de la estructura y pudimos establecer una relación directa entre esta dinámica y las magnitudes macroscópicas medibles tales como la viscosidad y los módulos viscoelásticos, para los cuales cubrimos regiones a muy bajas frecuencias que son experimentalmente inaccesibles.

Otro importante aspecto que estudiamos fue el efecto del solvente en la respuesta MR. Los fluidos MR convencionales tienen que ser modificados mediante la adición de agentes tixotrópicos, etc. para disminuir la velocidad de sedimentación de las partículas. En nuestro caso, hemos cambiado los disolventes comunes (aceites de silicona) por un fluido Boger, como un intento de mejorar la estabilidad de las partículas e introducir nuevas propiedades mecánicas de los sistemas MR. A partir de los resultados mostrados anteriormente, está claro que las propiedades intrínsecas del disolvente afectan



a la respuesta reológica de estos fluidos. Debido a la alta viscosidad del fluido Boger, el proceso de sedimentación es más lento y, además, las propiedades viscoelásticas del fluido Boger proporcionan una mejora en el comportamiento elástico, incluso en el estado sin campo. Sin embargo, el proceso de agitación para dispersar las partículas y la posible adsorción de poliacrilamida sobre la superficie de sílice de las partículas afecta en gran medida a la elasticidad del disolvente. Debido a ello, el desarrollo de sistemas MR basados en fluidos viscoelásticos podría ser una nueva línea de investigación en Magneto-reología.

Por lo tanto, de la comprensión de los parámetros fundamentales que controlan el comportamiento de los fluidos MR se puede obtener una visión completa acerca de estos sistemas y así, obtener poderosas herramientas para planificar y diseñar dispositivos y aplicaciones de una mejor y más eficiente manera. A lo largo de esta tesis hemos visto el uso de métodos teóricos, experimentales y computacionales, y este hecho demuestra claramente que la fusión de estas tres disciplinas proporciona a los investigadores una visión y una comprensión más amplias de los fluidos MR en particular, y de la Ciencia, en general.

APPENDIX: SIMULATION CODES

In this appendix the simulation codes used in this work are going to be shown. Codes were written and compiled with **Fortran 90** and all the equations are normalized by $k_B T$, m and a and to carry out simulations, these parameters were taken as the unit: $k_B T = m = a = 1$. Data obtained from the “main code” were analyzed by other external programs: structure factor, order parameters, mean square displacement, stress correlation function, bond correlation function, viscosity, etc.

Main simulation code

program particles

!Files

!50 "input.dat" phi, no, tmax, trelaj(1), ncorr, rand_file

!12 "pos.dat"

!17 "tensor.dat"

!18"energia_pot_cin.dat" nmax, phi, trelaj(1), lx

!14"long_pos.dat"

!Variable Definition

!Number of particles

parameter (nmax=1000)

*real*8* dkin,dpot,pcoseno,sumtau2



!Position vector components and integrals of the stress tensor components

*real*8* x0(1000),y0(1000),z0(1000),A12(500),A13(500),A23(500)

!Velocity components, stress tensor components, magnetic field parameters

*real*8* vx0(1000),vy0(1000),vz0(1000),tau(3,3),u0,uN

*real*8*

x0c(500,1000),y0c(500,1000),z0c(500,1000),rad(1000),mas(1000),mm,mastot

!particle radius; particle

mass

!Definition of total forces

*real*8* ftotx(1000),ftoty(1000),ftotz(1000),r2

!Number of correlators; maximum of iterations

*integer*4* i,imax,idn,j,k,rand_file,icorr,jcorr(500),alf,bet,ncorr

!lx,ly,lz dimensions of the simulation box, kt thermal energy, dt time step

*real*8*

dt,lx,ly,lz,t,sigma(1000),ddgamma,kt,dn(500),l,sumtau,nvecmedio,sumcol,volpar

t,diamed

!Relaxation time of the first correlator, trelaj(1)!phi, particle concentration (in volume)

!MSD, mean square displacement!tmax, maximum computation time

*real*8* trelaj(500),phi,distx,disty,distz,dcm(500),rc,tmax,dcmx,dcmz,dcmz,rm

*character*10* b(3)

*character*70* aaa

!Change the onset of the random number function

```

integer*4 date_time(8),icho
common /bloque/ dgamma,sigma,mas
common /blot/ dt,t,ncorr
common /caja/ lx,ly,lz,l
common /pos/ x0,y0,z0
common /vel/ vx0,vy0,vz0
common u0
common /force/ ftotx,ftoty,ftotz
common /radios/ rad

```

!Read from "input.dat" file these parameters: phi, u0, tmax, trelaj(1), ncorr,**rand_file**

```

open (50,file='input.dat',status='old') !input.dat
read (50,201) aaa
201    format (A70)
read (50,*) phi,u0 !Particle concentration!Magnetic control parameter
read (50,201) aaa
read (50,*) tmax,trelaj(1),ncorr !Total time!Relaxation time of the first
correlator
read (50,201) aaa
read (50,*) rand_file !If rand_file=1 is generated a random distribution (=1
read)
close (50)
write(*,*) 'rand_file',rand_file

```

!U0=4*PI*MU0*MUCR^2*BETA^2*H0^2



!The prefactor in the magnetic force is: $F_0=3*U_0*A(i)^3*A(j)^3$

$\pi=\text{acos}(-1.)$ **!number Pi**

!Generate a random seed with the milliseconds of the actual hour

call date_and_time(b(1),b(2),b(3),date_time)

*icho=date_time(8)+1000*date_time(7)*

call srand(icho)

!Values of the main variables

$dt=0.0005$ **!Time step**

$d\gamma=10.0$ **!Inverse of the diffusion coefficient**

$kt=1.0$ **!Normalized thermal energy**

$i_{\max}=\text{int}(t_{\max}/dt)$ **!Maximum of iterations**

!We give a very large relaxation time to all correlators, contrary to the first one

do icorr=2,ncorr

trelaj(icorr)=1e8

end do

!New files

$t=0.0$

open(unit=12,file='pos.dat',status='unknown',form='unformatted') **!Store all the positions and velocities as a function of time**

open(unit=15,file='prueba.dat',status='unknown') **!Store the mean square displacement**

open(unit=17,file='tensor.dat',status='unknown') **!Store the stress tensor components**

open(unit=18,file='energia_pot_cin.dat',status='unknown') **!Store the structural order parameters: potential energy, kinetic energy, number of neighbors**

open(unit=31,file='diam_alea.dat',status='unknown') **!Store particle radius**

open(unit=35,file='vol_alea.dat',status='unknown') **!Store particle volume**

!Read the diameter file, the particle volume and the average radius

read(31,*) volpart

read(31,*) diamed

read(31,*) mm **!Average particle mass**

mastot=0.

do i=1,nmax

read(31,*) rad(i) **!Read the particle radius**

mas(i)=(4./3.)*pi*(rad(i)**3.) **!Mass of each particle**

mas(i)=mas(i)/mm **!Normalized particle mass**

end do

do i=1,nmax

mastot=mastot+rad(i)**3

end do

mastot=mastot*(4./3.)*pi

mastot=mastot/mm

write(*,*) 'Total mass',mastot

write(*,*) 'Average radius',diamed

write(*,*) 'Average mass',mm

write(*,*) 'Total particle volume',volpart



!Calculation of the sigma coefficient for each particle; mass varies from one particle to another; Mass is divided by the average mass

```
do i=1,nmax
sigma(i)=SQRT(2.0*ddgamma*mas(i)*kt)
end do
```

!Volume of the simulation box

```
volcaja=volpart/phi
lx=(volcaja)**(1./3.)
ly=lx
lz=lx
write(*,*) 'Edge: ',lx
write(*,*) 'Particle concentration',phi
l=lx/((real(nmax))**(1./3.)) !Length of the edge segments: edge is divided in parts with the same length
write(*,*) 'Segments: ',l
```

!Write in "energia_pot_cin.dat" the values of nmax, phi, trelaj y l

call inicposvel(rand_file) **!Give the initial positions and velocities**

```
write(18,*) nmax
write(18,*) phi
write(18,*) trelaj(1)
write(18,*) lx
call flush(18) !Write instantaneously
write(12) lx
```

!Initialization of correlators



```

write(*,200) t,dkin,dpot,nvecmedio,pcoseno,sumcol
write(18,200) t,dkin,dpot,nvecmedio,pcoseno,sumcol
200 format(F10.5,F8.2,F8.2,F8.3,F8.3,F8.3) !Erase negligible decimals
call flush(18)
end if

```

!Every 200 steps positions and velocities are written in "longpos.dat" for safety

```

if (i/200 .eq. i/200.) then
open(unit=14,file='longpos.dat',status='unknown')
write(14,*) lx !Write the length of the edge of the simulation box
do j=1,nmax

```

!Write all the positions and velocities

```

write(14,*) x0(j),y0(j),z0(j),vx0(j),vy0(j),vz0(j)
end do
close(14)
end if

```

!Give the sum of the stresses in each time if the current time overcomes the relaxation time of the first correlator (first measurements), calculates the stress tensor with the corresponding subroutine. When t overcomes the relaxation time of the first correlator, the stress tensor will be always calculated.

```

if (t .gt. trelaj(1)) call tenes(tau)

```

!Sweep over all the correlators that have already started to measure.

do icorr=1,ncorr

**!dn(icorr) is the time step of the correlator icorr at which the correlator writes
!The measurement frequency of the correlator decreases with the total
computational time, i.e. firstly measurements are carried out more frequently
and progressively, this frequency decreases.**

idn=int(dn(icorr))

**!If the total time overcomes the relaxation time of the current correlator, then
this correlator starts to measure and it counts the number of times that this
correlator appears. For that purpose, we use jcorr**

if (t .ge. (trelaj(icorr)-dt/2.)) then

jcorr(icorr)=jcorr(icorr)+1

!Integrals 1,2; 1,3 y 2,3 via the rectangle method. alpha<beta

!It is integrating to finally calculate the viscosity

*A12(icorr)=A12(icorr)+tau(1,2)*dt*

*A13(icorr)=A13(icorr)+tau(1,3)*dt*

*A23(icorr)=A23(icorr)+tau(2,3)*dt*

**!If the last condition is true, it means that we are in the first measurement of
the current correlator**

if (abs(t-trelaj(icorr)) .lt. dt/2.) then

!Old positions are changed by the current positions

do k=1,nmax

x0c(icorr,k)=x0(k)



```

y0c(icorr,k)=y0(k)
z0c(icorr,k)=z0(k)
end do
end if

```

If the number of times that the current correlator has counted is greater than the integer part of its measurement frequency, its relaxation time is changed by the current time. At this moment, the mean square displacement is calculated for each coordinate axis and positions and velocities are written in “pos.dat”

```

if (jcorr(icorr) .ge. idn) then
write(12) t-trelaj(icorr),icorr
dcm(icorr)=0.
dcmx=0.0
dcmy=0.0
dcmz=0.0
do j=1,nmax

```

!Write positions and velocities

```

write (12) x0(j),y0(j),z0(j),vx0(j),vy0(j),vz0(j)

```

!Periodic boundary conditions are applied to distances

```

distx=x0(j)-x0c(icorr,j)
distx=distx-lx*anint(distx/lx) !Closer integer with + or -
disty=y0(j)-y0c(icorr,j)
disty=disty-lx*anint(disty/lx)
distz=z0(j)-z0c(icorr,j)

```

$\text{ditz} = \text{ditz} - lx * \text{anint}(\text{ditz}/lx)$

!Calculation of the mean square displacement

$\text{dcmx} = \text{dcmx} + \text{ditz} * \text{ditz}$

$\text{dcmy} = \text{dcmy} + \text{dity} * \text{dity}$

$\text{dcmz} = \text{dcmz} + \text{ditz} * \text{ditz}$

$\text{dcm}(\text{icorr}) = \text{dcm}(\text{icorr}) + \text{ditz} * \text{ditz} + \text{dity} * \text{dity} + \text{ditz} * \text{ditz}$

end do

$\text{dcmx} = \text{dcmx} / \text{nmax}$

$\text{dcmy} = \text{dcmy} / \text{nmax}$

$\text{dcmz} = \text{dcmz} / \text{nmax}$

$\text{dcm}(\text{icorr}) = \text{dcm}(\text{icorr}) / \text{nmax}$

!Determination of the viscosity approximation = $(\beta/6V) * \lim_{t \rightarrow \infty} (A^*A/t)$

$\text{sumtau} = (\text{A12}(\text{icorr}) * \text{A12}(\text{icorr}) + \text{A13}(\text{icorr}) * \text{A13}(\text{icorr}) + \text{A23}(\text{icorr}) * \text{A23}(\text{icorr})) / 3.$

!Only xz and yz components of the stress tensor

$\text{sumtau2} = (\text{A13}(\text{icorr}) * \text{A13}(\text{icorr}) + \text{A23}(\text{icorr}) * \text{A23}(\text{icorr})) / 2.$

if $((t - \text{trelaj}(\text{icorr})) .gt. 1.0e-5)$ *then*

write(15,*) $\text{icorr}, t - \text{trelaj}(\text{icorr}), \text{dcmx}, \text{dcmy}, \text{dcmz}, \text{sumtau} / (t -$

$\text{trelaj}(\text{icorr})), \text{sumtau2} / (t - \text{trelaj}(\text{icorr}))$

end if

if $(\text{icorr} .lt. \text{ncorr})$ *then*

!If the current correlator measures a mean square displacement greater than 0.5 and also the next correlator has not started yet, the relaxation time of the

!!

!Initial positions and velocities

!!

```

subroutine inicposvel(rand_file)
parameter (nmax=1000)
real*8 x0(nmax),y0(nmax),z0(nmax)
real*8 vx0(nmax),vy0(nmax),vz0(nmax)
real*8 x1,y1,z1,lx,ly,lz,l,vm2,f,v1,v2,v3
real*8 vxm2,vym2,vzm2,nmax3,mas(nmax),ddgamma,sigma(nmax)
integer*4 i,j,k,ipart,rand_file
common /bloque/ ddgamma,sigma,mas
common /caja/ lx,ly,lz,l
common /pos/ x0,y0,z0
common /vel/ vx0,vy0,vz0
nmax3=exp(log(nmax*1.)/3.)
vm2=0.
ipart=1
open(unit=334,file='posinicial.dat',status='unknown')

```

!If rand_file =1, random positions and velocities will be generated

```

if (rand_file.eq.1) then
do i=1,int(nmax3)
do j=1,int(nmax3)
do k=1,int(nmax3)
x1=rand()
y1=rand()
z1=rand()

```



```

v1=rand()
v2=rand()
v3=rand()
x1=x1-0.5
y1=y1-0.5
z1=z1-0.5
v1=v1-0.5
v2=v2-0.5
v3=v3-0.5
x0(ipart)=-lx/2.+((2.*real(i)-1)/2.)*l+*(1./4.)*x1 !Random term
y0(ipart)=-ly/2.+((2.*real(j)-1)/2.)*l+*(1./4.)*y1 !Random term
z0(ipart)=-lz/2.+((2.*real(k)-1)/2.)*l+*(1./4.)*z1 !Random term
vx0(ipart)=v1*3.
vy0(ipart)=v2*3.
vz0(ipart)=v3*3.
vxm2=vx0(ipart)*vx0(ipart)
vym2=vy0(ipart)*vy0(ipart)
vzm2=vz0(ipart)*vz0(ipart)

```

!Conservation of energy:

!Total kinetic energy must be $(3/2)kT=3/2$, then $vm2=3$

```

vm2=(vxm2+vym2+vzm2)*mas(ipart)
f=3./vm2
vx0(ipart)=v1*3.*SQRT(f)
vy0(ipart)=v2*3.*SQRT(f)
vz0(ipart)=v3*3.*SQRT(f)
vxm2=vx0(ipart)*vx0(ipart)

```




```

subroutine posvel(mastot)
parameter (nmax=1000)
real*8 vx(nmax),vy(nmax),vz(nmax),x(nmax),y(nmax),z(nmax)
real*8 dgg,fvelx(nmax)
real*8 dx(nmax),dy(nmax),dz(nmax)
real*8 fvely(nmax)
real*8 fvelz(nmax)
real*8 fx,fy,fz,fposx,fposy,fposz
real*8 x0(nmax),y0(nmax),z0(nmax),t,dt
real*8 vx0(nmax),vy0(nmax),vz0(nmax)
real*8 ftotx(nmax),ftoty(nmax),ftotz(nmax)
real*8 lx,ly,lz,l,ddgamma,sigma(nmax),mas(nmax),mastot
real*8 vxcm,vycm,vzcm
integer*4 i,j,ncorr
common /bloque/ dgamma,sigma,mas
common /blot/ dt,t,ncorr
common /pos/ x0,y0,z0
common /caja/ lx,ly,lz,l
common /vel/ vx0,vy0,vz0
common /force/ ftotx,ftoty,ftotz

call repmag!(ftotx,ftoty,ftotz)
call aleat(dx,dy,dz)
dgg=1.0-0.5*dgamma*dt !"1-0.5*gamma*h" en Paul 1995

```

!Calculation of positions

```
do i=1,nmax
```

```

fposx=0.5*dt*dt*(ftotx(i)) !"0.5*h^2*Fialfa(0)" en Paul 1995
fvelx(i)=(ftotx(i))*0.5*dt*(1.0-ddgamma*dt)/mas(i)           !"0.5*h*(1-
gamma*h)*Fialfa(0)"
fposy=0.5*dt*dt*(ftoty(i))
fvelx(i)=(ftoty(i))*0.5*dt*(1.0-ddgamma*dt)/mas(i)
fposz=0.5*dt*dt*(ftotz(i))
fvelz(i)=(ftotz(i))*0.5*dt*(1.0-ddgamma*dt)/mas(i)

```

!Equations of the Brownian motion

```

x(i)=x0(i)+vx0(i)*dt*dgg+fposx+0.5*sigma(i)*dt*dx(i)
y(i)=y0(i)+vy0(i)*dt*dgg+fposy+0.5*sigma(i)*dt*dy(i)
z(i)=z0(i)+vz0(i)*dt*dgg+fposz+0.5*sigma(i)*dt*dz(i)

```

!Periodic boundary conditions

```

x(i)=x(i)-lx*anint(x(i)/lx)
y(i)=y(i)-ly*anint(y(i)/ly)
z(i)=z(i)-lz*anint(z(i)/lz)

end do
do j=1,nmax
x0(j)=x(j)
y0(j)=y(j)
z0(j)=z(j)
end do

```

!Calculation of velocities

```

call repmag!(ftotx,ftoty,ftotz)
do i=1,nmax

```




```
fx=fvelx(i)+0.5*dt*(ftotx(i))/mas(i)"0.5*h*(1-gamma*h)*Fialfa(0) +
0.5*h*Fialfa(q(h))"
```

```
fy=fvely(i)+0.5*dt*(ftoty(i))/mas(i)
```

```
fz=fvelz(i)+0.5*dt*(ftotz(i))/mas(i)
```

```
vx(i)=vx0(i)+fx-ddgamma*dt*dgg*vx0(i)+(sigma(i)/mas(i))*dgg*dx(i)
```

```
vy(i)=vy0(i)+fy-ddgamma*dt*dgg*vy0(i)+(sigma(i)/mas(i))*dgg*dy(i)
```

```
vz(i)=vz0(i)+fz-ddgamma*dt*dgg*vz0(i)+(sigma(i)/mas(i))*dgg*dz(i)
```

```
end do
```

!Calculation of the velocity of the center of mass of the system

```
vxcm=0.0
```

```
vycm=0.0
```

```
vzcm=0.0
```

```
do j=1,nmax
```

```
vxcm=vxcm+(mas(j)*vx(j)/mastot)
```

```
vycm=vycm+(mas(j)*vy(j)/mastot)
```

```
vzcm=vzcm+(mas(j)*vz(j)/mastot)
```

```
end do
```

!The motion of the center of mass is corrected

```
do j=1,nmax
```

```
vx0(j)=vx(j)-vxcm
```

```
vy0(j)=vy(j)-vycm
```

```
vz0(j)=vz(j)-vzcm
```

```
end do
```

```
return
```

```
end
```



```

dixt=x0(j)-x0(i)
dixt=dixt-lx*anint(dixt/lx)
dixty=y0(j)-y0(i)
dixty=dixty-lx*anint(dixty/lx)
dixtz=z0(j)-z0(i)
dixtz=dixtz-lx*anint(dixtz/lx)
rv=sqrt(dixt*dixt+dixty*dixty+dixtz*dixtz)
uNrep=u0*rad(i)*rad(j)
r2=rad(i)+rad(j)
if (rv .lt. 4.) then!Cut-off for the repulsive force
f=-(.3/16.)*uNrep*exp(-50.*(rv-r2)/r2) !To obtain the initial equilibrium state
we have to eliminate the u0 dependence (in the case of u0=0)
else
f=0.
end if

!co=dixt/rv=rz: theta cosine
rx=dixt/rv
ry=dixty/rv
rz=dixtz/rv
co2=rz*rz !co2=co*co

!Magnetic force
uN=u0*(rad(i)*rad(i)*rad(i))*(rad(j)*rad(j)*rad(j)) !The new u0 depends on the
particle radius because of polydispersity. In the case of the monodisperse
system, uN=u0
rv4=rv*rv*rv*rv
fue=3.*uN*(1./rv4)

```



```

real*8 vx0(nmax),vy0(nmax),vz0(nmax),suma,rv3,f2
real*8 lx,ly,lz,l,distx,disty,distz,rv,rc,lcell
real*8 co,co2,se,se2tet,rx,ry,rz,tetx,tety,tetz
real*8 sigma(nmax),ddgamma,mas(nmax),rad(nmax),r2
integer*4 icajita(100,100,100)
common /bloque/ ddgamma,sigma,mas
common /pos/ x0,y0,z0
common /caja/ lx,ly,lz,l
common /vel/ vx0,vy0,vz0
common u0
common /radios/ rad

dkin=0.
nvecmedio=0.
pcoseno=0.
do j=1,nmax
dkin=dkin+(vx0(j)*vx0(j)+vy0(j)*vy0(j)+vz0(j)*vz0(j))*mas(j)
vecinos(j)=0.
coseno(j)=0.
end do
dkin=dkin/2./nmax !3/2 kT. Kinetic energy
dpot=0.
do i=1,nmax-1
do j=i+1,nmax
distx=x0(j)-x0(i)
distx=distx-lx*anint(distx/lx)
disty=y0(j)-y0(i)

```



```

disty=disty-lx*anint(disty/lx)
distrz=z0(j)-z0(i)
distrz=distrz-lx*anint(distrz/lx)
rv=sqrt(distrx*distrx+disty*disty+distrz*distrz)
uN=u0*(rad(i)*rad(i)*rad(i))*(rad(j)*rad(j)*rad(j))
uNrep=u0*rad(i)*rad(j)
r2=rad(i)+rad(j)
if (rv .lt. 4.) then
f2=-(3./16.)*uNrep*exp(-50.*(rv-r2)/r2)
else
f2=0.
end if

```

!Closer neighbors

```

co=distrz/rv
co2=co*co
rc=rad(i)+rad(j)+0.5
if (rv .le. rc) then
vecinos(i)=vecinos(i)+1.
vecinos(j)=vecinos(j)+1.
coseno(i)=coseno(i)+(co2-0.5)
coseno(j)=coseno(j)+(co2-0.5)
end if
rv3=rv*rv*rv

```

!Potential energy

```

dpot=dpot+2.*f2+uN*(1./(rv3))*(1.-3*co2)

```

```
end do
end do
do i=1,nmax
nvecmedio=nvecmedio+vecinos(i)/nmax
pcoseno=pcoseno+coseno(i)/nmax
end do
dpot = dpot/nmax
suma=0
```

!Columnar parameter: gives the structuration degree of particle columns

```
do ix=1,100
do iy=1,100
do iz=1,100
icajita(ix,iy,iz)=0
end do
end do
end do
ncell=int(lx/1.)+1
lcell=lx/ncell
do i=1,nmax
ix=int((x0(i)+lx/2.)/lcell)+1
iy=int((y0(i)+lx/2.)/lcell)+1
iz=int((z0(i)+lx/2.)/lcell)+1
icajita(ix,iy,iz)=1
end do
do izcor=1,ncell-1
do iz=izcor+1,ncell
```



```

real*8 co,co2,se,se2tet,rx,ry,rz,tetx,tety,tetz,fue,mas(nmax),rad(nmax)
common /radios/ rad
common /vel/ vx0,vy0,vz0
common /blot/ dt,t,ncorr
common /bloque/ ddgamma,sigma,mas
common u0
common /pos/ x0,y0,z0
common /caja/ lx,ly,lz,l

```

```
sumtau=0.0
```

!Calculation of the velocity components

```

do i=1,nmax
v(i,1)=vx0(i)
v(i,2)=vy0(i)
v(i,3)=vz0(i)
end do

```

!Initial conditions of the stress tensor components

```

do alf=1,2
do bet=alf+1,3
tau(alf,bet)=0.0
suma1(alf,bet)=0.0
suma1(bet,alf)=suma1(alf,bet)
suma2(alf,bet)=0.0
suma2(bet,alf)=suma2(alf,bet)
tau(bet,alf)=tau(alf,bet)

```



end do

end do

!Calculation of the stress tensor

do alf=1,3

do bet=1,3

do i=1,nmax

*suma1(alf,bet)=suma1(alf,bet)+mas(i)*v(i,alf)*v(i,bet)*

end do

end do

end do

!Calculation of the stress tensor component 3,3 (z,z). Normal force

do i=1,nmax-1

do j=i+1,nmax

*distx=x0(j)-x0(i)!*he cambiado j por i

*distx=distx-lx*anint(distx/lx)*

disty=y0(j)-y0(i)

*disty=disty-lx*anint(disty/lx)*

distz=z0(j)-z0(i)

*distz=distz-lx*anint(distz/lx)*

*rv=sqrt(distx*distx+disty*disty+distz*distz)*

dist(1)=distx

dist(2)=disty

dist(3)=distz

uN=u0(rad(i)*rad(i)*rad(i))*(rad(j)*rad(j)*rad(j))*

```

uNrep=u0*rad(i)*rad(j)
r2=rad(i)+rad(j)
if (rv .lt. 4.) then
f=-0.1875*uNrep*exp(-50.*(rv-r2)/r2)
else
f=0.
end if
rx=distx/rv
ry=disty/rv
rz=distz/rv
co2=rz*rz

```

!Magnetic force bewteen i and j

```

rv4=rv*rv*rv*rv
fue=3.*uN*(1./rv4)
fmagx=fue*((5.*co2-1.)*rx)
fmagy=fue*((5.*co2-1.)*ry)
fmagz=fue*((5.*co2-3.)*rz)
fmag(1)=fmagx
fmag(2)=fmagy
fmag(3)=fmagz
do alf=1,3
do bet=1,3

```

!Total force: magnetic + repulsive

```

suma2(alf,bet)=suma2(alf,bet)+dist(alf)*(f*(dist(bet)/rv)+fmag(bet)) !
end do

```



```

end do
end do
end do
do alf=1,3
do bet=1,3

```

!Total stress tensor component value

```

tau(alf,bet)=suma1(alf,bet)+suma2(alf,bet)
end do
end do
write(17,*) t,(tau(2,3)+tau(1,3))/2.,tau(3,3)
return
end

```

Structure factor $S(q)$

```

program factor
integer*4 nlim,cont,i,icorr,j,nz,k,nx,ny,cc
real*8lx,pi,mq,t,x(1000),y(1000),z(1000),va,vb,vc,coseno1,seno1,conseno2,seno
2,contador
real*8 pesc,sparal(500,-200:200),sperpen(500,-200:200,
200:200),suma1,suma2,q(0:10000)

```

!Opening files

```

open(12,file='pos.dat',status='old',form='unformatted')
open(15,file='sparal.dat',status='unknown')
open(20,file='sperpen.dat',status='unknown')

```



```
open(45,file='pantalla.dat',status='unknown')
```

```
read(12) lx
```

```
pi=acos(-1.) !Number Pi
```

```
mq=2.*pi/lx !Prefactor in the calculation of the wave vector
```

```
write(*,*) lx
```

```
nlim=200
```

```
cont=0
```

!Initialization of the parallel component

```
do icorr=1,500
```

```
do nz=-200,200
```

```
sparal(icorr,nz)=0.
```

```
end do
```

!Initialization of the perpendicular component

```
do nx=-200,200
```

```
do ny=-200,200
```

```
sperpen(icorr,nx,ny)=0.
```

```
end do
```

```
end do
```

```
end do
```

!Read the time and the correlator

```
do i=1,100000000
```

```
read(12,end=100) t,icorr
```

```
do j=1,1000
```



!Read the position of particles

```
read(12,end=100) x(j),y(j),z(j),va,vb,vc
end do
if (t .eq. 0.) then
cont=cont+1
write(*,*) icorr
```

!Wave vectors parallel to the magnetic field $n_x=n_y=0$

```
do nz=0,nlim
coseno1=0.
seno1=0.
do k=1,1000
pesc=z(k)*nz*mq
coseno1=coseno1+cos(pesc)
seno1=seno1+sin(pesc)
end do
sparal(icorr,nz)=coseno1*coseno1+seno1*seno1
end do
```

!Wave vectors perpendicular to the magnetic field $n_z=0$

```
do nx=1,nlim
do ny=1,nlim
coseno2=0.
seno2=0.
do k=1,1000
pesc=x(k)*nx*mq+y(k)*ny*mq !Scalar product q*r
```

```

coseno2=coseno2+cos(pesc)
seno2=seno2+sin(pesc)
end do
sperpen(icorr,nx,ny)=coseno2*coseno2+seno2*seno2
end do
end do
end if
end do
100 continue
do nz=1,nlim
suma1=0.
do icorr=1,cont
suma1=suma1+sparal(icorr,nz)
end do
write(15,*) abs(nz*mq),suma1/(1000.*cont)
end do
cc=0
q(0)=0.
contador=0.
do nx=1,nlim
do ny=1,nlim
suma2=0.
cc=cc+1
do icorr=1,cont
suma2=suma2+sperpen(icorr,nx,ny)
end do
q(cc)=sqrt((nx*mq)**2.+(ny*mq)**2.) !Magnitude of the wave vector

```




```

if (q(cc) .gt. contador) then
write(20,*) sqrt((nx*mq)**2.+(ny*mq)**2.),suma2/(1000.*cont)
contador=q(cc)+0.05
end if
end do
end do
stop
end

```

Crystal order parameters (Q_i)

```

program crystalorderparameter

implicit none
real*8
x(1100),y(1100),z(1100),vx(1100),vy(1100),vz(1100),distx,disty,distz,ntot,ALF
real*8r,lx,Alm(-10:10),pi,pj(-10:10,-10:10),pji(-10:10,-
10:10),rc,alfa(1100,1100),qtot
real*8 termcos1,termcos2,factor,Yima,Yreal,qreal,qima,alfatot,tt,mediaqtot
real*8 qimatot,qrealtot,nbondtot,jju(1100),liminf,limsup,aa,sen,a,b,c
integer*4 i,j,nbond(1100),h,gg,nvecver(1100),ii,jj,nvechor(1100),npart(0:20)
integer*4 l,m,nb,k,contador
real*8 fact,flmenosm,flmasm,flmasmmenosk,flmenosk,fkmenosm,fack
character*70 ffile
common /lon/ lx,pi,rc
common /nbond/ nbond
common /lm/ l,m

```

common /fact/ fact,flmenosm,flmasm,flmasmmenosk,flmenosk,fkmenosm,fack

common /pos/ x,y,z

common /alff/ alfa,ALF,nb

common /qq/ qimatot,qrealtot

common /coco/ jju

common /limites/ liminf,limsup

common /vecinos/ nvecver,nvechor

write(,*)* 'Positions file:'

read(,*)* ffile

open(12,file=ffile,status='old')

open(23,file='nbond-ji.dat',status='unknown')

!Definitions of the constants

pi=acos(-1.) **!Number Pi**

rc=2.47 **!Cut-off**

!Specification of parameter values

write(,*)* 'Harmonic parameters:'

write(,*)* '!' **!Parameter l**

read(,*)* l

!Initialization of some variables which are implied in the calculation of Spherical Harmonics

do i=1,1100

do j=1,1100

alfa(i,j)=0.



```
end do
end do
read(12,*) lx
mediaqtot=0.
contador=0
do i=1,110000
read(12,*,end=100) a,b,c,nb
write(*,*) i
ALF=0.
do j=1,1100
nbond(j)=0
end do
do j=1,nb
read(12,*,end=100) x(j),y(j),z(j)
end do
do j=1,nb-1
do k=j+1,nb
distx=x(k)-x(j)
disty=y(k)-y(j)
distz=z(k)-z(j)
r=sqrt(distx**2+disty**2+distz**2)
alfa(j,k)=((r-rc)/(2.-rc))*((r-rc)/(2.-rc))
alfa(k,j)=alfa(j,k)
ALF=ALF+alfa(j,k)+alfa(j,k)
if (r .le. rc) then
nbond(j)=nbond(j)+1
nbond(k)=nbond(k)+1
```




```

real*8
termcos1,termcos2,termcos3,termcos4,factor,Yima(1100,1100),Yreal(1100,110
0),qreal,qima
real*8 qimatot,qrealtot,alfatot,a,jju(1100),liminf,limsup
integer*4 i,j,h,nbond(1100),gg,ii,jj,nvecver(1100),nvechor(1100)
integer*4 l,m,nb
real*8 factl,flmenosm,flmasm,flmasmmenosk,flmenosk,fkmenosm,fack
common /nbon/ nbond
common /lm/ l,m
common /lon/ lx,pi,rc
common /fact/ factl,flmenosm,flmasm,flmasmmenosk,flmenosk,fkmenosm,fack
common /pos/ x,y,z
common /alff/ alfa,ALF,nb
common /qq/ qimatot,qrealtot
common /coco/ jju
common /limites/ liminf,limsup
common /vecinos/ nvecver,nvechor

```

!Initialization of the Associated Legendre Polynomials

```

do i=-10,10
do j=-10,10
pjj(i,j)=0.
pji(i,j)=0.
end do
end do
qimatot=0.
qrealtot=0.

```

qima=0.

qreal=0.

!Calculation of the Associated Legendre Polynomials

do i=1,nb-1

do j=i+1,nb

distx=x(j)-x(i)

distx=distx-lx*anint(distx/lx)

disty=y(j)-y(i)

disty=disty-lx*anint(disty/lx)

distz=z(j)-z(i)

distz=distz-lx*anint(distz/lx)

r=sqrt(distx**2+disty**2+distz**2)

a=distz/r

pij(0,0)=1.

pji(0,0)=1.

pij(1,0)=a

pji(1,0)=a

pij(1,1)=(1.-a**2)**0.5)

pji(1,1)=pij(1,1)

pij(1,-1)=(-1./2.)*pij(1,1)

pji(1,-1)=(-1./2.)*pji(1,1)

pij(2,0)=(1./8.)*(-4.+12.*(a**2))

pji(2,0)=pij(2,0)

pij(2,1)=-3.*a*(1.-a**2)**0.5

pji(2,1)=-3.*a*(1.-a**2)**0.5

pij(2,-1)=(-1./6.)*pij(2,1)



$$\begin{aligned}
 p_{ji}(2,-1) &= (-1./6.) * p_{ji}(2,1) \\
 p_{ij}(2,2) &= 3. * (1.-a^{**2}) \\
 p_{ji}(2,2) &= p_{ij}(2,2) \\
 p_{ij}(2,-2) &= (1./24.) * p_{ij}(2,2) \\
 p_{ji}(2,-2) &= (1./24.) * p_{ji}(2,2) \\
 p_{ij}(3,0) &= (1./48.) * 24. * a^{**(-3.+5. * (a^{**2}))} \\
 p_{ji}(3,0) &= p_{ij}(3,0) \\
 p_{ij}(3,1) &= -(3./2.) * (5. * (a^{**2}).-1.) * (1.-a^{**2})^{**0.5} \\
 p_{ji}(3,1) &= p_{ij}(3,1) \\
 p_{ij}(3,-1) &= (-1./12.) * p_{ij}(3,1) \\
 p_{ji}(3,-1) &= (-1./12.) * p_{ji}(3,1) \\
 p_{ij}(3,2) &= 15. * a^{** (1.-a^{**2})} \\
 p_{ji}(3,2) &= p_{ij}(3,2) \\
 p_{ij}(3,-2) &= (1./120.) * p_{ij}(3,2) \\
 p_{ji}(3,-2) &= (1./120.) * p_{ji}(3,2) \\
 p_{ij}(3,3) &= -15. * ((1.-a^{**2})^{**1.5}) \\
 p_{ji}(3,3) &= -15. * ((1.-a^{**2})^{**1.5}) \\
 p_{ij}(3,-3) &= (-1./720.) * p_{ij}(3,3) \\
 p_{ji}(3,-3) &= (-1./720.) * p_{ji}(3,3) \\
 p_{ij}(4,0) &= (1./8.) * (35. * (a^{**4}).-30. * (a^{**2}).)+3.) \\
 p_{ji}(4,0) &= p_{ij}(4,0) \\
 p_{ij}(4,1) &= (-5./2.) * a^{** (7. * (a^{**2}).-3.)} * (1.-a^{**2})^{**0.5} \\
 p_{ji}(4,1) &= p_{ij}(4,1) \\
 p_{ij}(4,-1) &= (-1./20.) * p_{ij}(4,1) \\
 p_{ji}(4,-1) &= (-1./20.) * p_{ji}(4,1) \\
 p_{ij}(4,2) &= (15./2.) * (7. * (a^{**2}).-1.) * (1.-a^{**2}) \\
 p_{ji}(4,2) &= p_{ij}(4,2)
 \end{aligned}$$

$$p_{ij}(4,-2)=p_{ij}(4,2)*(1./360.)$$

$$p_{ji}(4,-2)=p_{ji}(4,2)*(1./360.)$$

$$p_{ij}(4,3)=-105.*a*(1.-a^{**2})^{**1.5}$$

$$p_{ji}(4,3)=-105.*a*(1.-a^{**2})^{**1.5}$$

$$p_{ij}(4,-3)=p_{ij}(4,3)*(-1./5040.)$$

$$p_{ji}(4,-3)=p_{ji}(4,3)*(-1./5040.)$$

$$p_{ij}(4,4)=105.*((\sin(\text{distz}/r))^{**4}.)$$

$$p_{ji}(4,4)=p_{ij}(4,4)$$

$$p_{ij}(4,-4)=p_{ij}(4,4)*(1./40320.)$$

$$p_{ji}(4,-4)=p_{ji}(4,4)*(1./40320.)$$

$$p_{ij}(5,0)=(1./3840.)*480.*a*(15.-70.*a^{**2}+63.*(a^{**4}))$$

$$p_{ji}(5,0)=p_{ij}(5,0)$$

$$p_{ij}(5,1)=(-1./3840.)*((1.-a^{**2})^{**0.5})*7200.*(1.-14.*a^{**2}+21.*(a^{**4}))$$

$$p_{ji}(5,1)=p_{ij}(5,1)$$

$$p_{ij}(5,-1)=(-1./30.)*p_{ij}(5,1)$$

$$p_{ji}(5,-1)=(-1./30.)*p_{ij}(5,1)$$

$$p_{ij}(5,2)=(1./3840.)*(1.-a^{**2})*201600.*a*(-1.+3.*(a^{**2}))$$

$$p_{ji}(5,2)=p_{ij}(5,2)$$

$$p_{ij}(5,-2)=p_{ij}(5,2)*(1./840.)$$

$$p_{ji}(5,-2)=p_{ij}(5,2)*(1./840.)$$

$$p_{ij}(5,3)=(-1./3840.)*((1.-a^{**2})^{**1.5})*201600.*(-1.+9.*(a^{**2}))$$

$$p_{ji}(5,3)=p_{ij}(5,3)$$

$$p_{ij}(5,-3)=(-1./20160.)*p_{ij}(5,3)$$

$$p_{ji}(5,-3)=(-1./20160.)*p_{ij}(5,3)$$

$$p_{ij}(5,4)=(1./3840.)*((1.-a^{**2})^{**2})*3628800.*a$$

$$p_{ji}(5,4)=p_{ij}(5,4)$$



$$p_{ij}(5,-4)=p_{ij}(5,4)*(1./362880.)$$

$$p_{ji}(5,-4)=p_{ij}(5,-4)$$

$$p_{ij}(5,5)=(-1./3840.)*((1.-a^{**2})^{**2.5})*3628800.$$

$$p_{ji}(5,5)=p_{ij}(5,5)$$

$$p_{ij}(5,-5)=p_{ij}(5,5)*(-1./3628800.)$$

$$p_{ji}(5,-5)=p_{ij}(5,-5)$$

$$p_{ij}(6,0)=(1./46080.)*2880.*(-5.+105.*(a^{**2})-315.*(a^{**4})+231.*(a^{**6}))$$

$$p_{ji}(6,0)=p_{ij}(6,0)$$

$$p_{ij}(6,1)=(1./46080.)*((1.-a^{**2})^{**0.5})*120960.*a*(5.-30.*(a^{**2})+33.*(a^{**4}))$$

$$p_{ji}(6,1)=p_{ij}(6,1)$$

$$p_{ij}(6,-1)=p_{ij}(6,1)*(-1./42.)$$

$$p_{ji}(6,-1)=p_{ij}(6,-1)$$

$$p_{ij}(6,2)=(1./46080.)*((1.-a^{**2})^{**1.5})*604800.*(1.-18.*(a^{**2})+33.*(a^{**4}))$$

$$p_{ji}(6,2)=p_{ij}(6,2)$$

$$p_{ij}(6,-2)=p_{ij}(6,2)*(1./1680.)$$

$$p_{ji}(6,-2)=p_{ij}(6,-2)$$

$$p_{ij}(6,3)=(1./46080.)*((1.-a^{**2})^{**1.5})*7257600.*a*(-3.+11.*(a^{**2}))$$

$$p_{ji}(6,3)=p_{ij}(6,3)$$

$$p_{ij}(6,-3)=p_{ij}(6,3)*(-1./60480.)$$

$$p_{ji}(6,-3)=p_{ij}(6,-3)$$

$$p_{ij}(6,4)=(1./46080.)*((1.-a^{**2})^{**2})*21772800.*(-1.+11.*(a^{**2}))$$

$$p_{ji}(6,4)=p_{ij}(6,4)$$

$$p_{ij}(6,-4)=p_{ij}(6,4)*(1./1814400.)$$

$$p_{ji}(6,-4)=p_{ij}(6,-4)$$

$$p_{ij}(6,5)=(1./46080.)*((1.-a^{**2})^{**2.5})*479001600.*a$$

$$p_{ji}(6,5)=p_{ij}(6,5)$$

$p_{ij}(6,-5) = p_{ij}(6,5) * (-1./39916800.)$
 $p_{ji}(6,-5) = p_{ij}(6,-5)$
 $p_{ij}(6,6) = (1./46080.) * ((1.-a**2.)**3.) * 479001600.$
 $p_{ji}(6,6) = p_{ij}(6,6)$
 $p_{ij}(6,-6) = p_{ij}(6,6) * (1./479001600.)$
 $p_{ji}(6,-6) = p_{ij}(6,-6)$

!Spherical Harmonics $Y_{l,m}$

call factorial **!Call subroutine "factorial"**

$Alm(m) = \sqrt{(2.*l+1.) * flmenosm / (4.*pi * flmasm)}$

!Imaginary part I of the spherical harmonics

$Y_{ima}(i,j) = ((-$
 $1.)**abs(m)) * Alm(m) * p_{ij}(l,m) * \sin(abs(m)) * \cos(distx/\sqrt{distx**2.+disty**2.}))$

!Real part I of the spherical harmonics

$Y_{real}(i,j) = ((-$
 $1.)**abs(m)) * Alm(m) * p_{ij}(l,m) * \cos(abs(m)) * \cos(distx/\sqrt{distx**2.+disty**2.}))$

!Imaginary part II of the spherical harmonics

$Y_{ima}(j,i) = ((-1.)**abs(m)) * Alm(m) * p_{ji}(l,m) * \sin(abs(m)) * \cos((-$
 $distx)/\sqrt{distx**2.+disty**2.}))$

!Real part II of the spherical harmonics

$Y_{real}(j,i) = ((-1.)**abs(m)) * Alm(m) * p_{ji}(l,m) * \cos(abs(m)) * \cos((-$
 $distx)/\sqrt{distx**2.+disty**2.}))$

!Initialization of factorials

```
factl=1. !!!  
flmasm=1. !(l+m)!  
flmenosm=1. !(l-m)!  
flmasmmenosk=1. !(l+m-k)!  
flmenosk=1. !(l-k)!  
fkmenosm=1. !(k-m)!  
fack=1. !k!  
do t=0,l  
  if (t .eq. 0) then  
    factl=1.  
  else  
    factl=factl*(t)  
  end if  
end do  
do t=0,l+abs(m)  
  if (t .eq. 0) then  
    flmasm=1.  
  else  
    flmasm=flmasm*(t)  
  end if  
end do  
do t=0,l-abs(m)  
  if (t .eq. 0) then  
    flmenosm=1.  
  else  
    flmenosm=flmenosm*(t)
```



```
end if
end do
return
end
```

Mean square displacement (MSD)

```
program meansquaredisplacement
```

```
implicit none
```

```
real*8 x(1000),y(1000),z(1000),distx,disty,distz,despx,despy,despz
```

```
real*8 x0(1000,500),y0(1000,500),z0(1000,500),lx,ly,lz,phi,pi
```

```
real*8 vx0(1000,500),vy0(1000,500),vz0(1000,500),dcmtot,desptot
```

```
real*8 vx(1000),vy(1000),vz(1000)
```

```
real*8 t,dcmx,dcmz,mt(0:1000),md(500,1000,4),desp
```

```
integer*4 i,j,nmax,icorr,k,nfin,ncorr,cont(500)
```

```
character*70 ffile
```

```
write (*,*) 'File name:'
```

```
read (*,200) ffile
```

```
200 format (A70)
```

```
write (*,*) 'Particle concentration: '
```

```
read (*,*) phi
```

```
pi=acos(-1.) !Number Pi
```

```
nmax=1000
```

```
ncorr=1
```

```
!Opening of positions and mean square displacement files
```

open(unit=12,file=ffile,status='old',form='unformatted')
open(unit=14,file='dcm.dat',status='unknown')
read(12) lx
write(* ,*) lx
do icorr=1,500
cont(icorr)=0
end do
do j=1,1000000

!Read time and correlator

read(12,end=100) t,icorr
write(* ,*) t,icorr
if (icorr .gt. ncorr) ncorr=icorr
if (t .le. 1e-4) then
mt(cont(icorr))=t

!Read particle positions

do i=1,nmax
read(12,end=100)
x0(i,icorr),y0(i,icorr),z0(i,icorr),vx0(i,icorr),vy0(i,icorr),vz0(i,icorr)
end do
else
cont(icorr)=cont(icorr)+1

!Initialization of the mean square displacement

dcmx=0.0
dcmx=0.0



dcmz=0.0

dcmtot=0.0

do i=1,nmax

!Calculation of the mean square displacement

read(12,end=100) x(i),y(i),z(i),vx(i),vy(i),vz(i)

distx=x(i)-x0(i,icorr)

distx=distx-lx*anint(distx/lx)

disty=y(i)-y0(i,icorr)

disty=disty-lx*anint(disty/lx)

distz=z(i)-z0(i,icorr)

distz=distz-lx*anint(distz/lx)

dcmx=dcmx+distx*distx

dcmy=dcmy+disty*disty

dcmz=dcmz+distz*distz

dcmtot=dcmtot+distx*distx+disty*disty+distz*distz

end do

!Divide by the number of particles

dcmx=dcmx/nmax

dcmy=dcmy/nmax

dcmz=dcmz/nmax


dcmtot=dcmtot/(3.*nmax)

md(icorr,cont(icorr),1)=dcmx **!MSD x-axis**

md(icorr,cont(icorr),2)=dcmy **!MSD y-axis**

md(icorr,cont(icorr),3)=dcmz **!MSD z-axis**

md(icorr,cont(icorr),4)=dcmtot **!Total MSD**



```
mt(cont(icorr))=t
end if
end do
100 ncorr=ncorr-10
nfin=cont(ncorr)
do k=1,nfin
despx=0.0
despy=0.0
despz=0.0
desptot=0.0
do icorr=1,ncorr
```

!Divide by the number of correlators

```
despx=despx+md(icorr,k,1)/ncorr
despy=despy+md(icorr,k,2)/ncorr
despz=despz+md(icorr,k,3)/ncorr
desptot=desptot+md(icorr,k,4)/ncorr
end do
write(14,*) mt(k),despx,despy,despz,desptot
end do
close(12)
stop
end
```




Stress correlation function

program funcorrelacion

!Calculation of the stress tensor components

parameter (nmax=1000)

*integer**4 i,j,alf,bet,ncorr,icorr,kj,jcorr(500),nfin,k

*real**8 tau(3,3),v(nmax,3),dist(3),rv6,u0

*real**8 distx,disty,distz,rv,suma1(3,3),suma2(3,3)

*real**8 c,lx,m,sumtau(500,10000,3,3),dt,t,f,ekin

*real**8 x0(nmax),y0(nmax),z0(nmax),mt(0:10000),volpart,mm,diamed

*real**8 vx0(nmax),vy0(nmax),vz0(nmax),tau0(3,3,500),pi,mas(nmax)

*real**8 fmag(3),fmagx,fmagy,fmagz,rad(nmax),uN,uNrep,r2

*real**8 co,co2,se,se2tet,rx,ry,rz,tetx,tety,tetz,fue,fcorr(3,3),rv4

*real**8 A12(500),A13(500),A23(500),DeIA(500,10000),visc

*character**70 ffile

dt=0.0005 **!Time step**

ncorr=1

u0=x **!Introduce value of u0**

do icorr=1,500

!From Einstein relationship

A12(icorr)=0.

A13(icorr)=0.

A23(icorr)=0.

end do

do icorr=1,500

```

do k=1,10000
DeLA(icorr,k)=0.
end do
end do
do icorr=1,500

```

!Non-diagonal stress tensor components

```

tau0(1,2,icorr)=0.
tau0(1,3,icorr)=0.
tau0(2,3,icorr)=0.
end do
do icorr=1,500
jcorr(icorr)=0
end do

```

!Opening of files

```

open(12,file='pos.dat',status='old',form='unformatted') !Positions and velocities
file
open(17,file='funcorr-poli.dat',status='unknown')!fichero de salida
open(26,file='prom3tau+vis.dat',status='unknown')
open(unit=31,file='diam_alea.dat',status='unknown') !fichero de radios
open(unit=222,file='prueba_tensor.dat',status='unknown')
read(31,*) volpart
read(31,*) diamed
read(31,*) mm
pi=acos(-1.) !Number Pi
do i=1,nmax
read(31,*) rad(i)

```



```

mas(i)=(4./3.)*pi*(rad(i)**3.)
mas(i)=mas(i)/mm!normalizado por la masa media
end do
read(12) lx
write(*,*) lx
write(*,*) (volpart/0.05)**(1./3.)
do kj=1,1000000
read(12,end=100) t,icorr
if (icorr .gt. ncorr) then
ncorr=icorr
end if
if (t .lt. dt/2.) write (*,*) 'Starting correlator ',icorr
jcorr(icorr)=jcorr(icorr)+1
mt(jcorr(icorr))=t

```

!Read positions and velocities

```

do i=1,nmax
read(12,end=100) x0(i),y0(i),z0(i),vx0(i),vy0(i),vz0(i)
end do

```

!Calculation of the velocity components

```

do i=1,nmax
v(i,1)=vx0(i)
v(i,2)=vy0(i)
v(i,3)=vz0(i)
end do

```

!Initialization of the stress tensor components

```

do alf=1,3
do bet=1,3
tau(alf,bet)=0.0
suma1(alf,bet)=0.0
suma2(alf,bet)=0.0
end do
end do

```

!Calculation of the stress tensor

```

do alf=1,2
do bet=alf+1,3
do i=1,nmax
suma1(alf,bet)=suma1(alf,bet)+mas(i)*v(i,alf)*v(i,bet)!sumando de las
velocidades
end do
end do
end do
do i=1,nmax-1
do j=i+1,nmax

```

!Periodic boundary conditions

```

dix=x0(j)-x0(i)
dix=dix-lx*anint(dix/lx)
dix=y0(j)-y0(i)
dix=dix-lx*anint(dix/lx)
dix=z0(j)-z0(i)
dix=dix-lx*anint(dix/lx)

```



!Distance between particles

$rv = \sqrt{\text{distx}^2 + \text{disty}^2 + \text{distz}^2}$

$\text{dist}(1) = \text{distx}$

$\text{dist}(2) = \text{disty}$

$\text{dist}(3) = \text{distz}$

!u0 for polydispersity

$uN = u0 * (\text{rad}(i) * \text{rad}(i) * \text{rad}(i)) * (\text{rad}(j) * \text{rad}(j) * \text{rad}(j))$

$uN\text{rep} = u0 * \text{rad}(i) * \text{rad}(j)$

$r2 = \text{rad}(i) + \text{rad}(j)$

if (rv .lt. 4.) then

$f = -(3./16.) * uN\text{rep} * \exp(-50. * (rv - r2) / r2)$

else

$f = 0.$

end if

$rx = \text{distx} / rv$

$ry = \text{disty} / rv$

$rz = \text{distz} / rv$

$co2 = rz * rz$

!Components of the magnetic forces

$rv4 = rv * rv * rv * rv$

$fue = 3. * uN * (1./rv4)$ **!Magnitude of the magnetic force**

$f\text{magx} = fue * ((5. * co2 - 1.) * rx)$

$f\text{magy} = fue * ((5. * co2 - 1.) * ry)$

$f\text{magz} = fue * ((5. * co2 - 3.) * rz)$

$f\text{mag}(1) = f\text{magx}$

```

fmag(2)=fmagy
fmag(3)=fmagz
do alf=1,2
do bet=alf+1,3
suma2(alf,bet)=suma2(alf,bet)+dist(alf)*((dist(bet)/rv)*f+fmag(bet))
end do
end do
end do
end do

```

!Stress tensor components

```

do alf=1,2
do bet=alf+1,3
tau(alf,bet)=suma2(alf,bet)+suma1(alf,bet)
if (mt(jcorr(icorr)) .lt. dt/2.) then
tau0(alf,bet,icorr)=tau(alf,bet)!esfuerzo inicial para el correlador icorr
end if
sumtau(icorr,jcorr(icorr),alf,bet)=tau(alf,bet)*tau0(alf,bet,icorr)
end do
end do

```

!Calculation of the viscosity by means of the Einstein relationship

```

A12(icorr)=A12(icorr)+tau(1,2)*dt A13(icorr)=A13(icorr)+tau(1,3)*dt
A23(icorr)=A23(icorr)+tau(2,3)*dt
DeIA(icorr,jcorr(icorr))=((A13(icorr)+A23(icorr)+A12(icorr))*2.)
write(222,*) icorr,t,(tau(2,3)+tau(1,3))/2.,suma2(3,3)+suma1(3,3)
call flush(222)

```



end do

100 ncorr=ncorr-50

nfin=jcorr(ncorr) **!Total final time**

do k=2,nfin

!Initialization of the stress correlation functions

fcorr(1,2)=0.0

fcorr(1,3)=0.0

fcorr(2,3)=0.0

visc=0.

do icorr=1,ncorr

!At the moment k, there is an average over all the correlators

fcorr(1,2)=fcorr(1,2)+sumtau(icorr,k,1,2)/(lx*lx*lx*ncorr)

fcorr(1,3)=fcorr(1,3)+sumtau(icorr,k,1,3)/(lx*lx*lx*ncorr)

fcorr(2,3)=fcorr(2,3)+sumtau(icorr,k,2,3)/(lx*lx*lx*ncorr)

visc=visc+DeIA(icorr,k)/ncorr **!Calculation of the viscosity to compare with the**

other calculation method

end do

write(17,)* mt(k),fcorr(1,2),fcorr(1,3),fcorr(2,3),(fcorr(1,3)+fcorr(2,3))/2.

write(26,)* mt(k),(fcorr(1,2)+fcorr(1,3)+fcorr(2,3))/3.,visc/(mt(k)*lx*lx*lx*6.)

call flush(17)

call flush(26)

end do

stop

end

◆

Bond correlation function

program neighbors

*real*8* x(1000),y(1000),z(1000),distx,disty,distz,despx,despy,despz

*real*8* x0(1000,500),y0(1000,500),z0(1000,500),lx,ly,lz,phi,pi,g

*real*8* vx0,vy0,vz0,desv

*real*8* vx,vy,vz,p0(1000,1000),p(1000,1000)

*real*8* t,mt(1:1000),vec(500,1000),media

*integer*4* i,j,nmax,icorr,k,nfin,ncorr,cont(500)

*character*70* ffile

nmax=1000 **!Number of particles**

ncorr=1

!Opening of files

open(unit=12,file='pos.dat',status='old',form='unformatted')

open(unit=14,file='fvecinos.dat',status='unknown')

read(12) lx

write(* ,*) lx

do icorr=1,500

cont(icorr)=0

end do

do icorr=1,500

do k=1,1000

vec(icorr,k)=0.

end do



```
end do
do j=1,1000000
read(12,end=100) t,icorr
if (icorr .gt. ncorr) ncorr=icorr
if (t .lt. 0.0005) then
write(*,*) 'Starting correlator', icorr
cont(icorr)=1
mt(cont(icorr))=t
```

!Read positions and velocities

```
do i=1,nmax
read(12,end=100) x0(i,icorr),y0(i,icorr),z0(i,icorr),vx0,vy0,vz0
end do
else
cont(icorr)=cont(icorr)+1
mt(cont(icorr))=t
do i=1,nmax
read(12,end=100) x(i),y(i),z(i),vx,vy,vz
end do
end if
g=0.
do i=1,nmax-1
do k=i+1,nmax
```

!Periodic boundary conditions

```

distx=x0(i,icorr)-x0(k,icorr)
distx=distx-lx*anint(distx/lx)
disty=y0(i,icorr)-y0(k,icorr)
disty=disty-lx*anint(disty/lx)
distrz=z0(i,icorr)-z0(k,icorr)
distrz=distz-lx*anint(distz/lx)
r=distx*distx+disty*disty+distrz*distrz

```

if (r .le. 6.25) then

p0(i,k)=1.

p0(k,i)=1.

g=g+1.

else

p0(i,k)=0.

p0(k,i)=0.

end if

end do

end do

if (cont(icorr) .gt. 1) then

g=0.

do i=1,nmax-1

do k=i+1,nmax

distx=x0(i,icorr)-x(k)

*distx=distx-lx*anint(distx/lx)*

disty=y0(i,icorr)-y(k)

*disty=disty-lx*anint(disty/lx)*



```
distz=z0(i,icorr)-z(k)
distz=distz-lx*anint(distz/lx)
r=distx*distx+disty*disty+distz*distz
if (r .le. 6.25) then
  g=g+1.
  p(i,k)=1.
  p(k,i)=1.
else
  p(i,k)=0.
  p(k,i)=0.
end if
end do
end do
do i=1,nmax-1
  do k=i+1,nmax
    vec(icorr,cont(icorr))=vec(icorr,cont(icorr))+(p(i,k)*p0(i,k))/(g)
  end do
end do
else
  do i=1,nmax-1
    do k=i+1,nmax
      vec(icorr,cont(icorr))=vec(icorr,cont(icorr))+(p0(i,k))/(g)
    end do
  end do
end if
end do
100 ncorr=ncorr-200
```

```

nfin=cont(ncorr)
do k=1,nfin
media=0.
desv=0.
do icorr=1,ncorr
media=media+vec(icorr,k)/(ncorr)
desv=desv+vec(icorr,k)*vec(icorr,k)/(ncorr)
end do
desv=desv-media*media
write(14,*) mt(k),media,sqrt(desv)
end do
stop
end

```

Viscosity (From the Einstein relationship)

```

program viscosity
implicit none

```

```

real*8 Atot,A2,lx,ly,lz,phi,pi,eta(100000),A,dcmx,dcmz,var
real*8 t,dcm,mt(0:100000),At(500,100000),tpro,etapro,var1,var2
integer*4 j,icorr,k,nfin,ncorr,cont(500),nmax,pro
character*70 ffile

```

!Opening of files

```

write (*,*) 'File name:'
read (*,200) ffile
200 format (A70)

```



```
pi=acos(-1.)
```

```
nmax=1000
```

lx=x !Depending on the system: monodisperse or polydisperse. We have a cubic box.

```
ly=lx
```

```
lz=lx
```

```
write (*,*) lx
```

```
ncorr=1
```

```
open(unit=15,file=ffile,status='old')
```

```
open(unit=17,file='viscosidad.dat',status='unknown')
```

```
do icorr=1,500
```

```
cont(icorr)=0
```

```
end do
```

```
do icorr=1,500
```

```
do j=1,100000
```

```
At(icorr,j)=0.0
```

```
end do
```

```
end do
```

```
do j=1,1000000
```

!Read correlator, time, mean square displacement in three coordinate axes and the necessary magnitudes to calculate the viscosity from the Einstein relationship

```
read(15,*,end=100) icorr,t,dcmx,dcmx,dcmz,A,A2
```

```
if (icorr .gt. ncorr) then
```

```
ncorr=icorr
```

```
end if
```

```

cont(icorr)=cont(icorr)+1
At(icorr,cont(icorr))=A2
mt(cont(icorr))=t
end do
100 ncorr=ncorr-60 !We subtract correlators in order to achieve a larger time
in the evolution of the system
nfin=cont(ncorr)
etapro=0.
pro=0
do k=1,nfin
Atot=0.0
do icorr=1,ncorr
Atot=Atot+At(icorr,k)
end do
eta(k)=(Atot/(2.*lx*ly*lz))/ncorr
end do
do k=1,nfin
var1=0.
var2=0.
do icorr=1,ncorr
var1=var1+(At(icorr,k)/(2.*lx*ly*lz))*(At(icorr,k)/(2.*lx*ly*lz))
end do
var=var1/ncorr-eta(k)*eta(k)
write(17,*) mt(k),eta(k),var !Time, viscosity, standard deviation
end do
stop
end

```




BRIEF CV

El doctorando Juan Pablo Segovia Gutiérrez se licenció en Física por la Universidad de Granada en el año 2008 y a principios de 2009 pasó a formar parte del Grupo de Física de Fluidos y Biocoloides del Departamento de Física Aplicada de la Universidad de Granada, de la mano de Roque Hidalgo Álvarez y Juan de Vicente Álvarez Manzaneda, que serán sus directores de Tesis durante todo el doctorado, incorporándose después como tercer co-director, Antonio Manuel Puertas López, del Grupo de Física de Fluidos Complejos de la Universidad de Almería. El doctorando entró en la línea de investigación relacionada con Reología, y más concretamente, con Magneto-reología, que se encarga del estudio de fluidos magneto-reológicos, materiales inteligentes con propiedades que pueden ser modificadas mediante la aplicación de campos magnéticos externos. Durante su doctorado se especializó en el uso de técnicas experimentales basadas en reometría torsional (con un reómetro MCR 501, Anton Paar) con el fin de caracterizar estos fluidos, además de desarrollar habilidades en técnicas computacionales en Dinámica Browniana como complemento a la parte experimental. También adquirió conocimiento sobre las diversas teorías que modelan el comportamiento de los fluidos magneto-reológicos bajo diferentes condiciones de flujo. Realizó sus cursos predoctorales en Santiago de Compostela en junio de 2009, dentro del programa de doctorado “Ciencia y Tecnología de Coloides e Interfases”, obteniendo el Diploma de Estudios Avanzados (DEA) en octubre de 2010.

Como experiencia en congresos, el doctorando asistió a diversas conferencias de carácter científico tales como el Soft Matter Conference celebrado en Granada en 2010 (poster), el RIC14 celebrado en Oporto en 2011 (oral), los cursos de formación para jóvenes investigadores de Jülich en 2012 (poster), el



ERMR International Conference en Ankara en 2012 (oral) o el RIC15 en San Sebastián en 2013 (oral) y, además, impartió diversos seminarios de ámbito departamental.

Complementariamente a su formación en la Universidad de Granada, el doctorando realizó una estancia de tres meses y medio en Oporto con los profesores Fernando Pinho, Manuel Alves y Francisco J. Galindo, en el Departamento de Ingeniería Química, dentro del Transport Phenomena Research Center (CEFT), de la Universidad de Oporto, donde se instruyó en el uso y manejo de un reómetro extensional tipo Haake Caber 1, sumando así una técnica experimental más, que resulta fundamental dentro del ámbito de la reología.

Con todo, el doctorando ha conseguido, hasta la fecha y durante su época predoctoral, una producción científica que asciende a 9 publicaciones en JCR (a continuación), en revistas de primer impacto en el ámbito de la reología y los coloides, además de diversos capítulos de libro.

Publicaciones

J. de Vicente, J.P. Segovia-Gutiérrez, E. Andablo-Reyes, F. Vereda and R. Hidalgo-Álvarez, Dynamic Rheology of Sphere- and Rod-based Magnetorheological Fluids *Journal of Chemical Physics*, **131**, 194902-01-10, 2009.

J. de Vicente, F. Vereda, J. P. Segovia-Gutiérrez, M. P. Morales and R. Hidalgo-Álvarez, Effect of Particle Shape in Magnetorheology *Journal of Rheology*, **54**, 1337-1343, 2010.

F. Vereda, J. de Vicente, J. P. Segovia-Gutiérrez and R. Hidalgo-Álvarez, On the Effect of Particle Porosity and Roughness in Magnetorheology *Journal of Applied Physics*, **110**, 063520, 2011.

J. de Vicente, J. A. Ruiz-López, E. Andablo-Reyes, J. P. Segovia-Gutiérrez and R. Hidalgo-Álvarez, Squeeze Flow Magnetorheology *Journal of Rheology*, **55**, 753-779, 2011.

F. Vereda, J. de Vicente, J. P. Segovia-Gutiérrez and R. Hidalgo-Álvarez, Average Particle Magnetization as an Experimental Scaling Parameter for the Yield Stress of Dilute Magnetorheological Fluids *Journal of Physics D: Applied Physics*, **44**, 425002, 2011.

J. P. Segovia-Gutiérrez, C. L. A. Berli and J. de Vicente, Non-linear Viscoelasticity and Two-step Yielding in Magnetorheology: a Colloidal Gel Approach to Understand the Effect of Particle Concentration *Journal of Rheology*, **56(6)**, 1429-1448, 2012.

J. P. Segovia-Gutiérrez, J. de Vicente, R. Hidalgo-Alvarez and A. M. Puertas Brownian Dynamics Simulations in Magnetorheology and Comparison with Experiments, *Soft Matter*, **9**, 6970-6977, 2013.

J. P. Segovia-Gutiérrez, J. de Vicente, R. Hidalgo-Álvarez and A. M. Puertas Brownian Dynamic Simulations and Experiments of MR Fluids *Journal of Physics: Conference Series*, **412**, 012056, 2013.



Capítulos de libro

J. A. Ruiz-López, E. Andablo-Reyes, J. P. Segovia-Gutiérrez, R. Hidalgo-Álvarez and J. de Vicente, Squeeze Flow Magnetorheology in **IV Reunión Ibérica de Coloides e Interfases (RICI)**, and **IX Reunión del Grupo Especializado de Coloides e Interfases (GECI)**, ISBN 978-989-97397-0-3.

J. P. Segovia-Gutiérrez, J. de Vicente and R. Hidalgo-Álvarez, On the Validity of Strain-rate Frequency Superposition in Magnetic Field-induced Colloidal Structures in **IV Reunión Ibérica de Coloides e Interfases (RICI)**, and **IX Reunión del Grupo Especializado de Coloides e Interfases (GECI)**, ISBN 978-989-97397-0-3.

J. P. Segovia-Gutiérrez, A. M. Puertas, J. de Vicente and R. Hidalgo-Álvarez, A Rheological Probe of the Structural Relaxation of Magnetorheological Fluids in **First Workshop on Advances in Colloidal Materials**, ISBN 978-84-338-5324-0
F. Vereda, J. de Vicente, J. P. Segovia-Gutiérrez and R. Hidalgo-Álvarez, Particle Porosity in Magnetorheology in **First Workshop on Advances in Colloidal Materials**, ISBN 978-84-338-5324-0.